

RARE ISOTOPE BEAM ENERGY MEASUREMENTS AND SCINTILLATOR  
DEVELOPMENTS FOR REA3

By

Ling-Ying Lin

A DISSERTATION

Submitted to  
Michigan State University  
in partial fulfillment of the requirements  
for the degree of

Physics – Doctor of Philosophy

2015

## ABSTRACT

### RARE ISOTOPE BEAM ENERGY MEASUREMENTS AND SCINTILLATOR DEVELOPMENTS FOR REA3

By

Ling-Ying Lin

The ReAccelerator for 3 MeV/u beams (ReA3) at the National Superconducting Cyclotron Laboratory (NSCL) in Michigan State University can stop rare isotope beams produced by in-flight fragmentation and reaccelerate them in a superconducting linac. The precise knowledge of the energy and the energy spread of the ion beams extracted from the ReA3 linac is essential for experimental requirement in many applications. Beam energy determination methods such as implantation on a Si detector and/or using calibrated linac settings are precise within a few tens of keV/u. In order to determine beam energies with good resolution of  $\leq 0.5\%$  FWHM, a  $45^\circ$  bending magnet with a movable slit is used to determine the absolute beam energy based on the magnetic rigidity. Two methods have been developed for the energy calibration of the beam analyzing magnet:  $\gamma$ -ray nuclear resonance reactions and a time-of-flight (TOF) technique. The resonance energies of  $\gamma$ -ray resonant reactions provide well-known and precise calibration points. The gamma ray yields of the  $^{27}\text{Al}(p,\gamma)^{28}\text{Si}$  at  $E_p = 992$  keV and  $632$  keV resonances and  $^{58}\text{Ni}(p,\gamma)^{59}\text{Cu}$  at  $E_p = 1843$  keV resonance have been measured with the high efficiency CAESAR (CAESium iodide ARray) and SuN (Summing NaI(Tl)) detectors. By fitting the observed resonant  $\gamma$ -ray yields, not only the beam energy can be precisely correlated with the magnetic field but also beam energy spread can be obtained. The measured beam energy spread is consistent with beam optics calculations.

A time-of-flight system for determining the absolute energy of ion beams and calibrating the  $45^\circ$  magnetic analyzer has been developed in ReA3 by using two identical secondary electron monitors (grid-MCP detectors) with appropriate separation. The TOF technique is applicable to the variety of beam energies and ion particles. Velocities of ion beam are determined by simultaneously measuring the arrival time of beam bunches at the two detectors with respect to the accel-

eration RF clock. The time-of-flight system can provide beam energy information with precision of  $\Delta E/E < 0.1\%$ .

Scintillators are widely used to reliably measure beam profiles and beam distributions. At low energies, scintillator-based diagnostic devices are more problematic because of their fast light yield degradation under ion bombardment. The degradation of the scintillation yield of single crystal YAG:Ce under  $\text{He}^+$  irradiation at low energies between 28 and 58 keV has been systematically studied. The scintillator was irradiated at the rare isotope ReAccelerator (ReA) facility. The scintillation emission is attributed to its rapid  $5d-4f$  transition of  $\text{Ce}^{3+}$  ions. As the bombardment time increases, an exponential decay of the light output is observed due to the induced radiation damage of the crystal lattice. The decrease of the experimentally observed light yield as a function of particle fluence is found to be in fair agreement with the Birks model. Analysis indicates that the damage cross section of scintillation centers slightly decreases with the ion energy. The scintillator degrades slower under higher-energy irradiation.

In order to investigate scintillation degradation over a wide range of irradiation energies and scintillator materials, the scintillation processes for KBr, YAG:Ce,  $\text{CaF}_2:\text{Eu}$  and CsI:Tl crystals under  $\text{H}_2^+$  irradiation in the energy range of 600-2150 keV/u have been investigated. The data indicates that YAG:Ce and CsI:Tl can maintain stable luminescence under continuous ion bombardment for at least a total fluence of  $1.8 \times 10^{12}$  ions/ $\text{mm}^2$ . On the other hand, the luminescence of  $\text{CaF}_2:\text{Eu}$  shows a rapid initial decay but then maintains a nearly constant luminescence yield. The extraordinary scintillation response of KBr is initially enhanced under ion bombardment, approaches a maximum, and then eventually decays. The scintillation efficiency of the CsI:Tl scintillator is superior to the other materials. The low-energy  $\text{H}_2^+$  bombardment (25 keV/u) on the YAG:Ce scintillator can lead to the significant degradation of the scintillation yields. Different scintillation degradation responses for the low- and high-energy bombardments can be attributed to the transmission loss of the emitted light inside the crystal caused by displacement damages.

This dissertation is dedicated to my dear family.

## ACKNOWLEDGMENTS

First of all, I am extremely grateful and indebted to my advisor Daniela Leitner for her expertise, enthusiasm, wisdom, and valuable guidance extended to me. She has been very helpful and always there for me to answer my questions and give me suggestions. My Ph.D program would not have been possible without her support and encouragement. Through these years at the NSCL, I thank her for providing me all kinds of resources and making me a qualified researcher. Also, I would like to thank my supervisors Georgios Perdikakis and Fernando Montes for giving me the opportunity to work with them. Their expertise and knowledge in their fields helped me accomplish my dissertation projects. I also wish to express my gratitude to the remaining members of my guidance committee: Vladimir Zelevinsky, Felix Marti, Kirsten Tollefson, and Phillip M. Duxbury, for their continuous support, guidance and suggestions. I am especially grateful to Vladimir Zelevinsky for introducing me to the fantastic fields of nuclear physics and accelerator physics.

To the members of the ReA3 team: Walter Wittmer, Samuel Nash, Shannon Krause, Jose Alberto Rodriguez, Randy Rencsok, Scott Williams, Xiaoyu Wu, Michael Syphers, Alain Lapierre, Daniel Alt, Daniel Crisp, and Carla Benattia, my dissertation projects could not have been completed without their great effort, excellent expertise, and enthusiastic cooperation. They facilitated me with the essential resources necessary to accomplish my projects. It was a great pleasure for me to work with the ReA3 family.

I am deeply grateful to the CAESAR detector group, SuN detector group and ANASEN detector group for installing their instruments and giving me an opportunity to use their equipment. These people are : Artemis Spyrou, Stephen Quinn, Anna Simon, Alexander Dombos, Farheen Naqvi, Vincent Bader, Dirk Weisshaar, Grigory Rogachev, and Jeff Blackmon. Without their dedicated support and contributions, my experiment would not have been as successful as it was.

Many NSCL personnel also helped make a valuable contribution to my experimental success.

I would like to thank Jeffrey Wenstrom, David Ruddock, Ben Arend, and Alex Benson for great support with mechanical design; Shailendra Chouhan for providing simulation information of the dipole magnetic field; Ghulam Mujtaba for the installation of beam current monitors; John Yurkon for target fabrication; Scott Hitchcock for the support of the dipole field mapping; Jeromy Tompkins for the software support of the NSCL data acquisition system; Hendrik Schatz, Justin Browne, Antonios Kontos, Zachary Meisel, Tony Ahn for contributing their time to participate in my experiment.

It was very enjoyable to collaborate with the GSI diagnostic group in Germany for the scintillator screen study. I acknowledge fruitful discussions and comments from Beata Walasek-Höhne. I also sincerely thank her for providing a high performance CCD and spectrometer.

I am indebted to all my friends and family who have supported me all these years. Their unceasing encouragement and motivation helped me overcome setbacks and stay focused on my graduate study. I am very thankful for their confidence in me. Also, I would like to thank my loving husband for always believing in me and never doubting me in my educational endeavor. When I was depressed, he always found a way to make me laugh and make me feel better. His wisdom and unconditional love helped me become a better and stronger person.

Last but not least, I am thankful to God for the inspiration, motivation, guidance, and wisdom.

## TABLE OF CONTENTS

LIST OF TABLES . . . . .	ix
LIST OF FIGURES . . . . .	xi
CHAPTER 1 INTRODUCTION . . . . .	1
1.1 Conceptual overview of the Coupled Cyclotron Facility and ReA3 . . . . .	3
1.2 Energy measurement and calibration of a magnetic analyzer . . . . .	8
1.3 Scintillator screen . . . . .	13
CHAPTER 2 THEORY . . . . .	19
2.1 Dipole calibration factor . . . . .	19
2.2 Resonance nuclear reaction . . . . .	21
2.3 Scintillation mechanism and degradation . . . . .	31
2.3.1 Scintillation mechanism . . . . .	31
2.3.2 Scintillation degradation . . . . .	34
2.3.2.1 F centers . . . . .	34
2.3.2.2 V centers . . . . .	35
CHAPTER 3 BEAM ENERGY CALIBRATION . . . . .	37
3.1 (p, $\gamma$ ) resonant reactions . . . . .	37
3.1.1 Target thickness determination . . . . .	37
3.1.2 $\gamma$ -ray detectors . . . . .	40
3.1.2.1 CAESAR detector . . . . .	40
3.1.2.2 SuN detector . . . . .	46
3.1.3 Beam tune setup . . . . .	49
3.1.3.1 Beam simulation . . . . .	53
3.1.3.2 Cycling procedure and excitation curve of a magnet . . . . .	56
3.1.3.3 Consistent beam transport procedure . . . . .	60
3.1.4 Data analysis and result . . . . .	62
3.1.4.1 Detector calibration and $\gamma$ -ray spectra . . . . .	62
3.1.4.1.1 CAESAR analysis . . . . .	63
3.1.4.1.2 SuN analysis . . . . .	68
3.1.4.2 Magnetic field correction . . . . .	74
3.1.4.3 Fitting and error analysis . . . . .	80
3.1.5 Comparison of beam energy spread between data and beam simulation . . . . .	86
3.2 Time-of-flight measurements . . . . .	93
3.2.1 Time-resolution simulation of a grid-MCP detector . . . . .	95
3.2.1.1 Consideration of the initial energy and angular distribution of secondary electrons . . . . .	96
3.2.1.2 Consideration of the 45 degree incident angle of the bombard- ing ions . . . . .	98

3.2.1.3	Consideration of beam bunch length . . . . .	100
3.2.1.4	A Method for time-resolution improvement of a grid-MCP detector	101
3.2.2	Experimental setup . . . . .	102
3.2.2.1	Detector hardware . . . . .	102
3.2.2.2	Detector software implementation . . . . .	103
3.2.2.3	Beam transport . . . . .	105
3.2.3	Data analysis and results . . . . .	108
CHAPTER 4	SCINTILLATION DEGRADATION MEASUREMENT UNDER ION BOMBARDMENT . . . . .	115
4.1	Experimental setup . . . . .	116
4.2	Data analysis . . . . .	121
4.3	Results and discussion . . . . .	124
4.3.1	Scintillation investigation of YAG:Ce under low-energy ion bombardment .	124
4.3.1.1	Scintillation efficiency . . . . .	124
4.3.1.2	Scintillation degradation . . . . .	124
4.3.1.3	The Birks model . . . . .	127
4.3.2	Scintillation investigation of KBr, YAG:Ce, CaF <sub>2</sub> :Eu and CsI:Tl under high-energy ion bombardment . . . . .	133
4.3.2.1	Scintillation yield response . . . . .	133
4.3.2.2	Scintillation yield comparison . . . . .	140
4.3.2.3	Stability of beam profile width . . . . .	140
4.3.3	Scintillation stability comparison in low- and high-energy irradiation . . . .	145
CHAPTER 5	SUMMARY AND CONCLUSIONS . . . . .	149
5.1	Beam energy calibration and determination . . . . .	149
5.2	Scintillation degradation measurements . . . . .	151
BIBLIOGRAPHY . . . . .		153

## LIST OF TABLES

Table 1.1	(p, $\gamma$ ) resonances commonly used for beam energy calibration in most of accelerators. [ Uhrmacher et al. (1985)] [ Bondelid & Kennedy (1959)]. . . . .	12
Table 3.1	The resonance parameters used for the simulation of the resonance yields in Figure 3.1 and Figure 3.2 . . . . .	38
Table 3.2	The optimized amplitude and phase setting of the SRF cavities in CM1 and CM2 for the first and second parts of the beam energy calibration measurements. . . . .	54
Table 3.3	Calibration sources and $\gamma$ -ray energies for CAESAR. . . . .	63
Table 3.4	Calibration factor $k$ ( $\times 10^{-6}$ T/ $\sqrt{keV * amu}$ ) obtained in the first part of the beam energy calibration measurements. . . . .	84
Table 3.5	Beam energy spread (in %) with 68%, 95%, and 99.7% of the beam particles in the first part of the beam energy calibration measurements. . . . .	85
Table 3.6	Calibration factor $k$ (in T/ $\sqrt{keV * amu}$ ) obtained under the three different conditions of the horizontal slit in the diagnostic station 15 in the second part of the beam energy calibration measurements. . . . .	86
Table 3.7	Beam energy spread (in %) obtained with 68%, 95%, and 99.7% of the beam particles under the three different conditions of the horizontal slit in the diagnostic station 15. . . . .	86
Table 3.8	Comparison of the measurement and DYNAC simulation for beam energy spread (in %) with 95% of the beam particles enclosed in the first part of the beam energy calibration measurements. . . . .	90
Table 3.9	Comparison of the measurement and DYNAC simulation for beam energy spread (in %) with 95% of the beam particles enclosed when the horizontal slit in the diagnostic station 15 was fully open. . . . .	91
Table 3.10	Four SpecTcl windows. . . . .	105
Table 3.11	The average uncertainties in the estimation of the peak centroids by fitting peaks with a Gaussian for eight timing spectra measured by the two timing detectors at four different beam energies. . . . .	111
Table 3.12	Results of time-of-flight measurements at beam energies of 600 keV/u and 992 keV/u. The 600 keV/u is the RFQ output energy and the 992.098 keV/u beam energy was precisely determined by the 45 $^\circ$ magnetic analyzer. . . . .	111

Table 3.13	Results of time-of-flight measurements at beam energies of 1400 keV/u and 2100 keV/u. . . . .	111
Table 3.14	Dipole calibration factor $k$ obtained by the TOF energy measurements. . . . .	114
Table 3.15	Energy uncertainty estimation of TOF measurements. . . . .	114
Table 4.1	Test Specifications. . . . .	116
Table 4.2	The scintillator materials under study. . . . .	118
Table 4.3	The penetration depth of hydrogen ions in the four scintillators under different ion energies as estimated by the SRIM code [ Ziegler (2013)]. . . . .	121
Table 4.4	Uncertainty budget for the particle fluence. . . . .	128
Table 4.5	Results Summary of the relative exciton capture probability, the damage cross section and the half brightness fluence at low-energy He <sup>+</sup> bombardment in YAG: Ce. . . . .	128
Table 4.6	The SRIM calculation for evaluating the damage of the He <sup>+</sup> bombardment in YAG. . . . .	132
Table 5.1	Summary of the measurements of dipole calibration factor $k$ ( $T/\sqrt{keV \cdot amu}$ ). . .	149

## LIST OF FIGURES

Figure 1.1	Sketch of (a) a timing wire detector ; (b) a foil-silicon detector. [ Perdikakis et al. (2012)] . . . . .	2
Figure 1.2	The facility layout of the NSCL. . . . .	4
Figure 1.3	The layout of the ReA3 facility at MSU. The SuN detector was temporarily installed in the experimental hall for performing the gamma-ray resonance experiment in November, 2014. . . . .	5
Figure 1.4	(a) A room-temperature 4-rod RFQ at ReA3 [ Leitner et al. (2011)] and (b) two types of the ReA quarter wave resonator (QWR) cavities [ Facco et al. (2013)]. The value of $\beta\lambda$ is the distance that a beam particle with the velocity $\beta$ travels within a RF period. An inter-gap spacing of each cavity is designed to be $\beta\lambda/2$ in order to provide a positive electric field when the particle travels through each gap. . . . .	6
Figure 1.5	(left panel) The $45^\circ$ dipole located in the upstream of the S-bend section and (right panel) a half of the dipole showing the iron pole, coil and a Hall probe. . . . .	9
Figure 1.6	Schematics of the scintillation process in YAG: Ce. The electron-hole pair generated by the interaction of incident particles is being transported and trapped at the $Ce^{3+}$ site. The trapped exciton recombines to emit visible light through the 5d-4f transition. . . . .	14
Figure 1.7	The horizontal profile of the intensity distribution produced by a $He^+$ beam of energy $E=48$ keV as seen on a YAG: Ce screen under different irradiation time. . . . .	16
Figure 2.1	Illustration of a $\gamma$ -ray resonance reaction $A(X,\gamma)B$ [ Rolfs & Rodney (1988)]. . . . .	21
Figure 2.2	(Upper panel) Schematic diagram of a collision of a target nucleus with a projectile $X$ associated with the impact parameter $b$ . (Lower panel) Schematic bull-eye view of the target nucleus [ Rolfs & Rodney (1988)]. . . . .	23
Figure 2.3	Sketch of a normalized Breit-Wigner cross section derived in Equations 2.19. . . . .	26
Figure 2.4	Illustration of a cross section of a nuclear reaction for a thin target bombarded with beam particles. . . . .	27
Figure 2.5	Sketch of a normalized resonant yield curve in Equations 2.30 for a thick-target. The yield curve is normalized to the maximum yield for illustrative purposes. . . . .	29

Figure 2.6	Illustration of the resonance reaction happening at the target surface when the projectile incident energy is $E_0 = E_R$ (left), and inside the target when $E_0 > E_R$ (right). . . . .	29
Figure 2.7	Sketch of a normalized resonant yield curve of $^{27}\text{Al}(p,\gamma)^{28}\text{Si}$ at $E_p = 992$ keV for a thick target with varying beam energy spreads according to Equations 2.37. The yield curves are normalized to the maximum yield for illustrative purposes. The resonance width at this resonance is about 0.1 keV [ Endt & der leun (1978)]. . . . .	32
Figure 2.8	Transitions between molecular energy levels for an organic scintillator. [ McParland (2010)] . . . . .	33
Figure 2.9	Some of the color centers in alkali halides. . . . .	36
Figure 3.1	The simulated yield curves of the $^{27}\text{Al}(p,\gamma)^{28}\text{Si}$ reaction in the 632.2 keV (upper plot) and 992 keV (lower plot) resonance domains. The target thickness, the beam energy spread and the detector efficiency are supposed to be $0.45 \mu\text{m}$ , 0.5 % in FWHM and 0.2. . . . .	39
Figure 3.2	The simulated yield curves of the $^{58}\text{Ni}(p,\gamma)^{59}\text{Cu}$ reaction in the 1843 keV resonance domain. The target thickness, the beam energy spread and the detector efficiency are supposed to be $0.96 \mu\text{m}$ , 0.5 % in FWHM and 0.45. . . . .	40
Figure 3.3	The installation location of the CAESAR detector for the first part of the beam energy calibration measurements . . . . .	41
Figure 3.4	The decay scheme of the 992 keV resonance in $^{27}\text{Al}(p,\gamma)^{28}\text{Si}$ reaction. Each decay cascade is marked by the corresponding branching ratio in percentage. . . . .	42
Figure 3.5	The CAESAR $\gamma$ -detector array. . . . .	43
Figure 3.6	The target with the target holder apparatus for the CAESAR detector. The Al foil target was electrically isolated from the beam dump. By connecting a wire to the target frame, the current in the target and target frame can be read through a beam current monitor. The beam was collected on a tantalum sheet at the end of the beam-line. . . . .	44
Figure 3.7	Measured absolute full-energy peak efficiency for CAESAR with the standard calibration sources. The black squares are experimental data fitted with an empirical exponential function. . . . .	45
Figure 3.8	Simulated yield of the $^{27}\text{Al}(p,\gamma)^{28}\text{Si}$ reaction in the $E_p = 300\text{-}1100$ keV region with the detection limit. The $\text{H}_2^+$ beam current is 80 nA and the target thickness as well as the beam energy spread are the same as Figure 3.1 . . . . .	47
Figure 3.9	Schematic drawing of the SuN detector.[ Simon et al. (2013)] . . . . .	49

Figure 3.10	The SuN detector connected to the end of L-line extension beam line at ReA3. . . . .	50
Figure 3.11	Schematic diagram of the experimental setup for the SuN detector and the target system. . . . .	50
Figure 3.12	The target with the target holder for the SuN detector. . . . .	51
Figure 3.13	The ReA3 beam distribution line consisting of a vertical achromatic S-bend section, a high resolution horizontal 90° bending achromat with a slit system, an achromatic beam switchyard with two 45° dipoles, and the final beam focusing system to deliver the beam to the target station in the SuN location. . . . .	52
Figure 3.14	The layout of the RFQ and the first and second cryomodules in ReA3. . . . .	54
Figure 3.15	The simulated evolution of the beam envelop, energy spread and energy gain of a $H_2^+$ beam from the LEBT to the target station in the experimental hall for the beam tuning of $^{58}Ni(p,\gamma)^{59}Cu$ 1843 keV resonance experiment. The diagnostic stations as well as the beam optics elements along the ReA3 beam line are marked on the plots. . . . .	55
Figure 3.16	The excitation curves of the up branch (a) and the down branch (b) of the first 45° bending dipole in S bend. The black dots are the data and the red curves are the polynomial fit. . . . .	57
Figure 3.17	The ratio of difference in the field going up or down the hysteresis loop as a function of current for the first 45° dipole in S bend. The Y axis represents the magnetic field difference in % obtained from the measurements of going up and going down the hysteresis loop at a given magnet current. The different colors signify different experimental days. . . . .	58
Figure 3.18	The field reproducibility as a function of current for the first 45° dipole in S bend. The red and black colors represent the up branch and down branch, respectively. . . . .	59
Figure 3.19	An example of the 45° slit scan measurements in the diagnostic station 6 and 7 for two experimental runs. For each slit scan, the two peaks on the left show the horizontal and vertical beam profiles that are amplified by $\sqrt{2}$ . The right peak indicates the beam was centered at a 5 mm hole. The center of the 5 mm hole is supposed to be on the theoretical beam axis. . . . .	61
Figure 3.20	The deviations of individual detectors between the calibrated and theoretical energies for the well-known 1836 keV photopeak of $^{88}Y$ source with a linear (a) and a second-order polynomial (b) fitting. . . . .	64

Figure 3.21	The $\gamma$ -ray energies and their corresponding channel numbers of the photopeaks from the calibration sources listed in Table 3.3. The red curve is a second-order polynomial fit. . . . .	65
Figure 3.22	The reference background spectrum with a long recording time used to re-calibrate each CAESAR spectrum of the experimental runs. . . . .	66
Figure 3.23	The peak center distribution of the 1764 keV $\gamma$ -rays from $^{214}\text{Bi}$ on the CAESAR spectra of all 19 background runs before (upper panel) and after the re-calibration (lower panel). The horizontal axis represents the individual runs over a period of two months. . . . .	67
Figure 3.24	On-resonance spectra of $^{27}\text{Al}(p,\gamma)^{28}\text{Si}$ at $E_p = 992$ keV (a) and 632 keV (b) as well as a background spectrum (c), with photon counts normalized to the maximum height of the 1460.8 keV background peak for illustrative purposes. . . . .	68
Figure 3.25	The on-resonance spectrum of an experimental run acquired by CAESAR. (a) The raw data with peak shift correction, the background and background-subtracted spectra are labeled by the colors of dark, red and blue, respectively. (b) The 1779 keV photopeak was fitted with a Gaussian plus a second-order polynomial background. The green curve represents the net 1779 keV photopeak subtracted by the second-order polynomial background. . . . .	69
Figure 3.26	$^{60}\text{Co}$ decay scheme. . . . .	70
Figure 3.27	Energy Calibration curve for the SuN detector. . . . .	70
Figure 3.28	The $\gamma$ -summed spectra of $^{60}\text{Co}$ registered from (a) one single segment, (b) half of the detector and (c) the entire SuN array. . . . .	72
Figure 3.29	The raw data of $^{27}\text{Al}(p,\gamma)^{28}\text{Si}$ at $E_p = 992$ keV resonance, the background and background-subtracted SuN spectra are labeled by the colors of dark, red and blue, respectively. . . . .	73
Figure 3.30	The $\gamma$ -summed spectra of $^{27}\text{Al}(p,\gamma)^{28}\text{Si}$ at $E_p = 992$ keV resonance registered from (a) one single segment, (b) half of the detector and (c) the entire SuN array. . . . .	74
Figure 3.31	The $\gamma$ -summed spectra of $^{58}\text{Ni}(p,\gamma)^{59}\text{Cu}$ at $E_p = 1843$ keV resonance registered from (a) one single segment, (b) half of the detector and (c) the entire SuN array. . . . .	75
Figure 3.32	The decay scheme of $^{58}\text{Ni}(p,\gamma)^{59}\text{Cu}$ at $E_p = 1843$ keV resonance. [ Din & Al-Naser (1975)] . . . . .	76

Figure 3.33	The sum peaks of (a) $^{27}\text{Al}(p,\gamma)^{28}\text{Si}$ at $E_p = 992$ keV resonance and (b) $^{58}\text{Ni}(p,\gamma)^{59}\text{Cu}$ at $E_p = 1843$ keV resonance with a Gaussian and a linear-background fits. In (b), the green curve represents the net sum peak subtracted by the linear background. . . . .	77
Figure 3.34	(a) The inverse magnetic field vs. the beam phase difference between two BPMs for the experiential runs at $^{27}\text{Al}(p,\gamma)^{28}\text{Si}$ 632 keV resonance in the first part of the beam energy calibration measurements. (b) The square of magnetic field versus the cavity amplitude for the experiential runs at $^{58}\text{Ni}(p,\gamma)^{59}\text{Cu}$ 1843 keV resonance in the second part of the beam energy calibration measurements. . . . .	78
Figure 3.35	Some experiential runs at $^{27}\text{Al}(p,\gamma)^{28}\text{Si}$ 992 keV resonance in the second part of the beam energy calibration measurements. The upper panel shows the square of magnetic field versus the L084 cavity amplitude and the lower panel shows the beam vertical profiles in the diagnostic station 9 after the beam passed the first bending dipole in S bend. . . . .	79
Figure 3.36	Dependence of the least chi-square on the normalized factor ( $S$ ), the energy spread (% in FWHM) and the dipole calibration factor ( $k$ ) for $^{27}\text{Al}(p,\gamma)^{28}\text{Si}$ 992 keV/u resonance. The minimum of the chi-square is marked with an arrow. . . . .	83
Figure 3.37	The $^{27}\text{Al}(p,\gamma)^{28}\text{Si}$ yield curves of the 992 keV resonance (a) without and (b) with the L091 rebuncher cavity in the first part of the beam energy calibration measurements. The solid curves are a fit to the data with a theoretical yield model of Equation 3.19. . . . .	84
Figure 3.38	The $^{27}\text{Al}(p,\gamma)^{28}\text{Si}$ yield curve at $E_p = 632$ keV resonance in the first part of the beam energy calibration measurements. The solid curves are a fit to the data with a theoretical yield model of Equation 3.19. . . . .	85
Figure 3.39	The $^{27}\text{Al}(p,\gamma)^{28}\text{Si}$ yield curves at $E_p = 992$ keV resonance under the three different conditions of the horizontal slit in the diagnostic station 15: (a) slit fully open; (b) slit opening width : 3 mm; and (c) slit opening width : 1 mm in the second part of the beam energy calibration measurements. The solid curves are a fit to the data with a theoretical yield model of Equation 3.19. . . . .	87
Figure 3.40	The $^{58}\text{Ni}(p,\gamma)^{59}\text{Cu}$ yield curves at $E_p = 1843$ keV resonance under the three different conditions of the horizontal slit in the diagnostic station 15: (a) slit fully open; (b) slit opening width : 3 mm; and (c) slit opening width : 1 mm in the second part of the beam energy calibration measurements. The solid curves are a fit to the data with a theoretical yield model of Equation 3.19. . . . .	88

Figure 3.41	Comparison of the fitted resonance yield curves with various horizontal slit width in the diagnostic station 15 for (a) $^{27}\text{Al}(p,\gamma)^{28}\text{Si}$ 992 keV resonance and (b) $^{58}\text{Ni}(p,\gamma)^{59}\text{Cu}$ 1843 keV resonance in the second part of the beam energy calibration measurements. . . . .	89
Figure 3.42	Beam energy spread simulation in DYNAC with 95% of the beam particles enclosed for the $^{27}\text{Al}(p,\gamma)^{28}\text{Si}$ at $E_p=992$ keV resonance (a) without and (b) with the L091 rebuncher cavity as well as (c) the $^{27}\text{Al}(p,\gamma)^{28}\text{Si}$ at $E_p=632$ keV resonance in the first part of the beam energy calibration measurements. The colorful blocks displayed on the horizontal axis represent the beam optical elements, i.e. light green : quadrupole, light blue : solenoid, blue : SRF cavity and pink : bending dipole. . . . .	90
Figure 3.43	Beam energy spread simulation in DYNAC with 95% of the beam particles enclosed for (upper panel) the $^{27}\text{Al}(p,\gamma)^{28}\text{Si}$ at $E_p=992$ keV resonance and (lower panel) the $^{58}\text{Ni}(p,\gamma)^{59}\text{Cu}$ at $E_p=1843$ keV resonance in the second part of the beam energy calibration measurements. The horizontal slit in diagnostic station 15 was fully open. The colorful blocks displayed on the horizontal axis represent the beam optical elements, i.e. light green : quadrupole, light blue : solenoid, blue : SRF cavity and pink : bending dipole. . . . .	91
Figure 3.44	DYNAC beam simulation for the optimized beam tune of $^{58}\text{Ni}(p,\gamma)^{59}\text{Cu}$ at $E_p=1843$ keV resonance experiment in the location of the diagnostic station 15. . . . .	93
Figure 3.45	Principle of a time-of-flight measurement using two grid-MCP detectors. A dash blue line represents a mesh (grid) in a detector. . . . .	94
Figure 3.46	A schematic diagram and a picture of a grid-MCP detector. When the incoming beam hit the second mesh at -2 kV, secondary electrons will be emitted from the second mesh at the location of the ion impact and accelerated toward a MCP detector. . . . .	95
Figure 3.47	The timing detector as modeled in the SIMION program. The distance between the second mesh at -2kV and one of the grounded meshes is 3.1 mm. The MCP detector is 14.5 mm in diameter. The dimensions for the surfaces of these meshes are 37.7 mm $\times$ 37.7 mm. . . . .	97
Figure 3.48	Left: The sketch for measuring the time of flight for electrons with a cosine distribution of ejected angles. Right: The corresponding simulated TOF spectrum of electrons by assuming that electrons are emitted from the mesh at the same time with a cosine ejected angular distribution and a specific initial energy distribution. The time resolution (FWHM) of the TOF spectrum due to the initial energy and angular distributions of secondary electrons is about 12 ps. . . . .	98

Figure 3.49	Left: The sketch for measuring the trajectory of incoming ions. Right: the simulated TOF spectrum of incoming alpha particles with the 45° incident angle. . . . .	99
Figure 3.50	A simulated TOF spectrum of secondary electrons generated by the 1.2 MeV incoming alpha particles at the incident angle 45°. . . . .	100
Figure 3.51	The TOF spectra of secondary electrons generated by the 1.2 MeV incoming alpha particles at the incident angle 45 degree with (a) the beam bunch length 200 ps (FWHM) and (b) the beam bunch length 500 ps (FWHM). . . . .	101
Figure 3.52	Left: The collimator in front of the mesh. Middle: The sketch for measuring the trajectory of incoming ions. Right: The corresponding simulated TOF spectrum of secondary electrons from the mesh to the MCP plate. . . . .	101
Figure 3.53	Schematic diagrams of a fast micro-channel plate (MCP) Hamamatsu F4655-12. . . . .	103
Figure 3.54	The ReadoutShell program is responsible for data readout of a grid-MCP detector. . . . .	104
Figure 3.55	Left: The V812 CFD GUI for the timing detectors. Right: the XLM72 Scaler Control Panel. . . . .	105
Figure 3.56	SpecTcl, TKCon, Tregui windows in the SpecTcl program . . . . .	106
Figure 3.57	Xamine window in the SpecTcl program. The spectra of two grid-MCP detectors for TOF measurements is displayed as an example. The upper spectrum is the first timing detector in the diagnostic station 10 while the lower spectrum is the second detector in the diagnostic station 13. . . . .	107
Figure 3.58	The H <sub>2</sub> <sup>+</sup> ion beam timing spectra simultaneously measured by the two grid-MCP detectors in the diagnostic station 10 and 13 at the beam energies (a) 992 keV/u and (b) 600 keV/u. The peaks in each time spectrum are normalized to the maximum of the spectrum. $\Delta t$ represents the arrival time difference of beam bunches at the two detectors with respect to the RF signals. . . . .	109
Figure 3.59	The timing spectral peaks measured by (a) the first grid-MCP detector and (b) the second grid-MCP detector at 992 keV/u beam energy; (c) the first grid-MCP detector and (d) the second grid-MCP detector at 600 keV/u beam energy. Each peak is partially fitted with a Gaussian in order to estimate the peak center. . . . .	110

Figure 3.60	The $H_2^+$ ion beam timing spectra simultaneously measured by the two grid-MCP detectors in the diagnostic station 10 and 13 at the beam energies (a) 1400 keV/u and (b) 2100 keV/u. The peaks in each time spectrum are normalized to the maximum of the spectrum. $\Delta t$ represents the arrival time difference of beam bunches at the two detectors with respect to the RF signals. . . . .	112
Figure 3.61	The timing spectral peaks measured by (a) the first grid-MCP detector and (b) the second grid-MCP detector at 1400 keV/u beam energy; (c) the first grid-MCP detector and (d) the second grid-MCP detector at 2100 keV/u beam energy. Each peak is partially fitted with a Gaussian in order to estimate the peak center. . . . .	113
Figure 4.1	Locations of two irradiation measurements on various scintillator materials performed in the ReA3 facility of NSCL. . . . .	115
Figure 4.2	One set of irradiation images where the initial irradiation spots on the scintillator for 7 tests listed in Table 4.1 are overlaid. Each spot irradiated a different area of the scintillator surface for each measurement. . . . .	117
Figure 4.3	The setup of the YAG: Ce scintillator at the rare isotope ReAccelerator. . . . .	118
Figure 4.4	Illustration of the irradiation setup. The cause of image reflection in the scintillator is shown. The backward-emitted scintillation light is reflected at the substrate surface. The emitted light from the true beam spot and the reflected spot is both observed by the CCD camera. . . . .	119
Figure 4.5	(a) Experimental setup for ion beam profile measurements; (b) a rotating target wheel with the four different scintillator materials. The target chamber is the ANASEN detector vacuum chamber [ Linhardt et al. (2012). . . . .	120
Figure 4.6	The initial image and an intensity profile of a specific row (represented by the yellow line) for the test 1. . . . .	123
Figure 4.7	The degradation of YAG: Ce at incident ion energy $E=58$ keV and beam current $I=394$ pA. . . . .	125
Figure 4.8	The luminescence response of YAG: Ce as a function of the irradiation time with a beam energy $E=58$ keV and beam current $I=394$ pA. . . . .	126
Figure 4.9	The particle fluence vs. the inversely normalized scintillation intensity for (a) test 1 and (b) test 5. The dots with error bars are the experimental points and the solid line shows the fit of the Birks model. . . . .	129

Figure 4.10	The relative exciton capture probability and the damage cross section as a function of the $\text{He}^+$ energy. The error bars are the experimental uncertainty. Three symbols are used to represent different tests with different current at the same energy. . . . .	130
Figure 4.11	The half brightness fluence vs. the $\text{He}^+$ energy. Three symbols represent different tests with different current at the same energy. . . . .	131
Figure 4.12	The SRIM calculation for the ratio of the oxygen vacancies created per incident ion to the beam penetration depth as a function of the beam energy. . . . .	132
Figure 4.13	Scintillator luminescence response as a function of the accumulated particle fluence with $\text{H}_2^+$ beam energies of 600, 1010, 1500 and 2150 keV/u for (a) CsI:Tl and (b) YAG:Ce. All the light yield curves were recorded during 1-hour irradiation, except for the yield curve of CsI:Tl at 1500 keV/u recorded during 1/3-hour irradiation. The light output for each curve was extracted from the analyzed area of a scintillator. Longer irradiation time or more beam current impinging onto the analyzed area of a scintillator can lead to larger accumulated fluence (longer curve length in the horizontal axis). The luminescence of CsI:Tl and YAG:Ce both exhibited very stable behavior under this irradiation energy range and low particle fluence. . . . .	134
Figure 4.14	(a) Light yield of $\text{CaF}_2:\text{Eu}$ scintillators as a function of accumulated fluence for several beam energies. The light yield curves were recorded under the irradiation time of 1 hour for the $\text{H}_2^+$ beam energies of 600 and 1010 keV/u and 40 minutes for 1500 and 2150 keV/u. The particle fluence endpoint of the yield curve was determined by the irradiation time and the beam current impinging onto the analyzed area of a scintillator. (b) The luminescence intensity of $\text{CaF}_2:\text{Eu}$ was normalized by its initial luminescence. Plot (b) shows the detail of the scintillation degradation occurred when the particle fluence was below $\sim 2 \times 10^{10}$ ions/ $\text{mm}^2$ . . . . .	136
Figure 4.15	Illustration of possible radiation damages for $\text{CaF}_2:\text{Eu}$ at room temperature. . . . .	137
Figure 4.16	(a) Fluence dependence of the luminescence intensity of KBr under $\text{H}_2^+$ ion bombardment for several beam energies. All the light yield curves were recorded during 1-hour irradiation. The comparison of the beam current bombarding the analyzed area of the KBr scintillator for the yield curves at the three beam energies is $600 \text{ keV/u} > 1010 \text{ keV/u} > 2150 \text{ keV/u}$ . (b) The luminescence intensity of KBr was normalized by its maximum scintillation. The luminescence of KBr degraded faster at higher beam energy after reaching its maximum scintillation. . . . .	138

Figure 4.17 Schematic configuration of the F- and  $V_3^-$  centers as well as the F-center aggregates in KBr. The F-center is an electron trapped by a  $Br^-$  vacancy and the  $V_3^-$  center is formed by a  $Br_3^-$  molecule located at one cation and two anion vacancies. . . . . 139

Figure 4.18 The KBr, YAG:Ce and  $CaF_2$ :Eu samples after ion irradiation. The KBr crystal shows damaged spots in blue color. . . . . 139

Figure 4.19 The relative light output of all the materials under study as a function of beam energy. For YAG:Ce and CsI:Tl, the average luminescence during irradiation is estimated. For  $CaF_2$ :Eu, after the scintillation reaches its stable state, the average in the light yield was chosen for comparison. As comparison, the maximum luminescence of KBr is also plotted. The dots are the experimental points and the solid lines show a linear fit. . . . . 141

Figure 4.20 Normalized luminescence distributions of the initial beam spot images along a pixel column positioned at maximum luminescence for CsI:Tl,  $CaF_2$ :Eu and YAG:Ce under the same camera setting and the same beam condition of  $H_2^+$  irradiation at the beam energy of 2150 keV/u and the beam current of 12 pA. . . . . 142

Figure 4.21 Beam width of YAG:Ce,  $CaF_2$ :Eu and CsI:Tl materials determined from Gaussian fits to the vertical projection for  $H_2^+$  irradiation under the unchanged beam condition of the beam energy 2150 keV/u with the beam current 12 pA. . . . . 143

Figure 4.22 (a) Beam width of YAG:Ce and KBr materials determined from Gaussian fits to the vertical projection for  $H_2^+$  irradiation under the unchanged beam condition of the beam energy 600 keV/u with the beam current 380 pA. A constant beam width in YAG:Ce is plotted as a comparison. (b) The detail comparison of vertical projections at different irradiation time for the beam width evolution of KBr in plot (a). Curve (1), (2) and (3) represent the vertical projections at the irradiation time of 4, 82 and 2527 seconds, respectively. The dots are the experimental points and the solid lines show Gaussian fits. The beam widths in  $1-\sigma$  obtained from Gaussian fits are 0.616 mm for curve (1), 0.539 mm for curve (2) and 0.674 mm for curve (3). . . . . 144

Figure 4.23 Scintillation response of YAG:Ce during  $H_2^+$  continuous irradiation at the bombarding energies of 25 keV/u and 600 keV/u. The data are normalized to the initial light yield. The irradiation experiment of the YAG: Ce scintillator at 25 keV/u was performed in the low energy beam transport section of the rare isotope ReAccelerator (ReA) facility. . . . . 146

Figure 4.24 The simulated distributions of the electronic-energy deposition density and the target-atomic displacement number as a function of the ion penetration depth under proton bombardment at energies of (a) 600 keV/u and (b) 25 keV/u. . . . . 147

Figure 5.1 Results from the dipole calibration factor  $k$  are plotted as a function of beam energy for the three parts of the beam energy calibration measurements, as listed in Table 5.1. The error bar of each data point is mainly contributed from the systematic error of 0.18 % due to the inconsistent incident angle of the beam central ray into the magnetic analyzer (see the discussion in Section 3.1.4.3). The horizontal solid line with the pink color is the average  $k$  value with the standard deviation of 0.128 % as marked by the pink dashed lines. . . 150

# CHAPTER 1

## INTRODUCTION

The National Superconducting Laboratory (NSCL) located on the campus of Michigan State University is the leading rare isotope research facility to investigate the properties of rare isotopes and nuclear reactions. By commissioning a new re-accelerator facility (ReA3), the NSCL expands its capabilities to provide exotic rare isotope beams in the energy range of 0.3–12 MeV/u for heaviest ions and 0.3–20 MeV/u for light ions. In the future, the NSCL proposed upgrade – the Facility for Rare Isotope Beams (FRIB) – will replace the coupled cyclotrons with a powerful linear accelerator to boost intensities and varieties of rare isotope beams and become a preeminent facility for nuclear science in the world. The ReA3 facility can stop the rare isotope beams produced by in-flight fragmentation and reaccelerate them in a compact linac. ReA3 initially uses rare isotope beams provided from the existing Coupled Cyclotron Facility (CCF) at NSCL. Later, ReA3 will provide reacceleration capability for FRIB. Reaccelerated beams of rare isotopes can create a rich experimental opportunity of studying low-energy Coulomb excitation, transfer reactions and astrophysical reactions, etc.

In any accelerator, beam diagnostics serve as an essential tool to measure the physical properties and behavior of ion beams. These include the intensity, transverse size and emittance, position in each diagnostic station, bunch structure, energy and energy spread of ion beams. During the commissioning period of ReA3, beam diagnostics can help to build the normal performance of the linac operation, confirm the results of beam dynamics calculations, identify machine problems and optimize beam tunes. Several beam diagnostic devices have been built and routinely used for commissioning ReA3 and achieving project milestones. For the longitudinal beam profile diagnostics, a timing wire detector is used to extract the bunch length information of ion beams coming out of a multi harmonic buncher, a room temperature RFQ, a buncher cryomodule and/or a superconducting linac. The timing wire detector consists of a wire biased at negative voltage, a Multi Channel

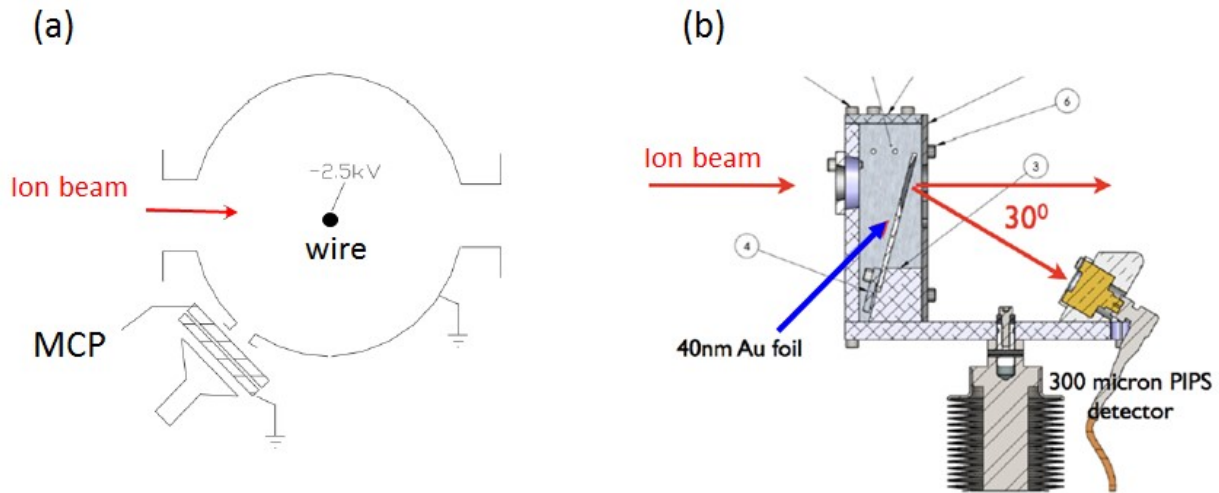


Figure 1.1 Sketch of (a) a timing wire detector ; (b) a foil-silicon detector. [ Perdikakis et al. (2012)]

Plate (MCP) detector, and an outer cylinder at ground potential, as shown in Figure 1.1 (a). The secondary electrons created by the beam bombardment on the wire are emitted and accelerated to the MCP. The MCP detector registers the timing signal of the secondary electrons in coincidence with the fundamental RF frequency of 80.5 MHz. The time resolution of the detector can achieve to be better than 200ps FWHM [ Leitner et al. (2011)]. A silicon detector coupled with a Au thin foil has been used for relative beam energy measurement and cavity phasing, as shown in Figure 1.1 (b). The ion beam experiences a Rutherford scattering in the Au foil of thickness 40 nm and is scattered towards a PIPS-type silicon detector which is mounted  $30^\circ$  with respect to the beam. The energy of the scattered beam is analyzed by the silicon detector. The elastically scattered beam from the gold foil at a certain angle is used in order to prevent the silicon detector from being damaged by the intensive incident beam. A  $^{241}\text{Am}$  alpha source with a known alpha energy of 5.486 MeV is placed off-axis into the diagnostic vacuum chamber to calibrate the detector. Due to the method of the detector calibration and the energy loss of the incident beam in the foil, the foil-silicon detector gives beam energy uncertainty of  $\sim 2\%$ . In order to determine beam energies with good resolution of  $\leq 0.5\%$  FWHM, a  $45^\circ$  bending magnet in ReA3 was calibrated in this dissertation. The beam energy can be precisely determined by measuring the magnetic field required to bend the ion beam through the magnet. A time-of-flight technique by using two grid-MCP timing

detectors was also developed to provide a quick and precise online method for measuring absolute beam energy in ReA3.

Scintillator screens are simple and reliable instruments for beam transverse profile monitoring in beam diagnostic applications. Since the ReA3 requires beam diagnostics used for the low energy and low intensity of the ion beams, the choice of a suitable scintillating material becomes very important. The lack of comprehensive data and understanding for scintillator screens used in the low-intensity and low-energy regime motivated the study presented in this dissertation. A systematic experiment for various scintillator materials irradiated by light ions with various ion energies is performed to develop adequate diagnostics for ReA operation.

The introductory chapter of this dissertation presents an overview of the CCF and the ReA3 facility in Section 1.1. The energy measurement and calibration methods for a bending magnet are introduced in Section 1.2, followed by the induction of scintillator screens in Section 1.3.

## **1.1 Conceptual overview of the Coupled Cyclotron Facility and ReA3**

The National Superconducting Cyclotron Laboratory (NSCL) has been successfully providing fast Rare Isotope Beams (RIBs) produced by the in-flight particle fragmentation method for nuclear science with great success since 1989. Figure 1.2 shows the layout of the NSCL facility. A stable high-energy ion beam produced by two Electron Cyclotron Resonance (ECR) ion sources is accelerated by two coupled superconducting cyclotrons (K500 and K1200) to energies up to  $\sim 170$  MeV/u, and focused onto a thin light production target, such as  ${}^9\text{Be}$  with thickness of  $240 \text{ mg/cm}^2$ . Rare isotopes are produced by fragmentation of the primary stable beam on a stationary target. The RIBs of interest are selected by the A1900 Fragment Separator, and delivered to multiple fast beam experimental halls for fast RIBs experiments. The selected fast RIBs can be used to study nuclear structure as well as cross sections or branching ratios of nuclear reactions with sophisticated detectors, such as the MODular Neutron Array and Large Multi-Institutional Scintillator Array (MoNA-LISA), the High Resolution Array Detector (HiRA) and the S800 Spectrograph. Some experiments require low energy beams to perform Penning trap mass measurements with the Low

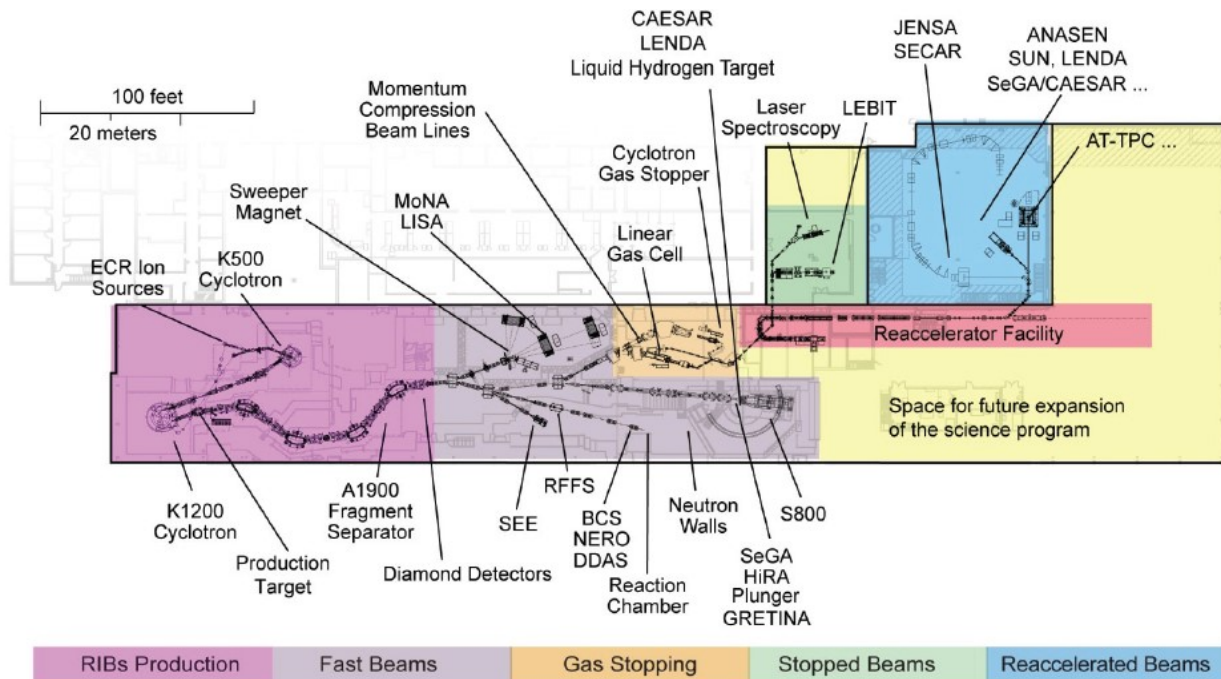


Figure 1.2 The facility layout of the NSCL.

Energy Beam and Ion Trap (LEBIT) facility or study nuclear magnetic resonance with the Beam Cooler and LAser spectroscopy (BECOLA). For these experiments, the energy of the fast RIBs must be reduced by stopping the fast beams in a gas cell filled with Helium, and consequently extracting them as low-energy beams. The process of beam cooling can also reduce the beam energy spread and emittance to an acceptable level for the high-precision low-energy experiments.

There is a variety of experiments in nuclear astrophysics and nuclear structure programs that require RIBs in the energy range from a couple of hundreds keV/u up to a few tens of MeV/u. In order to meet the strong demands for high quality low energy RIBs, the singly charge RIBs produced from the in-flight particle fragmentation and the gas cell are re-accelerated in the ReA3 facility.

The ReA3 facility, as shown in Figure 1.3, consists of an Electron Beam Ion Trap (EBIT), a charge-over-mass ( $Q/A$ ) section, a Low Energy Beam Transport (LEBT) section, a room temperature Multi-Harmonic Buncher (MHB), a room-temperature 4-rod RFQ, a superconducting (SC) linac, and a beam distribution system that delivers the beam to the experiments.

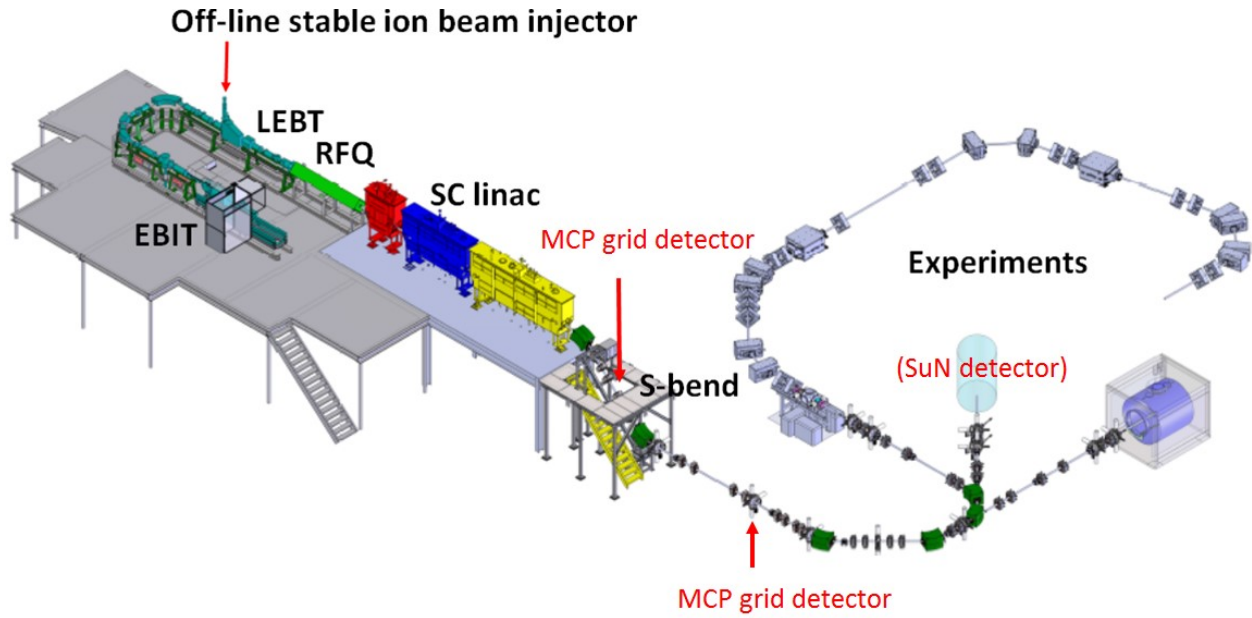


Figure 1.3 The layout of the ReA3 facility at MSU. The SuN detector was temporarily installed in the experimental hall for performing the gamma-ray resonance experiment in November, 2014.

The RIBs through the gas stopper are typically singly ionized. To achieve more efficient acceleration, the cooled singly charged beams are injected into the EBIT-type charge breeder which converts the RIBs from a  $1^+$  to a  $Q^+$  charge state by stripping away outer-shell electrons of the RIBs with a high-density, focused electron beam. Once the RIBs have reached an optimum charge state, the trap voltage is lowered and the RIBs are extracted. The highly charged ion beams are mass separated in an achromatic charge-over-mass ( $Q/A$ ) separator and delivered to the LEBT section. The separator can select the desired charge state and suppress unwanted background ions from the EBIT before the beam enters the accelerator section.

In addition, an off-line stable ion beam injector with the use of a small external filament provides singly charged  $\text{He}^+$  and  $\text{H}_2^+$  ion beams for commissioning the ReA3 and performing all the experiments of this dissertation study. The stable ion beams are mass analyzed by a compact velocity filter and accelerated by a DC accelerating gap to the nominal RFQ injection energy of 12 keV/u. In order to achieve the requirement of a small longitudinal beam emittance of less than  $0.3 \pi\text{-ns}\cdot\text{keV/u}$  from ReA3, either the stable pilot ion beams or the RIBs from the EBIT are guided into the MHB to produce a bunched beam for adequate acceptance into the RFQ. Several diagnostic

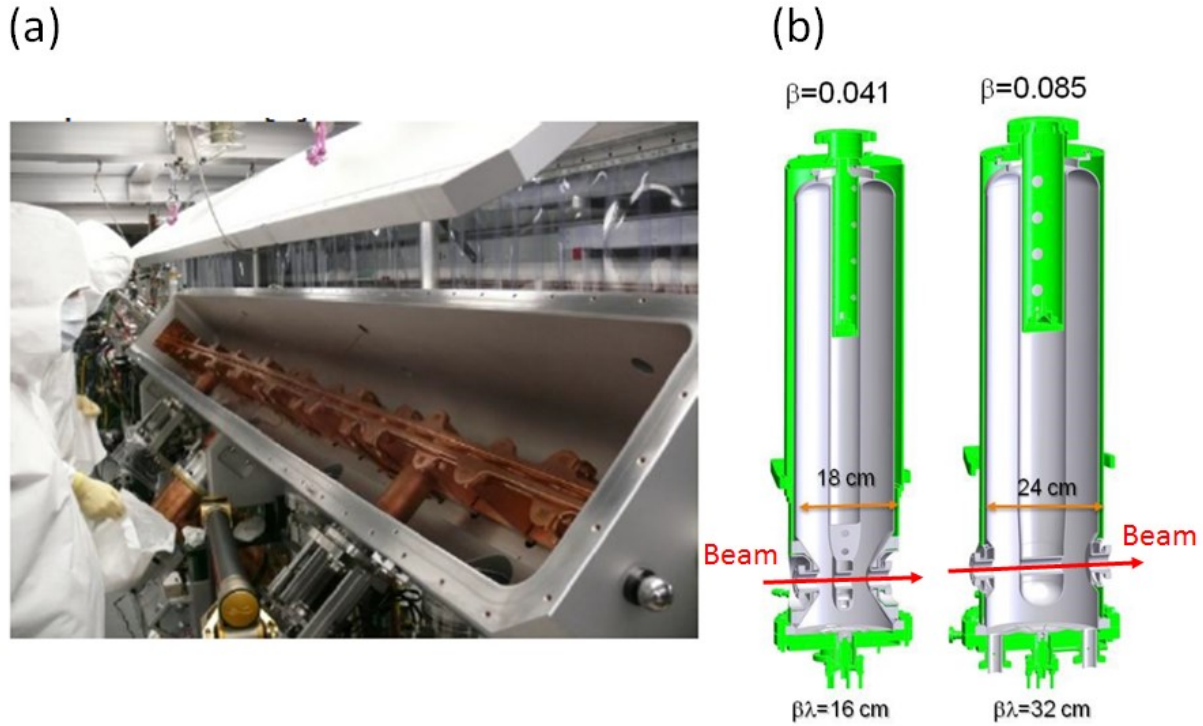


Figure 1.4 (a) A room-temperature 4-rod RFQ at ReA3 [ Leitner et al. (2011)] and (b) two types of the ReA quarter wave resonator (QWR) cavities [ Facco et al. (2013)]. The value of  $\beta\lambda$  is the distance that a beam particle with the velocity  $\beta$  travels within a RF period. An inter-gap spacing of each cavity is designed to be  $\beta\lambda/2$  in order to provide a positive electric field when the particle travels through each gap.

devices in the LEBT, such as a timing wire detector and a scintillator screen coupled with a pepperpot [ Strohmeier et al. (2010)], are available to measure the ion beam properties and achieve proper matching into the RFQ.

The 3.3 m long 4-rod RFQ (Figure 1.4 (a)) accelerates the ion beam from  $\sim 12$  keV/u to 600 keV/u with a Q/A ratio between 0.2 and 0.5 [ Kester et al. (2009)]. Because a prebunched beam is injected into RFQ, it was possible to design the RFQ to achieve a high accelerating efficiency and to produce a beam with a small longitudinal emittance. The ion beam from the RFQ is injected into the SC linac, which uses two types of 80.5 MHz quarter wave resonator (QWR) cavities (Figure 1.4 (b)) in three cryomodules. The first cryomodule (CM1) after the RFQ consists of one  $\beta=0.041$  cavity set in the rebunching mode and two 9T superconducting solenoid magnets. The QWR cavity in the CM1 is used to re-bunch the beam as it travels from the RFQ to the second

cryomodule. The second cryomodule (CM2) contains six QWR cavities with  $\beta=0.041$  and three superconducting 9T solenoids. The beam energy can be accelerated up to  $\sim 1.5$  MeV/nucleon or decelerated down to 300 keV/nucleon. The third cryomodule (CM3) was installed in 2014 and contains eight QWR cavities with  $\beta=0.085$  and three 9T solenoids. The eight QWR cavities in the CM3 can either accelerate the beam to 3 MeV/nucleon or be used to transport and bunch the beam. The operational RF frequency of the linac is 80.5 MHz, leading to the beam bunch period of 12.4 nsec. Four beam diagnostic stations located after the RFQ and the three individual cryomodules are used for commissioning the SC linac and beam tuning. The diagnostic devices include Faraday cups for checking beam transmission,  $45^\circ$  slit scanners for beam profile measurement, timing wire detectors for determining beam bunch length and foil-silicon detectors for phasing the cavities.

The vertical achromatic S-bend section guides the ion beams from the SC linac on the platform to the ground level. In the S-bend beam line, the beam passes through two  $45^\circ$  bending magnets and six magnetic quadrupoles in a such way that the transverse and longitudinal emittances of the beam are preserved. One diagnostic station located after the first quadrupole contains a vertical movable slit. Combined with this vertical slit, the first bending magnet in the S-bend beam line is developed to provide the precise information of absolute beam energy. After the S-bend section was completed in July of 2012, the CAESium iodide ARray (CAESAR)  $\gamma$ -ray detector was installed after the S-bend for beam energy calibration of the magnetic analyzer.

The ion beams are delivered from the S-bend section to three target stations in the ReA3 experimental hall by passing through (1) a beam matching section consisting of eight magnetic quadrupoles and a space for a future rebunching cryomodule, (2) a horizontal  $90^\circ$  bending achromatic section consisting of two  $45^\circ$  bending magnets and four magnetic quadrupoles, (3) an achromatic beam switchyard, and (4) the final focusing systems to optimize the beam size on the targets. The future rebunching cryomodule will use one  $\beta=0.041$  QWR rebuncher cavity to achieve the required beam energy spread and bunch length on the targets. The horizontal  $90^\circ$  bending achromat is designed to control the beam energy spread with the help of a horizontal movable slit in a dispersive focal plane of the bending achromatic system.

The Summing NaI:Tl (SuN)  $\gamma$ -ray detector was installed in one of the target stations, as shown in Figure 1.3, for beam energy calibration of the magnetic analyzer. The scintillation measurement of various scintillator materials under high-energy irradiation was also performed in the same target station.

## 1.2 Energy measurement and calibration of a magnetic analyzer

A precise knowledge of the absolute beam energy is essential for experimental requirement in many fields of nuclear physics (e.g. nuclear structures and nuclear astrophysics). The ReA3 beam line includes a  $90^\circ$  achromatic analyzing section (S-bend section, see Figure 1.3) that contains two  $45^\circ$  magnets, two quadrupole doublets and two vertical quadrupoles. The absolute energy of an ion beam in ReA can be measured with this achromatic section. The  $45^\circ$  dipole magnets generate the magnetic field to guide the charged particles into the  $45^\circ$  arc of beam central ray trajectory. The dipoles consist of coils and a magnet iron yoke, as shown in Figure 1.5. The flow of electric current in the wire winding of the coils induces the magnetic field perpendicular to the plane of the beam orbit. A Hall probe is located at the edge of the iron pole in the center of the magnet to measure the magnetic field. In order to maintain a constant bending trajectory of the ion beams through the dipoles, the magnetic field in the dipoles needs to be adjusted according to the incident ion energies since the magnetic rigidity  $B\rho$  is proportional to the square root of the beam energy. Therefore, these bending dipoles as magnetic analyzers can provide a precise method of measuring absolute beam energy of the ion beams from ReA3. The magnetic field  $B$  of a bending dipole can be measured with a Hall probe and converted into the beam energy  $E$  using a conversion formula:

$$B = k \frac{\sqrt{A}}{q} \sqrt{E(keV)} \quad (1.1)$$

where  $A$  is the ion mass given in terms of an atomic mass unit and  $q$  is the charge state of the incident particles. The  $k$  (in  $T/\sqrt{keV * amu}$ ) is the calibration factor for the dipole. A good calibration procedure for direct measurements of the calibration factor  $k$  in a wide domain of magnet

## Hall Probe

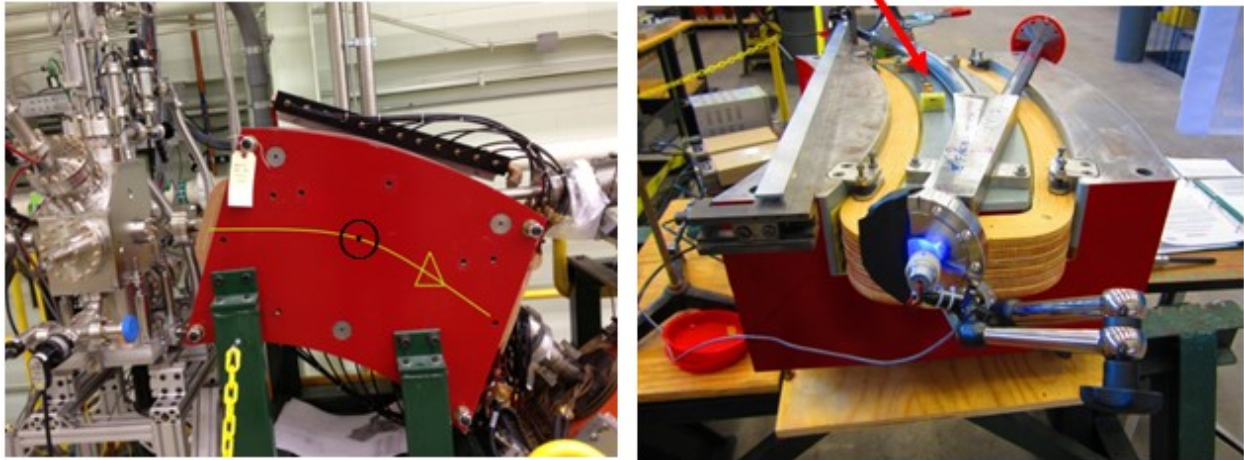


Figure 1.5 (left panel) The 45° dipole located in the upstream of the S-bend section and (right panel) a half of the dipole showing the iron pole, coil and a Hall probe.

operation is essential for the precise measurement of beam energies.

Various methods for calibrating magnetic analyzers have been published. For example, there are many reports in literature describing how magnetic analyzers have been calibrated in energy by using  $\gamma$ -ray nuclear resonances and neutron thresholds [ Marion (1966)]. When a projectile nucleus impinges onto a target nucleus with an energy equal to the resonance energy (threshold energy),  $\gamma$  ray (neutrons) will be emitted as reaction yield. The resonance energies for  $\gamma$ -ray resonant reactions or the threshold energies for neutron threshold determinations can provide precise calibration points. For the use of proton-induced  $\gamma$ -ray resonances, the suitable proton energy for precise calibration is limited in the range of 0.3-3.5 MeV [ Trautvetter et al. (1979)]. However, the use of (p,n) threshold determinations can achieve higher energy calibration at  $E_p=4.2$ -9.5 MeV [ Trautvetter et al. (1979)]. The calibration energy range can be even extended further by using (p,p) resonances such as  $^{16}\text{O}(p,p)^{16}\text{O}$  at  $E_p= 12.7$  MeV and  $^{12}\text{C}(p,p)^{12}\text{C}$  at  $E_p= 14.2$  MeV [ Wilkerson et al. (1983)]. For the calibration of a magnetic analyzer in heavy-ion accelerators, inverse (p, $\alpha\gamma$ ) resonances, i.e. with heavy-ion beam on hydrogen targets, can be used. Some examples would be the reactions of  $^1\text{H}(^{19}\text{F},\alpha\gamma)^{16}\text{O}$  and  $^1\text{H}(^{15}\text{N},\alpha\gamma)^{12}\text{C}$  [ Evers et al. (1987)]. In addition, the non-resonant proton capture reaction of  $^{12}\text{C}(p,\gamma)^{13}\text{N}$  provides a method to calibrate a mag-

net in the low-energy region of  $E_p=150-350$  keV with good precision of  $\sim 0.4$  keV [ Freye et al. (1977)]. The energy calibration using these direct capture reactions can be performed at all beam energies of interest. From the determination of the  $\gamma$ -ray energy, the incident proton energy can be calculated through a precisely known Q-value.

In contrast with the measurements of the resonances or thresholds, which are time-consuming and only occur at specific energies, a time-of-flight technique [ Mak et al. (1973)] provides a relatively quick and simple method for measuring absolute beam energy over a wide range of ion species and energies.

A simple calibration method for heavy-ion-beam accelerators involves the bombardment of a thin hydrogenous target with the heavy-ion beams and the energy measurement of recoiling protons knocked forward at  $0^\circ$  [ Olsen et al. (1974)]. From the recoiling proton energy, the bombarding energy of the heavy-ion beam can be estimated through a simple kinetic relation. The method has been successfully used for ion beams ranging in mass from  $^{12}\text{C}$  to  $^{84}\text{Kr}$  in the energy range of 3-5 MeV/u. Furthermore, some investigators [ Ferrero et al. (1989)] have improved this method by using two detectors placed at equal angles on opposite sides of the beam to measure the energies of the protons knocked out. The use of two detectors can minimize experimental errors due to uncertainties of the incident angle at which the beam hit the target and extend the calibration energies beyond 5 MeV/u.

A similar scattering method is the use of the Back Scattering (BS) measurements to calibrate a magnetic analyzer with various beams of different charge states and energies. The ion beams such as  $^1\text{H}$ ,  $^7\text{Li}$  or  $^{12}\text{C}$  are elastically scattered by a self-supporting foil of  $^{197}\text{Au}$ ,  $^{181}\text{Ta}$  or  $^{93}\text{Nb}$  and the energy of the scattered beam particles is detected at a certain backward angle. The incident beam energy can be determined through a kinematic relation with the scattered energy [ Santra et al. (2003)].

Another method for the absolute energy calibration of a heavy ion accelerator is based on the fact that the magnetic rigidity  $B\rho$  is determined by the beam energy and the charge state of the ion beam. In this method, a heavy-ion beam is stripped with a thin carbon foil in front of the

entrance of a magnetic analyzer to create particles with different charge states but same energy. A standard  $\alpha$ -source with precisely known energies is used to provide known magnetic rigidities. The energy of the ion beam with the highest charge state needs to be selected to match the known rigidities of the  $\alpha$ -source. Therefore this selected beam energy can be exactly calculated and the different rigidities of the particles with all other charge states can be also determined to calibrate the magnetic analyzer in a full rigidity range [ Martin et al. (1985)].

A cross-over technique allows energy calibration of a magnetic analyzer in a wide energy range up to several tens MeV and is not limited to some particular energies. When a beam of charge particles bombards a very thin target made of two different nuclei, the particles can be elastically scattered by light nuclei or inelastically scattered by heavy nuclei. For example, the proton beam impinges onto Mylar which consists of hydrogen and carbon. There must be a unique scattered angle  $\Theta_c$  at which the elastically scattered energy from hydrogen target nuclei equals the inelastically scattered energy from the first excited state of carbon target nuclei. The determination of the “crossover” angle  $\Theta_c$  allows the determination of the incident energy [ Birattari et al. (1992)].

The precise knowledge of the energy and the energy spread of the ion beams extracted from the ReA linac is very important and mandatory in many applications. The aim of this dissertation was to develop some techniques capable of supplying an absolute and precise measurement of the beam energy. The  $45^\circ$  analyzing magnets can provide precise energy determination but the magnets need to be calibrated. Two different methods were accomplished to perform energy calibration of the magnets. Since the ReA3 energy range of 0.3-3 MeV/u is available in the first stage of the project, the first method employed a simple but precise calibration technique based on gamma-ray resonances. Table 1.1 lists several narrow, high-yield (p, $\gamma$ ) resonances at  $E_p=300\text{--}2000$  keV which have been widely used for beam energy calibration in many electrostatic accelerators. The  $^{27}\text{Al}(p,\gamma)^{28}\text{Si}$  and  $^{58}\text{Ni}(p,\gamma)^{59}\text{Cu}$  resonance reactions are ideally suited for our calibration purpose because some of their resonances have narrow resonance width ( $<0.1$  keV) and large resonance strength around the beam energy region of our interest. The use of the resonance reactions also can be applied to evaluate the energy spread of the ion beams.

Reaction	Resonance energy (keV)	Resonance width (keV)
$^{24}\text{Mg}(p,\gamma)^{25}\text{Al}$	419.1	0.098
$^{26}\text{Mg}(p,\gamma)^{27}\text{Al}$	338.4	0.079
	453.8	0.11
$^{23}\text{Na}(p,\gamma)^{24}\text{Mg}$	309	0.02
	512.1	0.05
	677	0.07
$^{27}\text{Al}(p,\gamma)^{28}\text{Si}$	405.5	0.042
	632.2	0.0048
	991.88	0.1
	1315.88	0.07
$^{20}\text{Ne}(p,\gamma)^{21}\text{Na}$	1168.8	0.015
$^{58}\text{Ni}(p,\gamma)^{59}\text{Cu}$	1424.1	0.05
	1843.6	0.1
$^{13}\text{C}(p,\gamma)^{14}\text{N}$	1747.6	0.075

Table 1.1 (p, $\gamma$ ) resonances commonly used for beam energy calibration in most of accelerators. [ Uhrmacher et al. (1985)] [ Bondelid & Kennedy (1959)].

The second method used a novel bunch time-of-flight technique which is using an existing beam bunching system and two secondary electron emission monitors with appropriate separation. In an approach presented in this dissertation, we calibrated the first 45° bending magnet in S bend and the bunch TOF system with the  $\gamma$ -ray resonant reactions. In the first part of the beam energy calibration measurements for the 45° bending magnet, we utilized the CAESium iodide ARray (CAESAR) detector [ Weisshaar et al. (2010)] which consists of 192 CsI(Na) scintillation crystals with excellent 95% covering angle around the target to determine the resonances of  $^{27}\text{Al}(p,\gamma)^{28}\text{Si}$  at  $E_p=992$  keV and 632.2 keV served as the calibration points. In the second part of the beam energy calibration measurements, we used the  $^{58}\text{Ni}(p,\gamma)^{59}\text{Cu}$  resonances at  $E_p=1843$  keV as well as the  $^{27}\text{Al}(p,\gamma)^{28}\text{Si}$  at  $E_p=992$  keV using the high efficiency Summing NaI:Tl (SuN) detector [ Simon et al. (2013)] to extent the calibration of the bend magnet to higher energies. In the third part of the beam energy calibration measurements, the calibration factor of the magnet can be determined by the well-calibrated TOF system over a wide range of beam energies. As a result, a

number of precise calibration points were obtained by using these two techniques. The calibrated TOF system can also provide a quick online method of carrying out beam energy determination for ReA3 diagnostic system.

The theory of dipole calibration factor and  $\gamma$ -ray resonance reactions is illustrated in Section 2.1 and Section 2.2, respectively. A detail description of the experimental setup, procedure, results and discussion for  $^{27}\text{Al}(p,\gamma)^{28}\text{Si}$  and  $^{58}\text{Ni}(p,\gamma)^{59}\text{Cu}$  resonance reactions in the first and second parts of the beam energy calibration measurements is presented in Section 3.1. The determination of beam energy spread by  $\gamma$ -ray resonance reactions is compared with the beam dynamics simulation in Section 3.1.5. The calibration and measurements of the bunch time-of-flight technique for the third part of the beam energy calibration measurements are described in Section 3.2. Finally, the conclusion of the dipole energy calibration is given in Section 5.1.

### 1.3 Scintillator screen

Scintillators are the primary radiation sensors in medical diagnostics, industrial inspection, dosimetry, accelerator physics, nuclear and particle physics [ Greskovich & Duclos (1997)]. Scintillation detectors can convert energy of incident x-ray, gamma-ray, or charged particles into visible light that can be recorded by a CCD camera, photodiodes or photomultiplier tubes. The main process of the scintillation mechanism involves several stages [ Dujardin et al. (1997)]: (a) multiplication of electronic excitations through inelastic electron-electron scattering and Auger processes; (b) thermalization of hot electrons and holes with the production of phonons; (c) formation of self-trapped excitons and self-trapped holes or capture of electrons and holes by defect traps; (d) localization of the excitons to the states in the band gap; (e) radiative recombination of localized excitons; (f) emission of photons. Efficient scintillation is often achieved by doping scintillator crystals with very small amounts of certain impurities known as luminescence centers (or activators). For example, a  $\text{Ce}^{3+}$  is doped in a Yttrium Aluminium Garnet ( $\text{Y}_3\text{Al}_5\text{O}_{12}$ ) crystal. The scintillation spectrum of YAG: Ce ( $\text{Y}_3\text{Al}_5\text{O}_{12}$ : Ce) consists of a broad peak at about 550 nm coming from the recombination of excitons near a  $\text{Ce}^{3+}$  ion which serves as a “luminescence center”. Figure 1.6

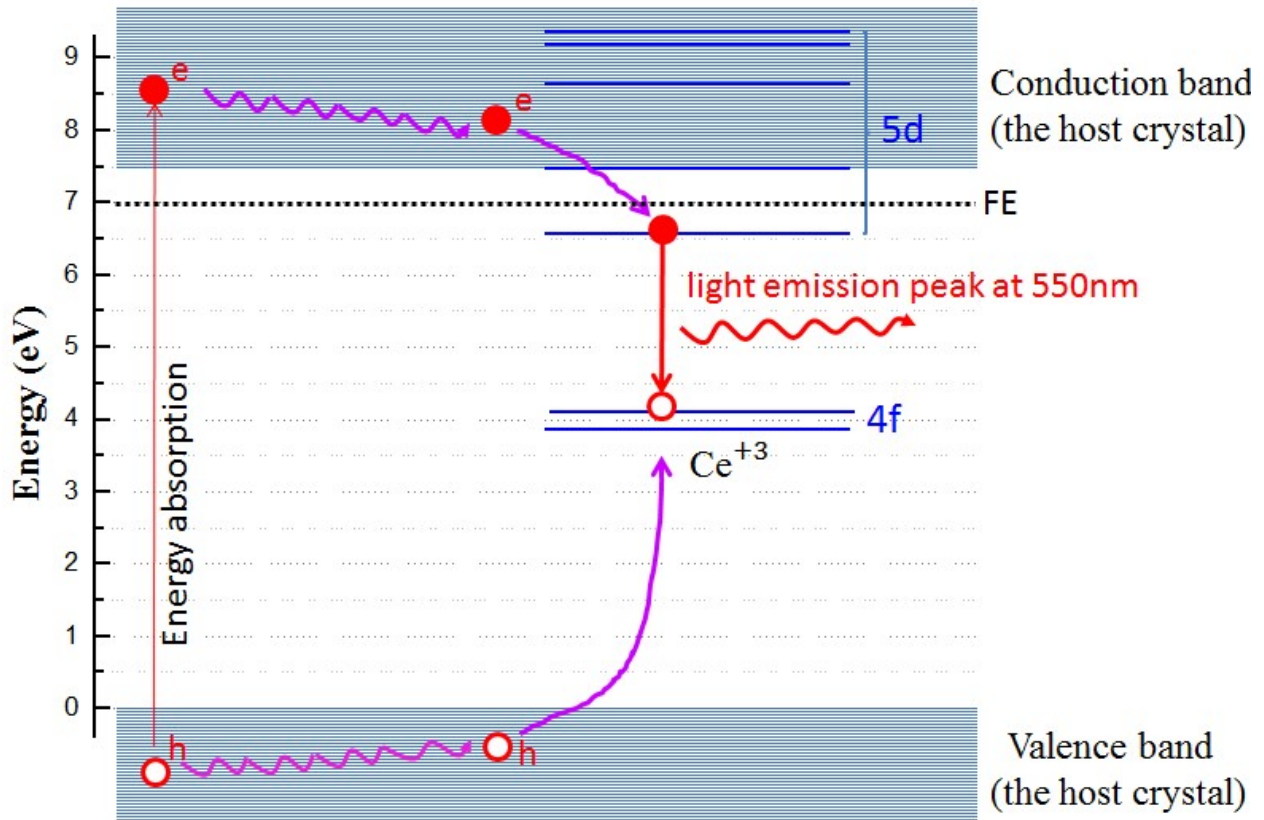


Figure 1.6 Schematics of the scintillation process in YAG: Ce. The electron-hole pair generated by the interaction of incident particles is being transported and trapped at the  $\text{Ce}^{3+}$  site. The trapped exciton recombines to emit visible light through the 5d-4f transition.

illustrates the structure of Ce ion energy levels together with the scintillation mechanism. This mechanism can be described as follows [ Eijk et al. (1994)] [ You et al. (2012)]: The energy difference  $E_{VC}$  between the top of the valence band and the bottom of the conduction band of YAG is chosen at 7.5 eV.  $E_{VC}$  is obtained by adding the energy of the fundamental excitation  $E_{FE}$  with the electron-hole binding energy in the exciton. The value for  $E_{FE}$  is about 6.96 eV (178 nm). A Cerium ion has an electron configuration of  $[\text{Xe}]4f^1$ . The 4f electron can be excited into the empty 5f shell. When a  $\text{Ce}^{3+}$  is doped in a lattice of YAG, the electron cloud expands so that the crystal field splits the 4f level into two and 5d level into five sublevels. The 4f sublevels are well shielded from the host material and therefore the splitting is very small. On the contrary, the unshielded 5d excited state is intensively perturbed by the crystal field of the host. Once incident particles and the subsequent  $\delta$ -rays ionize the atoms in the crystal, electrons can be excited into the conduction

band and leave behind an equal number of holes in the valence band. These electron-hole pairs eventually thermalize and drift through the lattice. A small energy difference between 5d and 4f levels of a  $Ce^{3+}$  makes it more likely that the electron-hole pairs preferentially move toward the local activator  $Ce^{3+}$  sites and recombine as a result of the 5d-4f electric dipole transition. The photons are emitted usually due to the transitions from the lowest 5d level to the two 4f levels ( $^2F_{5/2}$  and  $^2F_{7/2}$ ). The rapid 5d-4f transition of a Cerium activator can produce high light yield with short decay time. For YAG: Ce single crystal, the photon yield is 17,000 photons per MeV of ionizing radiation absorbed [ Greskovich & Duclos (1997)]. YAG: Ce also has a decay time less than 100 ns and good linearity between the incident particle flux and the light output [ Moszyński et al. (1994)].

Because of their optical characteristics, scintillators can provide a method to measure transverse beam profiles in beam diagnostic applications. A two dimensional high resolution beam image can be directly observed by placing a scintillator screen into the beam path and viewing the emitted luminescence with a CCD camera. In addition, an emittance meter based on a pepper-pot coupled with a scintillator has been developed by several groups [ Strohmeier et al. (2010)] to provide on-line 4-D emittance measurements. For this diagnostic method, the ion beam is intercepted by a hole-mask and the beamlets transmitted by these holes are imaged on a downstream scintillator. The angular distribution of the ion beam is extracted from the images of the beamlets on the scintillation screen. However, the accuracy of this pepper-pot method is vulnerable to the light degradation of the scintillator caused by radiation damage for low-energy ion beams, which can lead to significant errors for the emittance values. If the beam intensity is not homogeneous across the beam profile, the speed of the scintillation degradation will be different for each beamlet because the degradation speed of a scintillator depends on the accumulated fluence of beam on the scintillator screen. The central intense region of the beam usually degrades faster than the outer region with lower intensity. This results in an overestimation of statically determined (rms) emittance values.

The scintillation degradation can also deteriorate the spatial resolution of beam size measure-

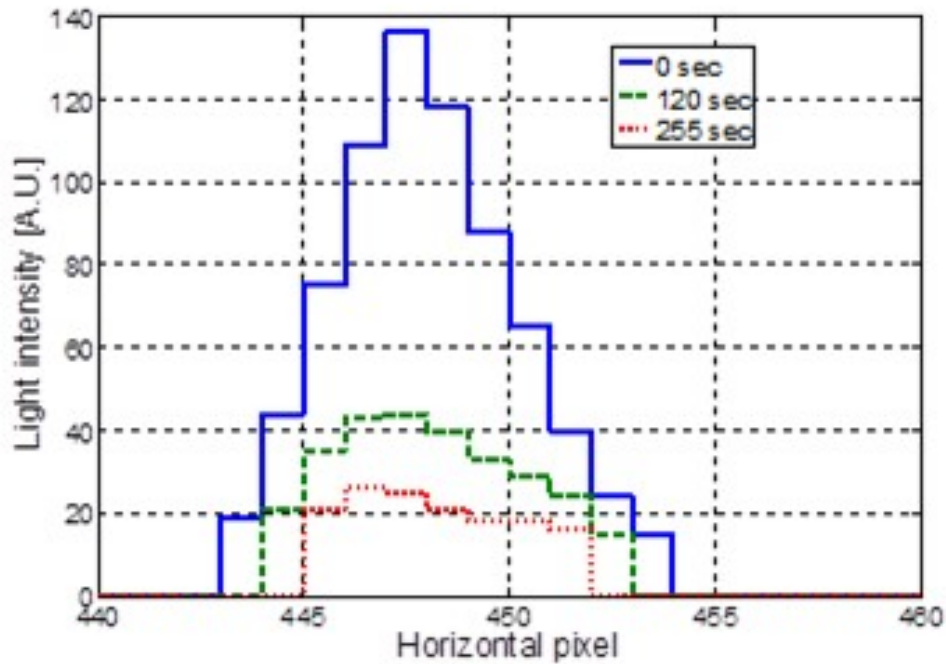


Figure 1.7 The horizontal profile of the intensity distribution produced by a  $\text{He}^+$  beam of energy  $E=48$  keV as seen on a YAG: Ce screen under different irradiation time.

ments. The degradation is particularly pronounced under low-energy ion bombardment, typically found in heavy ion injector systems. As an example Figure 1.7 shows subsequent horizontal profile measurements of a 48 keV  $\text{He}^+$  beam taken in the low energy beam transport section of the Re-Accelerator (ReA) at MSU using a YAG: Ce scintillator. It can be clearly seen that the light intensity as well as the beam size decrease with the irradiation time.

The most common radiation damage in a crystal scintillator is the formation of color centers due to ion beam bombardment. Once an incident beam of particles impinges upon a scintillator, free electrons and holes produced from the ionization process diffuse through the crystal and have a large probability of being captured by lattice defects. These defects such as vacancies and interstitial imperfections can be created by external particle bombardments. The number of these created defects depends on the nature of the scintillator crystals and the energy of the bombarding particles. Due to the formation of the defects, the color centers can arise from electrons trapped in anion vacancies (F-center) and from holes trapped in cation vacancies (V-center) [Zhu (1998)].

Color centers whose optical absorption bands are around the scintillation emission wavelength can absorb photons generated from the luminescence centers and reduce the light attenuation length. However, the appearance of radiation-induced color centers may or may not cause an overall reduced light output and a deformation of the light response uniformity during irradiation [ Zhu (1998)]. In most scintillator screens, the reduction of light output is attributed to the degradation in the transmission of light inside the crystal as a result of light absorption by displacement damages. Under ion irradiation, the scintillator can convert the deposited radiation energy into the defect creation and the exciton luminescence. Therefore the competition between the production of luminescence emission and displacement damage defects in the irradiation region along the ion path plays an important role in determining the light output loss. It has been noticed that the creation of color centers under irradiation has a dependence on the particle fluence, ion energy and energy loss along the track of the beam particles ( $dE/dx$ ). However, studies on the degradation response of scintillation yield at various irradiation energies are sparse and the degradation mechanisms are not yet fully understood [ Broggio et al. (2005)]. Efforts still need to be made to investigate scintillation degradation over a wide range of irradiation energy and scintillator materials.

The rare isotope ReAccelerator (ReA) facility of the National Superconducting Cyclotron Laboratory (NSCL) uses several scintillator-based diagnostic devices to measure transverse beam profiles. Therefore, we have measured the light degradation of scintillator viewers placed in the low energy beam transport section before RFQ. A quantitative description of the scintillator degradation as a function of fluence and beam energy under low-energy ( $< 12$  keV/u) ion irradiation is highly desirable. In this dissertation, I report results on the scintillation light response as a function of irradiation fluence for YAG: Ce ( $Y_3Al_5O_{12} : Ce$ ) single crystals under  $He^+$  irradiation at various low energies below 60 keV. The data can be described by a simple empirical model (the Birks model) of competition between light-emitting undamaged scintillator molecules and light-absorbing damaged molecules. It has to be noted that no time-dependent recovery mechanism was needed to describe the data. This may suggest that any recovery time is much longer than our irradiation times of  $\leq 10$  min and that the damage can be seen as uniquely influenced by the fluence

during our short irradiations. The speed of the degradation has been evaluated in terms of half brightness fluence  $N_{1/2}$  [ Birks & Black (1951)] defined as the particle fluence required to degrade the luminescence to one half of its original value.

A variety of scintillator materials are being tested for their suitability for ReA operations. It is of great interest to obtain suitable scintillator screens with good radiation hardness and scintillation performance in the ReA operational range of beam intensities between  $10$ - $10^{10}$  pps and energies between  $0.3$ - $6$  MeV/u. I have investigated the scintillation performance of single crystals KBr, YAG:Ce ( $Y_3Al_5O_{12}$ :Ce),  $CaF_2$ :Eu and CsI:Tl under  $H_2^+$  irradiation as a function of ion beam energy and fluence at energies between  $600$  and  $2150$  keV/u as delivered by the ReA linac. These materials were selected based on their availability, good light yield, radiation hardness, fast response or common use in beam diagnostics. In order to identify which scintillator material is suitable for ReA beam viewers, the systematic measurements presented in this dissertation were performed at room temperature and in vacuum.

The theory of scintillation mechanism and degradation is briefly described in Section 2.3. A discussion of the experimental setup, data analysis and result for the measurements of scintillator performance under low-energy ( $< 12$  keV/u) and high-energy ( $600$ - $2150$  keV/u) ion bombardment is presented in Chapter 4.

## CHAPTER 2

### THEORY

As discussed in Chapter 1, the two goals of this research are to determine the ion beam energy by an analyzing magnet with the help of nuclear resonance reactions and the time-of-flight technique, and to investigate scintillation performance of various scintillator materials for ReA diagnostic application. This chapter explains the theoretical concepts that form the foundation of the dipole calibration factor and the  $(p,\gamma)$  resonance measurements. This chapter also briefly introduces the basic principles of the ion-induced luminescence and damaged defects of a scintillator screen.

#### 2.1 Dipole calibration factor

When a particle with the mass  $M$  and charge state  $Q$  from an accelerator linac passes through a bending magnet, this charged particle with the incident velocity  $\vec{v}$  in a dipole magnetic field  $\vec{B}$  will experience a magnetic Lorentz force  $\vec{F}_B$

$$\vec{F}_B = \frac{d}{dt}(m \cdot \vec{v}) = Q \cdot \vec{v} \times \vec{B} \quad (2.1)$$

Since the force  $\vec{F}_B$  is perpendicular to the particle velocity, the net effect is a change in the velocity direction instead of the velocity magnitude. As a result, the direction of magnetic force also changes. The force  $\vec{F}_B$  provides the centripetal force required for circular motion. If the magnetic field  $\vec{B}$  is uniform and perpendicular to the particle velocity, the vector  $\vec{v} \times \vec{B}$  is replaced by  $vB$ . Equation 2.1 transforms to

$$m \frac{v^2}{\rho} = QvB \quad (2.2)$$

where  $\rho$  is the bending radius of the circular trajectory. This can be rewritten in terms of the magnetic rigidity  $B\rho$  defined as a measure of the particle's resistance to deflection in a magnetic field:

$$B\rho = \frac{mv}{Q} \quad (2.3)$$

In a low-energy accelerator, the non-relativistic relationship between the energy  $E$  of an ion and the magnetic field  $B$  is given by the expression

$$B = \frac{\sqrt{2ME}}{Q\rho} \quad (2.4)$$

The effective bending radius  $\rho$  of the magnet depends on the effective length of the magnet which is the integration of magnetic field along the reference orbit divided by the central magnetic field of the magnet. The reference orbit is the ideal beam trajectory inside the magnet and has enough length to include the fringe field at the entry and exit of the magnet. In the present work,  $\rho$  is in meter, the energy  $E$  is in keV, and  $B$  is in Tesla (T). The mass  $M$  is expressed as  $M=Am_u$  where  $A$  is the ion mass given in terms of an atomic mass unit and  $m_u$  is in kg/a.m.u. The charge  $Q$  of the particle in unit of Coulomb is written as  $Q=qe$ . Equation 2.4 can become

$$B = k \frac{\sqrt{A}}{q} \sqrt{E(keV)} \quad (2.5)$$

where  $k$  (in  $T/\sqrt{keV * amu}$ ) is the calibration factor for the magnet given by

$$k = \frac{0.004553111}{\rho} \quad (2.6)$$

The calibration factor  $k$  is characteristic of the particular magnet and essentially depends on the magnet geometry [ Rotberg et al. (1976)]. In principle, the value of  $k$  can be constant and obtained by a given magnet geometry. However, due to iron saturation and the presence of the fringing fields, the calibration factor may exhibit a small dependence on the applied magnetic field or may not remain constant over a wide range of  $E$  and  $B$  values [ Rotberg et al. (1976)]. A good calibration procedure for the analyzing magnet requires direct measurements of the calibration factor  $k$  in a wide magnet operational range. The calibration factor  $k$  can be acquired from some precisely known particle energies with the corresponding applied magnetic field. Several techniques, such as measurements of  $\gamma$ -ray resonances, (p,p) resonances, inverse (p, $\alpha\gamma$ ) resonances, non-resonant proton capture reactions, neutron threshold energies, Back Scattering (BS) , recoil protons , a time-of-flight technique and a cross-over technique, are commonly used to obtain the calibration factor  $k$  in accelerators.

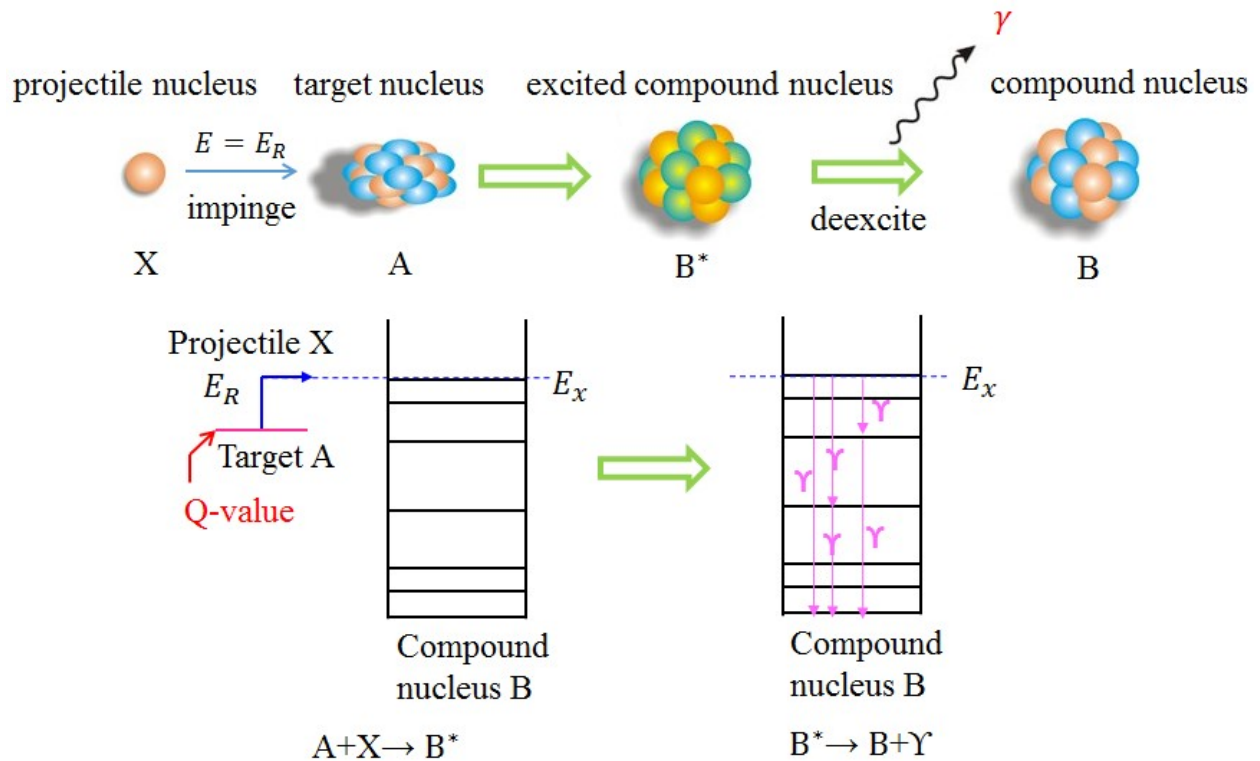


Figure 2.1 Illustration of a  $\gamma$ -ray resonance reaction  $A(X,\gamma)B$  [ Rolfs & Rodney (1988)].

## 2.2 Resonance nuclear reaction

A  $\gamma$ -ray resonance reaction is the process that when a projectile impinges onto a target nucleus with incoming energy equal to the resonance energy, the projectile will be captured by the target nucleus to form a compound nucleus in an excited state, and then decays to emit  $\gamma$  rays, as shown in Figure 2.1 [ Rolfs & Rodney (1988)]. A  $\gamma$ -ray nuclear reaction can be written in the notation  $A(X,\gamma)B$ , where  $A$  is the target nucleus,  $B$  is the final compound nucleus and  $X$  is the projectile nucleus. The resonant capture reaction involves two steps. The entrance channel of  $A+X$  forms an excited state  $E_x$  of the compound nucleus  $B$  with an incident energy  $E=E_R$ , where  $E_R$  is called the resonance energy. Then the excited state  $E_x$  subsequently decays to lower-lying states through the emission of  $\gamma$  rays with various gamma energies. The resonant reaction happens only when

$$E = E_R = E_x - Q \quad (2.7)$$

The cross section  $\sigma$  of a nuclear reaction is used to characterize the probability of a given nuclear reaction to occur. When the projectile incident energy  $E$  is near the resonant energies  $E_R$ , the cross section can be extremely high. Complete information concerning the cross section at resonance is the necessary requirement for the determination of the resonant reaction rate. The exact form of the cross section on resonance is derived through the following steps [ Rolfs & Rodney (1988)].

First, a collision between a projectile and a target nucleus can be characterized in terms of the orbital angular momentum of the projectile and the impact parameter  $b$  which represents the perpendicular distance from the projectile to the target as shown in Figure 2.2 (upper panel). The orbital angular momentum in this collision  $L$  is expressed by

$$l\hbar = L = |\vec{r} \times \vec{p}| = bp = b\frac{h}{\lambda} \quad (2.8)$$

where  $l$  is an integer value. Therefore, the impact parameter  $b$  becomes

$$b = l\frac{\lambda}{2\pi} \quad (2.9)$$

The lower panel of Figure 2.2 illustrates that a plane around the target nucleus perpendicular to the incident beam is divided into several zones with different impact parameters  $b$ . The range of  $b$  is from 0 to  $\frac{\lambda}{2\pi}$  for head-on collisions ( $l=0$ ), and can be from  $\frac{\lambda}{2\pi}$  to  $2 \cdot \frac{\lambda}{2\pi}$  for  $l=1$  collision. The zones associated with larger impact parameters lead to larger cross section. The maximum possible reaction cross section for a specific value of  $l$  can be characterized by the corresponding zone if all particles inside this zone are absorbed [ Rolfs & Rodney (1988)]:

$$\sigma_{l,max} = \pi b_{l+1}^2 - \pi b_l^2 = \pi(l+1)^2 \left(\frac{\lambda}{2\pi}\right)^2 - \pi(l)^2 \left(\frac{\lambda}{2\pi}\right)^2 = (2l+1)\pi \left(\frac{\lambda}{2\pi}\right)^2 \quad (2.10)$$

The  $(2l+1)$  term in Equation 2.10 is a statistical factor, signifying that there are more projectiles with higher orbital angular quantum numbers in an incident plane wave. In general, the spin of the projectile and the target nucleus should be taken into consideration. Therefore, the  $(2l+1)$  term in Equation 2.10 is replaced by the spin statistical factor  $\omega$

$$\omega = \frac{2J_1 + 1}{(2J_1 + 1)(2J_2 + 1)} \quad (2.11)$$

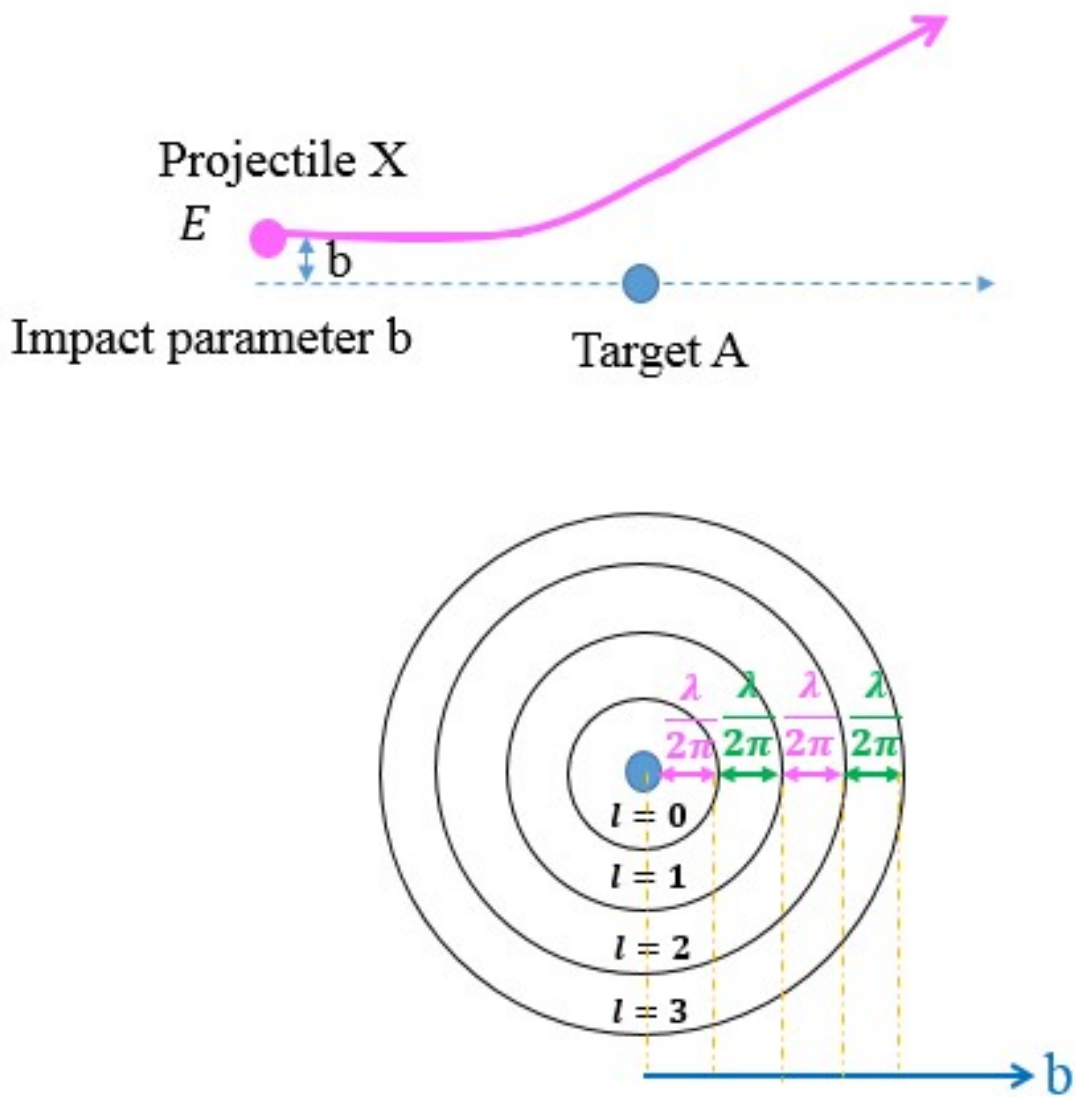


Figure 2.2 (Upper panel) Schematic diagram of a collision of a target nucleus with a projectile  $X$  associated with the impact parameter  $b$ . (Lower panel) Schematic bull-eye view of the target nucleus [ Rofls & Rodney (1988)].

where  $J$  is the angular momentum of the excited state in the compound nucleus  $B$ .  $J_1$  and  $J_2$  are the spin of the projectile and the target nucleus. The  $(2J+1)$  term represents the probability of finding the compound nucleus  $B$  in an excited state for a specific  $J$  with  $(2J+1)$  possible substates in the exit channel. The term of  $\frac{1}{(2J_1+1)(2J_2+1)}$  shows the probability of finding the projectile and target in one of  $(2J_1+1)$   $(2J_2+1)$  initial substates in the entrance channel. To combine these two probabilities leads to the spin statistical factor  $\omega$ . The maximum cross section can be rewritten in the form [ Rolfs & Rodney (1988)]:

$$\sigma_{max} = \frac{2J+1}{(2J_1+1)(2J_2+1)} \pi \left(\frac{\lambda}{2\pi}\right)^2 \quad (2.12)$$

Secondly, since the resonance reaction is a two-step process, the cross section can be described by [ Rolfs & Rodney (1988)]

$$\sigma \propto |\langle E_f | H_r | E_x \rangle|^2 |\langle E_x | H_f | A + X \rangle|^2 \quad (2.13)$$

where the operator  $H_f$  is for the formation of the compound nucleus  $B$  in an excited state  $E_x$  from the entrance channel  $A+X$ , and  $H_r$  describes the  $\gamma$ -ray emission because the excited state  $E_x$  decays to a lower-level state  $E_f$ . Each matrix element in Equation 2.13 represents the probability that this corresponding step will occur and can be assigned by a partial width. Therefore, Equation 2.13 becomes

$$\sigma \propto \Gamma_a \Gamma_b \quad (2.14)$$

where  $\Gamma_a$  is defined as the partial width for the formation of the compound nucleus  $B$  in an excited state  $E_x$  and the partial width  $\Gamma_b$  can represent  $\gamma$ -ray emission through the decay of the excited state  $E_x$ .

Thirdly, when plotted as a function of the projectile energy, the cross section at resonances usually shows characteristically as a Lorentzian with a maximum at the resonant energies  $E_R$  and the energy range given in terms of the full width at half-maximum  $\Gamma$ . Hence, the resonant cross section can be expressed in a Lorentzian form [ Rolfs & Rodney (1988)]

$$\sigma \propto \frac{1}{(E - E_R)^2 + \left(\frac{\Gamma}{2}\right)^2} \quad (2.15)$$

The total width (resonance width)  $\Gamma$  is the sum of all partial widths for each possible channel for this reaction:

$$\Gamma = \Gamma_a + \Gamma_b \quad (2.16)$$

Finally, combining Equations 2.12, 2.14 and 2.15 yields the exact form of the resonant cross section:

$$\sigma = \frac{2J+1}{(2J_1+1)(2J_2+1)} \pi \left( \frac{\lambda}{2\pi} \right)^2 \frac{\Gamma_a \Gamma_b}{(E - E_R)^2 + \left( \frac{\Gamma}{2} \right)^2} \quad (2.17)$$

This is the Breit-Wigner form of the cross section for a narrow and isolated resonance. A resonance is defined as “narrow” when  $\frac{\Gamma}{E_R} \leq 0.1$  [ Rolfs & Rodney (1988)] and isolated when the energy separation between two neighbour resonances ( $E_{R_{i+1}} - E_{R_i}$ ) is larger than the sum of their total widths ( $\Gamma_{i+1} + \Gamma_i$ ). It should be noticed that all energies and widths are in the center-of-mass system. The width ratio  $\gamma$  and resonance strength  $\omega\gamma$  are introduced in the forms:

$$\gamma = \frac{\Gamma_a \Gamma_b}{\Gamma}; \omega\gamma = \frac{2J+1}{(2J_1+1)(2J_2+1)} \cdot \frac{\Gamma_a \Gamma_b}{\Gamma} \quad (2.18)$$

By substituting Equations 2.18 into Equations 2.17, the cross section can be condensed into the form:

$$\sigma = \omega\gamma\pi \left( \frac{\lambda}{2\pi} \right)^2 \frac{\Gamma}{(E - E_R)^2 + \left( \frac{\Gamma}{2} \right)^2} \quad (2.19)$$

The de Broglie wavelength  $\lambda$  is obtained through the formula [ Rolfs & Rodney (1988)]

$$\lambda = \frac{m_p + m_t}{m_t} \frac{h}{\sqrt{2m_p E_{lab}}} \quad (2.20)$$

where  $m_p$  and  $m_t$  are the masses of the projectile and target nucleus ;  $E_{lab}$  is the laboratory energy of the incident projectile. A sketch of a normalized resonant cross section is illustrated in Figure 2.3.

Whether or not a resonant state  $E_x$  in the compound nucleus  $B$  can be formed from the entrance channel  $A+X$  is governed by the selection rules of angular momentum and parity conservation. The angular momentum  $J$  and parity  $\pi(J)$  of the resonant state in the compound nucleus  $B$  must follow

$$|J_1 - J_2| \leq s \leq |J_1 + J_2|; |l - s| \leq J \leq |l + s|; \quad (2.21)$$

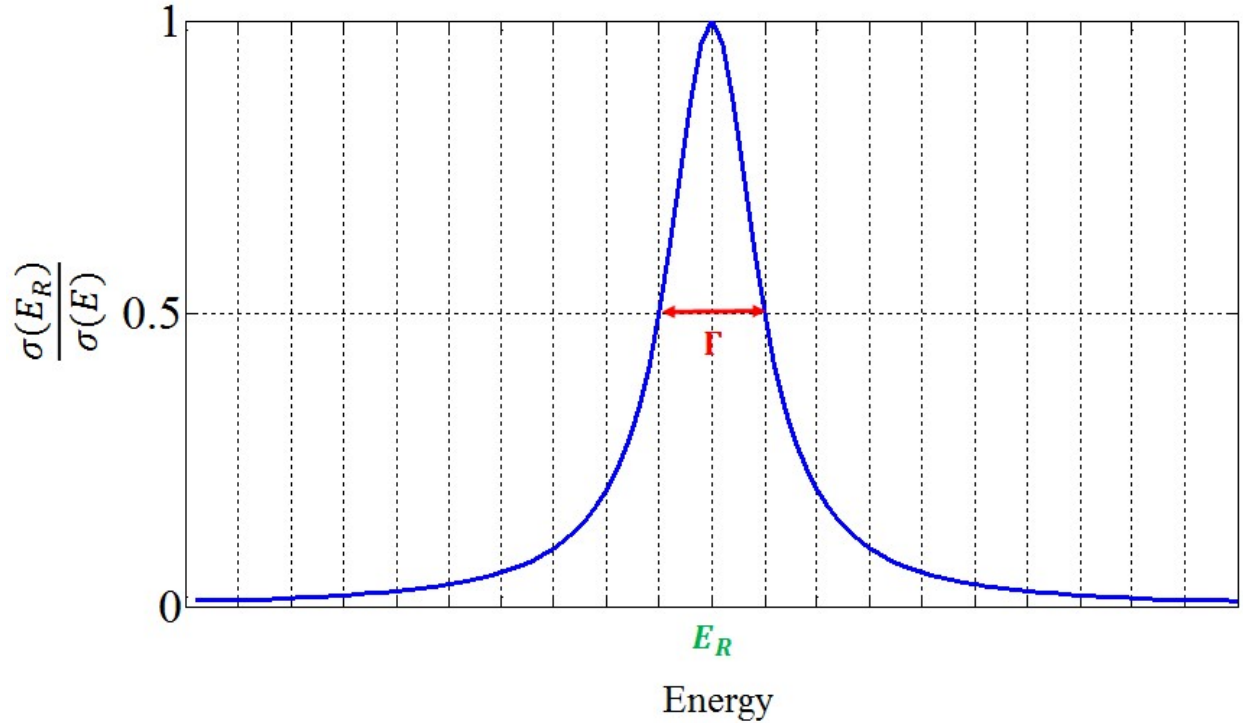


Figure 2.3 Sketch of a normalized Breit-Wigner cross section derived in Equations 2.19.

$$(-1)^l \pi(J_1) \pi(J_2) = \pi(J) \quad (2.22)$$

where  $s$  is the sum of the spins of the projectile and the target nucleus and  $l$  is the relative orbital angular momentum of the projectile and the target.  $\pi(J_1)$  and  $\pi(J_2)$  are the parities of the projectile and the target, respectively. The probability of forming a resonant state with high  $l$  is small. The values of  $l$  is most likely 0 (s-wave) or 1 (p-wave). However, higher values of  $l$  still cannot be completely ruled out.

Once the form of the cross section on resonance is determined, the  $\gamma$ -ray yield of resonance reaction would be the next. Consider a number of incident projectiles,  $N_p$ , bombarding a thin target of thickness  $\Delta x$  on an impinged area  $A$ , as shown in Figure 2.4. There are  $N_t$  target nuclei within the area  $A$ . The effective area of a target nucleus is introduced in terms of a reaction cross section  $\sigma$ . When a projectile impinges onto the effective area of a target nucleus, the probability for the reaction of  $A(X, \gamma)B$  to occur is one. It is assumed that the target thickness  $\Delta x$  is small enough so

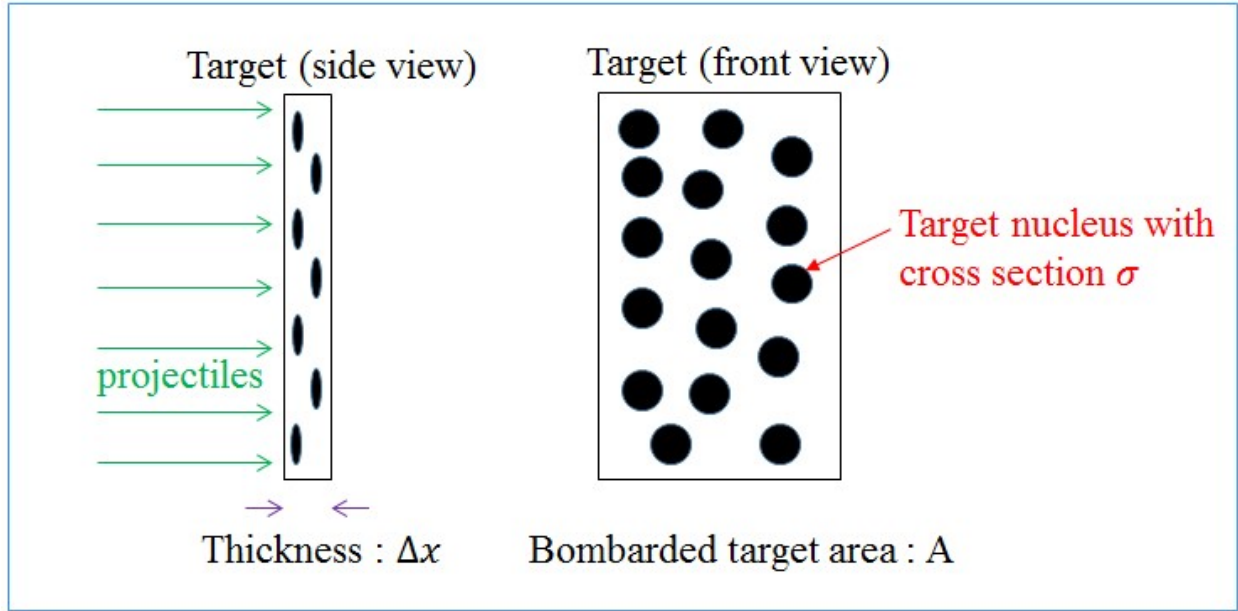


Figure 2.4 Illustration of a cross section of a nuclear reaction for a thin target bombarded with beam particles.

that the individual cross sections of the target nuclei do not overlap. The reaction yield  $Y$  would be

$$Y = \sigma \frac{N_p N_t}{A} = \sigma \cdot N_p \cdot n_t \cdot \Delta x \quad (2.23)$$

where  $n_t = \frac{N_t}{A \Delta x}$  is the number of target nuclei per unit volume. If the energy loss  $\Delta$  of the incident projectile in the target is much smaller than the resonance width  $\Gamma$ , the thin-target yield of a narrow resonance as a function of the projectile energy can be expressed by the Breit-Wigner distribution as shown in Figure 2.3:

$$Y = \sigma \cdot N_p \cdot n_t \cdot \Delta x = \omega \gamma \pi \left( \frac{\lambda}{2\pi} \right)^2 \frac{\Gamma}{(E - E_R)^2 + \left( \frac{\Gamma}{2} \right)^2} \cdot N_p \cdot n_t \cdot \Delta x \quad (2.24)$$

The projectile energy at the maximum yield corresponds to the resonant energy and the full width at half maximum of the resonance peak is the resonant width if the beam energy spread is negligible.

Furthermore, the target thickness  $\Delta x$  can be written as,

$$\Delta x = \frac{\Delta}{\frac{dE}{dx}} = \frac{\Delta}{\epsilon \cdot n_t} \quad (2.25)$$

where  $\Delta$  is the energy loss of the incident projectile through the target in the center-of-mass system, and  $\frac{dE}{dx}$  is the energy loss per unit length as the projectile passes through the target medium. The

stopping cross section  $\varepsilon$  is defined as

$$\varepsilon = \frac{1}{n_t} \cdot \frac{dE}{dx} \quad (2.26)$$

In terms of  $\Delta$  and  $\varepsilon$ , the thin-target yield can be given alternatively as

$$Y = \sigma \cdot N_p \cdot \frac{\Delta}{\varepsilon} = \omega\gamma\pi \left(\frac{\lambda}{2\pi}\right)^2 \frac{\Gamma}{(E - E_R)^2 + \left(\frac{\Gamma}{2}\right)^2} \cdot N_p \cdot \frac{\Delta}{\varepsilon} \quad (2.27)$$

In case of a thick target where  $\Delta \gg \Gamma$ , the reaction yield becomes an integral of the cross section over the target thickness:

$$\begin{aligned} Y &= \int \sigma \cdot N_p \cdot n_t dx = \int_{E_{0,cm}-\Delta}^{E_{0,cm}} \sigma \cdot N_p \cdot \frac{dE}{\varepsilon} \\ &= \int_{E_{0,cm}-\Delta}^{E_{0,cm}} \omega\gamma\pi \left(\frac{\lambda}{2\pi}\right)^2 \frac{\Gamma}{(E - E_R)^2 + \left(\frac{\Gamma}{2}\right)^2} \cdot N_p \cdot \frac{dE}{\varepsilon} \end{aligned} \quad (2.28)$$

where  $E_{0,cm}$  represents the incident energy of the projectile in the center-of-mass system.  $E_{0,cm}$  can be obtained by the laboratory energy of the incident projectile  $E_{0,lab}$ :

$$E_{0,cm} = \frac{m_t}{m_t + m_p} E_{0,lab} \quad (2.29)$$

The integral in Equations 2.28 is solved in terms of arc tan function. If the energy dependence of  $\lambda$ ,  $\Gamma$ ,  $\omega\gamma$ ,  $\varepsilon$  and  $\Delta$  is approximately negligible over the region of the resonance, the thick-target yield in Equations 2.28 can be rewritten as [ Rolfs & Rodney (1988)]

$$Y = \omega\gamma \left(\frac{\lambda^2}{2\pi}\right) \frac{m_p + m_t}{m_t} \frac{N_p}{\varepsilon} \left[ \arctan\left(\frac{E_{0,cm} - E_R}{\frac{\Gamma}{2}}\right) - \arctan\left(\frac{E_{0,cm} - E_R - \Delta}{\frac{\Gamma}{2}}\right) \right] \quad (2.30)$$

The  $\left(\frac{m_p + m_t}{m_t}\right)$  term is added because  $\varepsilon$  is usually given in the laboratory system. The resonant yield curve for a thick-target is illustrated in Figure 2.5. The middle of the rise of the yield curve is taken to be the resonance energy  $E_R$  and the energy interval between the 25% and 75% points of the maximum yield is the resonance width if the resonance width is much larger than the energy spread. Figure 2.6 illustrates that when a projectile with incident energy  $E_0 > E_R$  passes through a thick target, its energy inside the target gradually decreases due to energy loss and eventually matches the resonance energy. The resonance yield is still observed. As a result, the resonance

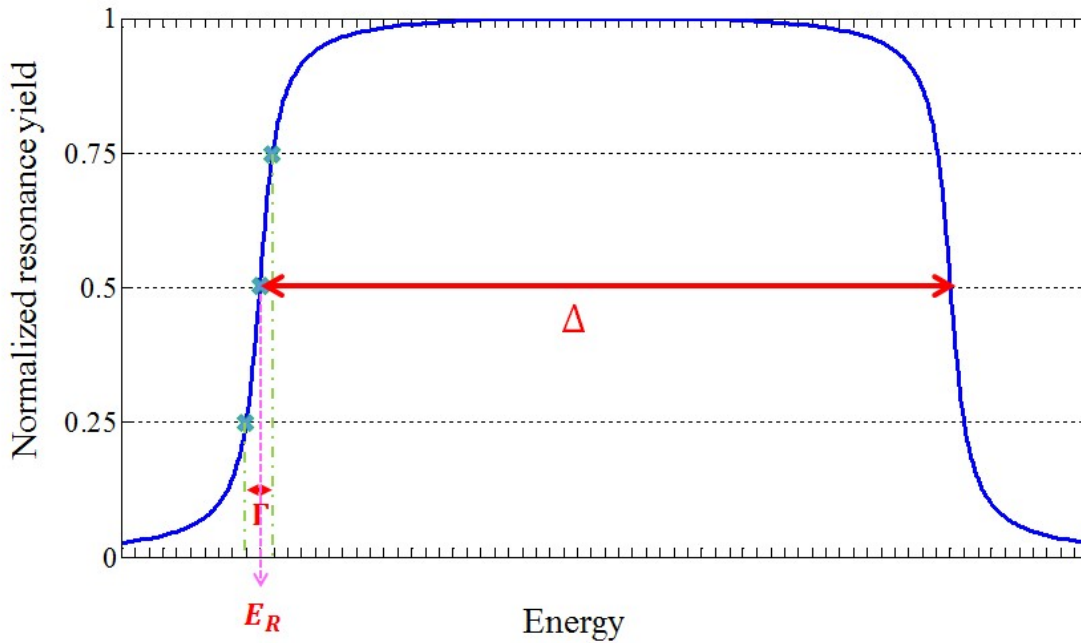


Figure 2.5 Sketch of a normalized resonant yield curve in Equations 2.30 for a thick-target. The yield curve is normalized to the maximum yield for illustrative purposes.



Figure 2.6 Illustration of the resonance reaction happening at the target surface when the projectile incident energy is  $E_0 = E_R$  (left), and inside the target when  $E_0 > E_R$  (right).

yield curve in Figure 2.5 shows a flat plateau in the energy region of  $E_0 > E_R$ . The height of the plateau corresponds to the maximum yield:

$$Y_{max} = \omega\gamma\left(\frac{\lambda^2}{2}\right) \frac{m_p + m_t}{m_t} \frac{N_p}{\varepsilon} \quad (2.31)$$

The energy interval between the middle points of the rise and fall of the yield curve corresponds to the target thickness  $\Delta$ , as shown in Figure 2.5.

In actual beam delivery systems, ion beams from accelerators are not monoenergetic, but have an intrinsic energy spread. Therefore, the reaction yield is influenced by the intrinsic beam energy distribution. In addition, the Doppler broadening effect which is attributed to the thermal motion of the target atoms also broadens the signal. The velocities of the target atoms can be describes with a Maxwell-Boltzmann distribution, leading to broaden the projectile energy inside the target [ Rolfs & Rodney (1988)]. Both effects can be included in a single Gaussian function to introduce the probability distribution of the projectile energy  $g(E, E_{0,cm})$ :

$$g(E, E_{0,cm}) = \frac{1}{\sqrt{2\pi} \cdot \delta} \exp \left[ -\frac{(E - E_{0,cm})^2}{2\delta^2} \right]; \quad (2.32)$$

$$\int_0^{\infty} g(E, E_{0,cm}) dE = 1 \quad (2.33)$$

where  $E_{0,cm}$  is the mean incident energy. The standard deviation of this beam energy distribution  $\delta$  is contributed from the beam intrinsic energy spread  $\delta_b$  and the Doppler broadening width  $\delta_D$ :

$$\delta = \sqrt{\delta_b^2 + \delta_D^2} \quad (2.34)$$

The Doppler broadening width is given by

$$\delta_b = \sqrt{2 \frac{m_p}{m_t} \cdot E \cdot kT} \quad (2.35)$$

where  $T$  is the target temperature. The Doppler broadening width is usually much smaller than the beam intrinsic energy spread if the incident energies are low. For example, the  $\delta_D$  in the reaction of  $^{27}\text{Al}(p, \gamma)^{28}\text{Si}$  is found to be 40~53 eV in the proton energy range of 770–1360 keV. Therefore, we can assume  $\delta \approx \delta_b$  [ Rolfs & Rodney (1988)].

Consequently, based on Equation 2.28 and Equation 2.33, the resonance yield should be folded with the beam energy distribution:

$$Y(E_{0,cm}) = N_p \int_{E_{0,cm}-\Delta}^{E_{0,cm}} \int_0^{\infty} \frac{\sigma(E')}{\epsilon(E')} g(E', E_{0,cm}) dE' dE \quad (2.36)$$

or

$$Y(E_{0,cm}) = \omega \gamma \left( \frac{\lambda^2}{2\pi} \right) \frac{m_p + m_t}{m_t} \frac{N_p}{\epsilon} \int_0^{\infty} \left[ \arctan\left(\frac{E - E_R}{\frac{\Gamma}{2}}\right) - \arctan\left(\frac{E - E_R - \Delta}{\frac{\Gamma}{2}}\right) \right] \frac{1}{\sqrt{2\pi} \cdot \delta} \exp\left[-\frac{(E - E_{0,cm})^2}{2\delta^2}\right] dE \quad (2.37)$$

Hence, the shape of a thick-target yield curve from a resonance is determined by the resonance width as well as the projectile incident energy spread. But if the incident energy spread is much large compared to the resonance width, the yield curve can be used to estimate the beam energy spread. Figure 2.7 illustrates how the shape of a yield curve is dominated by the incident-beam energy spread. A very accurate method of determining the beam energy spread is to set  $\delta$  as a parameter and fit the experimental yield curve with the above yield equation.

## 2.3 Scintillation mechanism and degradation

### 2.3.1 Scintillation mechanism

Scintillators can absorb and convert the deposited energy of an incident ionizing radiation into visible photons. This property leads to the use of scintillator screens as means of monitoring beam transverse profiles in most of accelerator facilities. Scintillators are mainly classified as organic and inorganic. The scintillation mechanism responsible for the light emitting characteristic of these two types is fundamentally different. Organic scintillators consist of aromatic hydrocarbons and the scintillation is due to the transition between molecular energy levels in a single molecule. A molecular energy structure of an organic scintillator is composed of electronic, vibrational and rotational levels as shown in Figure 2.8 [ McParland (2010)]. As incident radiation deposits energy in the scintillator, the molecule is excited from the ground state to higher singlet states labeled as

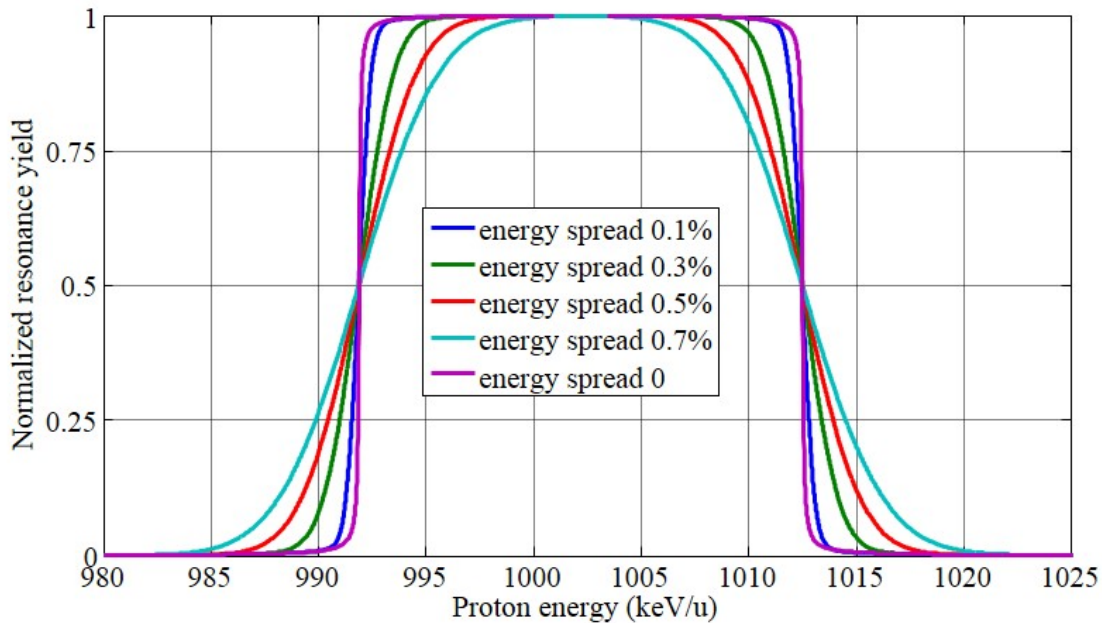


Figure 2.7 Sketch of a normalized resonant yield curve of  $^{27}\text{Al}(p,\gamma)^{28}\text{Si}$  at  $E_p= 992$  keV for a thick target with varying beam energy spreads according to Equations 2.37. The yield curves are normalized to the maximum yield for illustrative purposes. The resonance width at this resonance is about 0.1 keV [ Endt & der leun (1978)].

$S_1$ ,  $S_2$ ,  $S_3$  in Figure 2.8. The  $S_2$  and  $S_3$  states de-excite promptly in picoseconds to the  $S_1$  state through internal conversion without the emission of photons. The transition from the  $S_1$  state to the ground state  $S_0$  is prompt (in a few nanoseconds ) with the emission of scintillation fluorescence. The  $S_1$  state can also decay to the  $T_1$  state which has the lifetime of  $\sim$ ms and the transition of  $T_1 \rightarrow S_0$  gives rise to the emission of scintillation phosphorescence. The scintillation fluorescence can be distinguished from the scintillation phosphorescence due to its fast decay time and shorter wavelength.

Inorganic scintillators are usually crystals made of halides and oxides and the scintillation depends on the band structure of the crystal lattice. Most inorganic scintillators are impurity activated, which means the luminescence is emitted from small amounts of specific impurity atoms as luminescence centers. when the deposited energy of incident radiation excites an electron from the valence band of the crystal to the conduction band, the electron freely travels through the crystal. Eventually, with an hole in the valence band, an electron-hole pair is created as an exciton.

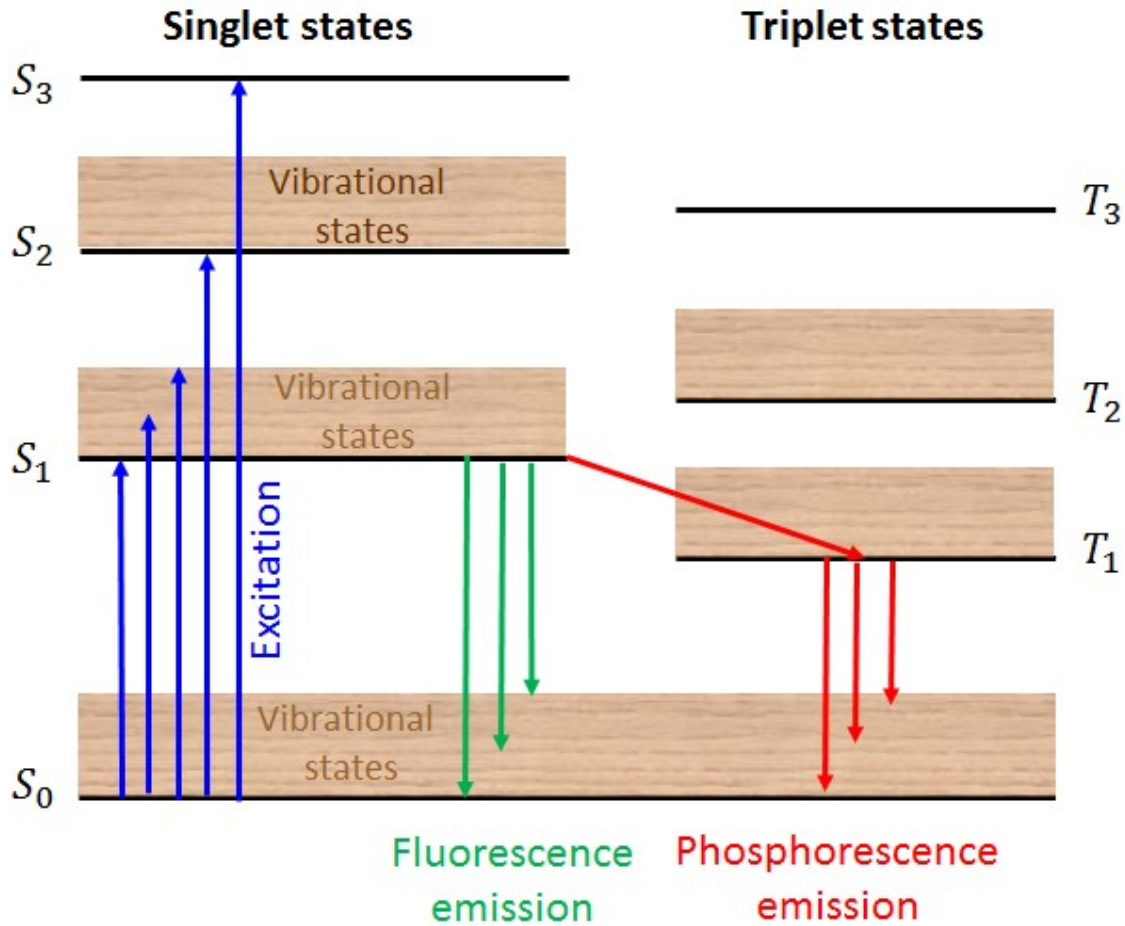


Figure 2.8 Transitions between molecular energy levels for an organic scintillator. [ McParland (2010)]

The electron-hole pair is fairly stable and can migrate to the impurities. The impurities produce electronic energy levels existed in the band gap between the conduction and valence bands. If these energy levels in the band gap are unoccupied, they can act as recombination centers for the electron-hole pairs, leading to the emission of light in the visible range as shown in Figure 1.6.

Either type of scintillators can be used for beam profile measurements. However, inorganic scintillators exhibit a better efficiency of the interaction between matter and radiation due to their large atomic number. Since inorganic scintillators can provide several desirable properties, such as high stopping power, excellent efficiency of energy conversion into light, and energy resolution, they are chosen for beam profile diagnostics in ReA3.

### **2.3.2 Scintillation degradation**

Scintillation stability and reproducibility of a scintillator are essentially critical to beam diagnostic applications. Radiation damage can result in the change of the light output of a crystal scintillator. The possible radiation damage effect in a crystal scintillator is the radiation-induced absorption by defects. These defects can be excessively created by ion bombardments, providing local energy levels in the band gap of the host crystal to absorb the photons emitted from luminescence centers. The locations of the energy levels of the defects are determined by the nature of the defects and the host lattice. If the absorption wavelength of the defects occurs in the visible region, a characteristic color would be appeared to the crystal. Hence, a color center is commonly a lattice defect, which can absorb scintillation photons.

Radiation damage can create point defects and extend defects in a crystal scintillator. The simplest point defects in the crystal lattice are interstitials or vacancies. An interstitial is an atom which occupies a position between the bulk atoms of the lattice structure, and a vacancy is an empty (unoccupied) site where an atom is missing from the perfect lattice structure. These defects are capable to trap electrons or holes. Extended defects are aggregates of point defects due to intensive radiation exposure. Depending on the type of the defects, there are several color centers formed by radiation dose in a crystal scintillator as described below.

#### **2.3.2.1 F centers**

The F centers are the most simple trapped electron centers induced by ionizing radiation and can be readily formed in alkaline halides. The name of F center is derived from the German word Farbe which represents color. When sufficient F centers absorb white light in a narrow visible wavelength range, the crystal is colored. In an example of alkali halide crystals, when the incident radiation ionizes an electrons from a halide ion in the crystal, the electron is not bound to the halide atom. This electron would drift through the crystal and become trapped in a negative ion vacancy which has the effect of an isolated positive charge. The negative ion vacancy with the trapped electron is called as a F center. In alkali halides, the F center is electrically neutral. However, the F

center can lose its trapped electron to form an anion vacancy (the  $\alpha$  center) or trap another electron to become a charged center ( $F'$  center). The  $F'$  center is only stable at the temperature of  $< 100$  K [ Hayes & Stoneham (1985)]. In contrast to alkali halides, in ionic oxides an oxygen vacancy may trap one electron ( $F^+$  center), two electrons ( $F^0$  center) and three electrons ( $F^-$  center) [ Popov et al. (2010)]. The  $F^-$  center is found in  $Y_3Al_5O_{12}$  and  $Al_2O_3$  [ Popov et al. (2010)]. When the single F centers diffuse in alkali halides, the F center aggregates can be formed and characterized as M centers (two F centers,  $F_2$ ), R centers (three F centers,  $F_3$ ) and N centers (four F centers,  $F_4$ ) [ Hayes & Stoneham (1985)]. Under intensive irradiation, the F center aggregation can lead to the metal colloid formation which is discussed in Section 4.3.2.1.

### 2.3.2.2 V centers

In order to maintain electroneutrality of the crystal, for each electron trapped at a negative ion vacancy, a hole is produced and might migrate to a cation vacancy. A trapped hole at a positive ion vacancy can be formed as a V center. The V centers are the antimorph of the F centers. The name of the V center is called due to the fact that these centers can form a group of defects to absorb light in the violet wavelength region. In ionic oxides, one cation vacancy can trap one hole (the  $V^-$  center) or two holes (the  $V^0$  center) [ Kotomin & Popov (1998)]. The V center aggregates are formed of positive-ion vacancies and holes. In alkali halides, the main trapped hole centers at low temperature are the H,  $V_k$ , and  $V_F$  centers. When an electron is removed from a halide ion during radiation ionization, this halogen atom becomes neutral and not bound electrostatically to the lattice. The unbound neutral halogen atom can diffuse away from its original location and occupy an interstitial position. The interstitial halogen atom can share one electron with another halide ion to form the H center. In other words, the H center is one hole trapped by two bound halide ions ( $X_2^-$ ) in a halogen site. The vacancy which this unbound neutral halogen atom left behind forms an F center by trapping an electron [ Sunta (2014)]. The F and H centers are the Frenkel pair [ SCHWARTZ (1996)] as shown in Figure 2.9. The H centers are stable at the temperature below 30 K [ SCHWARTZ (1996)]. Above this critical temperature, The H centers

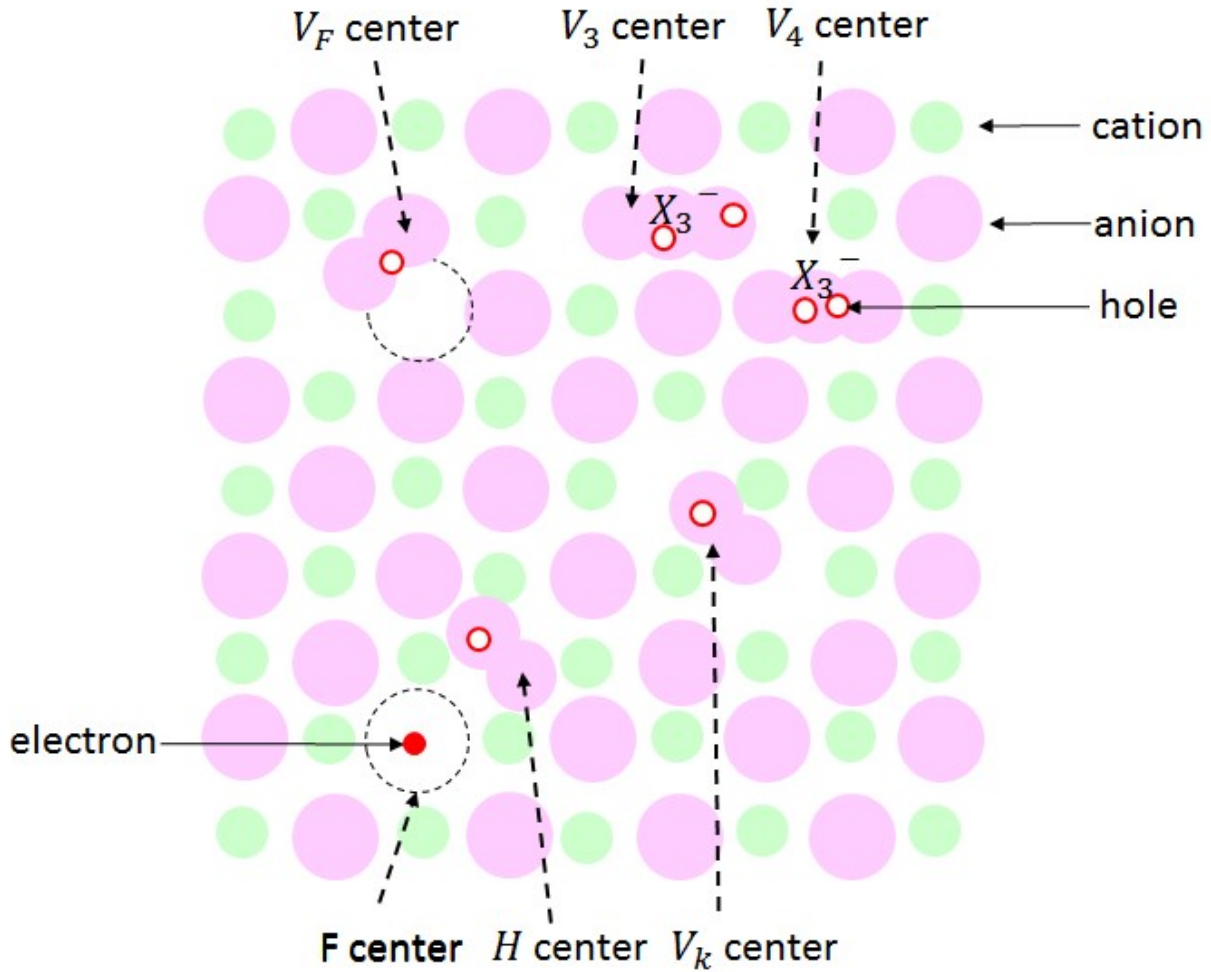


Figure 2.9 Some of the color centers in alkali halides.

become mobile and transformed into the  $V_k$  centers. The  $V_k$  center is a form of a self-trapped hole which consists of a hole trapped by two neighboring halide ions ( $X_2^-$ ) at two negative ion locations oriented along a  $\langle 110 \rangle$  direction. The  $V_k$  center is only stable at low temperature [ SCHWARTZ (1996)]. If a  $V_k$  center center is adjacent to a cation vacancy, the  $V_F$  center is formed and more stable than the  $V_k$  center. At room temperature, the stable hole centers would be the  $V_3$  and  $V_4$  centers [ Bazhin et al. (1976)]. The  $V_3$  center is formed of two holes trapped by three halide ions ( $X_3^-$ ), occupying one cation and two anion vacancies. The  $V_4$  center is the  $X_3^-$  molecular located at one cation and one anion vacancies. The  $V_3$  and  $V_4$  centers may be responsible for the luminescence of alkali halides [ Bazhin et al. (1976)] which is discussed in Section 4.3.2.1.

## CHAPTER 3

### BEAM ENERGY CALIBRATION

In this chapter, the two techniques to calibrate the  $45^\circ$  bending magnet are described. The determination of the beam energy spread extracted from the  $(p,\gamma)$  resonance experiments is also explained in more detail.

### 3.1 $(p,\gamma)$ resonant reactions

#### 3.1.1 Target thickness determination

The target thickness for the measurement of  $\gamma$ -ray resonances can be divided into two thickness categories.

(a) Thin target. If the energy loss of an incident projectile through the target is much less than the resonance width ( $\Delta \ll \Gamma$ ), the position of the resonance-yield peak corresponds to the resonance energy. The preparation of thin targets is very challenging. The narrow width of the resonance peak makes the resonance energy determination quite difficult. Hence, the thin-target method is not very practical as a general technique for precise energy calibration of magnetic analyzers.

(b) Thick or semi-thick targets. This method is easier in the target fabrication and widely used for the measurement of resonance energies. In cases of a thick target where  $\Delta \gg \Gamma$ , all projectiles are stopped inside the target. A thick target allows the projectiles with bombarding energies larger than the resonance energies perform the resonance reaction within the target because the target atoms can slow down the projectiles to reach resonance energies. The “thick-target” yield curve is described by an arc tangent function. The energy of the resonance is determined from the midpoint of the rise of the yield curve. If the beam energy covers several resonances within the target, the observed yield curve would be the sum of arc tangent functions [ Uhrmacher et al. (1985)]. In order to reduce the background of unwanted lower resonances, a semi-thick target can be used in a

Reaction	Resonance energy (keV)	Resonance width (keV)	Resonance strength (keV)
$^{27}\text{Al}(p,\gamma)^{28}\text{Si}$	632.2	0.0048	0.00029
	654.65	0.03	0.00012
	679.3	0.075	0.000058
	937.25	0.15	0.000176
	991.88	0.1	0.002
	1025.29	0.075	0.00035
$^{58}\text{Ni}(p,\gamma)^{59}\text{Cu}$	1843.5	*	0.00012
	1881	0.1	0.01

Table 3.1 The resonance parameters used for the simulation of the resonance yields in Figure 3.1 and Figure 3.2

way that the beam energy loss inside the target is smaller than the energy distance to the next lower resonance. The resonance-yield curve of a semi-thick target has a plateau and its plateau width represents the beam energy loss through the target.

In this dissertation, the method of a semi-thick target was used for (p, $\gamma$ ) resonant reaction measurements. The target thickness was determined in such a way that the plateaus of the  $\gamma$ -ray resonance yield curves were well-developed and not contaminated with the background of lower resonances. The thickness of the Al targets used for  $^{27}\text{Al}(p,\gamma)^{28}\text{Si}$  resonance reaction was  $0.4 \sim 0.45 \mu\text{m}$ . For  $^{58}\text{Ni}(p,\gamma)^{59}\text{Cu}$  reaction, the Ni target thickness was about  $0.96 \mu\text{m}$  ( $0.856 \text{ mg/cm}^2$ ). The simulated resonance yield curves with the corresponding target thickness for  $^{27}\text{Al}(p,\gamma)^{28}\text{Si}$  and  $^{58}\text{Ni}(p,\gamma)^{59}\text{Cu}$  reactions are shown in Figure 3.1 and Figure 3.2, respectively. All of the resonance properties (resonance energy, width and strength) in Figures 3.1 and 3.2 are taken from literature [ Meyer et al. (1975)] [ Maas et al. (1978)] [ Harissopoulos1 et al. (2000)] as listed in Table 3.1. During the calibration procedure, we measured the rise of the  $\gamma$ -ray yield curves for the 992 keV and 632.2 keV resonances in the  $^{27}\text{Al}(p,\gamma)^{28}\text{Si}$  reaction and 1843 keV resonance in the  $^{58}\text{Ni}(p,\gamma)^{59}\text{Cu}$  reaction.

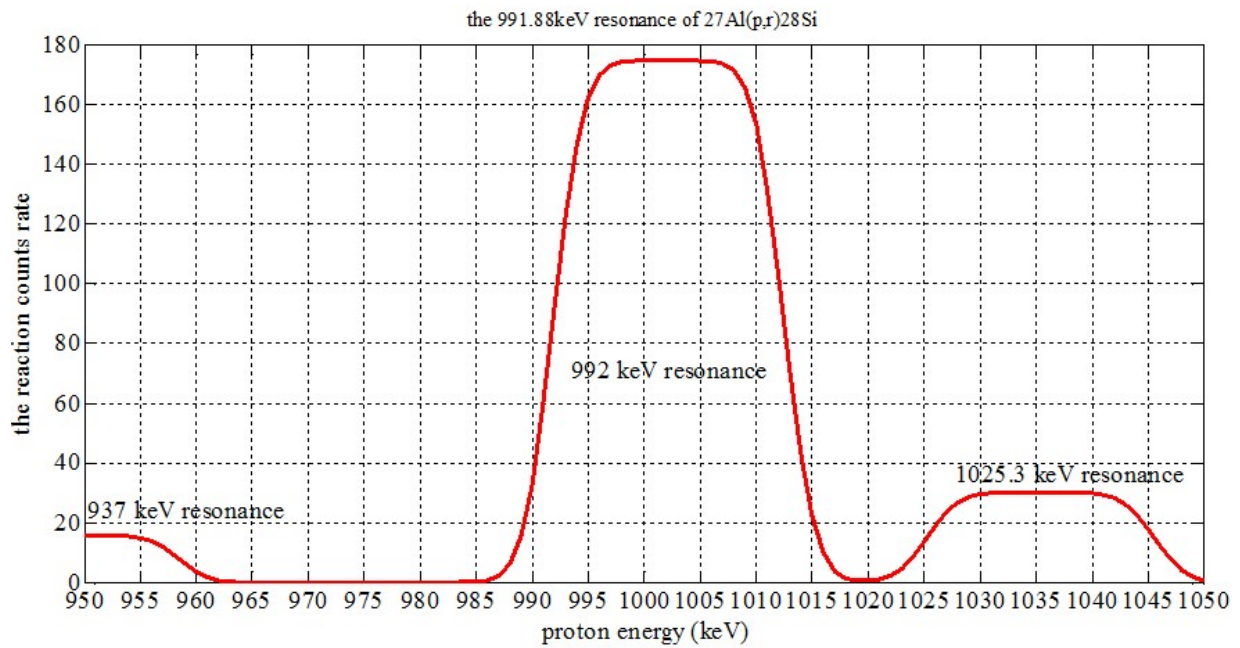
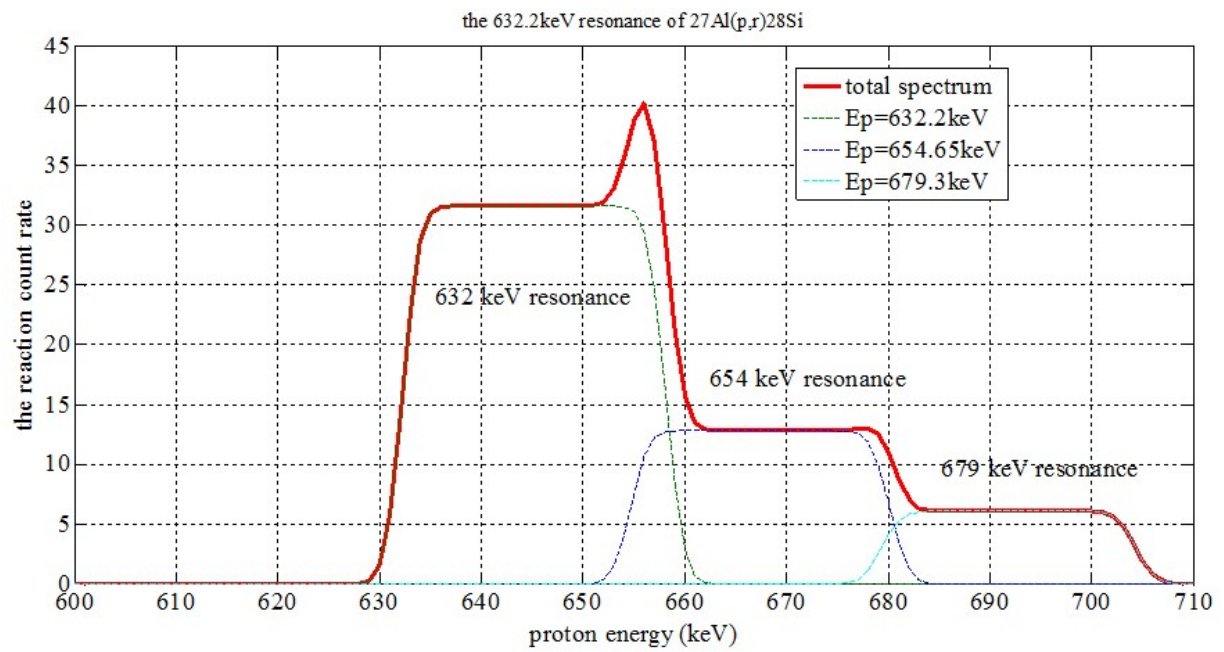


Figure 3.1 The simulated yield curves of the  $^{27}\text{Al}(p,\gamma)^{28}\text{Si}$  reaction in the 632.2 keV (upper plot) and 992 keV (lower plot) resonance domains. The target thickness, the beam energy spread and the detector efficiency are supposed to be  $0.45\ \mu\text{m}$ , 0.5 % in FWHM and 0.2.

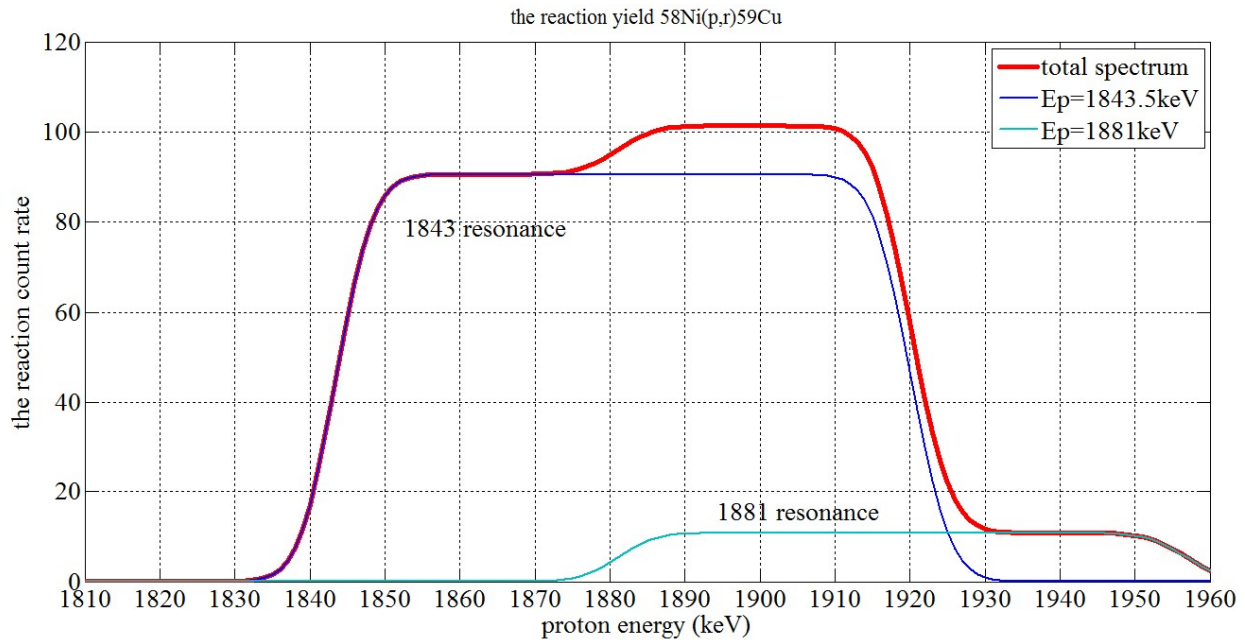


Figure 3.2 The simulated yield curves of the  $^{58}\text{Ni}(p,\gamma)^{59}\text{Cu}$  reaction in the 1843 keV resonance domain. The target thickness, the beam energy spread and the detector efficiency are supposed to be  $0.96\ \mu\text{m}$ ,  $0.5\%$  in FWHM and  $0.45$ .

### 3.1.2 $\gamma$ -ray detectors

To measure  $\gamma$  rays produced from  $(p,\gamma)$  resonance reactions, the CAESAR and SuN detectors were used for the first and second parts of the beam energy calibration measurements, respectively. The CAESAR detector was installed in the end of S bend (see Figure 3.3) during the period of June - December, 2012. After the commissioning of the L-line extension construction was complete, the SuN detector was placed in the end of the L-line extension (see Figure 1.3) for three weeks in November, 2014.

#### 3.1.2.1 CAESAR detector

For  $^{27}\text{Al}(p,\gamma)^{28}\text{Si}$  resonance reaction, a proton projectile with an incident energy  $E_p = E_R$  (resonance energy) is captured by the target nucleus to produce a compound Si nucleus in an excited state  $E_x$ . The de-excitation process involves  $\gamma$ -ray emission. Figure 3.4 shows an example of the decay scheme of  $^{27}\text{Al}(p,\gamma)^{28}\text{Si}$  resonance at  $E_p=992\ \text{keV}$ . The branching ratio of each decay

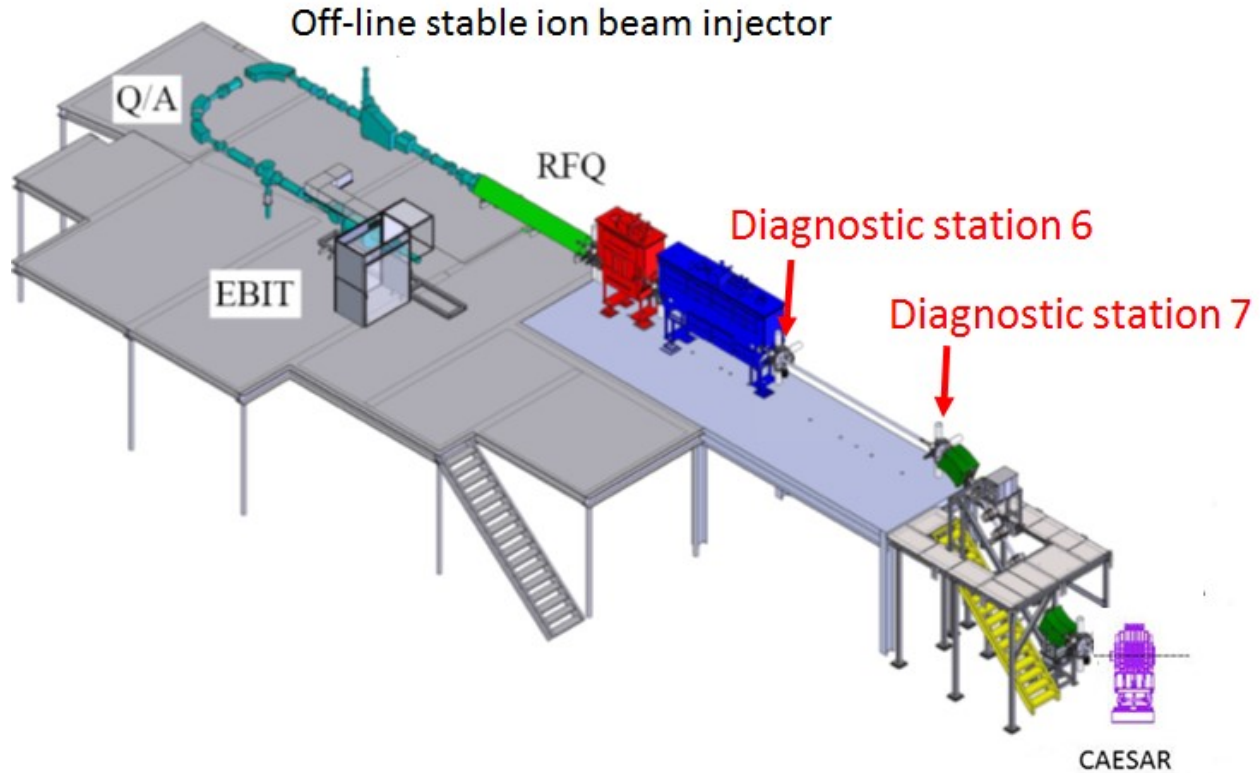


Figure 3.3 The installation location of the CAESAR detector for the first part of the beam energy calibration measurements

cascade is taken from literature [ Meyer et al. (1975)]. Most of  $\gamma$ -rays decay from the resonance state to the first excited state ( $2+$ ) in Si, and then to the ground state ( $0+$ ). The branching ratios of the dominant  $\gamma$ -ray decay mode,  $2+ \rightarrow 0+$ , for the 992 and 632.2 keV resonances are 94 % and 97 % [ Meyer et al. (1975)], respectively. To measure the  $^{27}\text{Al}(p,\gamma)^{28}\text{Si}$  resonances at  $E_p=992$  keV and 632 keV in the first part of the beam energy calibration measurements, the resonance yield curves were deduced by measuring the dominant  $\gamma$ -ray decay ( $2+ \rightarrow 0+$ ) at  $E_\gamma=1.779$  MeV with the CAESAR detector (CAESium iodide ARray) [ Weisshaar et al. (2010)]. The CAESAR detector consists of 192 CsI(Na) scintillation crystals that are arranged around the reaction target to provide an angular coverage of 95 % of  $4\pi$  as shown in Figure 3.5. CAESAR is designed in 10 rings as seen in Figure 3.5. The 1st and 10th rings hold 10 detectors each, the 2nd and 9th rings hold 14 detectors each, and the six central rings (3rd–8th) hold 24 detectors each. This geometric arrangement of 192 detectors is optimized for high detection efficiency.

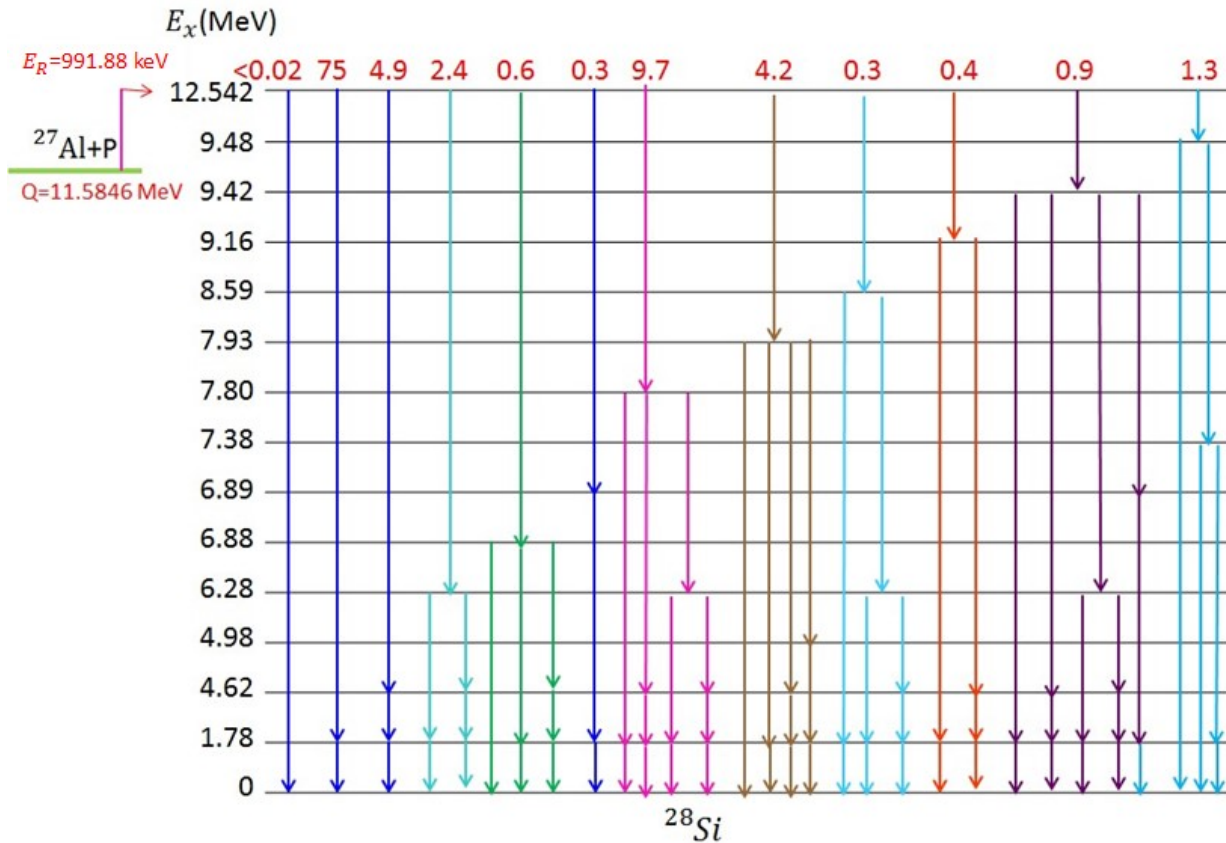


Figure 3.4 The decay scheme of the 992 keV resonance in  $^{27}\text{Al}(p,\gamma)^{28}\text{Si}$  reaction. Each decay cascade is marked by the corresponding branching ratio in percentage.

The Al target was located at the center of CAESAR. The Al target with a stainless steel frame was mounted on a Macor target holder, as shown in Figure 3.6, inside the stainless steel beam tube which was electrically isolated from the beam dump by a ceramic tube. The beam was dumped into a tantalum sheet at the end of the beam dump. The entire assembly of the beam dump was used as a Faraday cup for beam current integration. For the long term successful operation of the superconducting ReA linac, it is very important to avoid any contamination into the inner surfaces of beam transport components. Therefore, I used clean bags filled with nitrogen gas to install or change the target without exposing the target chamber to unfiltered air, as shown in Figure 3.5. A vacuum of typical  $2 \times 10^{-7}$  torr was maintained in the target chamber during operation.

Because CAESAR was made of 192 detector units that each had individual signal read out, each detector unit was calibrated using standard  $^{88}\text{Y}$ ,  $^{60}\text{Co}$ ,  $^{137}\text{Cs}$  and  $^{22}\text{Na}$  sources placed at

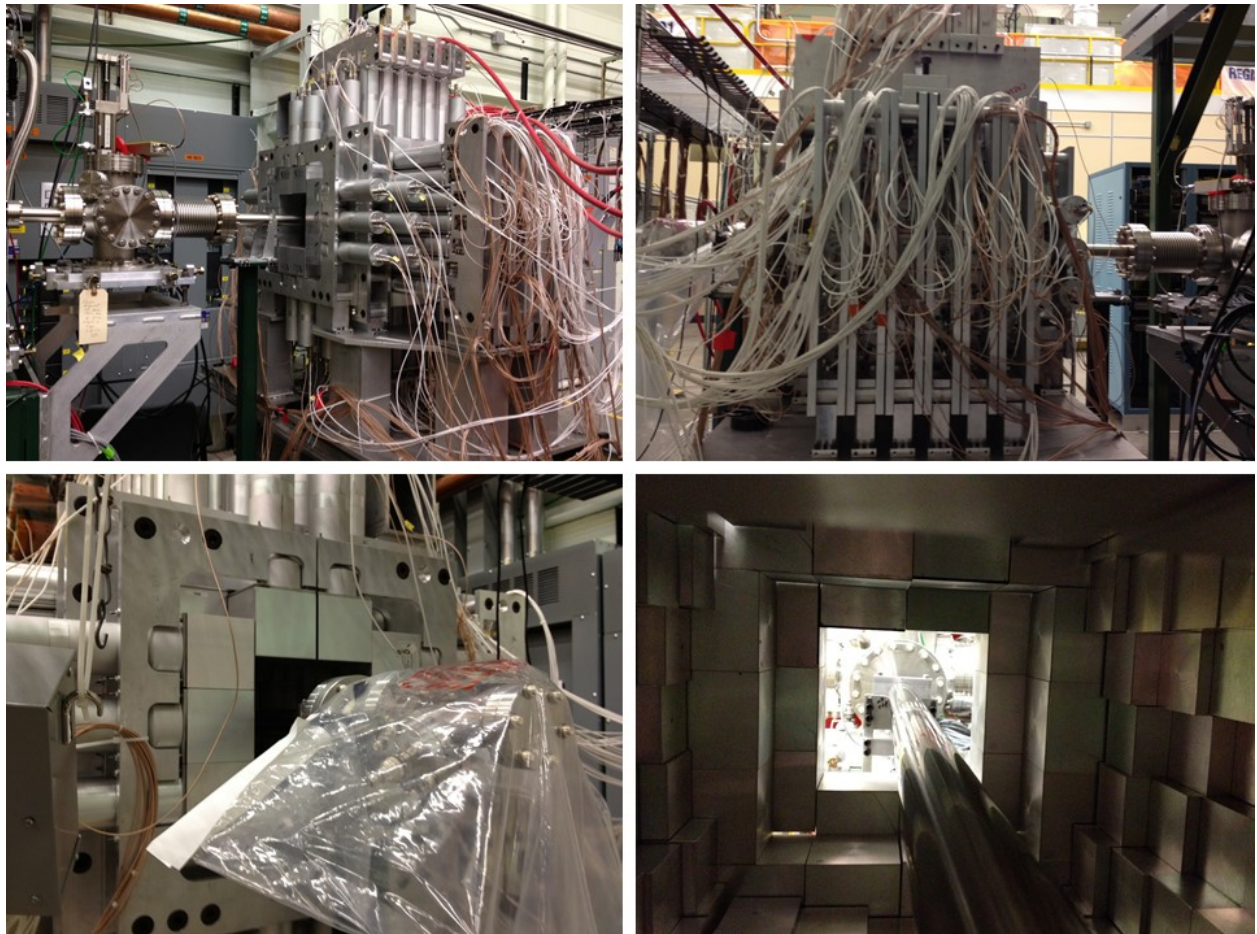


Figure 3.5 The CAESAR  $\gamma$ -detector array.

the target position inside CAESAR. Each CAESAR spectrum was obtained by summing all 192 spectra after calibrating the energy scale of each detector. Since CAESAR was located a distance 1.1 m away from the second  $45^\circ$  magnet in the S bend, the detector was subject to significant fringe fields, which can affect the response of its photomultiplier tubes. To account for this, all of the 192 detectors were calibrated with the magnet set to the approximate field value at which the experiment was performed. Since the change of the fringe field was deemed negligible in the small range of energy changes during the  $^{27}\text{Al}(p,\gamma)^{28}\text{Si}$  resonance measurements, a recalibration run using  $\gamma$ -ray sources was not taken every time the field of the magnet was varied in 0.2–0.3 mT steps.



Figure 3.6 The target with the target holder apparatus for the CAESAR detector. The Al foil target was electrically isolated from the beam dump. By connecting a wire to the target frame, the current in the target and target frame can be read through a beam current monitor. The beam was collected on a tantalum sheet at the end of the beam-line.

The energy resolution of a  $\gamma$ -ray detector is defined as [ Knoll (2010)]

$$\frac{\Delta E_{\gamma}}{E_{\gamma}} \times 100\% \quad (3.1)$$

where  $\Delta E_{\gamma}$  is the full width at half maximum of a given  $\gamma$ -ray energy peak at energy  $E_{\gamma}$ . The "intrinsic" energy resolution of CAESAR for 1.836 MeV  $\gamma$ -rays from the  $^{88}\text{Y}$  source was measured to be 3.84 %. The absolute full-energy-peak efficiency of CAESAR in the energy range between 600 keV and 2 MeV was determined with the  $^{88}\text{Y}$  and  $^{137}\text{Cs}$  sources as shown in Figure 3.7. The peak area of a free-standing  $\gamma$ -ray peak was subtracted by a linear background to determine the counts in the peak above the background. The absolute detector efficiency was calculated by

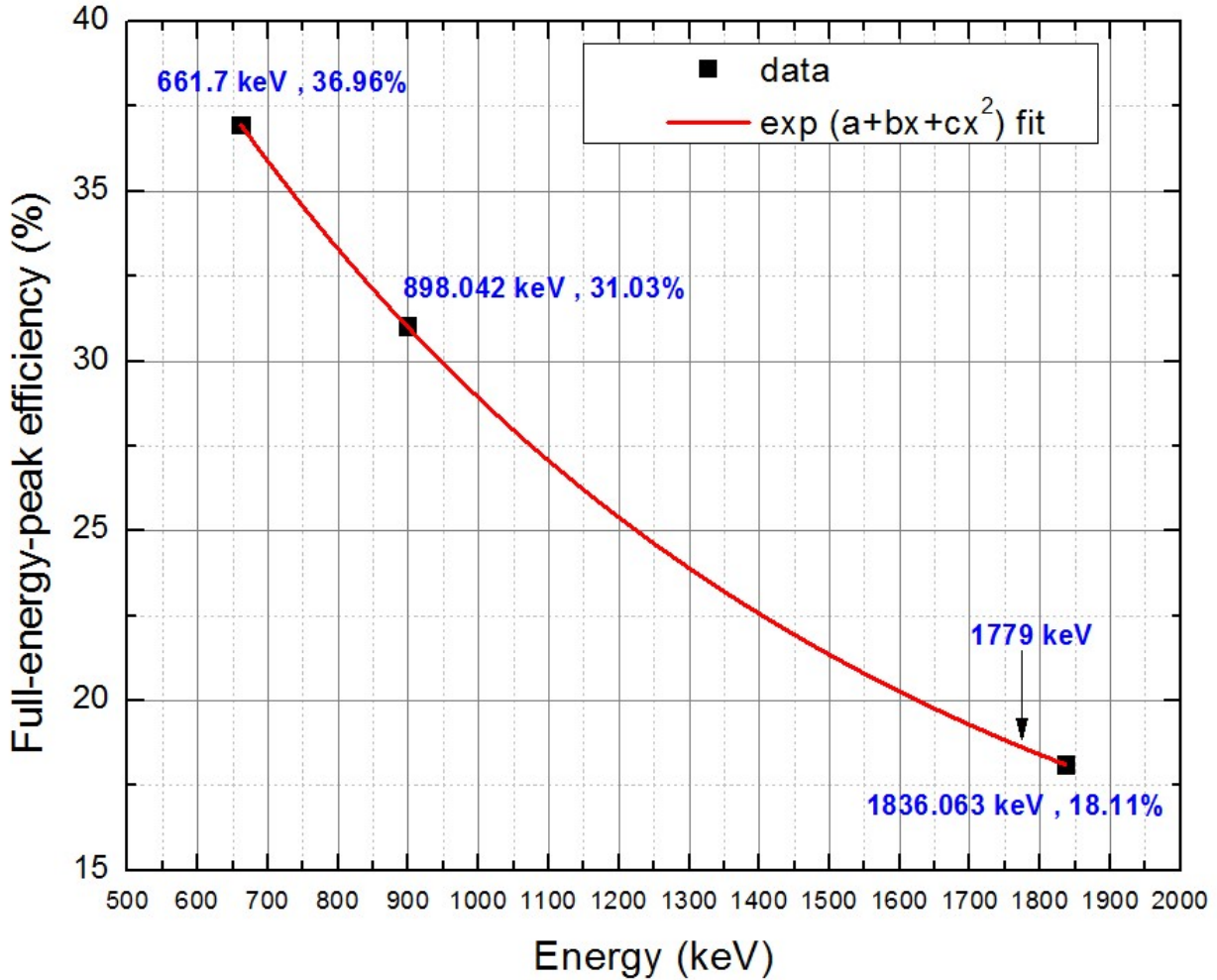


Figure 3.7 Measured absolute full-energy peak efficiency for CAESAR with the standard calibration sources. The black squares are experimental data fitted with an empirical exponential function.

dividing the net count rate in the full-energy peak by the gamma-ray-emission rate of a radioactive source [ Weisshaar et al. (2010)]. The efficiency of CAESAR as a function of gamma-ray energy was well fitted with an empirical exponential function  $e^{(a+b \cdot E\gamma+c \cdot E\gamma^2)}$  which was taken from previous CAESAR experiments [ Weisshaar et al. (2010)]. I estimated that CAESAR has  $\sim 19\%$  efficiency for 1.779 MeV  $\gamma$ -rays emitted from the  $^{27}\text{Al}(p,\gamma)^{28}\text{Si}$  resonances.

In  $\gamma$ -ray spectra, the background radiation at 1.764 MeV attributed to the decay of  $^{214}\text{Bi}$  is located close to the 1.779 MeV  $\gamma$ -rays [ Minty (1997)]. For the very weak resonance yield, the acquired spectrum may consist mainly of background radiation without being able to detect the 1.779 MeV  $\gamma$ -rays. A detection limit for a peak was calculated as the smallest count rate which

can be detected with 95 % confidence of source signal,

$$DL(\text{counts/minutes}) = \frac{2.71 + 4.65\sqrt{N_B}}{t_B} \quad (3.2)$$

where  $N_B$  and  $t_B$  are the number of the background counts and the counting time, respectively [ Knoll (2010)]. Reducing the detection limit as well as statistical errors and uncertainties in background corrections can be accomplished by increasing the counting time and beam current. Figure 3.8 shows as an example of the simulated resonance yield rate of the 1.779 MeV  $\gamma$ -rays at the beam current 80 nA in the proton energy range of 300 keV to 1100 keV with the detection limit. The factors of detector efficiency and branching ratios of the 1.779 MeV  $\gamma$ -rays for all resonances shown in Figure 3.8 are included in the simulation. In our measurement a  $\text{H}_2^+$  beam of 80-100 nA was used in taking the spectra at  $E_p=992$  and 632.2 keV resonances and good statistics can be achieved in 20 minutes.

### 3.1.2.2 SuN detector

The measurement of the 1.779 MeV  $\gamma$ -rays as the resonance yield of  $^{27}\text{Al}(p,\gamma)^{28}\text{Si}$  reaction with CAESAR suffered from the background radiation, especially when the resonance yield was low. The overlap between the 1.779 MeV  $\gamma$ -rays and the 1.764 MeV background radiation in CAESAR  $\gamma$ -ray spectrum induced uncertainty in the estimation of the resonance yield. An alternative method for  $(p,\gamma)$  resonance yield measurements is to exploit the gamma summing technique [ Simon et al. (2013)]. The principle of this method is based on the use of a large-volume NaI(Tl) scintillator detector to provide a solid angular coverage of close to  $4\pi$  for high energy photons emitted from a target placed at its center. The large volume of the detector gives a full absorption of a photon, whereas the NaI(Tl) scintillator crystal makes the photomultipliers unable to distinguish between different photons emitted within a short time interval smaller than the long response time of the crystal (typically  $\gtrsim 250$  ns for NaI(Tl) [ Spyrou et al. (2007)]). As a result, two factors of long response time and large volume ensure full absorption of all the gamma rays emitted from each single decay cascade during the de-excitation process of  $(p,\gamma)$  resonances. By collecting all photons

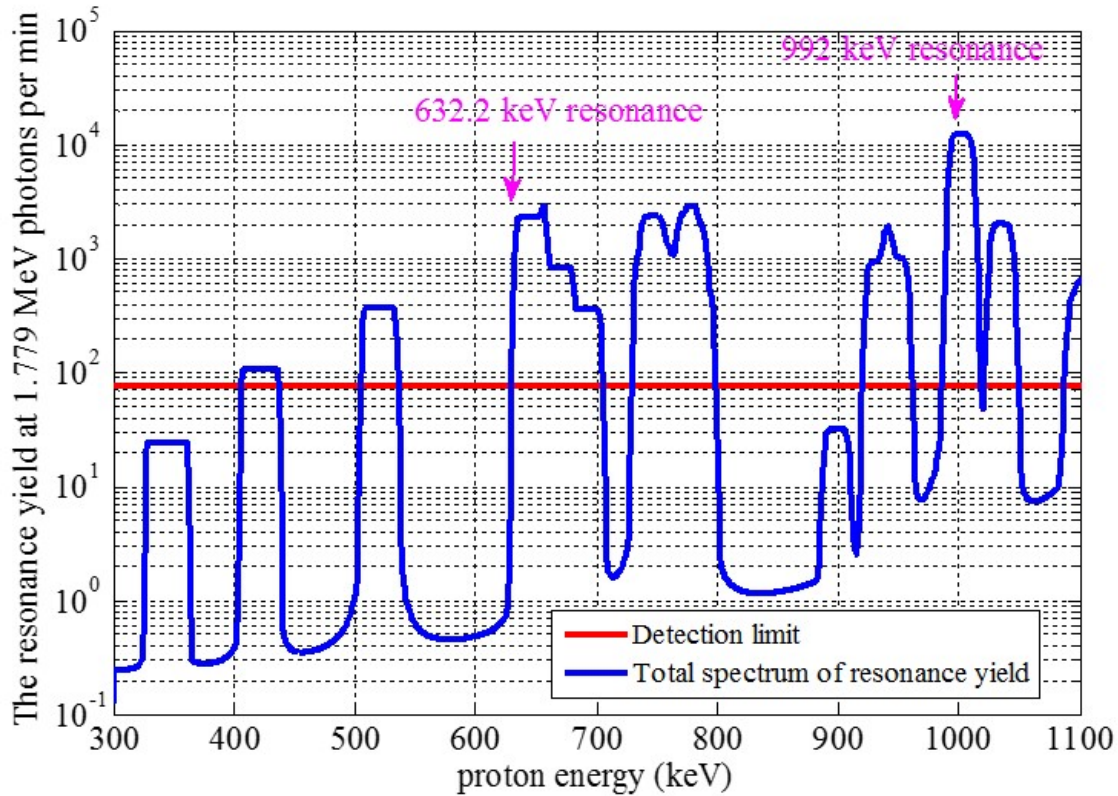


Figure 3.8 Simulated yield of the  $^{27}\text{Al}(p,\gamma)^{28}\text{Si}$  reaction in the  $E_p=300\text{-}1100$  keV region with the detection limit. The  $\text{H}_2^+$  beam current is 80 nA and the target thickness as well as the beam energy spread are the same as Figure 3.1

emitted during one decay cascade in the detector, these photons are summed to one signal with the corresponding energy equal to the sum of the individual photon energies. For example, in the case of the  $^{27}\text{Al}(p,\gamma)^{28}\text{Si}$  reaction at  $E_p=992$  keV resonance, the compound nucleus,  $^{28}\text{Si}$ , decays to the ground state via several cascade as shown in Figure 3.4. The decay cascade with the largest branching ratio of 75 % is the de-excitation from the resonance state to the first excited state, and then to the ground state. Two photons with the energies  $E_{\gamma_1}$  and  $E_{\gamma_2}$  are emitted from this decay cascade. A typical  $\gamma$  spectrum measured with a small-size detector for this cascade may show the  $E_{\gamma_1}$  and  $E_{\gamma_2}$  peaks with their accompanying Compton continuum. However, the spectrum measured with this  $4\pi$   $\gamma$ -summing method will display only one peak which is located at an energy  $E_\gamma = E_{\gamma_1} + E_{\gamma_2}$  since all photons are fully absorbed. The energy of this so-called sum peak is the

energy difference between the resonance state and ground state,

$$E_{\gamma} = Q + E_{cm} ; E_{cm} = E_p \frac{m_t}{m_t + m_p} \quad (3.3)$$

where  $E_{cm}$  is the total kinetic energy in the center of mass system,  $Q$  is the reaction  $Q$ -value and  $m_t$  and  $m_p$  are the target and projectile mass, respectively. Therefore, the final sum peak for the  $^{27}\text{Al}(p,\gamma)^{28}\text{Si}$  at  $E_p = 992$  keV resonance is the sum of all the photons emitted from all  $\gamma$  cascades. Since the reaction  $Q$ -value of  $^{27}\text{Al}(p,\gamma)^{28}\text{Si}$  is about 11584.6 keV [ Chronidou et al. (1999)], the location of the resulting sum peak in a  $\gamma$  spectrum is very far away from room or beam-induced background. Hence, this technique enables to reduce the background influence on the yield estimation of the  $^{27}\text{Al}(p,\gamma)^{28}\text{Si}$  resonances because the sum peak is registered within a low-background region in the gamma spectrum.

SuN (Summing NaI(Tl)), as shown in Figure 3.9 [ Simon et al. (2013)], is a scintillator (NaI(Tl)) detector that implements the gamma summing technique. The core of the SuN detector is a cylinder with 16-inch diameter, 16-inch length and 1.8-inch diameter borehole along its axis. The entire SuN detector comprises 8 semi-cylindrical segments. Each of the segments is optically isolated from others and read out by three photomultiplier tubes. The 24 photomultipliers have equal spacing between each other around the beam pipe with  $60^\circ$ . The photomultiplier signals are recorded using the NSCL Digital Data Acquisition System. The average energy resolution of individual segments is  $\sim 6.1\%$  for the 662 keV  $^{137}\text{Cs}$  source [ Simon et al. (2013)].

To perform the  $^{58}\text{Ni}(p,\gamma)^{59}\text{Cu}$  resonance at  $E_p = 1843$  keV and the  $^{27}\text{Al}(p,\gamma)^{28}\text{Si}$  resonance at  $E_p = 992$  keV for the second part of the beam energy calibration measurements, the SuN detector was installed in the end of the ReA3 L-line extension beam line, as shown in Figure 3.10. The SuN detector was fixed on a metal frame which was movable on a railway. Hence, the target can be placed at the center of the detector. Before the target station, one diagnostic station which consists of a scintillator viewer and a Faraday cup was available to measure the beam size and current on the target, as seen in Figure 3.11. An electrically isolated collimator with the diameter of 5 mm was placed between the diagnostic station and the target, and its current was read by a beam current monitor. Figure 3.12 shows the  $^{58}\text{Ni}$  target with an aluminum frame was mounted

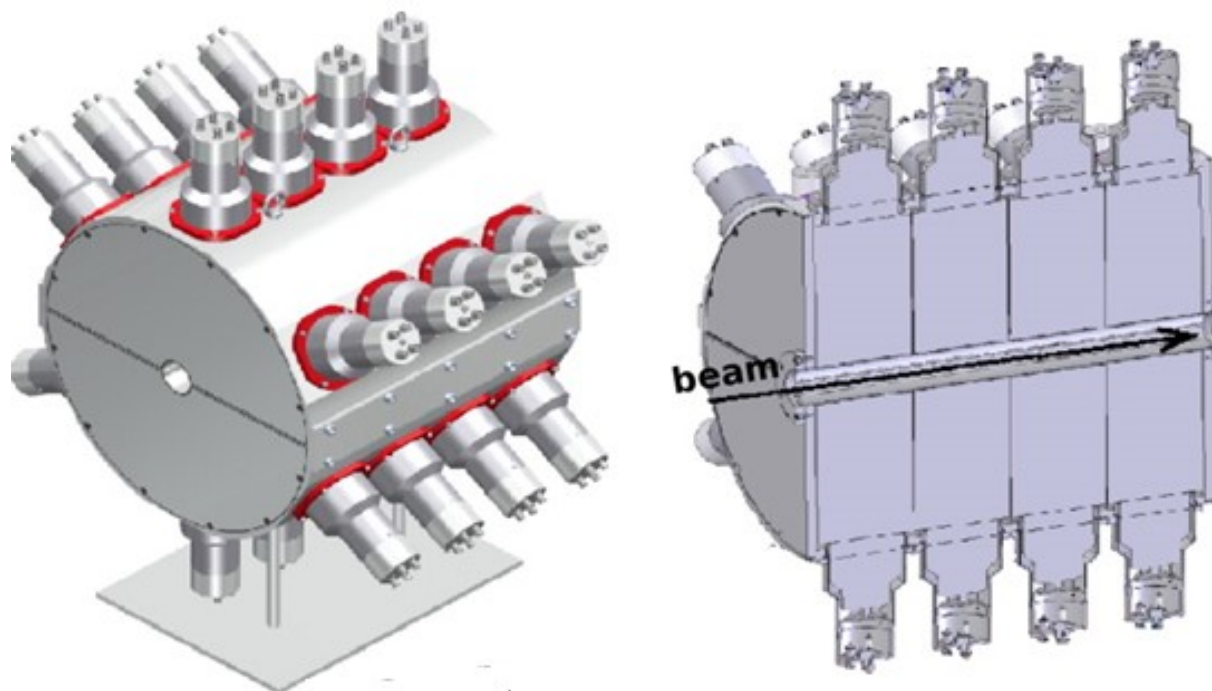


Figure 3.9 Schematic drawing of the SuN detector.[ Simon et al. (2013)]

on an aluminum target holder inside the stainless steel beam tube, and electrically isolated from the target holder with plastic tapes. The current on the target and target frame can be read through a beam current monitor (see Figure 3.11 left panel). The beam was dumped into a tantalum sheet at the end of the beam line. The assembly of the target holder, the stainless steel beam tube and beam dump was electrically isolated from the upstream beam line and served as a deep Faraday cup to determine the total number of projectiles bombarding the target.

### 3.1.3 Beam tune setup

The  $(p,\gamma)$  resonance experiments were performed at the rare isotope ReAccelerator (ReA3) facility in November–December of 2012 and November of 2014. The layouts of ReA3 during these experiments for the first and second parts of the beam energy calibration measurements are depicted in Figure 3.3 and Figure 1.3, respectively. The  $H_2^+$  beam was obtained from an off-line stable ion beam injector. The Low Energy Beam Transport (LEBT) system, which consists of electrostatic quadrupole doublets and a solenoid, as well as an external Multi-Harmonic Buncher (MHB) deliv-



Figure 3.10 The SuN detector connected to the end of L-line extension beam line at ReA3.

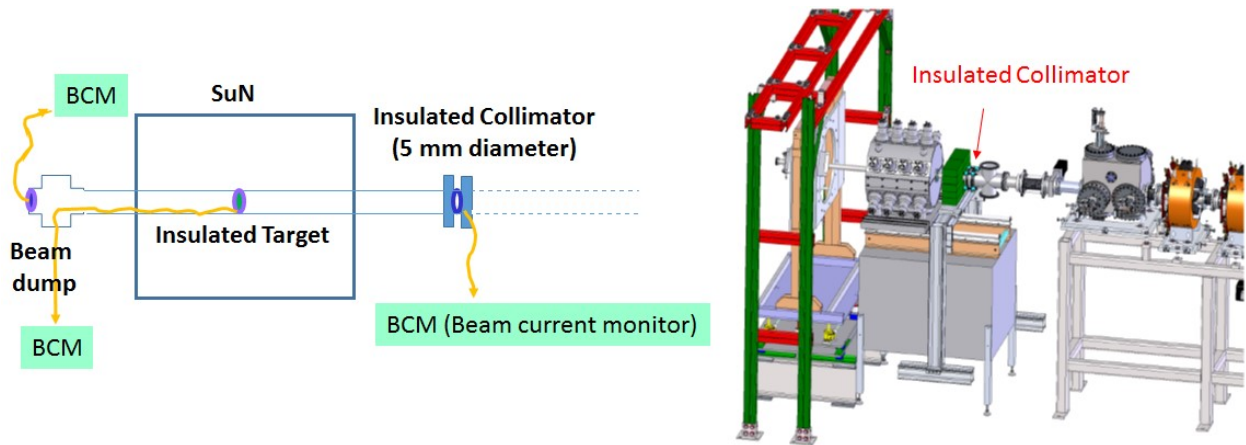


Figure 3.11 Schematic diagram of the experimental setup for the SuN detector and the target system.

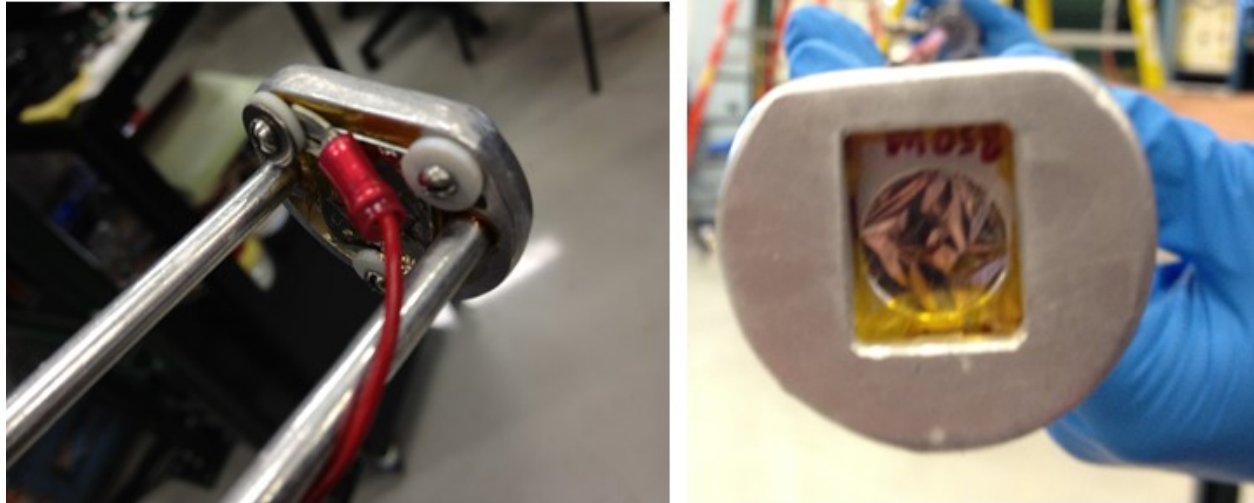


Figure 3.12 The target with the target holder for the SuN detector.

ered and matched the beam into a room temperature RFQ, which accelerates the ion beam from 12 keV/u to 600 keV/u. After the RFQ, the beam was further transported through the first rebuncher cryomodule which contains a single  $\beta = 0.041$  superconducting quarter wave cavity. The rebuncher cavity was set to zero crossing (in the rebunching mode) so that the beam energy was unchanged. In the second cryomodule,  $\beta = 0.041$  QWR cavities were operated to achieve the required energy for the experiments. The beam energy was varied in 1-2 keV steps by changing the amplitude of one QWR cavity in the second cryomodule and fixing the cavity phase to measure the resonances over the energy region of interest.

During the period of the first part of the beam energy calibration measurements in 2012, the third cryomodule consisting of eight  $\beta = 0.085$  QWR cavities was under development. Therefore, a long drift tube following the linac was temporarily installed in the position of the third cryomodule for beam transport. After the third cryomodule was installed, the second part of the beam energy calibration measurements was performed in 2014. During the experiment, the cavities, solenoids and steerers in the third cryomodule remained off, resulting in a long drift to establish a parallel beam entering the first  $45^\circ$  bending magnet in the S-bend section.

In the first part of the beam energy calibration measurements, the beam was delivered to the CAESAR location where the calibration reaction measurement was performed.

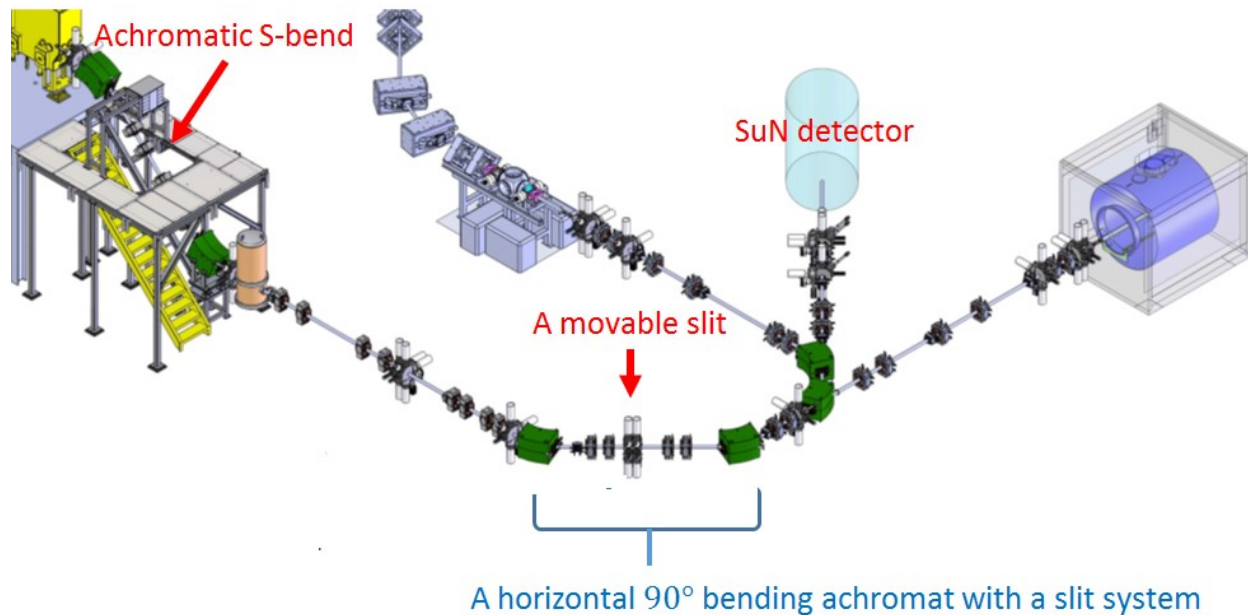


Figure 3.13 The ReA3 beam distribution line consisting of a vertical achromatic S-bend section, a high resolution horizontal 90° bending achromat with a slit system, an achromatic beam switchyard with two 45° dipoles, and the final beam focusing system to deliver the beam to the target station in the SuN location.

In the second part of the beam energy calibration measurements, the beam was transported through the S-bend section, a horizontal 90° bending achromat and two 90 ° dipoles. Eventually, the final beam focusing system consisting of five quadrupoles focused the beam on the target in the SuN station, as shown in Figure 3.13. The high-resolution horizontal achromatic dipole beamline segment which includes a horizontal slit in the dispersive image plane between the dipoles, can be used to limit the beam energy spread on the target.

The beam tuning of the energy calibration experiments involves (a) the optimization of beam line element parameters to achieve the desire beam condition on the target by performing the end-to-end beam dynamic simulation of the ReA linac, (b) the setup of a reproducible magnetic field of the 45° magnet analyzer, and (c) the development of the consistent transport procedures to follow. These concepts are described in more detail below.

### 3.1.3.1 Beam simulation

DYNAC [ Tanke et al. (2002)] is a multi-particle beam dynamics code that uses macroparticles to model the six-dimensional motion of the particles in the beams. The input beam in a 6-D coordinate can be generated from various hit-or-miss Monte Carlo processes or can be read directly from a user-defined file. The information of the initial beam condition, which includes beam Twiss parameters, beam distribution, beam energy, energy spread, the centers of beam positions and total beam particle number, are defined by the users through a DYNAC input file. In the DYNAC input file, the users also specify transport elements with the corresponding electromagnetic field in a specific sequence along a beam line. The transport elements may contain drifts, quadrupoles, solenoids, bending magnets, rf cavities, or other user-defined elements. Based on a set of beam dynamics equations, DYNAC can provide a detailed numerical calculation of the beam parameters and trajectories through each transport element. The DYNAC computation code can be executed in Linux and Microsoft Windows systems. The DYNAC output files will print information concerning the beam dynamics computations and display the graphs of the beam envelopes along a beam line or the phase-space ellipses at any given position.

The DYNAC code has been developed as a beam simulation tool for the ReA beam line [ Tanke et al. (2012)]. The beam simulation begins from the exit of the EBIT with assumption of initial conditions. DYNAC is capable of simulating the multi-harmonic buncher, RFQ, superconducting quarter wave cavities, electrostatic and magnetic elements. For the  $(p, \gamma)$  resonance experiments, we used DYNAC to optimize the beam parameters in support of the beam tuning. In order to achieve a desired beam energy and beam energy spread, the setting of the rebuncher and acceleration cavities was optimized according to the DYNAC simulation, as listed in Table 3.2. Figure 3.14 shows the individual locations of the SRF cavities in CM1 and CM2. In the first part of the beam energy calibration measurements for the  $^{27}\text{Al}(p, \gamma)^{28}\text{Si}$  992 keV resonance, one of the experimental goals was to investigate the use of the L091 cavity in the rebuncher mode to reduce the beam energy spread. Therefore, we performed DYNAC simulation for the experiment of the  $^{27}\text{Al}(p, \gamma)^{28}\text{Si}$  992 keV resonance with and without using the L091 cavity. All of the cavity setting obtained from

Cavity	The first part		The second part			
	$E_k=990.3$ keV/u		$E_k=992.035$ keV/u	$E_k=1843.35$ keV/u		
L077 cavity	2.155 MV/m	$-90^\circ$	2.669 MV/m	$-90^\circ$	2.669 MV/m	$-90^\circ$
L082 cavity	12.667 MV/m	$-20^\circ$	12.265 MV/m	$-20^\circ$	12.265 MV/m	$-20^\circ$
L084 cavity	12.483 MV/m	$-20^\circ$	12.964 MV/m	$-20^\circ$	18.851 MV/m	$-20^\circ$
L085 cavity	Off		Off		16.127 MV/m	$-20^\circ$
L088 cavity	Off		Off		20.835 MV/m	$-20^\circ$
L089 cavity	Off		Off		21.254 MV/m	$-20^\circ$
L091 cavity	1.423 MV/m	$-90^\circ$	Off		Off	

Table 3.2 The optimized amplitude and phase setting of the SRF cavities in CM1 and CM2 for the first and second parts of the beam energy calibration measurements.

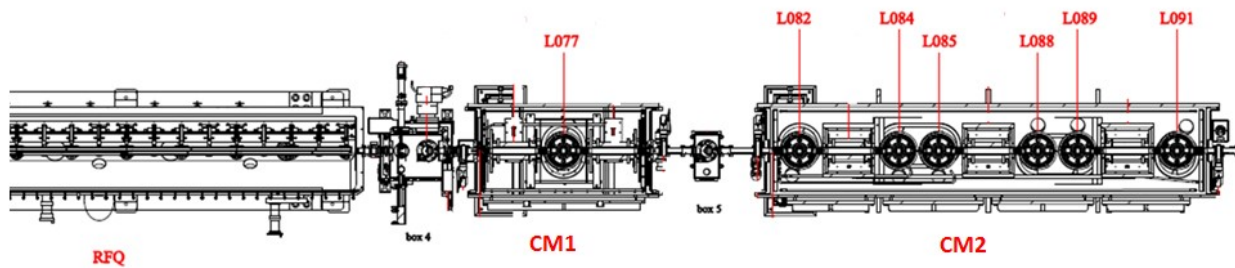


Figure 3.14 The layout of the RFQ and the first and second cryomodules in ReA3.

DYNAC simulations in Table 3.2 were applied to the real machine setting for the  $(p,\gamma)$  resonance experiments with very good agreement.

Figure 3.15 presents one example of DYNAC simulations for the evolution of the beam envelop, energy spread and energy gain of a  $H_2^+$  beam along the ReA3 beam line with the SRF cavity setting listed in Table 3.2 for  $E_k=1843$  keV/u. The simulation simply used 5000 particles with a cylinder-shape uniform distribution as the initial condition. Each particle began from the electrostatic quadrupoles in the LEPT toward the target station in the experimental hall. The initial beam Twiss parameters were determined from the quadrupole scan measurement by Daniel Alt. The initial beam Twiss parameters in the entrance of the LEPT were determined by varying one electrostatic quadrupole in the LEPT and measuring the change of the beam width in the horizontal and vertical directions at a subsequent point. With the calculation of the transfer matrix for this

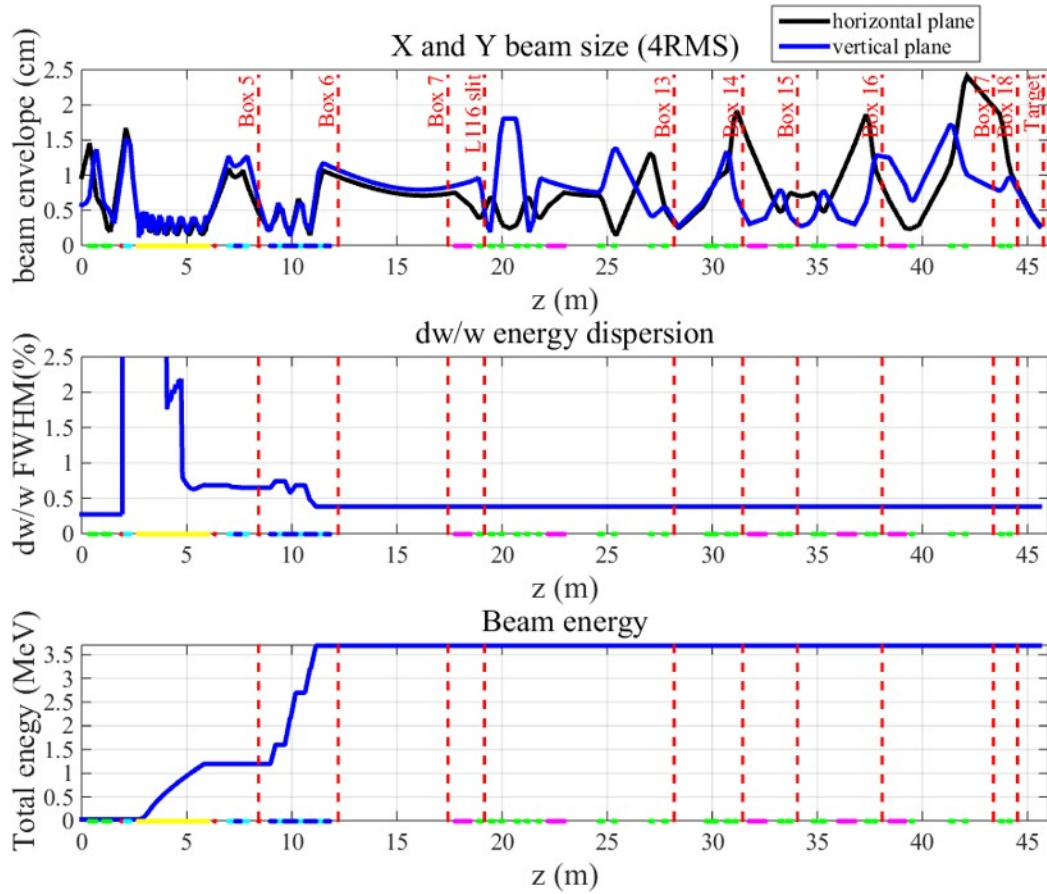


Figure 3.15 The simulated evolution of the beam envelop, energy spread and energy gain of a  $H_2^+$  beam from the LEBT to the target station in the experimental hall for the beam tuning of  $^{58}\text{Ni}(p,\gamma)^{59}\text{Cu}$  1843 keV resonance experiment. The diagnostic stations as well as the beam optics elements along the ReA3 beam line are marked on the plots.

quadrupole setting, the initial Twiss parameters can be obtained.

The simulation result of Figure 3.15 shows that the solenoids and quadrupoles elements can keep the beam envelope below 2.5 cm along the beam line. There is no noticeable beam transverse or longitudinal emittance growths observed in the simulation. The energy spread is rising after RFQ but gets significantly reduced after the second cryomodule with the use of the superconductive cavities in the phase of  $-20^\circ$ .

### 3.1.3.2 Cycling procedure and excitation curve of a magnet

The 45° magnetic dipoles in ReA3 include an iron yoke to increase the magnetic field. These magnets are strongly dependent on their hysteresis history. To obtain a desired and reproducible magnetic field, a particular current must be applied with respect to its hysteresis curve. Therefore, a standard procedure of cycling the magnets needs to be performed in order to prevent differential hysteresis effects. A desired magnetic field can be obtained by adjusting the dipole current according to the excitation curves of the magnets.

Based on the standard cycling procedure developed for magnet operation at ReA, the magnets are cycled twice using a programmed ramp rate to de-magnetize and re-magnetize the magnets. On each cycle, the magnetic current goes up from 0 A to 300 A at 10 A/second, stays at 300 A for 3 minutes and then goes back to 0 A at the same rate. The aim of this standard cycling procedure is to establish a high degree of field reproducibility.

In order to obtain the relation between the dipole current and field, the field mapping of the first 45° bending dipole in S bend was measured. After cycling the dipole in the standard procedure, the dipole current was adjusted from 0 A to 300 A and back to 0 A at the intended ramp rate of 10 A per step. After each step, a 3 minutes delay is programmed into the ramp to stabilize the magnetic field. Figure 3.16 shows the excitation curves of the first 45° bending dipole in S bend. The up branch in Figure 3.16 (a) was taken by increasing the current from 0 A to 300 A and the down branch in Figure 3.16 (b) was taken decreasing the current from 300 A to 0 A. The data can be well fitted with a polynomial function. The excitation curves are nearly linear for the current range of 0 A and 220 A and begin to approach the magnetic saturation at a current of 220 A. A desired magnetic field of the first 45° dipole in S bend can be obtained by adjusting the dipole current through the experimental formulas for the up branch

$$B(\text{Tesla}) = 0.00238 + 0.00488 \cdot I + 8.59277 \cdot 10^{-6} \cdot I^2 - 1.34478 \cdot 10^{-7} \cdot I^3 \\ + 9.62812 \cdot 10^{-10} \cdot I^4 - 3.14343 \cdot 10^{-12} \cdot I^5 + 3.61387 \cdot 10^{-15} \cdot I^6 \quad (3.4)$$

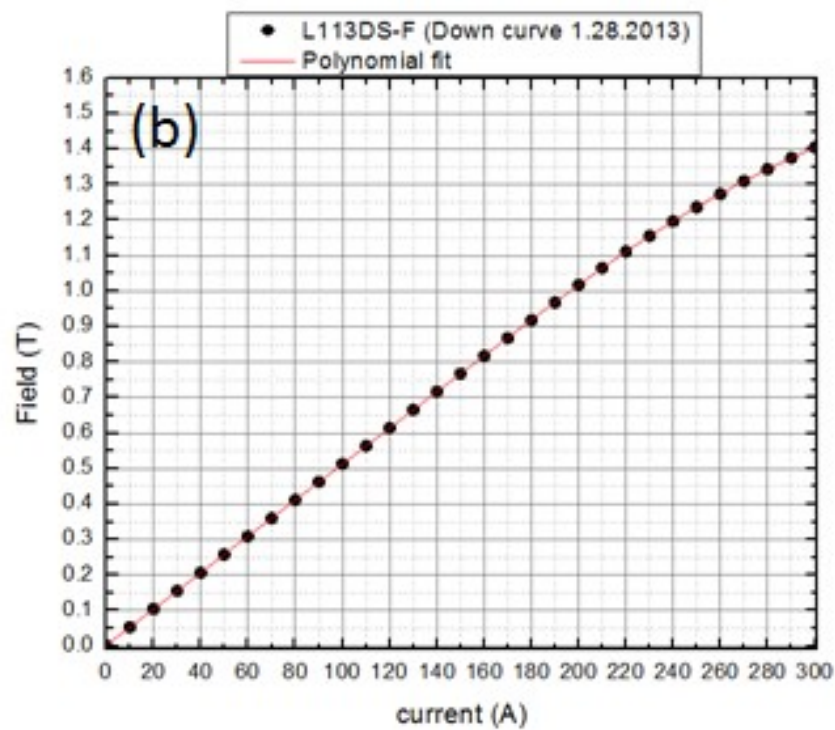
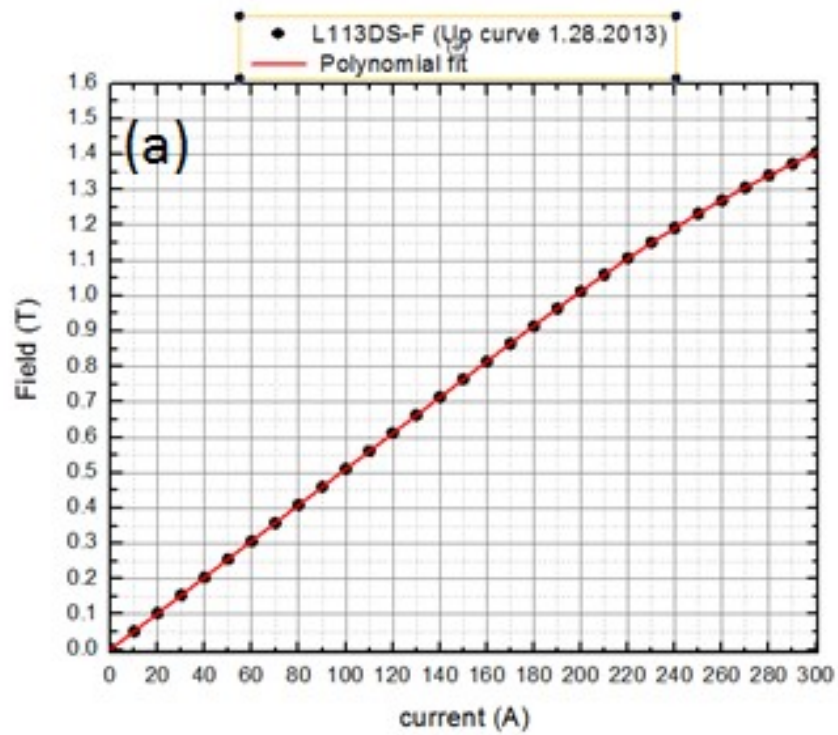


Figure 3.16 The excitation curves of the up branch (a) and the down branch (b) of the first  $45^\circ$  bending dipole in S bend. The black dots are the data and the red curves are the polynomial fit.

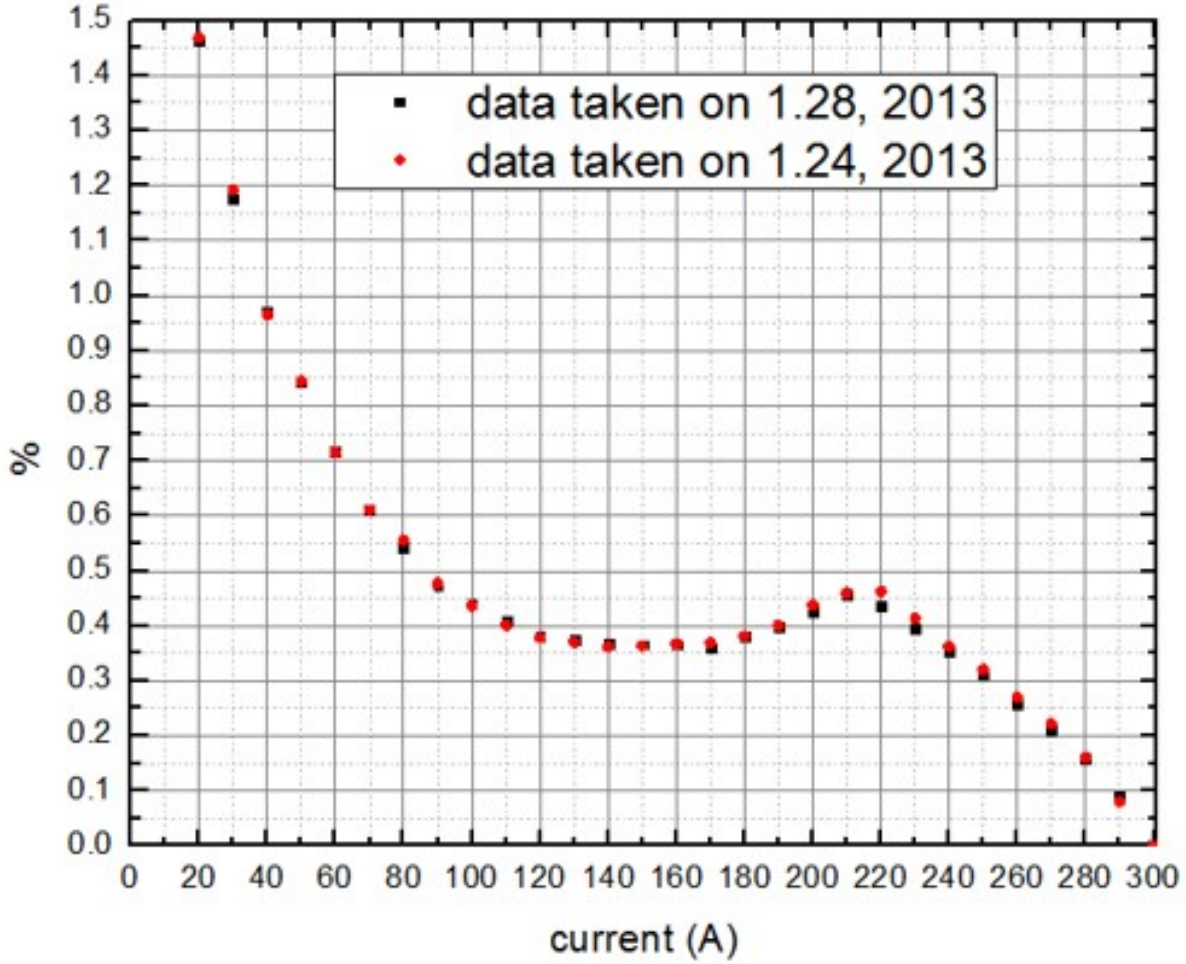


Figure 3.17 The ratio of difference in the field going up or down the hysteresis loop as a function of current for the first 45° dipole in S bend. The Y axis represents the magnetic field difference in % obtained from the measurements of going up and going down the hysteresis loop at a given magnet current. The different colors signify different experimental days.

and for the down branch

$$\begin{aligned}
 B(\text{Tesla}) = & 0.00307 + 0.00492 \cdot I + 8.70223 \cdot 10^{-6} \cdot I^2 - 1.45644 \cdot 10^{-7} \cdot I^3 \\
 & + 1.07316 \cdot 10^{-9} \cdot I^4 - 3.53825 \cdot 10^{-12} \cdot I^5 + 4.0866 \cdot 10^{-15} \cdot I^6. \quad (3.5)
 \end{aligned}$$

Figure 3.17 shows the difference in the field going up or down the hysteresis loop for the first 45° dipole in S bend. The ratio (%) of difference in Figure 3.17 was calculated by:

$$\frac{\text{the down branch} - \text{the up branch}}{\text{the up branch}} \cdot 100\%. \quad (3.6)$$

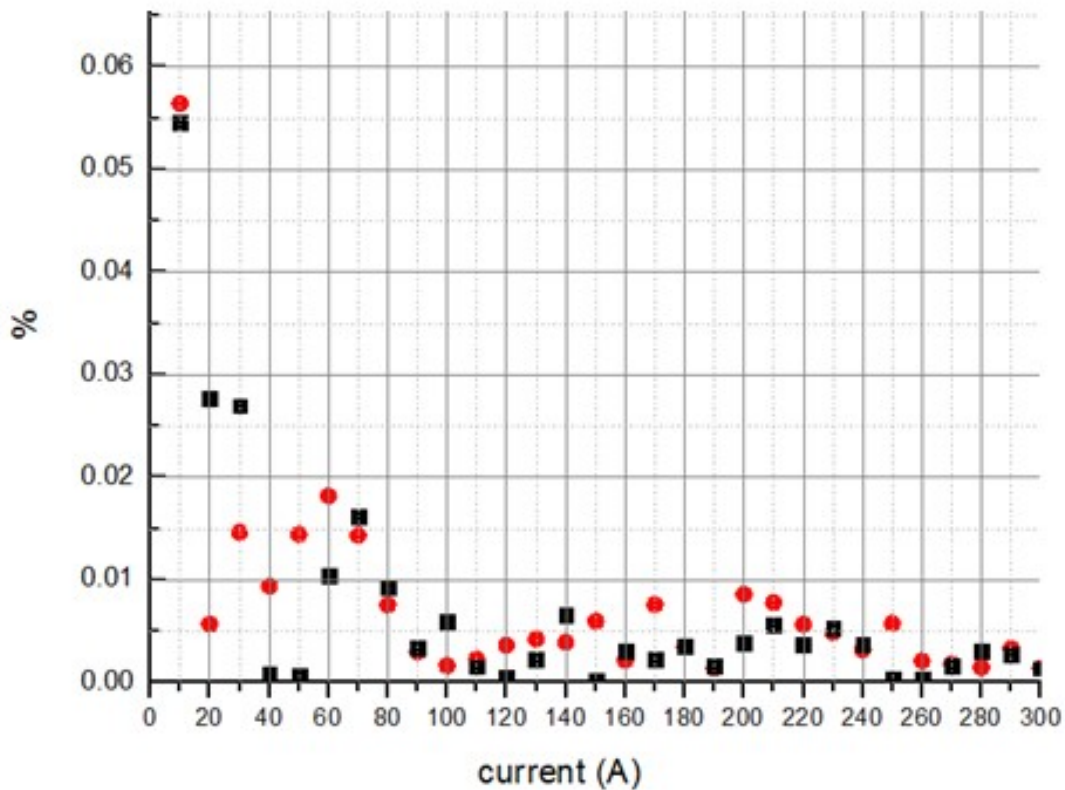


Figure 3.18 The field reproducibility as a function of current for the first 45° dipole in S bend. The red and black colors represent the up branch and down branch, respectively.

Because of the difference between the down branch and the up branch (i.e., the width of the hysteresis loop), it is appropriate to adjust the dipole current by going up or down on the hysteresis loop for the operation of the dipole. Figure 3.18 shows the field reproducibility as a function of current, along the up and down branches for the first 45 degree dipole in S bend. The highest field of the dipoles in ReA3 operation is 0.16517 Tesla at roughly 142 A for 6 MeV/u  $H_2^+$  ( $Q/A=0.5$ ). Therefore, within the field range of ReA3 operation, once the dipoles are cycled in the standard procedure, the field reproducibility in up or down ramp can be up to 99.98%. Compared with the accuracy 0.01% of the Hall probes, the field reproducibility in up or down ramp is acceptable.

### 3.1.3.3 Consistent beam transport procedure

The calibration measurement of the  $(p,\gamma)$  resonance reactions required mapping the resonance excitation functions over the region of interest in 1-2 keV steps. In order to achieve an accurate and reproducible magnet calibration, we developed and followed a consistent beam transport procedure through all the runs. We also kept monitoring the stability of the machine performance. For each measurement run, several steps were consistently followed to obtain a tuned beam.

*Step 1:* The phase of a rebuncher cavity at zero crossing was monitored carefully by using a scattering-gold foil silicon detector to verify that the beam energy was unchanged when the amplitude of the cavity was increased.

*Step 2:* The field of the first  $45^\circ$  magnet in the S bend was set to a desired value by going down the hysteresis loop. If the magnetic field was lower than the desired field, the cycling procedure was repeated to eliminate hysteresis effects. The second  $45^\circ$  magnet in S bend was set to the same field as the first one, based on optical symmetry.

*Step 3:* The beam energy was subsequently adjusted by changing the acceleration voltage of one specific cavity in the second cryomodule (CM2) such that the beam was allowed to pass through the first magnet.

*Step 4:* The trajectory of the beam was tuned to enter the magnet parallel to the horizontal plane of the first dipole using the two 5-mm diameter apertures of the 45 degree slit assembly in the upstream diagnostic stations (station 6 and 7). The beam centroid positions at these two locations needed to be verified by the  $45^\circ$  slit scanners and the Faraday cups for each experimental run, as shown in Figure 3.19.

*Step 5:* Once the beam passed through the first  $45^\circ$  magnet, a movable slit in the diagnostic station 9 located after the first quadrupole of the S bend was used to measure the beam vertical transverse profiles while the first quadrupole was turned off. We repeated the above procedure of the *Step 3* and *Step 4* until the peak centroid of the beam intensity coincided with the center of the vertical slit which was placed to the beam axis. After these steps had been completed, we turned on the first quadrupole and brought the beam through the S-bend section.

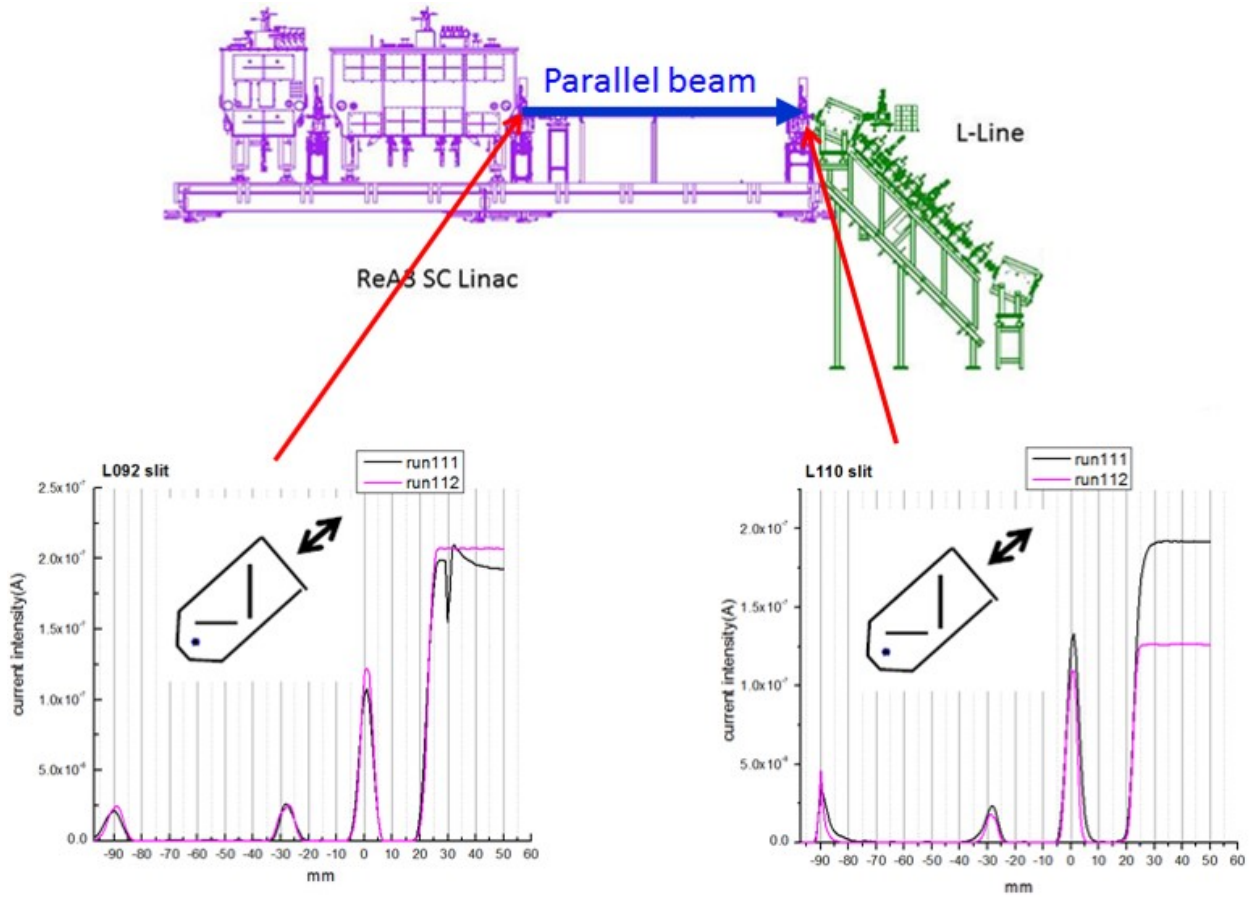


Figure 3.19 An example of the  $45^\circ$  slit scan measurements in the diagnostic station 6 and 7 for two experimental runs. For each slit scan, the two peaks on the left show the horizontal and vertical beam profiles that are amplified by  $\sqrt{2}$ . The right peak indicates the beam was centered at a 5 mm hole. The center of the 5 mm hole is supposed to be on the theoretical beam axis.

An alternative method for Step 4 and Step 5 was developed in the experiment of the  $^{58}\text{Ni}(p,\gamma)^{59}\text{Cu}$  reaction at  $E_p=1843$  keV resonance. The two 5-mm aperture of the  $45^\circ$  slit scanners in the diagnostic station 6 and 7 were inserted into the beam trajectory for collimating the beam entering the first  $45^\circ$  magnet. After the beam passed through the magnet and the first quadrupole of the S bend was turned off, the vertical centroid position of the beam was adjusted to be at the center of the vertical slit in the diagnostic station 9 by changing the cavity amplitude. Next, the first quadrupole of the S bend was turned on and the beam was delivered through the S bend.

*Step 6: (Optional)* In the second part of the beam energy calibration measurements, once the beam was delivered to the horizontal  $90^\circ$  bending achromat, the movable horizontal slit in the

diagnostic station 15 near the dispersive focal plane was used to limit the beam energy spread with the slit width 1 mm or 3 mm.

*Step 7:* The beam transmission through the target system was optimized by maximizing the beam current in the beam dump and minimizing the current on target frame. In the second part of the beam energy calibration measurements, the current on the electrically isolated collimator in front of the target (see Figure 3.11) was also minimized.

*Step 8:* The data acquisition of the resonance excitation functions was started by monitoring the beam current stability in the beam dump and being careful not to tune any beam transport parameter. The current of the incoming beam impinging on the target was determined with a Faraday cup in the diagnostic station before the target and a beam current monitor connected to the beam dump. During acquiring spectra by the  $\gamma$ -ray detectors, detailed logs of the analyzing magnet field and other beam transport system operating parameters were also recorded for tracking the overall machine and beam stability. In the first stage of the beam energy calibration, two successive BPMs (beam position monitors) that were installed 2.08 m apart in the long drift space between CM2 and the first  $45^\circ$  magnet. The BPMs can be used if the beam intensity is larger than 50 nA [Crisp et al. (2013)]. Simultaneous beam phase measurement of these two BPMs can provide relative beam energy information. Therefore, the beam phase at each of the two BPMs was recorded during the data acquisition of the CAESAR detector.

*Step 9:* After finishing the data acquisition, the first quadrupole in the S bend was turned off and the vertical slit scan after the first quadrupole was performed again to monitor the beam energy stability by observing any vertical shift of the peak intensity.

### **3.1.4 Data analysis and result**

#### **3.1.4.1 Detector calibration and $\gamma$ -ray spectra**

For the  $(p,\gamma)$  resonance experiments, data offline analysis and histogramming are processed within the ROOT analysis program developed at CERN. Hence, in the first step, the raw data needs to be

Source	$\gamma$ -ray energy (keV)
$^{60}\text{Co}$	1332.501
	1173.237
$^{137}\text{Cs}$	661.657
$^{88}\text{Y}$	898.042
	1836.042
$^{22}\text{Na}$	1274.53
$^{40}\text{K}$	1460.82

Table 3.3 Calibration sources and  $\gamma$ -ray energies for CAESAR.

extracted from the evt-files written by the NSCL data acquisition program and converted into the ROOT file format. This step is done by the Unpacker programs written by Kathrin Wimmer for CAESAR and Anna Simon for SuN. In the second step, analyzing the raw data in the ROOT files for individual detectors results in the development of calibration function that transforms the raw data into the calibrated data with physical meaning, i.e. the energy deposited in a given detector. The calibrated data for individual detectors can be histogram and summed event-by-event. The processing detail of the calibration and  $\gamma$ -ray spectra for the CAESAR and SuN detectors are described below.

#### 3.1.4.1.1 CAESAR analysis

Each CAESAR individual detector with its signal processing chain has a different response to a  $\gamma$ -ray of a given energy deposited in the detector, resulting in the full-energy peak of the  $\gamma$ -ray registered in a different ADC channel. Hence, it is necessary to calibrate each detector individually. Calibrating all the CAESAR detectors allows us to use all the 192 detectors as one large detector. The  $^{88}\text{Y}$ ,  $^{60}\text{Co}$ ,  $^{137}\text{Cs}$  and  $^{22}\text{Na}$  radioactive sources as well as  $^{40}\text{K}$  background radiation were used to perform the energy calibration of all 192 CAESAR detectors. The  $\gamma$ -ray energies of these sources used for the energy calibration are listed in Table 3.3. The photopeaks of the well-known energies from these calibration sources in the  $\gamma$ -ray spectra for all the CAESAR detectors were fitted with a Gaussian on top of a linear background in order to determine the peak centers. After

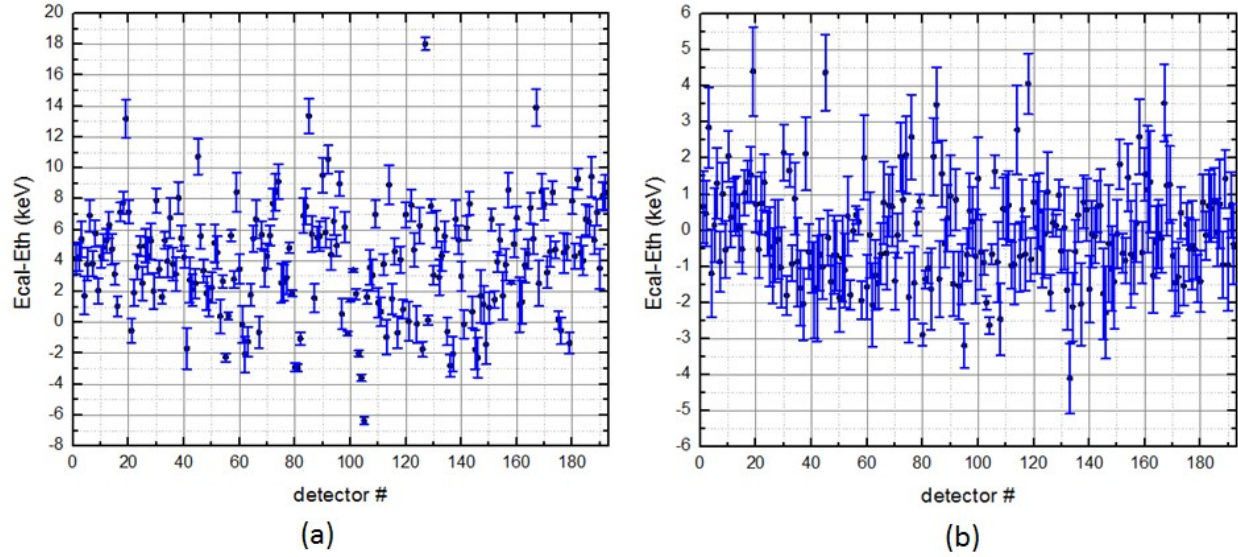


Figure 3.20 The deviations of individual detectors between the calibrated and theoretical energies for the well-known 1836 keV photopeak of  $^{88}\text{Y}$  source with a linear (a) and a second-order polynomial (b) fitting.

the channel numbers of the peak center positions were extracted, the calibration function for each detector was obtained by comparing the two different fitting functions:

$$E = a + b \cdot C + c \cdot C^2 \quad (3.7)$$

and

$$E = a + b \cdot C \quad (3.8)$$

where  $E$  and  $C$  are the  $\gamma$ -ray energy and its corresponding channel number of the peak center. Figure 3.20 shows the deviations of individual detectors between the calibrated and theoretical energies ( $E_{\text{cal}} - E_{\text{th}}$ ) for the known 1836 keV photopeak of  $^{88}\text{Y}$  with a linear (Equation 3.8) and a second-order polynomial (Equation 3.7) fitting. As we can see, using a second-order polynomial of the fitting function was the best approach for energy calibration. Figure 3.21 shows the calibration fit for one detector with a second-order polynomial. Since the CAESAR consisted of 192 CsI detectors, a CAESAR spectrum was obtained by summing all 192 histograms after calibrating the energy scale of each detector. The deviation between the photopeak center in the CAESAR spectrum and the theoretical value for the 1836 keV  $\gamma$ -rays from the  $^{88}\text{Y}$  source was sufficiently small (0.317 keV).

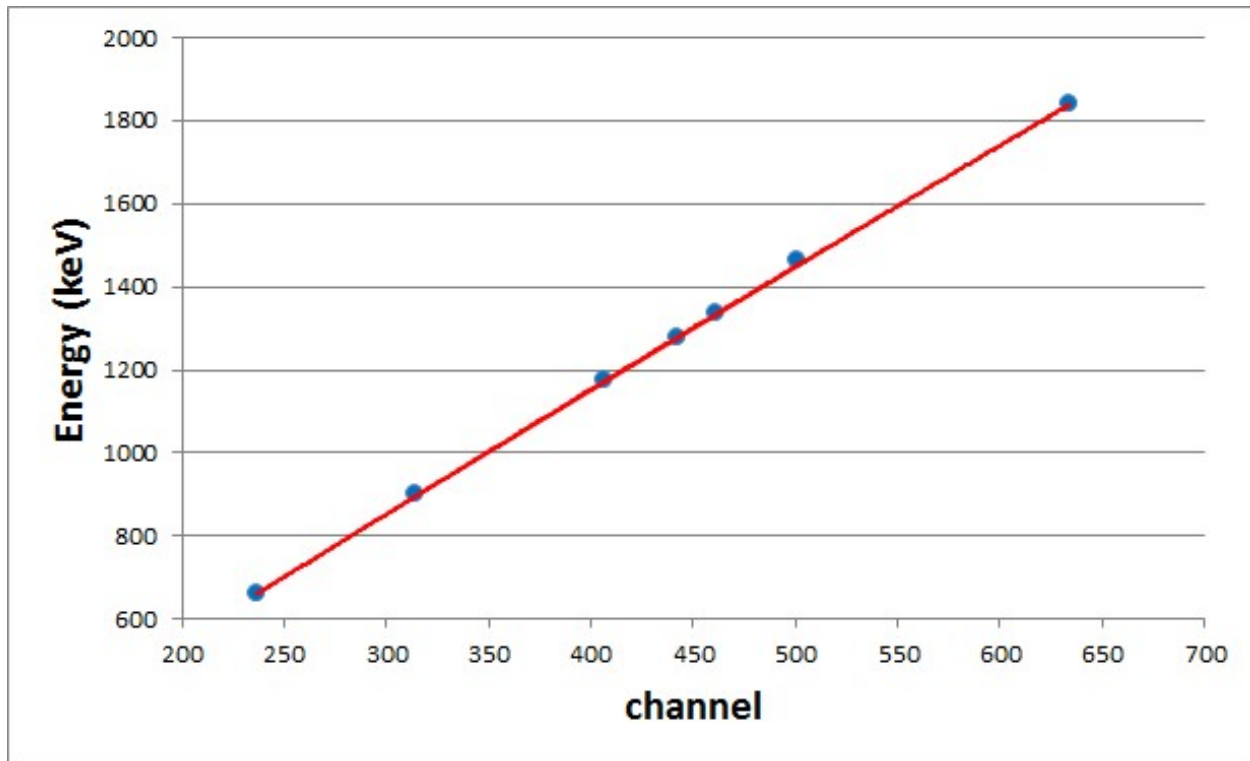


Figure 3.21 The  $\gamma$ -ray energies and their corresponding channel numbers of the photopeaks from the calibration sources listed in Table 3.3. The red curve is a second-order polynomial fit.

Since data were acquired over a period of almost two month, the changes in the environmental temperature of the experimental area led to instabilities of the detector gains and resulted in a shift on the horizontal axis (energy scale) of CAESAR spectra. As a result, energy peak drifts of 15 keV or more were commonly observed. The natural gamma radiation peaks of  $^{40}\text{K}$  and  $^{214}\text{Bi}$  with known energies at 1460.82, 1120.29 and 2204.21keV [ Minty (1997)] were used to monitor the detector calibration drift and provide a means for a realignment of the calibration. The peak positions of the three natural gamma rays on each CAESAR spectrum were realigned to match those on a reference background spectrum, assuming that there is a linear relationship between them. The reference background spectrum, as shown in Figure 3.22, was carefully calibrated with radioactive sources using a Gaussian fit and a second-order polynomial background to find the peak positions. The new energy calibration of each CAESAR spectrum was achieved by applying the linear function, derived from the realignment of the background radiations, to the old energy calibration scale. Our result, as shown in Figure 3.23, indicates that this method can be reliably used

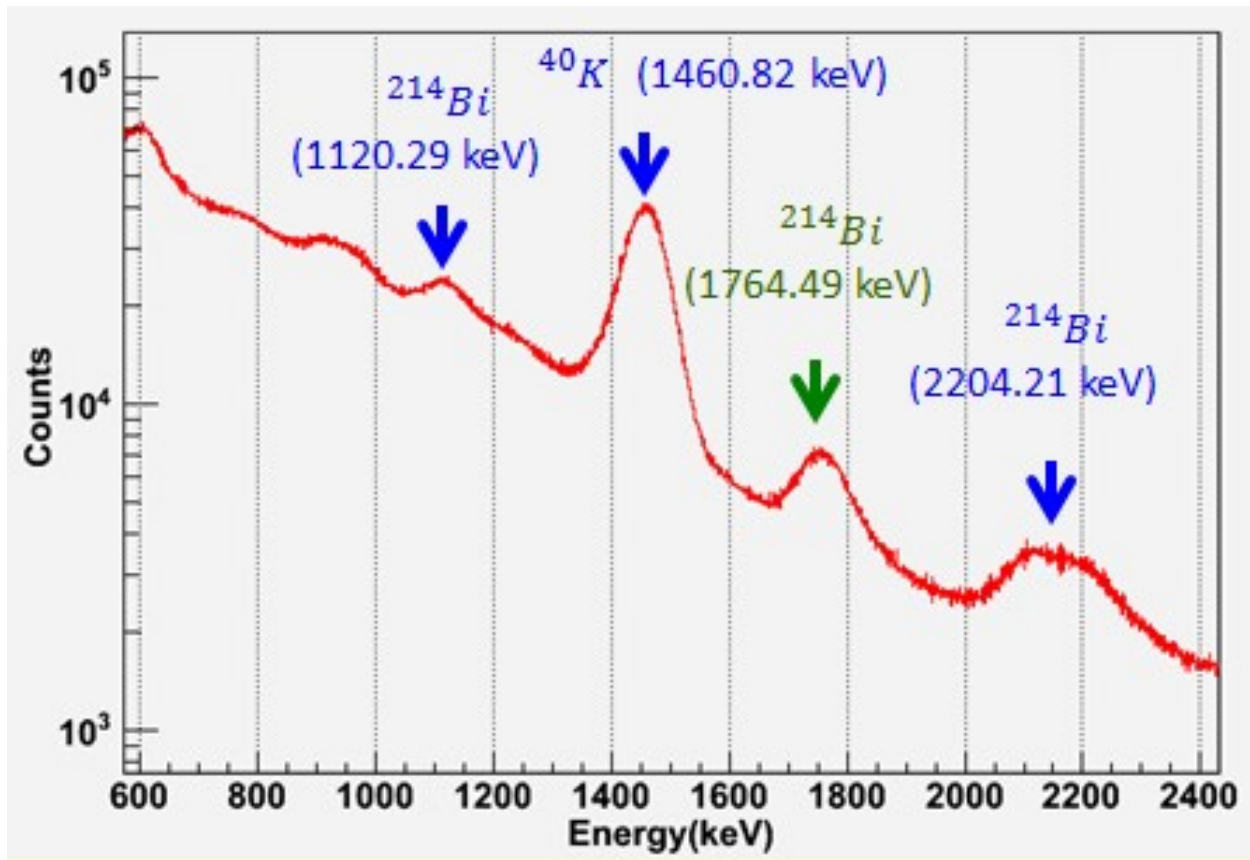


Figure 3.22 The reference background spectrum with a long recording time used to re-calibrate each CAESAR spectrum of the experimental runs.

as CAESAR re-calibration around the gamma energy region of our interest ( 1.779 MeV). Figure 3.23 is an example of the peak position distributions of the 1.764 MeV background radiation from  $^{214}\text{Bi}$  on CAESAR background spectra before and after the re-calibration. The peak shift ( $\leq 2.5$  keV) at 1.764 MeV  $\gamma$ -rays after re-calibration was significantly reduced.

Figure 3.24 illustrates one example of the re-calibrated  $\gamma$ -ray spectra accumulated at beam energies around the 992 and 632.2 keV resonances of  $^{27}\text{Al}(p,\gamma)^{28}\text{Si}$  as well as a background spectrum. The yield and position of  $E_\gamma=1.779$  MeV peak in Figure 3.24 can be easily compared and identified. Since the separation between 1.779 MeV  $\gamma$ -rays and the 1.764 MeV background radiation is less than the detector resolution, the peaks overlap occur in the spectra. However, the resonant  $\gamma$  transition at  $E_\gamma=1.779$  MeV can still be identified by comparison with background spectra. As raising the beam energy toward the resonance energies, the yield of  $E_\gamma=1.779$  MeV

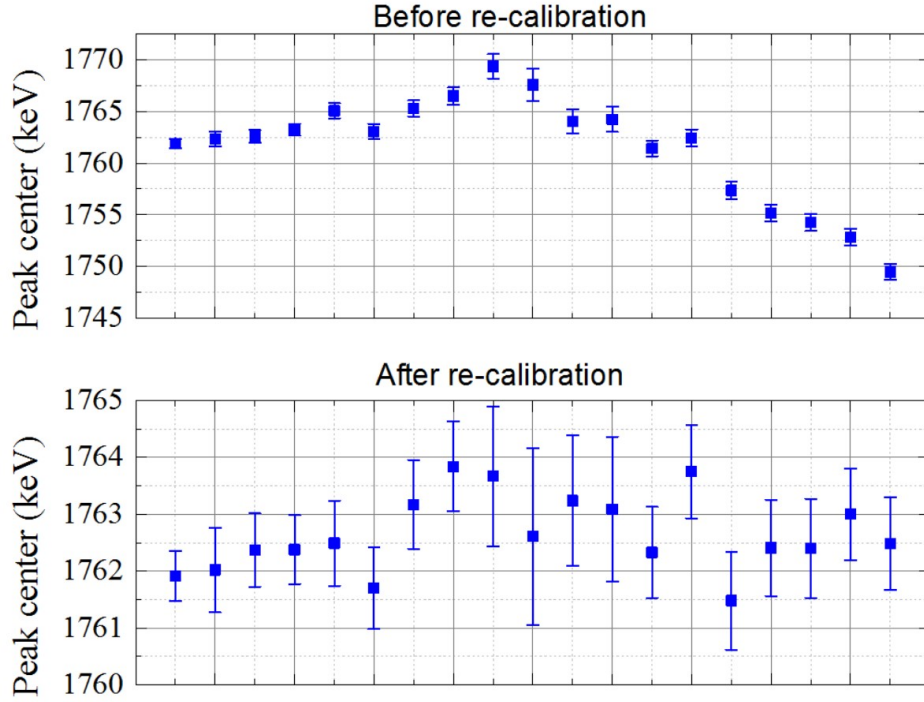


Figure 3.23 The peak center distribution of the 1764 keV  $\gamma$ -rays from  $^{214}\text{Bi}$  on the CAESAR spectra of all 19 background runs before (upper panel) and after the re-calibration (lower panel). The horizontal axis represents the individual runs over a period of two months.

peak becomes dominant and much easier to observe in the on-resonance spectra. As expected, the resonance at  $E_p = 992$  keV has much stronger resonance yield than the resonance at  $E_p = 632.2$  keV due to higher resonance strength (see Table 3.1).

The resonance yield curves were deduced from the gamma-ray yield of 1.779 MeV peak by the following steps. For each experimental run, a re-calibrated spectrum was subtracted by a background spectrum, as seen in Figure 3.25 (a). The 1.779 MeV peak on the background-subtracted CAESAR spectrum was fitted with a Gaussian plus a second-order polynomial background with the least chi-square (see Figure 3.25 (b)). Next, the net intensity ( $I$ ) in the 1.779 MeV peak was extracted by subtracting this background from the 1.779 MeV photopeak and then integrating the peak area. The experimental resonance yield rate  $Y'$  at the 1.779 MeV  $\gamma$ -ray decay was calculated by:

$$Y' = \frac{I}{\Delta Q} = \frac{I}{c \cdot t} \quad (3.9)$$

where  $\Delta Q$  is the total charges of projectiles impinging on the target, and  $c$  represents the average

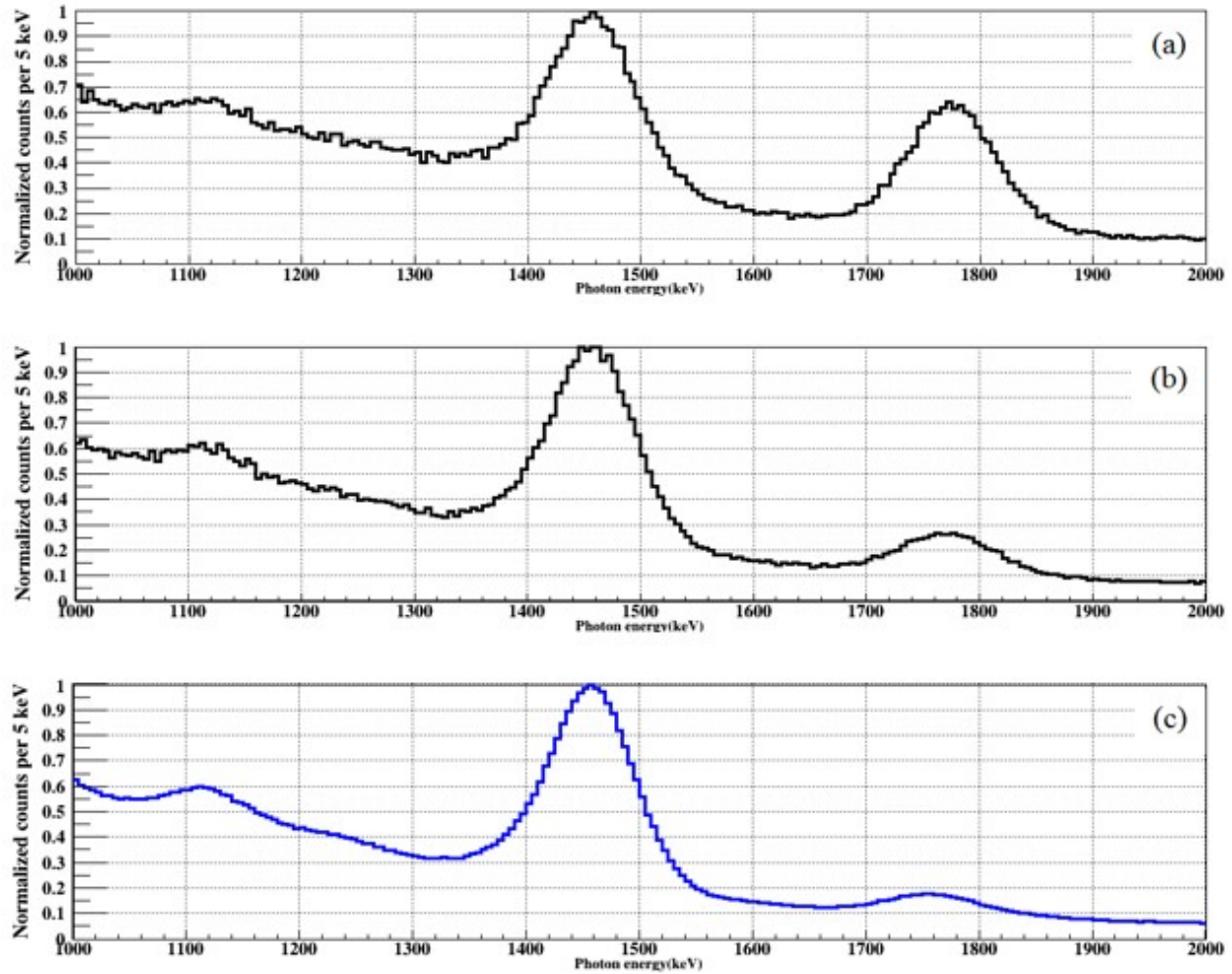


Figure 3.24 On-resonance spectra of  $^{27}\text{Al}(p,\gamma)^{28}\text{Si}$  at  $E_p = 992$  keV (a) and  $632$  keV (b) as well as a background spectrum (c), with photon counts normalized to the maximum height of the  $1460.8$  keV background peak for illustrative purposes.

beam current bombarding on the target in a record time  $t$  which is corrected with dead time.

### 3.1.4.1.2 SuN analysis

The energy calibration of the SuN detector was performed with the use of the  $^{60}\text{Co}$  and  $^{137}\text{Cs}$  radioactive sources and the measured  $\gamma$ -summed peaks from the de-excitation of a final compound nucleus produced by  $(p,\gamma)$  resonance reaction. The energy calibration process involved several steps. The SuN detector consisted of 8 segments with 24 photomultiplier tubes. The first step was to align the  $1460$  keV background radiation from  $^{40}\text{K}$  on the spectra of all 24 PMTs. The  $1460$  keV photopeak of  $^{40}\text{K}$  on each PMT  $\gamma$ -ray spectrum was fitted with a Gaussian on top of

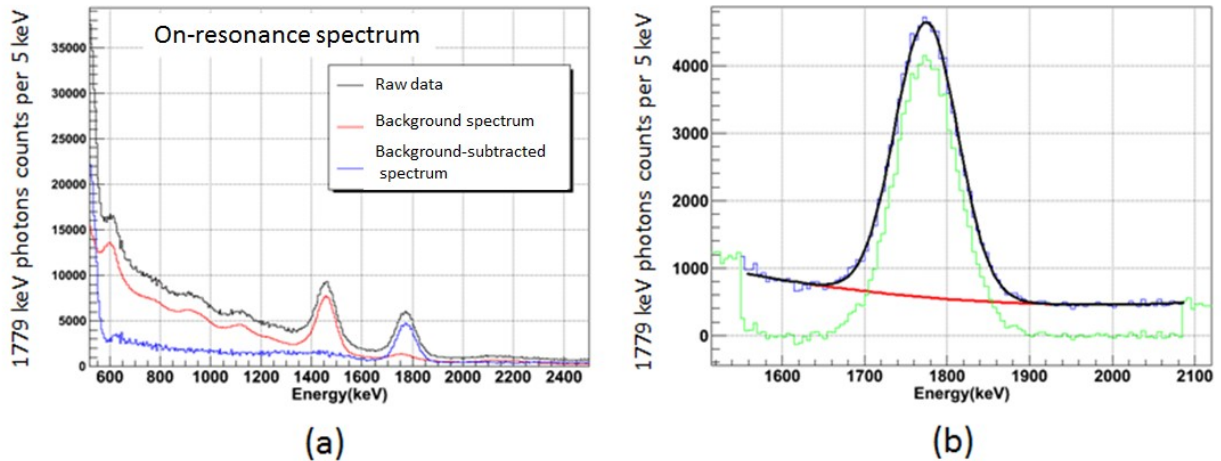


Figure 3.25 The on-resonance spectrum of an experimental run acquired by CAESAR. (a) The raw data with peak shift correction, the background and background-subtracted spectra are labeled by the colors of dark, red and blue, respectively. (b) The 1779 keV photopeak was fitted with a Gaussian plus a second-order polynomial background. The green curve represents the net 1779 keV photopeak subtracted by the second-order polynomial background.

a linear background to obtain the channel number of the peak center. After all the PMTs were well aligned, the second step was the alignment of the 662 keV  $^{137}\text{Cs}$  line and the gamma lines of 1173 and 1332 keV from  $^{60}\text{Co}$  source on the spectra of all the segments. The spectrum of each segment was acquired by summing all  $\gamma$  rays collected by its three PMTs in every cascade event. When all the segments and PMTs were well aligned, a final sum spectrum can be obtained from the sum of all the photons collected by the eight segments in every cascade event. In the third step, the 662 keV photopeak from  $^{137}\text{Cs}$  and the 1173 and 1332 keV photopeaks from  $^{60}\text{Co}$  were used to calibrate the final sum spectrum in the low gamma energy region. For high-energy calibration, the coincidence sum peaks were exploited for extending the energy range of a limited set of calibration sources. In the case of the  $^{60}\text{Co}$  sum spectrum, the simultaneous detection of the 1173 keV and 1332 keV coincident  $\gamma$ -ray photons provided a sum peak at 2506 keV which can be used for the energy calibration of the detector. Figure 3.26 illustrates the decay scheme of  $^{60}\text{Co}$ . In addition, the measured sum peak at 12.538 MeV emitted in the de-excitation of the 12.538 MeV level of  $^{28}\text{Si}$  from  $^{27}\text{Al}(p,\gamma)^{28}\text{Si}$  at  $E_p = 992$  keV resonance and the sum peak at 5.227 MeV from the de-excitation of  $^{58}\text{Ni}(p,\gamma)^{59}\text{Cu}$  at  $E_p = 1843$  keV resonance were included in the calibration.

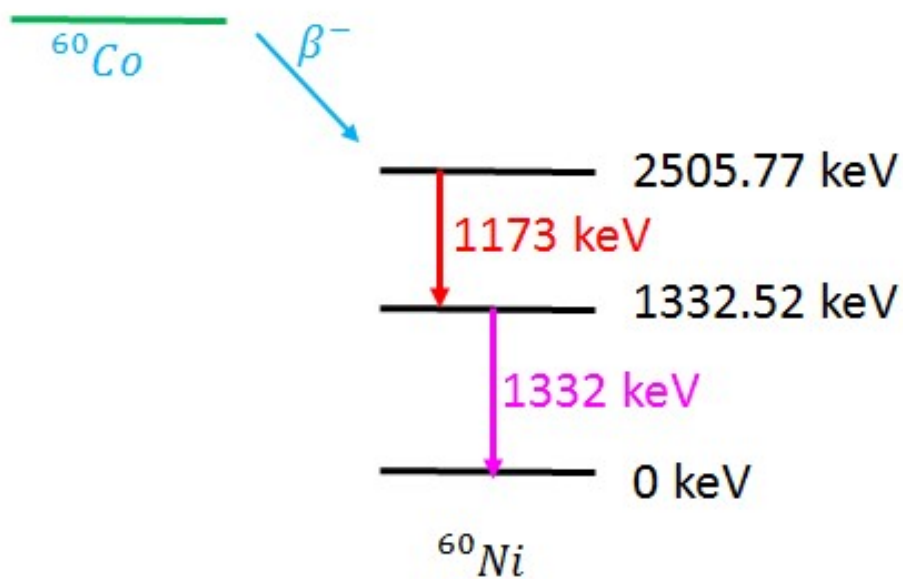


Figure 3.26  $^{60}\text{Co}$  decay scheme.

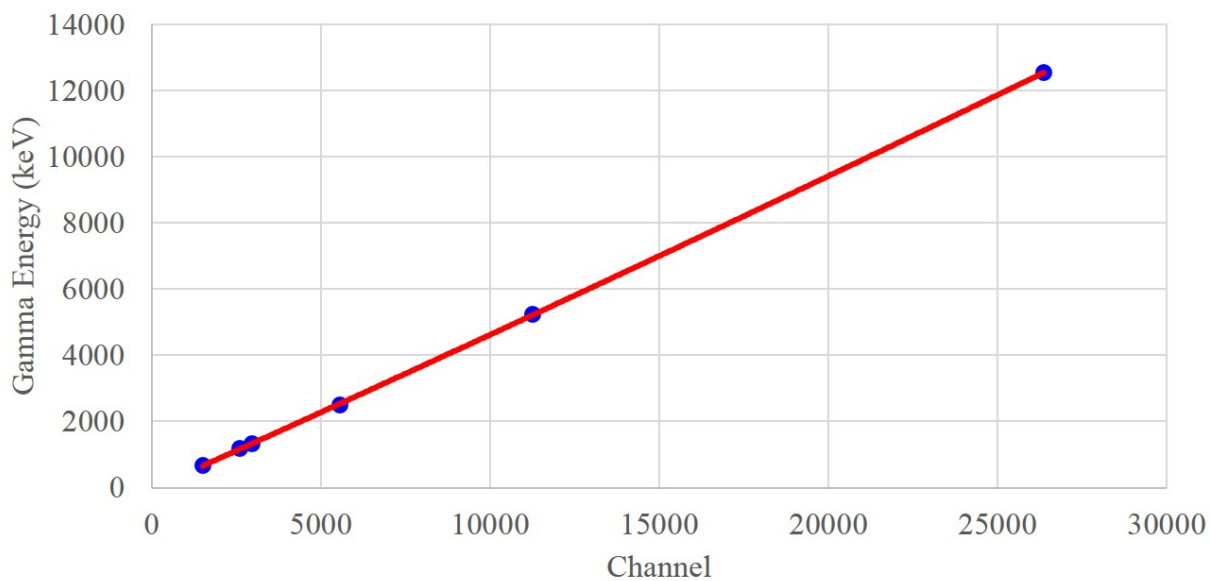


Figure 3.27 Energy Calibration curve for the SuN detector.

Once energy calibration points were established to cover the entire  $\gamma$ -ray energy range of interest, the calibration function relating  $\gamma$ -ray energy to channel number was derived with a second-order polynomial fit, as shown in Figure 3.27.

The  $\gamma$ -summing effect of the SuN detector can be seen in an example of  $^{60}\text{Co}$  spectra. Figure 3.28 shows the  $^{60}\text{Co}$  spectra registered from one single segment, half of the detector and the entire SuN array. The source was placed at the center of the SuN detector. As we can see, the intensity ratio of the sum peak to a single  $^{60}\text{Co}$  gamma line was raised as increasing the solid angle coverage around the source.

Figure 3.29 shows the calibrated  $\gamma$ -ray sum spectrum at beam energy around the 992 resonance of  $^{27}\text{Al}(p,\gamma)^{28}\text{Si}$  as well as a background spectrum. The blue curve in Figure 3.29 is the background-subtracted on-resonance spectrum. The peaks at 1461, 2204, and 2615 keV are the background radiation from  $^{40}\text{K}$ ,  $^{214}\text{Bi}$ , and  $^{208}\text{Tl}$ , respectively. The sum peak for  $^{27}\text{Al}(p,\gamma)^{28}\text{Si}$  at  $E_p = 992$  keV resonance is around the gamma energy  $E_\gamma = E_{c.m} + Q = 12538$  keV, based on Equation 3.3. The sum peak is prominent above the background spectrum. On the contrary, the resonant  $\gamma$  transition at  $E_\gamma = 1779$  keV overlapped with the 1764 keV background radiation on the spectrum. With this  $4\pi$   $\gamma$ -summing technique, the background influence on the estimation of the resonance yield from the sum peak was clearly small.

Figure 3.30 shows on-resonance  $^{27}\text{Al}(p,\gamma)^{28}\text{Si}$  spectra registered by one signal segment, half of the detector and the entire detector. The spectrum of individual segments near the target exhibited the details of the decay cascades, including the 10.762 MeV  $\gamma$  ray emitted from the resonant state to the first excited state of  $^{28}\text{Si}$ . The ratio intensity of the sum peak to the 1779 keV gamma line was apparently enhanced when the all  $\gamma$  rays emitted from each decay cascade were summed over the  $4\pi$  angle coverage around the target.

For the  $^{58}\text{Ni}(p,\gamma)^{59}\text{Cu}$  at  $E_p = 1843$  keV resonance, The  $\gamma$ -summed spectra registered by one segment, half of the detector and the whole detector are shown in Figure 3.31. The decay scheme of this resonance is illustrated in Figure 3.32 [Din & Al-Naser (1975)]. The Q value of the reaction is 3419 keV so that the sum peak is located at  $E_\gamma = E_{c.m} + Q = 5227$  keV. The strongest

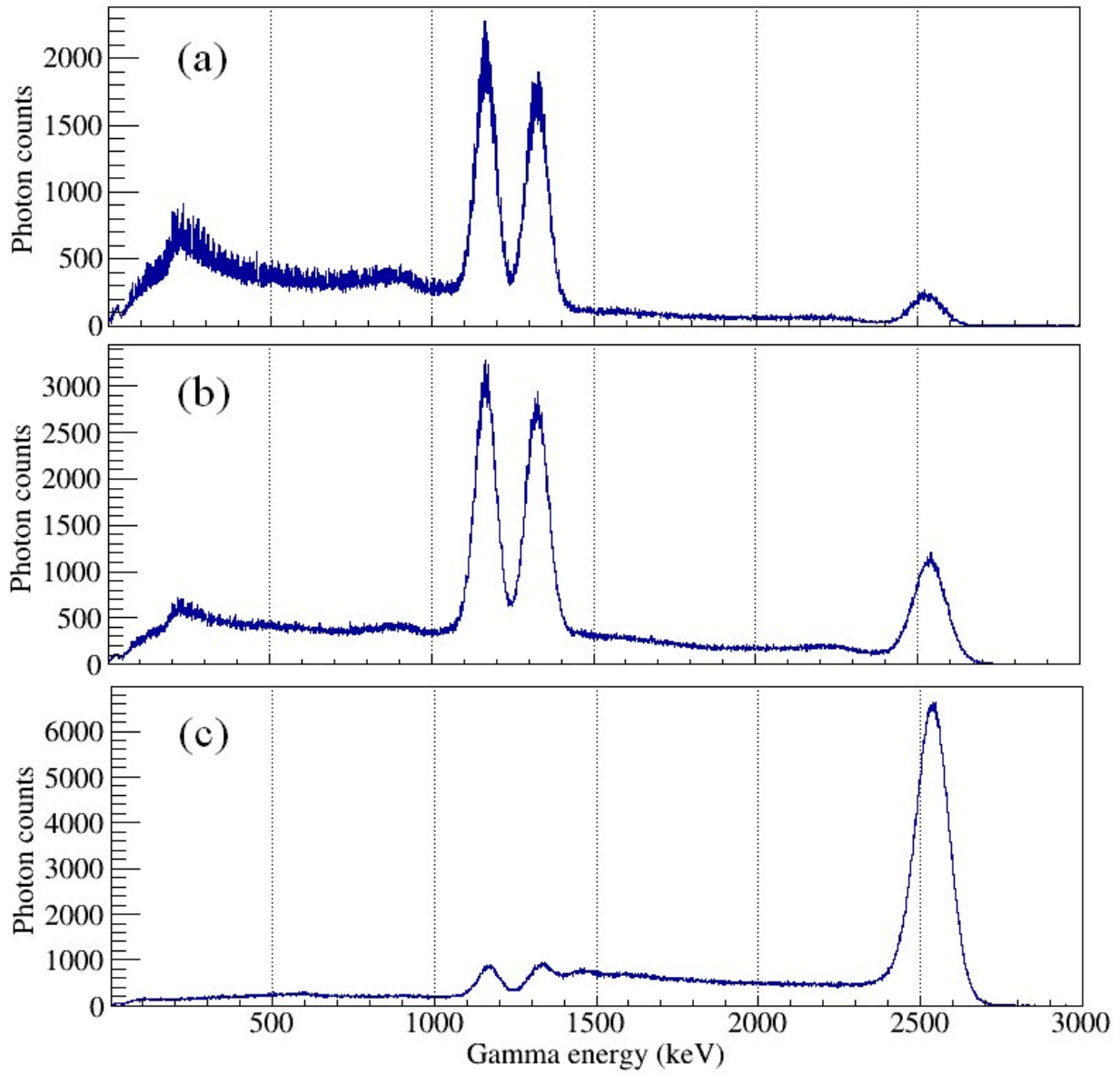


Figure 3.28 The  $\gamma$ -summed spectra of  $^{60}\text{Co}$  registered from (a) one single segment, (b) half of the detector and (c) the entire SuN array.

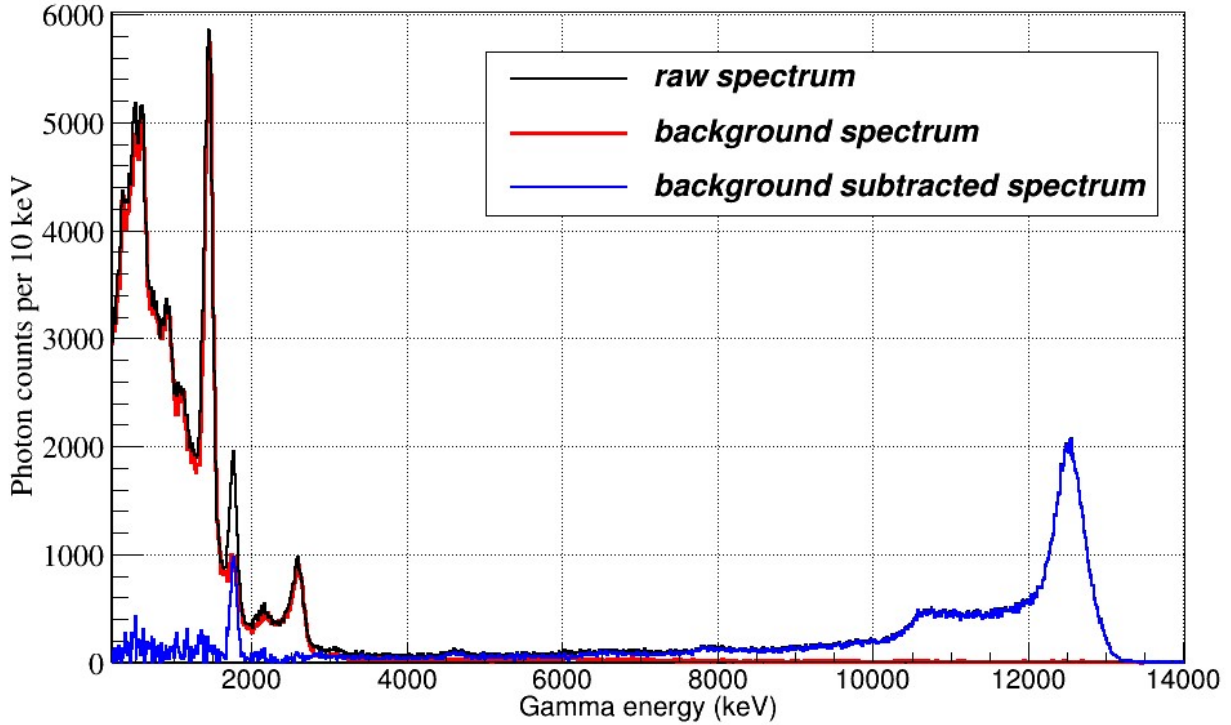


Figure 3.29 The raw data of  $^{27}\text{Al}(p,\gamma)^{28}\text{Si}$  at  $E_p = 992$  keV resonance, the background and background-subtracted SuN spectra are labeled by the colors of dark, red and blue, respectively.

transition (86%) in the de-excitation of  $^{59}\text{Cu}$  from this resonance is the decay from the resonance state to the ground state with the emission of 5227 keV  $\gamma$  rays. The second strongest transition (6%) is to the first excited state and then to the ground state with  $\gamma$ -ray emission at 492 and 4735 keV. The 492 keV and 4735 keV coincident  $\gamma$  rays are clearly observed on the  $\gamma$ -summed spectra of individual segments near the target (see Figure 3.31 (a)). As increasing  $\gamma$ -summing angle coverage around the target, the intensity ratio of the sum peak at  $E_\gamma=5227$  keV to the 492 keV gamma line increases. The low energy range (below 4000 keV) of the spectra is mainly attributed to the background radiation. The fluorine contamination in the target can be observed by the 6129 and 6917 keV gamma lines from  $^{19}\text{F}(p,\alpha\gamma)^{16}\text{O}$  on the spectra.

The number of counts in the sum peak for  $^{27}\text{Al}(p,\gamma)^{28}\text{Si}$  and  $^{58}\text{Ni}(p,\gamma)^{59}\text{Cu}$  resonances were determined by the following procedure. First, the sum peak was fitted with a Gaussian on top of a linear background. The net counts in the sum peak ( $I$ ) were obtained by subtracting the linear background and integrating the peak area within the region of  $(E_\Sigma-3\sigma, E_\Sigma+3\sigma)$ .  $E_\Sigma$  and  $\sigma$

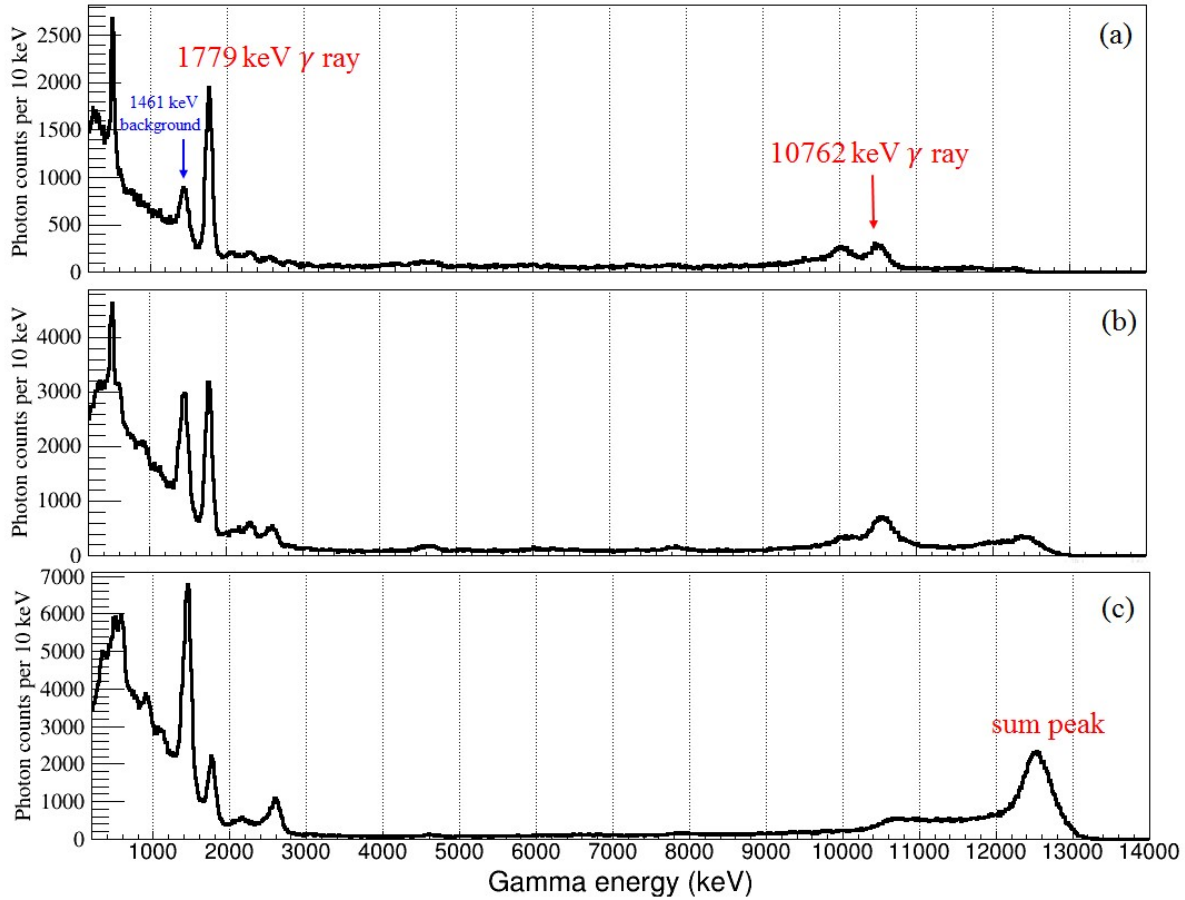


Figure 3.30 The  $\gamma$ -summed spectra of  $^{27}\text{Al}(p,\gamma)^{28}\text{Si}$  at  $E_p = 992$  keV resonance registered from (a) one single segment, (b) half of the detector and (c) the entire SuN array.

were the sum peak centroid and the standard deviation estimated from the Gaussian fit. Figure 3.33 depicts the sum peaks of  $^{27}\text{Al}(p,\gamma)^{28}\text{Si}$  and  $^{58}\text{Ni}(p,\gamma)^{59}\text{Cu}$  resonances with a Gaussian and a linear-background fit. The resonance yield rate of each experimental run was determined from the net counts of the sum peak and the total charge of projectiles accumulated on the target by Equation 3.9.

### 3.1.4.2 Magnetic field correction

The beam trajectory incidence of the central ray into the  $45^\circ$  magnetic analyzer can cause a serious error in determining the correct magnetic field related to the actual beam energy. For improving

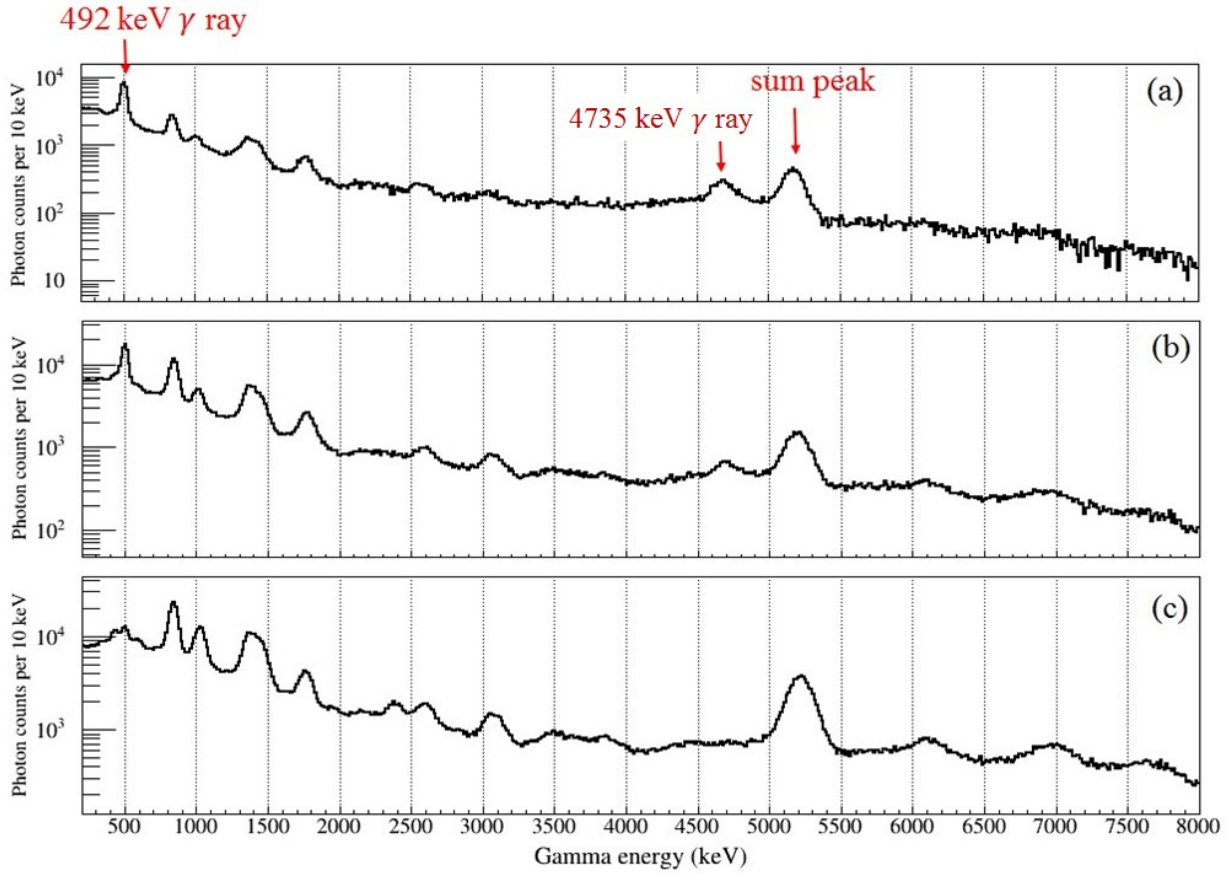


Figure 3.31 The  $\gamma$ -summed spectra of  $^{58}\text{Ni}(p,\gamma)^{59}\text{Cu}$  at  $E_p = 1843$  keV resonance registered from (a) one single segment, (b) half of the detector and (c) the entire SuN array.

this issue, in the first part of the beam energy calibration measurements, the magnetic field ( $B$ ) of the first  $45^\circ$  bending dipole in S bend was monitored and examined by measuring the time-of-flight of bunches between two successive BPMs (beam position monitors) installed in front of the magnet. The phase difference  $\Delta\phi$  between the two BPMs can be translated into the time of flight  $TOF$  by

$$TOF = T_{RF} \left( n + \frac{\Delta\phi}{360^\circ} \right) \quad (3.10)$$

where  $n$  is the consecutive bunch numbers between the two BPMs, and  $T_{RF}$  is the RF period. By substitution of Equation 3.10 into Equation 2.5, we obtain a relationship between the magnetic field ( $B$ ) and the phase difference  $\Delta\phi$ :

$$B \propto \sqrt{E} \propto \sqrt{\frac{m}{2}} \cdot \frac{L}{T_{RF}} \cdot \frac{1}{n + \frac{\Delta\phi}{360^\circ}} \quad (3.11)$$

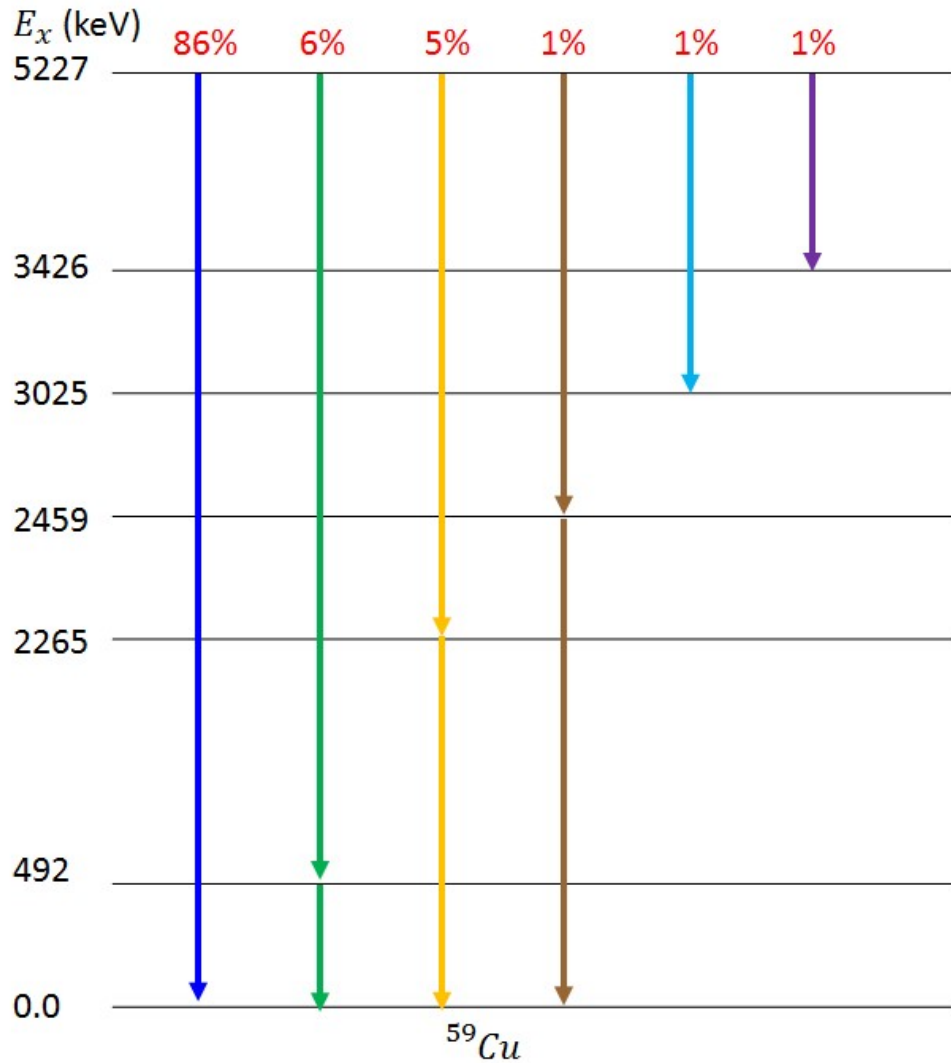


Figure 3.32 The decay scheme of  $^{58}\text{Ni}(p,\gamma)^{59}\text{Cu}$  at  $E_p = 1843$  keV resonance. [Din & Al-Naser (1975)]

where  $E$  and  $m$  are the particle energy and mass, and  $L$  is the distance between the two BPMs.

Equation 3.11 can be simply expressed as

$$\frac{1}{B} = a \cdot \Delta\phi + b \quad (3.12)$$

where  $a$  and  $b$  are determined constants. Figure 3.34 (a) displays one example of the experimental data and a linear fit of the inverse magnetic field versus the beam phase difference between two BPMs.

In the second part of the beam energy calibration measurements, the accuracy of the central ray

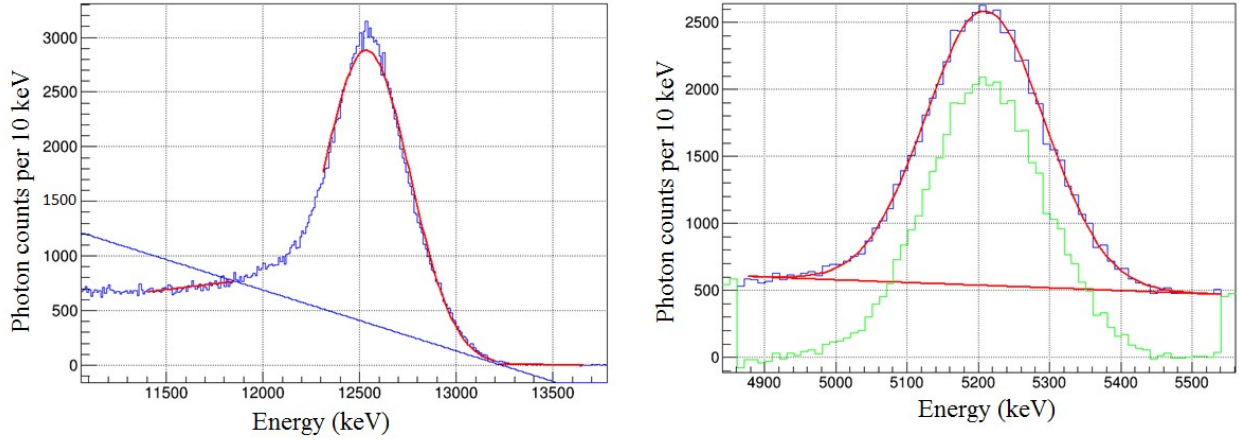


Figure 3.33 The sum peaks of (a)  $^{27}\text{Al}(p,\gamma)^{28}\text{Si}$  at  $E_p = 992$  keV resonance and (b)  $^{58}\text{Ni}(p,\gamma)^{59}\text{Cu}$  at  $E_p = 1843$  keV resonance with a Gaussian and a linear-background fits. In (b), the green curve represents the net sum peak subtracted by the linear background.

was controlled by plotting the amplitude of one SRF cavity, which was used to vary beam energies in 1-2 keV per step, versus the square of the magnetic field. The beam energy was adjusted by changing this cavity amplitude, based on the equation

$$E = E_0 + Q \cdot \text{Amp} \cdot \sin(\Phi - \Phi_0) \quad (3.13)$$

where  $\text{Amp}$  and  $\Phi$  are the cavity amplitude and phase.  $E_0$  and  $\Phi_0$  are the zero-crossing energy and phase, respectively.  $Q$  is the beam charge state. Equation 3.13 reveals a relationship of the magnetic field and the cavity amplitude:

$$B^2 = a' + b' \cdot \text{Amp} \quad (3.14)$$

where  $a'$  and  $b'$  are determined constants. Figure 3.34 (b) shows one example of the experimental data for the square of magnetic field versus the cavity amplitude with a linear fit.

The ambiguous magnetic field due to the oblique incidence on the magnet can be monitored and corrected by the analytic calculations based on the linear equations of Equation 3.12 and Equation 3.14 once the linear constants of  $(a, b)$  and  $(a', b')$  were determined. One example for the field correction is illustrated in Figure 3.35. The oblique angle entering the magnet can lead to the peak centroid of the beam intensity off the center of the vertical slit in the diagnostic station 9 and induce an error in determining the magnetic field that corresponds to the actual beam energy.

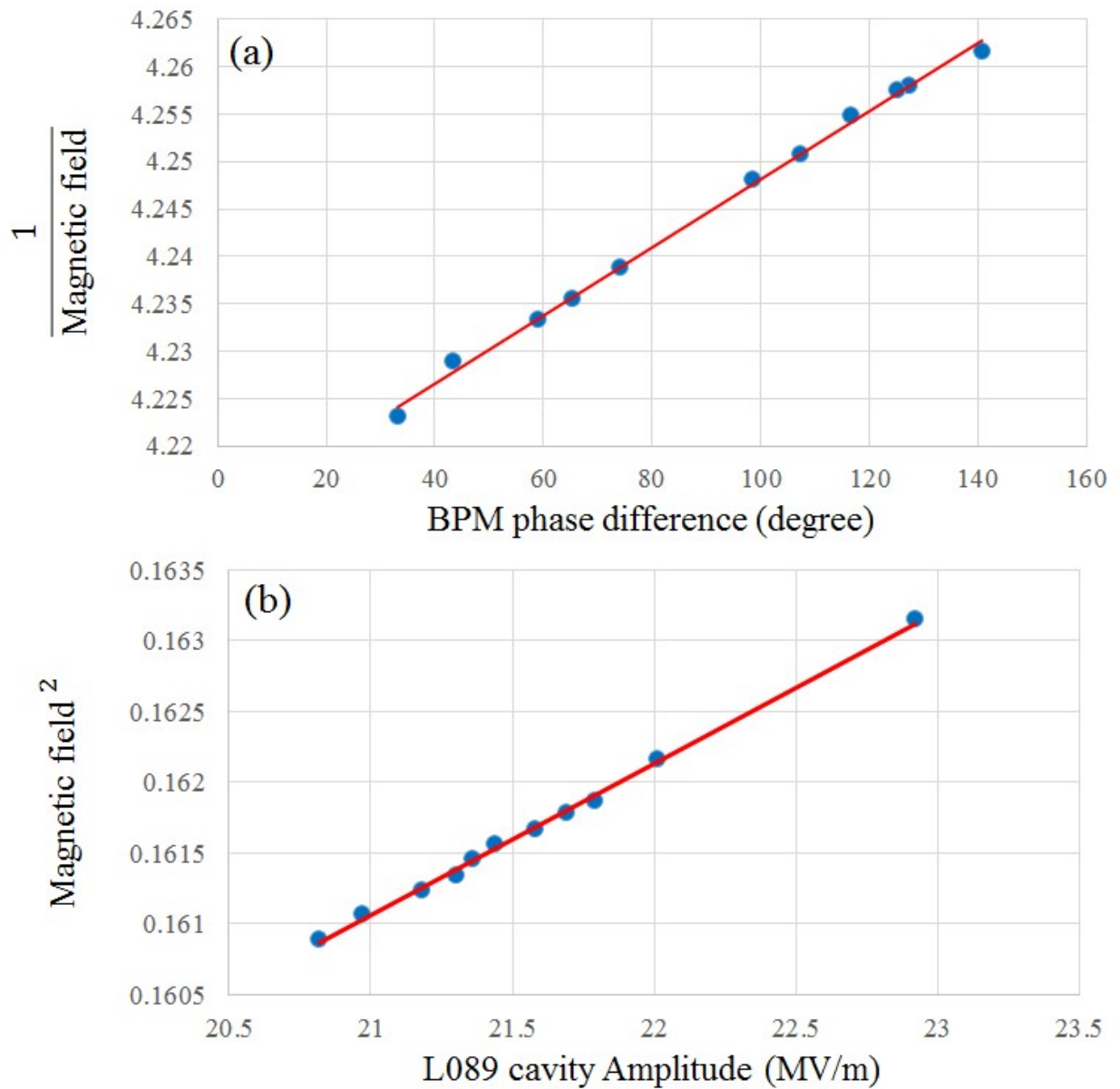


Figure 3.34 (a) The inverse magnetic field vs. the beam phase difference between two BPMs for the experiential runs at  $^{27}\text{Al}(p,\gamma)^{28}\text{Si}$  632 keV resonance in the first part of the beam energy calibration measurements. (b) The square of magnetic field versus the cavity amplitude for the experiential runs at  $^{58}\text{Ni}(p,\gamma)^{59}\text{Cu}$  1843 keV resonance in the second part of the beam energy calibration measurements.

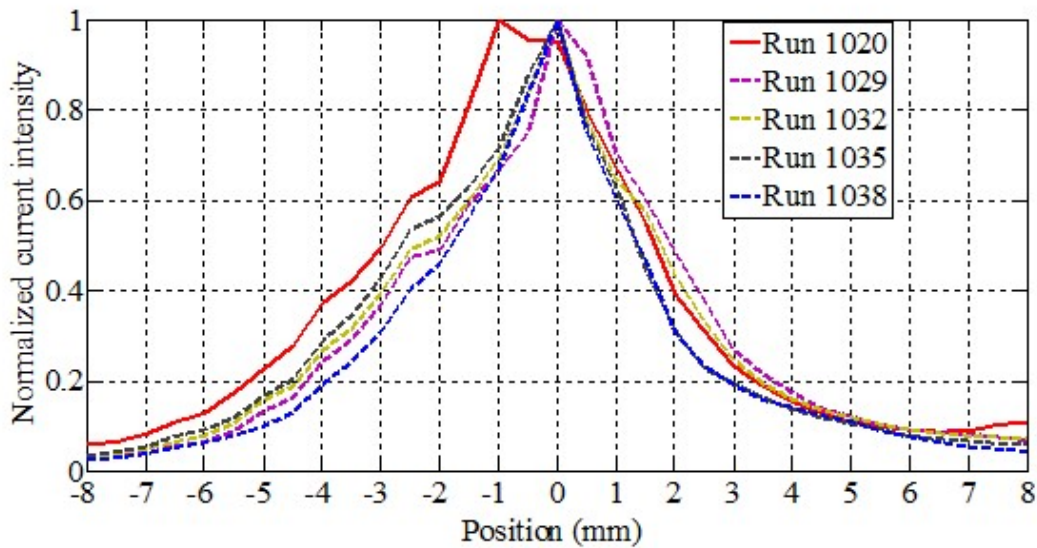
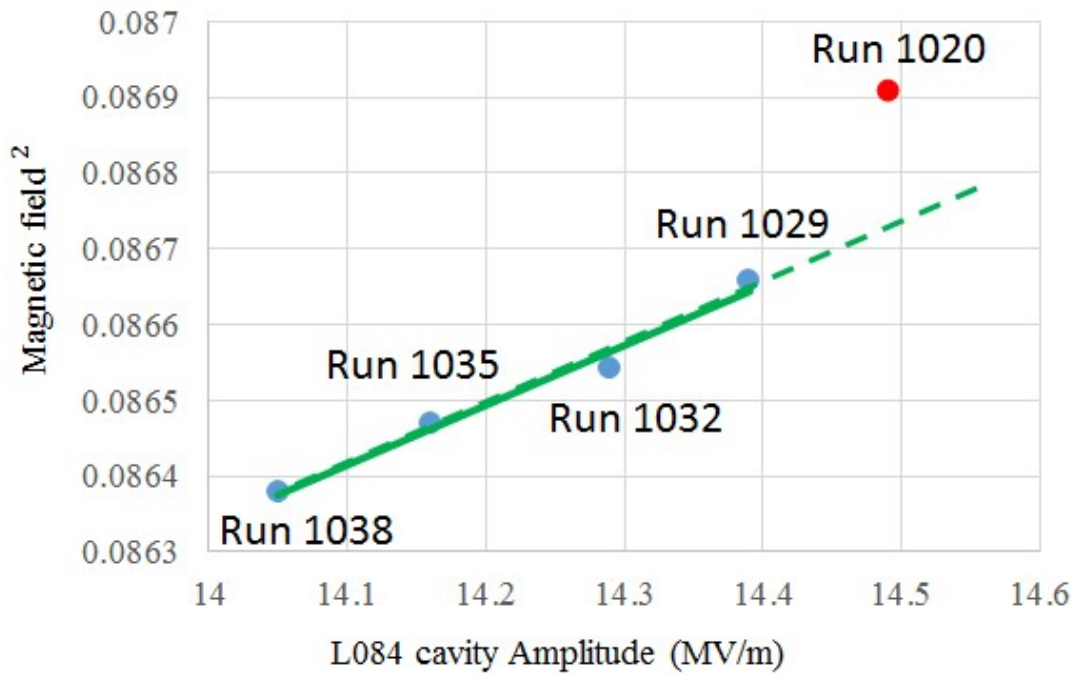


Figure 3.35 Some experiential runs at  $^{27}\text{Al}(p,\gamma)^{28}\text{Si}$  992 keV resonance in the second part of the beam energy calibration measurements. The upper panel shows the square of magnetic field versus the L084 cavity amplitude and the lower panel shows the beam vertical profiles in the diagnostic station 9 after the beam passed the first bending dipole in S bend.

This issue can be seen on the experimental run #1020 as an example in Figure 3.35. However, the ambiguous magnetic field on the experimental run #1020 was reasonably corrected based on the relationship between the magnetic field and the L084 cavity amplitude, leading to a correction of 0.25 mT.

### 3.1.4.3 Fitting and error analysis

The shape of the resonance yield curve for a narrow resonance (the resonance width  $\Gamma \leq$  the resonance energy  $E_R$ ) can be expressed as a Breit-Wigner function [ Rolfs & Rodney (1988)]

$$\sigma(E, E_R) = \lambda^2 \frac{1}{4\pi} \frac{\omega\gamma \cdot \Gamma}{(E - E_R)^2 + (\frac{\Gamma}{2})^2} \quad (3.15)$$

where  $\sigma$  is the cross section,  $\omega\gamma$  is the resonance strength and  $\lambda$  is the de Broglie wavelength of the projectile. For a homogeneous thick target (where the energy loss  $\Delta$  of the projectiles in the target is much larger than the resonance width), the yield has to be integrated over the target thickness:

$$Y(E_0) \sim \int_{E_0-\Delta}^{E_0} \frac{\sigma(E)}{\varepsilon(E)} dE \quad (3.16)$$

where  $\varepsilon$  is the atomic stopping cross section of the target. The shape of a thick-target yield curve is determined by the uniformity of target composition, resonance width, and also the spread in the energy of the bombarding particles. The total energy distribution is the result of contributions from the regulation of the SRF cavities and RFQ, the Doppler broadening due to the thermal motion of the target atoms, the energy straggling of protons inside the target, and the intrinsic energy spread of the beam. All effects can be included in a single Gaussian function to simplify the calculation, namely [ Rolfs & Rodney (1988)]

$$g(E, E_0) = \frac{1}{\sqrt{2\pi} \cdot \delta} \exp \left[ -\frac{(E - E_0)^2}{2\delta^2} \right]; \quad (3.17)$$

$$Y(E_0) \sim \int_{E_0-\Delta}^{E_0} \int_0^\infty \frac{\sigma(E')}{\varepsilon(E')} g(E', E_0) dE' dE \quad (3.18)$$

where  $E_0$  is the mean incident energy and  $\delta$  is the total standard deviation of the energy spread. The function  $g(E', E_0) dE'$  describes the energy distribution within the proton energy. If the energy

dependence of these quantities  $\lambda$ ,  $\omega\gamma$ ,  $\Delta$  and  $\varepsilon$  is negligibly small over the resonance region, the resonance  $\gamma$ -ray yield per nA (beam current unit) per min (record time unit)  $Y'$  is represented by

$$Y'(E_0) = \omega\gamma \left( \frac{\lambda^2}{2\pi} \right) \frac{m_p + m_t}{m_t} \frac{\eta}{\varepsilon} \left( \frac{10^{-9} \cdot 60}{1.6 \cdot 10^{-19}} \right) \int_0^\infty \left[ \arctan\left(\frac{E - E_R}{\frac{\Gamma}{2}}\right) - \arctan\left(\frac{E - E_R - \Delta}{\frac{\Gamma}{2}}\right) \right] \frac{1}{\sqrt{2\pi} \cdot \delta} \exp\left[-\frac{(E - E_0)^2}{2\delta^2}\right] dE \quad (3.19)$$

where  $\eta$  is the detector efficiency,  $m_t$  is the mass of a target nucleus, and  $m_p$  is the mass of a proton. For the measurement of the 1.779 MeV  $\gamma$  rays in  $^{27}\text{Al}(p,\gamma)^{28}\text{Si}$  resonances, the resonance yield rate of Equation 3.19 needs to be multiplied by the branching ratio  $B_r$  of the 1.779 MeV  $\gamma$ -ray decay. In the present work, the resonance properties  $B_r$ ,  $\omega\gamma$ ,  $E_R$  and  $\Gamma$  are well-known from literature [ Meyer et al. (1975)] [ Maas et al. (1978)] [ Harissopoulos1 et al. (2000)]. The stopping cross section  $\varepsilon$  and the energy loss  $\Delta$  through the target are obtained from the SRIM code [ Ziegler (2013)]. This equation can be evaluated numerically to obtain a value of beam energy spread  $\delta$ .

Energy calibration is usually achieved by taking the midpoint of the rise of the yield curve as the energy of the resonance and relating the corresponding the magnetic field to the resonance energy. However, it is noticed that this method of determining the resonance energy may introduce the error about the order of the half-width of the resonance [ Bondelid & Kennedy (1959)]. A more satisfying method for precisely calibrating the magnet is to fit the data by a theoretical yield model of Equation 3.19 with the calibration factor  $k$  as one of the fit parameters. The calibration factor  $k$  is defined by Equation 2.5. The other fitting parameters are the beam energy spread  $\delta$  and the yield scaling factor  $S$  for normalizing the maximum experimental yield at the plateau of the excitation function to the maximum yield at the plateau of the fitting curve.

The error of the experimental resonance yield rate  $Y'$  in Equation 3.9 is determined by

$$\sigma_{Y'} = Y' \sqrt{\left(\frac{\sigma_I}{I}\right)^2 + \left(\frac{\sigma_c}{c}\right)^2} \quad (3.20)$$

where  $I$  and  $c$  are the  $\gamma$ -ray resonant yield counts and the mean beam current impinging on the target. The standard deviation  $\sigma_I$  of the  $\gamma$ -ray counts in an analyzed peak is assumed as  $\sqrt{I}$ . The measurement of the beam current on the target with an estimated error of  $\frac{\sigma_c}{c}=10\%$  dominates the

error contribution of the resonance yield rate. The error  $\sigma_B$  in determining the magnetic field of the magnetic analyzer is derived by two steps of (a) finding a best-fitting straight line (called as the regression line) through the data of the magnetic field vs. the beam phase difference between two BPMs or one cavity amplitude (more detail in Section 3.1.4.2); (b) estimating the error of prediction through the regression line and the data points. The factors which contribute to the uncertainty of the magnetic field determination are the resolution of the Hall probe (0.01%), the stability of the magnet, the regulation of the SRF cavities and the consistency of the incoming beam projectiles entering the magnet. A fitting algorithm was written in Matlab to fit the experimental  $\gamma$ -ray resonance yield curves with the consideration of both the resonance yield rate and magnetic field errors. The chi-square statistic is defined by the formula

$$\chi^2 = \sum_i^N \frac{(Y'_i - Y'_{si})^2}{\sigma_{Y'_i}^2 + \left(\frac{dY'(B)}{dB} \cdot \sigma_{B_i}\right)^2} \quad (3.21)$$

where  $Y'_i$  and  $Y'_{si}$  are the measured and simulated yield rates for a given data point  $i$  with the yield error  $\sigma_{Y'_i}$  and the field error  $\sigma_{B_i}$ . The fitting iteration was continued until the valley in the 3-D plot of the chi-square versus the three fitting parameters ( $k, \delta, S$ ) was found, as shown in Figure 3.36. A grid search method [Johnson & Faunt (1992)] was used to evaluate the confidence intervals of the determined parameters ( $k, \delta, S$ ) obtained from fitting experimental data. This method involves creating an M-dimensional grid space, if there are M fitting parameters, with a chi-square value determined at each point. A series of contours in this grid space is represented by constant chi-square values  $\chi^2$  defined as

$$\frac{\chi^2}{\chi_{min}^2} = 1 + \frac{M}{N-M} \cdot F(M, N-M, 1-P) \quad (3.22)$$

where  $\chi_{min}^2$  is the least chi-square,  $N$  is the number of data points,  $(1-P)$  is the probability of finding the true value of the fitting parameters, and  $F$  is Fisher's F distribution. In this present work, the confidence interval of the fitting parameters is chosen as 68% probability (one standard deviation) by searching a contour at the value of  $\chi_{68\%}^2$  where  $(1-P)$  is 68%.

In the first part of the beam energy calibration measurements, the  $^{27}\text{Al}(p,\gamma)^{28}\text{Si}$  at  $E_p = 992$  keV resonance was measured with and without the L091 rebuncher cavity to control the energy

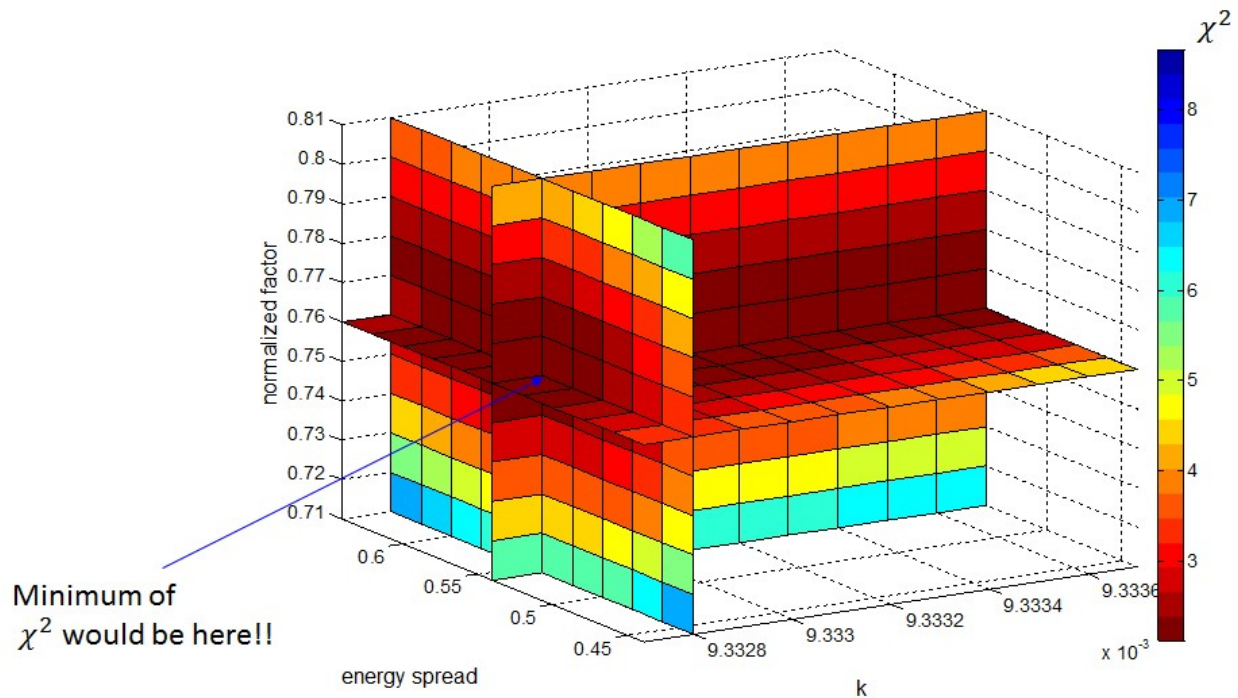


Figure 3.36 Dependence of the least chi-square on the normalized factor ( $S$ ), the energy spread (% in FWHM) and the dipole calibration factor ( $k$ ) for  $^{27}\text{Al}(p,\gamma)^{28}\text{Si}$  992 keV/u resonance. The minimum of the chi-square is marked with an arrow.

spread and the experimental  $\gamma$ -ray yield results as a function of the magnetic field were well fitted using Equation 3.19, as shown in Figure 3.37. Compared with no use of L091 rebuncher cavity, the shape of the  $\gamma$ -ray yield curve measured with the use of the L091 rebuncher cavity exhibits a steeper rise, indicating a smaller energy spread. However, the measurement of the  $^{27}\text{Al}(p,\gamma)^{28}\text{Si}$  992 keV resonance with the use of the L091 rebuncher cavity suffers a large error in determining magnetic field due to the phase instability of the L091 cavity. Figure 3.38 shows the yield curve of  $^{27}\text{Al}(p,\gamma)^{28}\text{Si}$  at  $E_p=632$  keV resonance. The present results for the calibration factor ( $k$ ) and beam energy spread obtained from the first part of the beam energy calibration measurements are summarized in Table 3.4 and Table 3.5, respectively. The result of the  $k$  value for  $^{27}\text{Al}(p,\gamma)^{28}\text{Si}$  992 keV resonance with and without using the L091 rebuncher cavity is very reproducible with a precision of 0.0043%.

In the second part of the beam energy calibration measurements, each resonance reaction was measured under various open width of the horizontal slit in the diagnostic station 15. The experi-

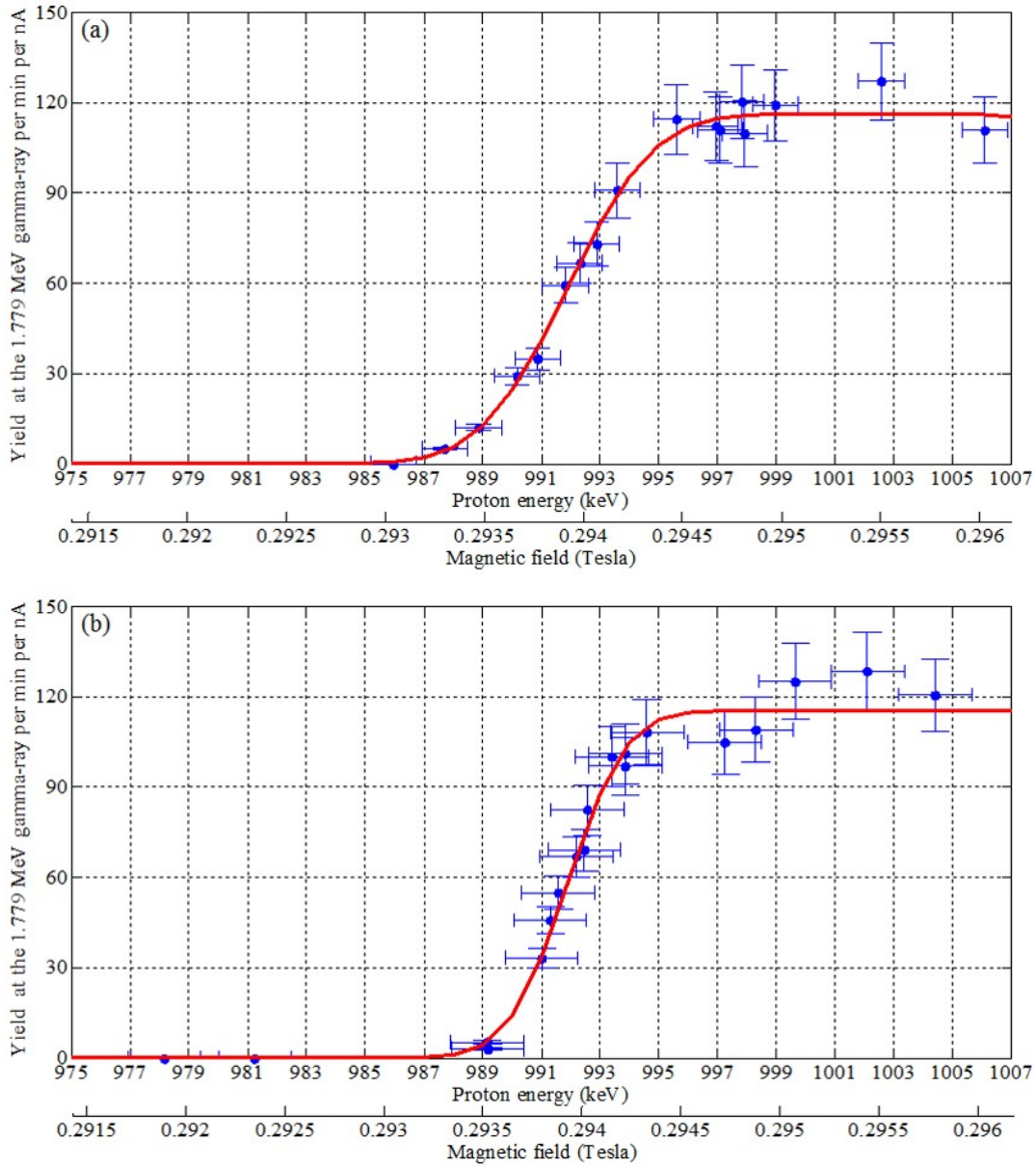


Figure 3.37 The  $^{27}\text{Al}(p,\gamma)^{28}\text{Si}$  yield curves of the 992 keV resonance (a) without and (b) with the L091 rebuncher cavity in the first part of the beam energy calibration measurements. The solid curves are a fit to the data with a theoretical yield model of Equation 3.19.

$^{27}\text{Al}(p,\gamma)^{28}\text{Si}$ 992 keV resonance		$^{27}\text{Al}(p,\gamma)^{28}\text{Si}$ 632 keV resonance
without the L091 rebuncher	with the L091 rebuncher	
<b>4648.66</b> + 0.75 / -0.70	<b>4648.86</b> + 1.06 / -1.15	<b>4651.12</b> + 0.73 / -0.68

Table 3.4 Calibration factor  $k$  ( $\times 10^{-6} \text{ T}/\sqrt{\text{keV} * \text{amu}}$ ) obtained in the first part of the beam energy calibration measurements.

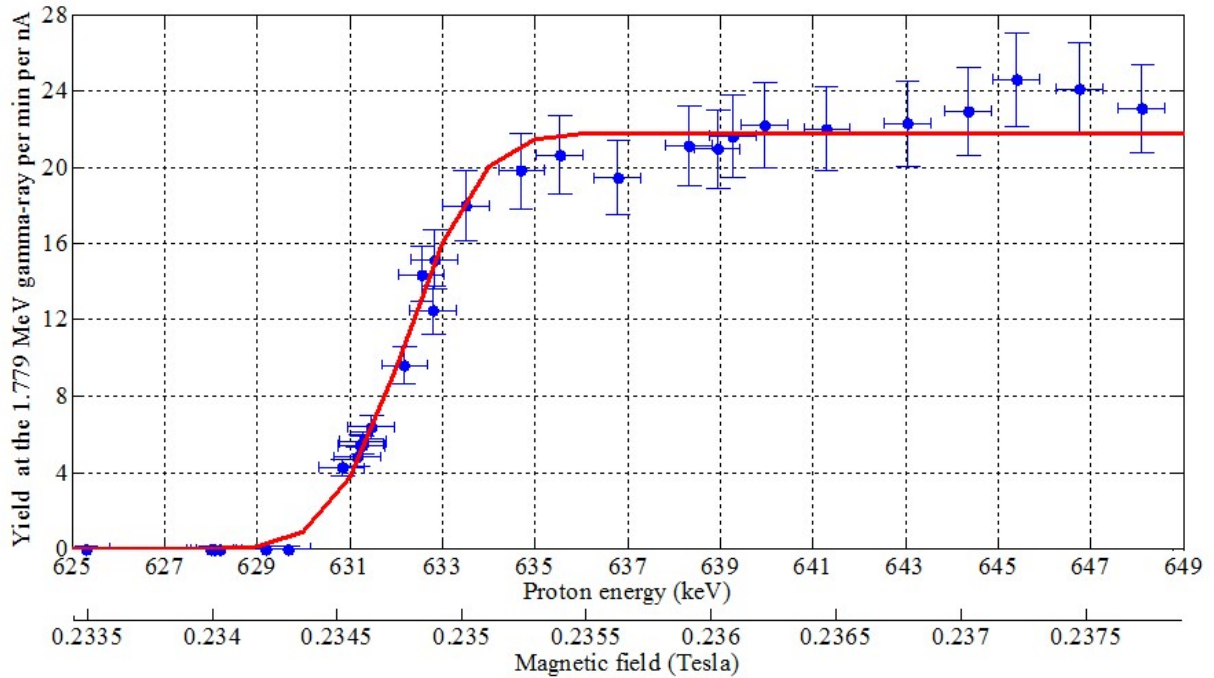


Figure 3.38 The  $^{27}\text{Al}(p,\gamma)^{28}\text{Si}$  yield curve at  $E_p = 632$  keV resonance in the first part of the beam energy calibration measurements. The solid curves are a fit to the data with a theoretical yield model of Equation 3.19.

$^{27}\text{Al}(p,\gamma)^{28}\text{Si}$ 992 keV resonance		$^{27}\text{Al}(p,\gamma)^{28}\text{Si}$ 632 keV resonance
without the L091 rebuncher	with the L091 rebuncher	
<b>0.46</b> + 0.06/-0.05 (68%)	<b>0.31</b> + 0.12/-0.07 (68%)	<b>0.40</b> ± 0.07 (68%)
<b>0.92</b> + 0.12/-0.11 (95%)	<b>0.63</b> + 0.24/-0.15 (95%)	<b>0.80</b> ± 0.14 (95%)
<b>1.38</b> + 0.18/-0.16 (99.7%)	<b>0.94</b> + 0.37/-0.22 (99.7%)	<b>1.20</b> ± 0.21 (99.7%)

Table 3.5 Beam energy spread (in %) with 68%, 95%, and 99.7% of the beam particles in the first part of the beam energy calibration measurements.

mental yield curves of  $^{27}\text{Al}(p,\gamma)^{28}\text{Si}$  992 keV resonance and  $^{58}\text{Ni}(p,\gamma)^{59}\text{Cu}$  1843 keV resonance with a fit of Equation 3.19 are shown in Figure 3.39 and Figure 3.40. Table 3.6 and Table 3.7 represent a summary of the fitting results, including the magnetic calibration factor  $k$  and beam energy spread for each reaction with varying slit widths. Figure 3.41 illustrates that reducing the slit width in the diagnostic station 15 leads to a rapid rise of the resonance yield curves and small beam energy spread. For each reaction, the result of the calibration factor  $k$  for three different slit widths coincides within 0.0072%. The comparison in the  $k$  values obtained from the  $^{27}\text{Al}(p,\gamma)^{28}\text{Si}$  992 keV resonance between the first and second parts of the beam energy calibration measurements

	$^{27}\text{Al}(p,\gamma)^{28}\text{Si}$ 992 keV resonance	$^{58}\text{Ni}(p,\gamma)^{59}\text{Cu}$ 1843 keV resonances
Slit open	$(4657.146 + 0.697 / -0.687) \times 10^{-6}$	$(4662.968 + 0.664 / -0.641) \times 10^{-6}$
Slit width : 3 mm	$(4657.37 + 0.96 / -0.93) \times 10^{-6}$	$(4663.68 + 0.86 / -0.83) \times 10^{-6}$
Slit width : 1 mm	$(4657.48 + 0.89 / -0.86) \times 10^{-6}$	$(4663.88 + 0.65 / -0.64) \times 10^{-6}$

Table 3.6 Calibration factor  $k$  (in  $\text{T}/\sqrt{\text{keV} * \text{amu}}$ ) obtained under the three different conditions of the horizontal slit in the diagnostic station 15 in the second part of the beam energy calibration measurements.

Reaction	Slit condition	68% of particles	95% of particles	99.7% of particles
$^{27}\text{Al}(p,\gamma)^{28}\text{Si}$ 992 keV resonance	Slit open	$0.34 + 0.05/-0.04$	$0.69 + 0.10/-0.08$	$1.03 + 0.15/-0.12$
	Slit width:3mm	$0.29 + 0.06/-0.05$	$0.57 + 0.13/-0.10$	$0.86 + 0.19/-0.14$
	Slit width:1mm	$0.23 + 0.06/-0.05$	$0.46 + 0.13/-0.10$	$0.70 + 0.19/-0.14$
$^{58}\text{Ni}(p,\gamma)^{59}\text{Cu}$ 1843 keV resonance	Slit open	$0.33 \pm 0.04$	$0.66 + 0.09/-0.08$	$0.98 + 0.13/-0.12$
	Slit width:3mm	$0.27 \pm 0.05$	$0.55 \pm 0.10$	$0.82 + 0.16/-0.14$
	Slit width:1mm	$0.22 + 0.05/-0.04$	$0.44 + 0.10/-0.09$	$0.66 + 0.14/-0.13$

Table 3.7 Beam energy spread (in %) obtained with 68%, 95%, and 99.7% of the beam particles under the three different conditions of the horizontal slit in the diagnostic station 15.

leads to the experimental uncertainty of  $\sim 0.18$  %. This error can be treated as the systematic error due to the inconsistent incident angle of the beam trajectory entering the magnet. During the period between the first and second parts of the beam energy calibration measurements, the third cryomodule was installed on the ReA3 platform, probably resulting in a slight incline of the platform altitude as well as the change of the beam trajectory incident angle into the magnetic analyzer. Other factors which may cause the inconsistent incident angle of the beam trajectory into the magnet are discussed in Section 5.1.

### 3.1.5 Comparison of beam energy spread between data and beam simulation

The measured beam energy spread from the  $\gamma$ -ray resonance reactions has been systematically compared with the beam simulation by DYNAC. The performance of the beam dynamics simulation started from the low energy transport section before RFQ toward the target stations. The 70000 particles in DYNAC for the initial beam condition were randomly generated as a cylinder-

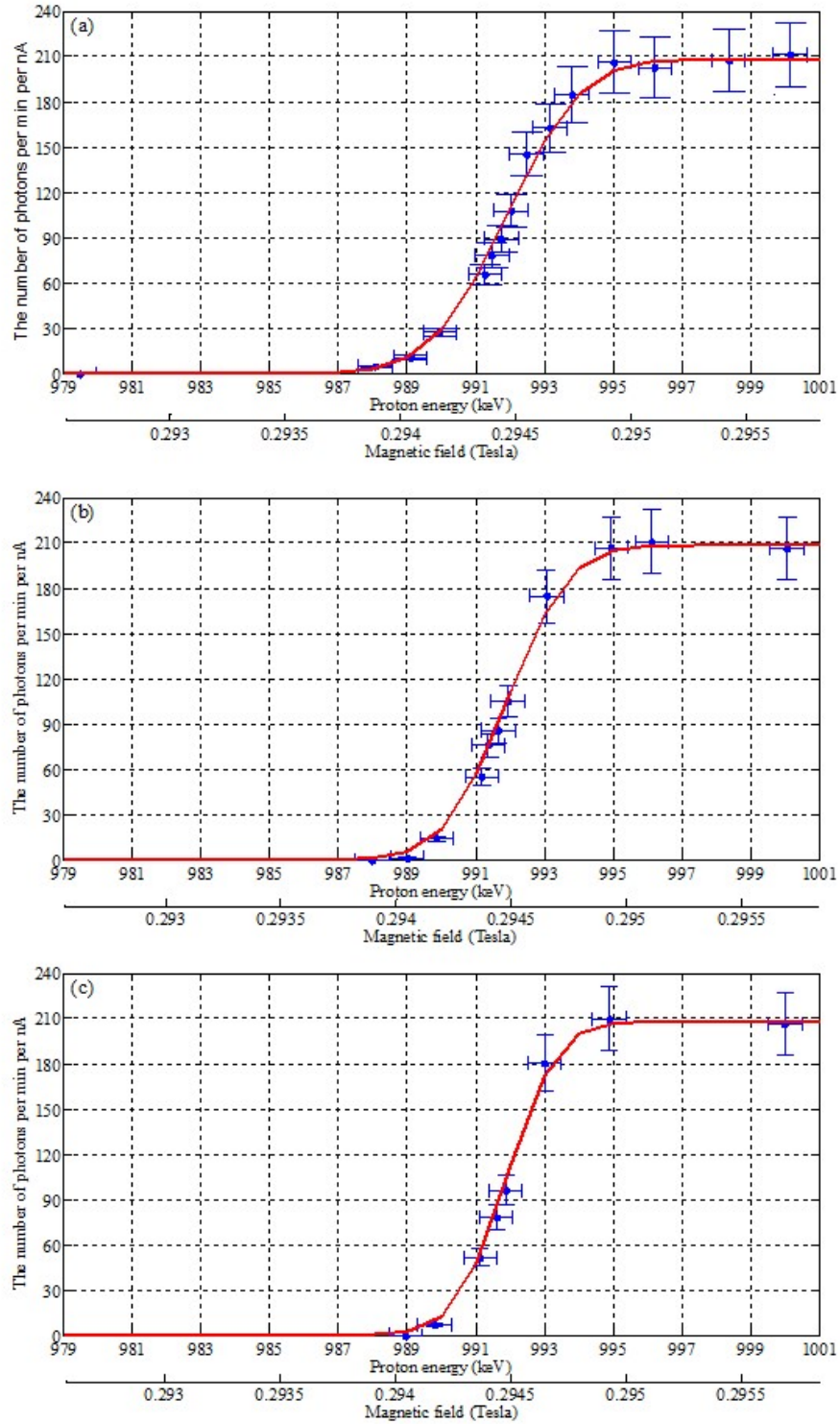


Figure 3.39 The  $^{27}\text{Al}(p,\gamma)^{28}\text{Si}$  yield curves at  $E_p = 992$  keV resonance under the three different conditions of the horizontal slit in the diagnostic station 15: (a) slit fully open; (b) slit opening width : 3 mm; and (c) slit opening width : 1 mm in the second part of the beam energy calibration measurements. The solid curves are a fit to the data with a theoretical yield model of Equation 3.19.

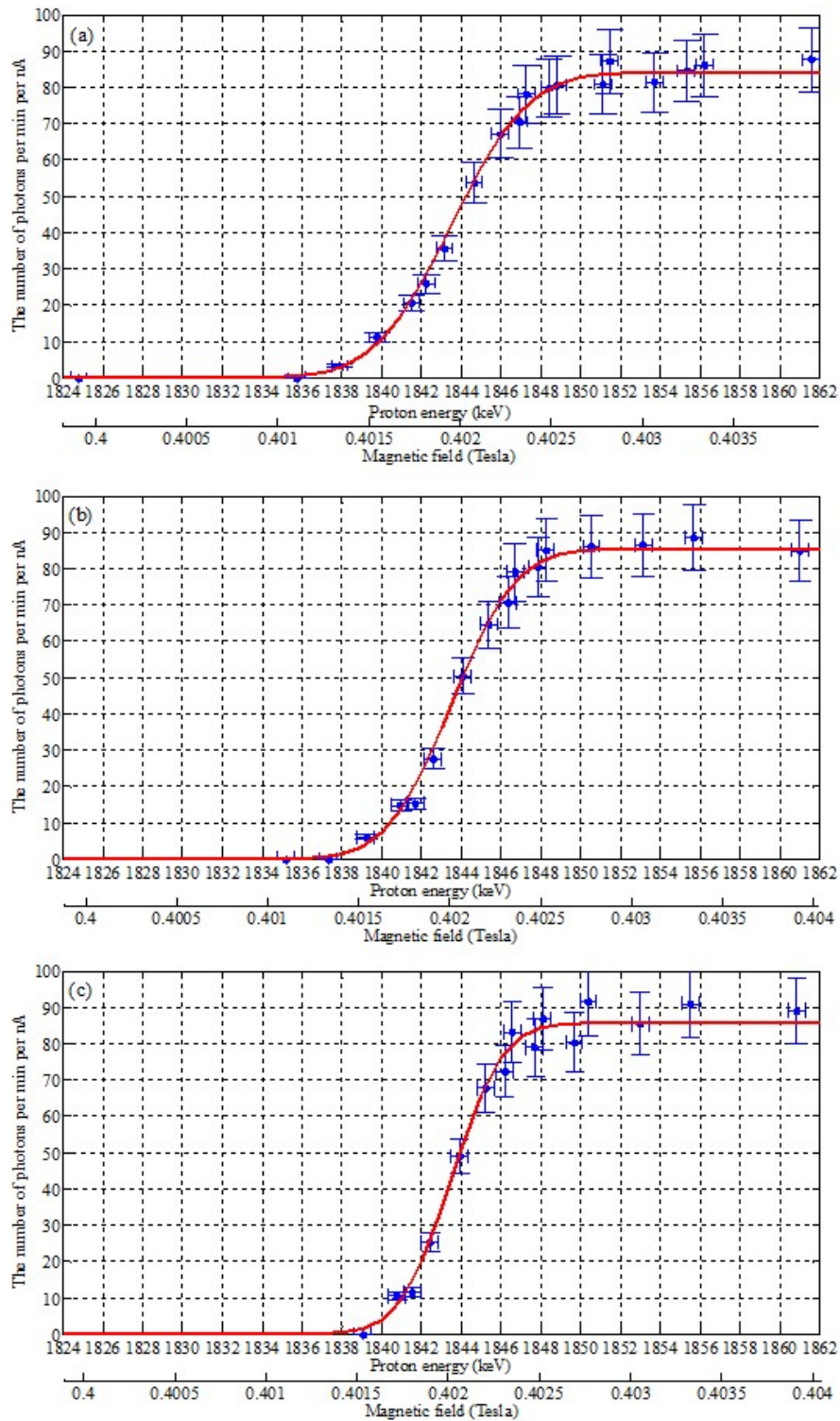


Figure 3.40 The  $^{58}\text{Ni}(p,\gamma)^{59}\text{Cu}$  yield curves at  $E_p = 1843$  keV resonance under the three different conditions of the horizontal slit in the diagnostic station 15: (a) slit fully open; (b) slit opening width : 3 mm; and (c) slit opening width : 1 mm in the second part of the beam energy calibration measurements. The solid curves are a fit to the data with a theoretical yield model of Equation 3.19.

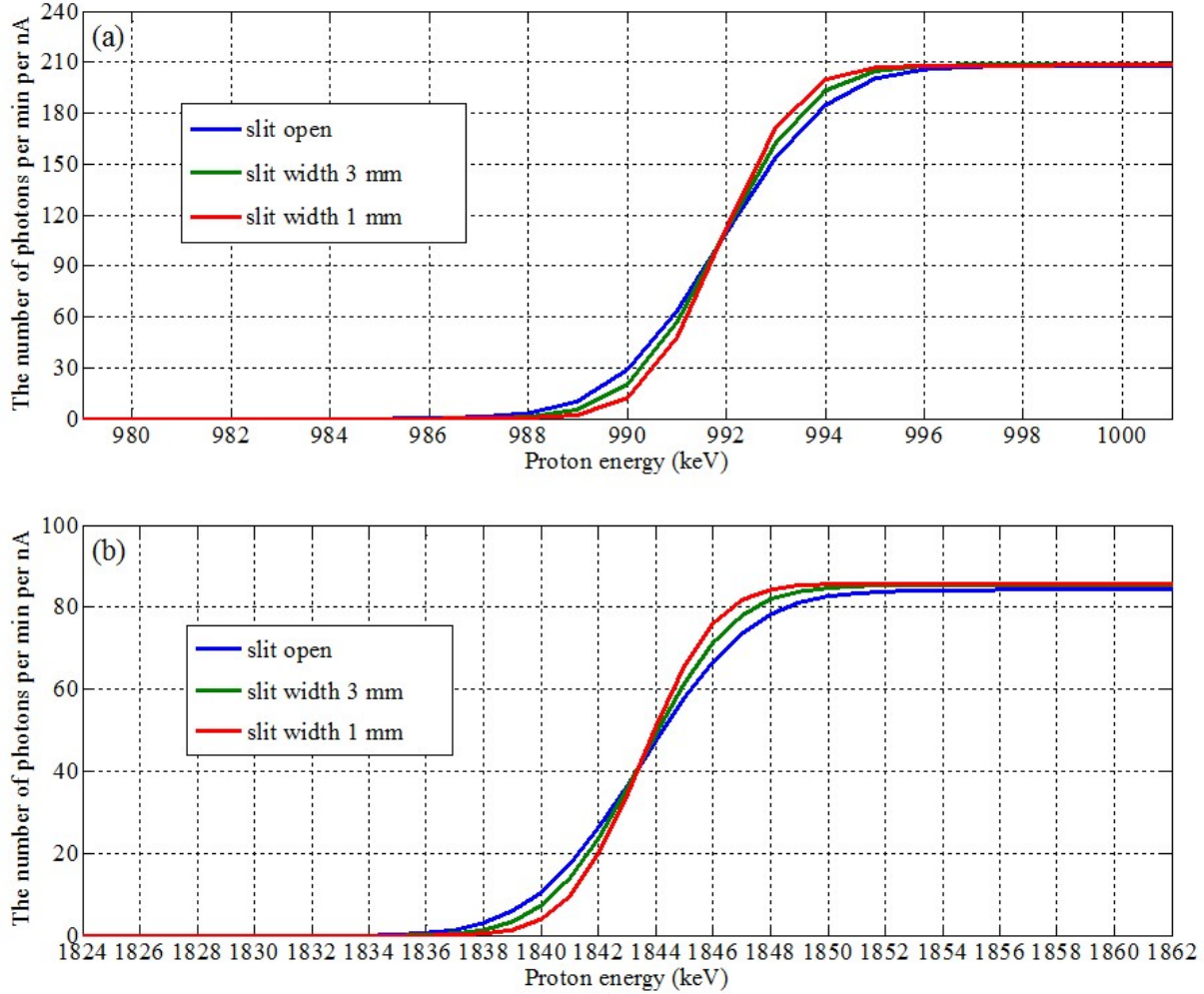


Figure 3.41 Comparison of the fitted resonance yield curves with various horizontal slit width in the diagnostic station 15 for (a)  $^{27}\text{Al}(p,\gamma)^{28}\text{Si}$  992 keV resonance and (b)  $^{58}\text{Ni}(p,\gamma)^{59}\text{Cu}$  1843 keV resonance in the second part of the beam energy calibration measurements.

shape uniform distribution with its axis in the  $z$  direction (e.g. continuous beam). The initial beam energy and half energy spread were 24 keV and 0.0549 keV with  $\beta_z=0$  and  $\epsilon_z=0$ . The initial transverse emittance in 4RMS determined by the quadrupole scan measurement ( more detail in Section 3.1.3.1 ) was  $\epsilon_x=6.6$  mm.mrad and  $\epsilon_y=18$  mm.mrad, with  $\alpha_x=-4.68$  and  $\beta_x=3.6$  mm/mrad and  $\alpha_y=0.12$  and  $\beta_y=0.46$  mm/mrad. Misalignment and operation errors as well as a vertical kick induced by a SRF quarter wave cavity were not included in the DYNAC simulation. The energy spread on the target was calculated in DYNAC, based on the control system set points of the SRF cavities, solenoids and magnetic quadrupoles in ReA beam line. Table 3.8 and Table 3.9 show a

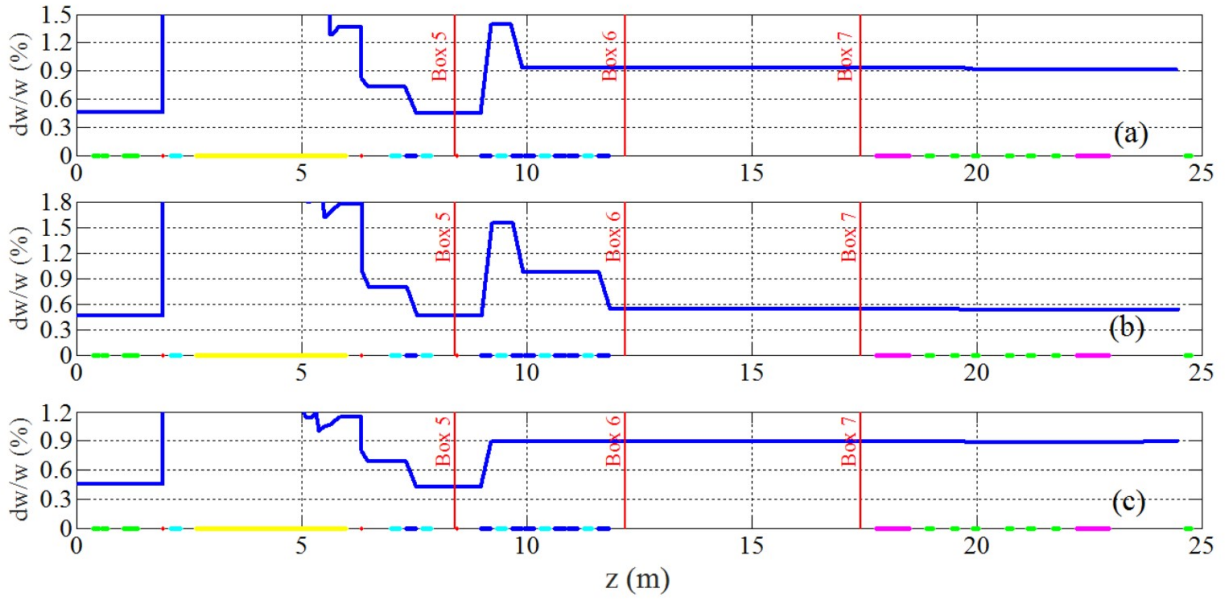


Figure 3.42 Beam energy spread simulation in DYNAC with 95% of the beam particles enclosed for the  $^{27}\text{Al}(p,\gamma)^{28}\text{Si}$  at  $E_p=992$  keV resonance (a) without and (b) with the L091 rebuncher cavity as well as (c) the  $^{27}\text{Al}(p,\gamma)^{28}\text{Si}$  at  $E_p=632$  keV resonance in the first part of the beam energy calibration measurements. The colorful blocks displayed on the horizontal axis represent the beam optical elements, i.e. light green : quadrupole, light blue : solenoid, blue : SRF cavity and pink : bending dipole.

	$^{27}\text{Al}(p,\gamma)^{28}\text{Si}$ 992 keV resonance		$^{27}\text{Al}(p,\gamma)^{28}\text{Si}$ 632 keV resonance
	without the L091 rebuncher	with the L091 rebuncher	
Measurement	<b>0.92</b> + 0.12/-0.11	<b>0.63</b> + 0.24/-0.15	<b>0.80</b> ± 0.14
Simulation	<b>0.91</b>	<b>0.53</b>	<b>0.89</b>

Table 3.8 Comparison of the measurement and DYNAC simulation for beam energy spread (in %) with 95% of the beam particles enclosed in the first part of the beam energy calibration measurements.

good agreement, within the experimental uncertainty, between DYNAC simulation and the measurements in the first and second parts of the beam energy calibration measurements. Figure 3.42 and Figure 3.43 illustrate the simulated beam energy spread from the LEBT to the target location in the first and second parts of the beam energy calibration measurements, respectively.

The beam energy spread on target can be reduced either by modifying ReA3 linac settings or by using a horizontal slit on a dispersive plane of the bending achromatic system (at the expense

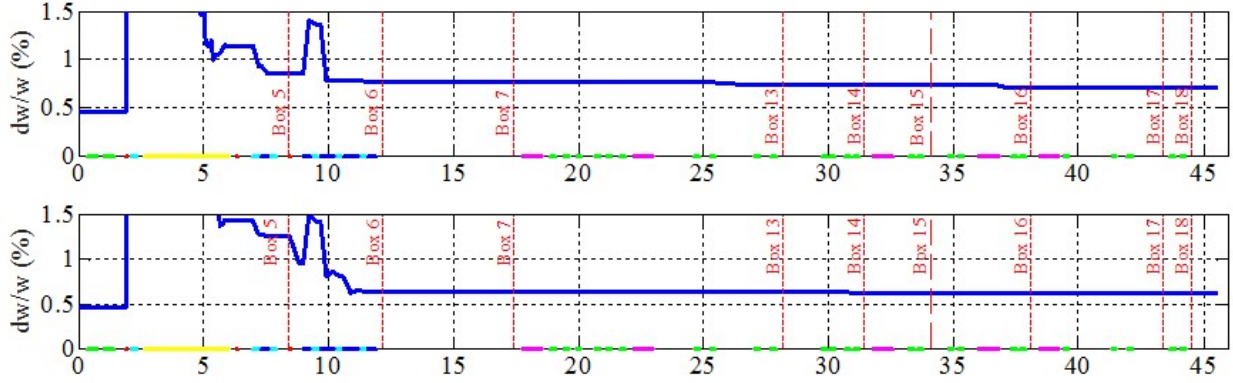


Figure 3.43 Beam energy spread simulation in DYNAC with 95% of the beam particles enclosed for (upper panel) the  $^{27}\text{Al}(p,\gamma)^{28}\text{Si}$  at  $E_p=992$  keV resonance and (lower panel) the  $^{58}\text{Ni}(p,\gamma)^{59}\text{Cu}$  at  $E_p=1843$  keV resonance in the second part of the beam energy calibration measurements. The horizontal slit in diagnostic station 15 was fully open. The colorful blocks displayed on the horizontal axis represent the beam optical elements, i.e. light green : quadrupole, light blue : solenoid, blue : SRF cavity and pink : bending dipole.

Reaction	Slit condition	Measurement	Simulation
$^{27}\text{Al}(p,\gamma)^{28}\text{Si}$ 992 keV resonance	Slit open	$0.69 + 0.10/-0.08$	<b>0.71</b>
$^{58}\text{Ni}(p,\gamma)^{59}\text{Cu}$ 1843 keV resonance	Slit open	$0.66 + 0.09/-0.08$	<b>0.64</b>

Table 3.9 Comparison of the measurement and DYNAC simulation for beam energy spread (in %) with 95% of the beam particles enclosed when the horizontal slit in the diagnostic station 15 was fully open.

of beam intensity on target). During the measurement of  $^{27}\text{Al}(p,\gamma)^{28}\text{Si}$  at  $E_p=992$  keV resonance in the first part of the beam energy calibration measurements, the first two SRF cavities (L082 and L084 cavities) in CM2 were used for acceleration and the last cavity (L091 cavity) was adjusted in the rebuncher mode, as shown in Table 3.2, creating a sufficient drift between L084 and L091 cavities for rebunching the ion beams. Figure 3.42 (a) and (b) illustrate the simulated comparison of beam energy spread changes after the ReA3 linac while the L091 cavity was tuned off and on as a rebuncher. The results from the DYNAC simulation and measurement both show a good agreement that using one of SRF cavities in CM2 as a rebuncher can achieve a reduction of the beam energy spread by 30 ~ 40%. During the (p,γ) measurement in the second part of the beam energy calibration, the horizontal 90° bending achromat was used to limit the beam energy spread

using the horizontal slit placed in the dispersive image of the third bending magnet. In principle, the r.m.s horizontal beam size on the slit location in the bending achromatic system is affected by the horizontal  $\beta$  function on the slit location and the horizontal dispersion function  $\eta$ , based on the formula

$$\sigma_x = \sqrt{\beta_x \varepsilon_x + (\eta \cdot \delta)^2} \quad (3.23)$$

where  $\varepsilon_x$  is the horizontal r.m.s emittance and  $\delta (= \frac{\Delta p}{p})$  is the relative momentum deviation. According to Equation 3.23, one way to reduce the energy spread in a linac is the adjustment of the slit gap in the bending achromatic system. Figure 3.44 displays one example of the beam energy spread versus the horizontal position distribution on the location of the horizontal slit in the bending achromatic system for the optimized beam tune of  $^{58}\text{Ni}(p,\gamma)^{59}\text{Cu}$  at  $E_p = 1843$  keV resonance experiment. The optics of the bending achromatic system is designed to minimize the horizontal  $\beta$  function in such a way that the horizontal beam size on the slit location mainly depends on the energy spread. In the ideal beam tune for  $^{58}\text{Ni}(p,\gamma)^{59}\text{Cu}$  1843 keV resonance experiment, the high dispersion on the slit location can lead to a reduction of beam energy spread by  $\sim 35\%$  for the 3-mm slit gap and  $\sim 60\%$  for 1-mm slit gap. In this simulation case, the beam transmission through the slit is 65 % for 3-mm slit gap and 23 % for 1-mm slit gap. However, based on the measurement result shown in Table 3.7, the ReA3 linac delivered a beam with an energy spread of  $0.65 \sim 0.7\%$  (95 % of the beam particles) for the two  $(p,\gamma)$  experiments in the second part of the beam energy calibration measurements. The use of the horizontal slit with 3 mm gap and 1 mm gap resulted in a reduction of the beam energy spread by about 17% and 30% while the beam transmission passing through the slit was approximately 50% and 20%. There is a discrepancy of the reduction values of energy spread with 3-mm and 1-mm slit gaps between the measurement and simulation. This difference may be due to the fact that the real beam tune could not achieve the optimized values of the horizontal  $\beta$  function and emittance on the slit location. The beam tune on the four magnetic quadrupoles between the diagnostic station 13 and the third bending dipole plays a critical rule in optimizing high dispersion on the slit location and still needs to be improved.

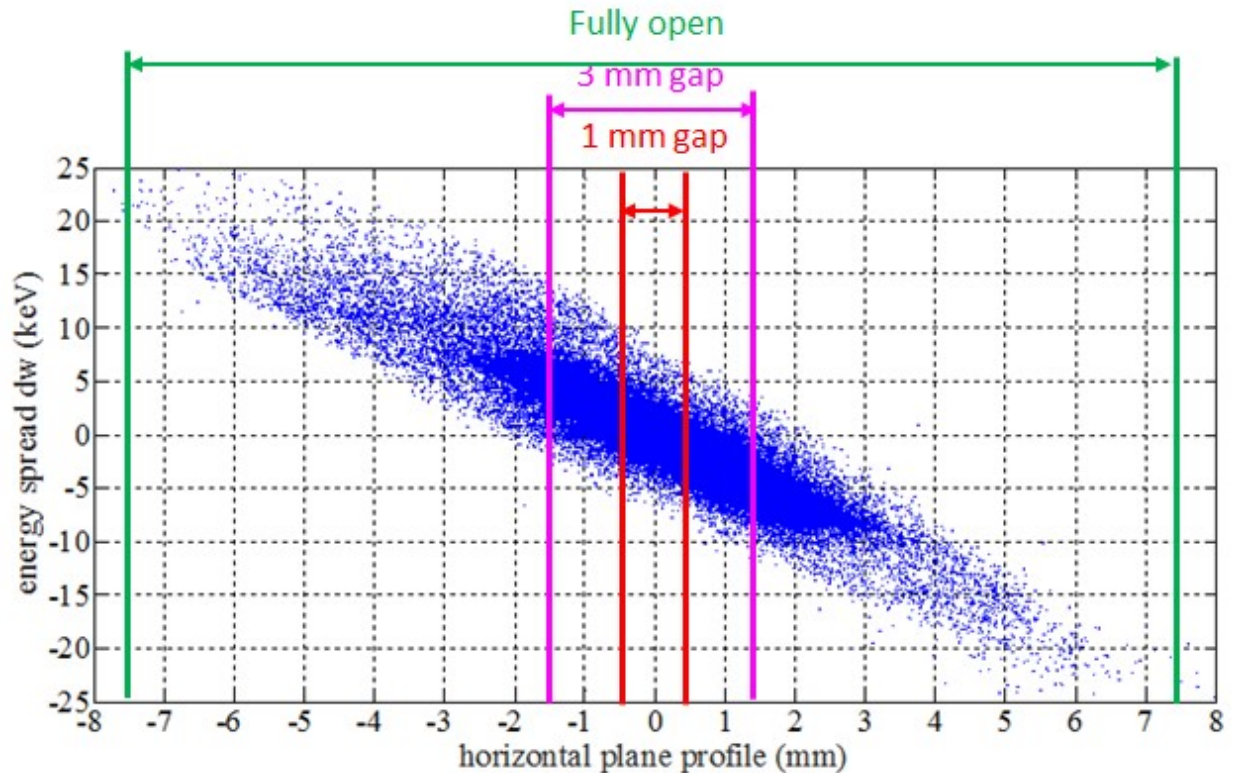


Figure 3.44 DYNAC beam simulation for the optimized beam tune of  $^{58}\text{Ni}(p,\gamma)^{59}\text{Cu}$  at  $E_p=1843$  keV resonance experiment in the location of the diagnostic station 15.

### 3.2 Time-of-flight measurements

Compared with the use of  $(p,\gamma)$  resonances, the time-of-flight (TOF) technique is a relatively quick method to calibrate the magnetic analyzer and measure absolute beam energy. Velocities of ion beams can be measured by determining the TOF of beam bunches between two identical secondary electron emission monitors (grid-MCP detectors) with appropriate separation, as illustrated in Figure 3.45. As shown in the schematic diagram, several bunches travel between the two timing detectors. It should be noticed that in the TOF measurements presented here, the time signals registered from the two detectors do not originate from the same beam particles. The arrival time of beam bunches at the two detectors are simultaneously measured but independent. Both time measurements of beam bunches from the two detectors are compared with the RF clock. With the use of the  $45^\circ$  magnetic analyzer, the integer number  $n$  of beam bunches between the two detectors

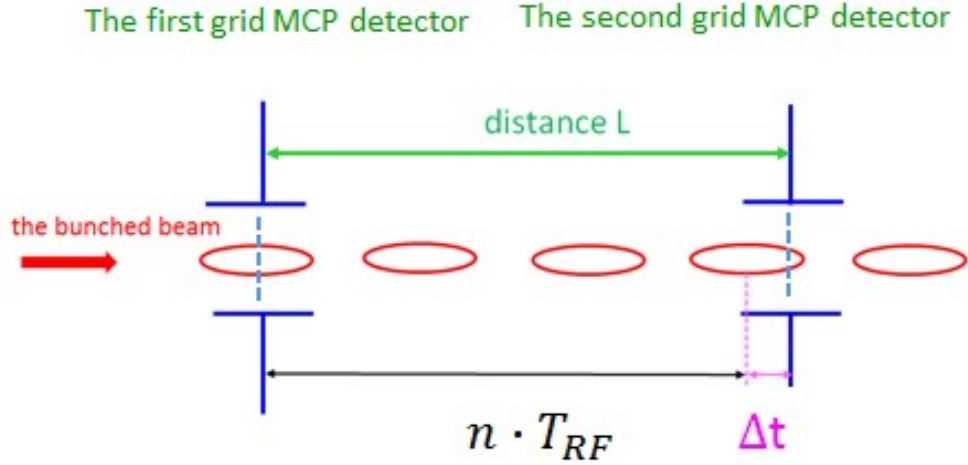


Figure 3.45 Principle of a time-of-flight measurement using two grid-MCP detectors. A dash blue line represents a mesh (grid) in a detector.

is known. The flight time of the bunched beam from the first detector to the second detector is

$$t_{TOF} = n \cdot T_{RF} + \Delta t + t_0 \quad (3.24)$$

where  $T_{RF}$  is the RF period and  $t_0$  is the time off-set of the system due to the different length of the signal cables of the two detectors. The  $\Delta t$  is smaller than a RF period, which represents the arrival time difference of beam bunches at the two detectors with respect to the RF signals. The  $\Delta t$  can be obtained from the timing spectra of the two grid-MCP detectors.

Therefore, the beam energy can be calculated from the relation

$$E = \frac{m}{2} \cdot \left( \frac{L}{n \cdot T_{RF} + \Delta t + t_0} \right)^2 \quad (3.25)$$

where  $L$  is the distance between the two detectors and  $m$  is the mass of one beam particle.

In the next section, I present the mechanical design and time-resolution simulation of a grid-MCP detector (Section 3.2.1). I also describe the experimental setup and procedure for the TOF measurements in Section 3.2.2, along with a discussion of data analysis and result in Section 3.2.3.

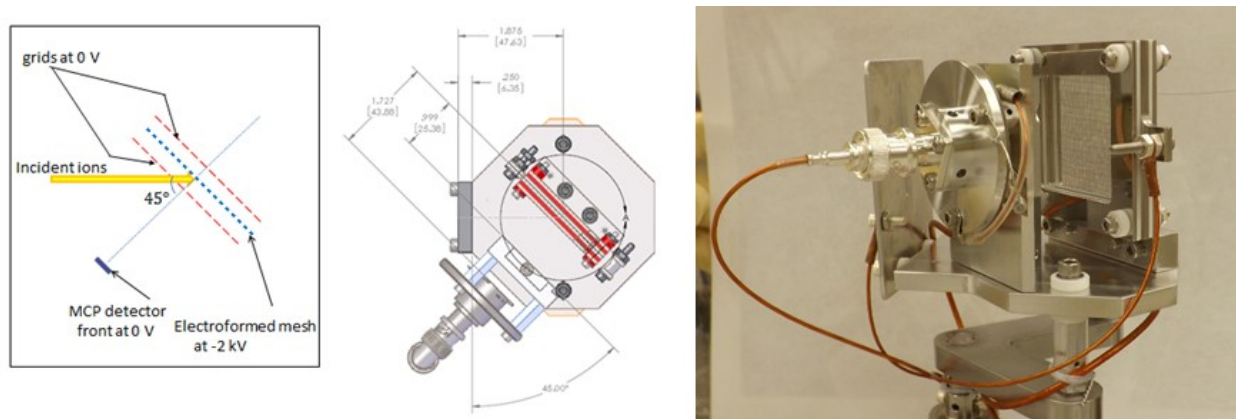


Figure 3.46 A schematic diagram and a picture of a grid-MCP detector. When the incoming beam hit the second mesh at -2 kV, secondary electrons will be emitted from the second mesh at the location of the ion impact and accelerated toward a MCP detector.

### 3.2.1 Time-resolution simulation of a grid-MCP detector

Figure 3.46 shows the schematic layout of a grid-MCP detector designed to acquire timing information of ions impinging on a thin electroformed mesh (grid). The detector consists of three layers of thin electroformed meshes and a micro-channel plate (MCP). The whole assembly of three meshes is tilted at  $45^\circ$  to the beam axis and the MCP is placed far enough away from the meshes so that the incoming beam can pass through unimpeded. The second mesh at high negative voltage is flanked symmetrically by the first and third grounded meshes with an equal spacing of 3.1 mm. The total transparency of three meshes is  $90\% \times 70\% \times 90\% \approx 57\%$ . The dimension for each mesh is  $37.7 \text{ mm} \times 37.7 \text{ mm}$ . The MCP and the nearest mesh are 36.5 mm apart. The MCP surface is 14.5 mm in diameter. When charged particles pass through the first mesh and impact on the second mesh, they transfer part of the kinetic energies to electrons in the second mesh, resulting that some of these electrons migrate to the surface and have sufficient energy to escape from the mesh surface. Therefore, secondary electrons (SEs) are emitted from the second mesh at the location of the ion impact, and are accelerated toward a MCP which is used as a fast electron multiplier. The voltage applied to the second mesh is  $-(1.5 \sim 2) \text{ kV}$  in order to boost the electron velocity and accelerate them toward the MCP. Electron ejection from the second mesh is confined to the limited area where the bombarding ions hit the mesh. In principle, the electrons which are accelerated to-

ward the MCP will be detected. When a secondary electron impacts the input surface of the MCP, it produces one or more secondary electrons. These electrons are subsequently accelerated by the MCP channel electric field and impact the channel wall, consequently producing more secondary electrons. The growing electron avalanche which propagates along the channel is detected at the output of the MCP, providing the timing information for the ion particles bombarding the second mesh.

In order to optimize the detector timing resolution, I investigated the capabilities and limitations of this detector type. In order to obtain some ideas of what limits the detector time resolution, I used SIMION program [ Manura & Dahl (2007)] to measure the transit time of secondary electrons from the second mesh to the MCP surface under several different conditions. SIMION is an electron and ion optics software program used to simulate electron or ion paths in the presence of electric fields. SIMION uses electrostatic potential arrays to define the geometry and potentials of electrodes. The potentials at points in space between the electrodes are calculated by solving the Laplace equation for electric fields with specified boundary conditions. Once the solution has been obtained, ions can be traced within the volume between the electrodes.

For the estimation of the time resolution of the detector, the detector geometric shapes and voltages of electrodes in the SIMION simulation were based on the mechanical design of the detector. The 3D geometric simulation is shown in Figure 3.47

### **3.2.1.1 Consideration of the initial energy and angular distribution of secondary electrons**

Chung and Everhart [ Chung & Everhart (1974)] have derived a semi-empirical theory for the energy distribution of low-energy secondary electrons emitted from metals for a normal incidence angle of bombarding particles:

$$\frac{dN}{dE} \propto \frac{E}{(E + \Phi)^4} \quad (3.26)$$

where  $\Phi$  is the metal work function (for Nickel,  $\Phi = 4.6$  eV). Based on the Equation 3.26, the most probable energy of the secondary electrons is 1.52 eV for a Nickel mesh.

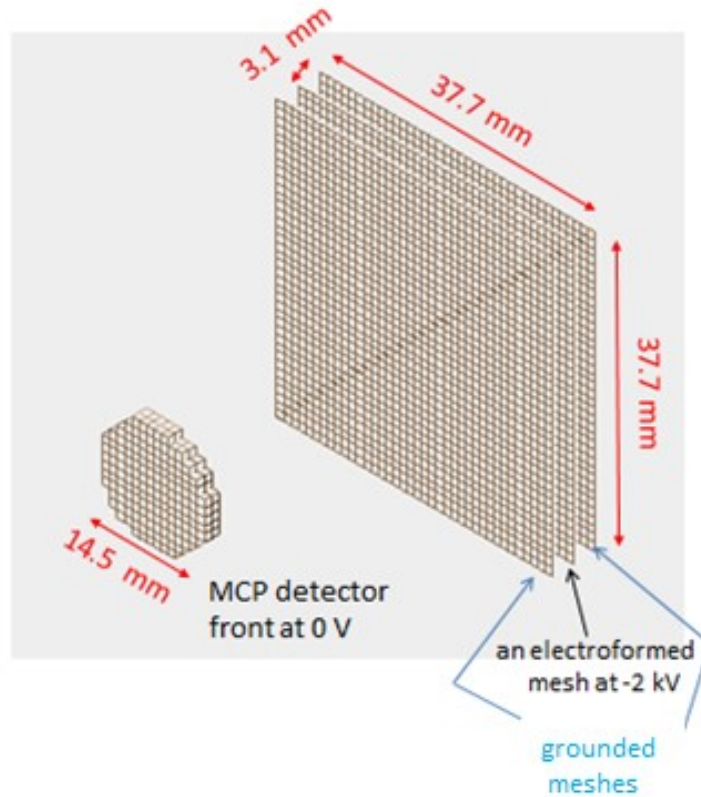


Figure 3.47 The timing detector as modeled in the SIMION program. The distance between the second mesh at -2kV and one of the grounded meshes is 3.1 mm. The MCP detector is 14.5 mm in diameter. The dimensions for the surfaces of these meshes are 37.7 mm  $\times$  37.7 mm.

The angular distributions of secondary electrons produced by ion bombardment have been measured in some experiments [ Krebs (1968)]. From those previous experimental results, the total number of emitted electrons as a function of the polar ejection angle  $\theta_e$  can be approximated by the expression  $C \cdot \cos \theta_e$ . The isotropic cosine distribution is independent of the incident direction of bombarding particles. For the initial angular condition of ejected SEs in SIMION, the ejected polar angle is set to be a cosine distribution in a such way that the maximum of emitted electron number corresponds to the ejection direction perpendicular to the mesh. If all the electrons are emitted from the mesh at the same time with a cosine ejected angular distribution and a specific initial energy distribution obtained by the Equation 3.26, the simulated time-of-flight spectrum of SEs from the mesh to MCP plane is shown in Figure 3.48. The time resolution of time-of-flight spectrum can be estimated by fitting the peak with a Gaussian distribution. The 12 ps of time

Simulated time-of-flight spectrum of SEs from the mesh to MCP plane

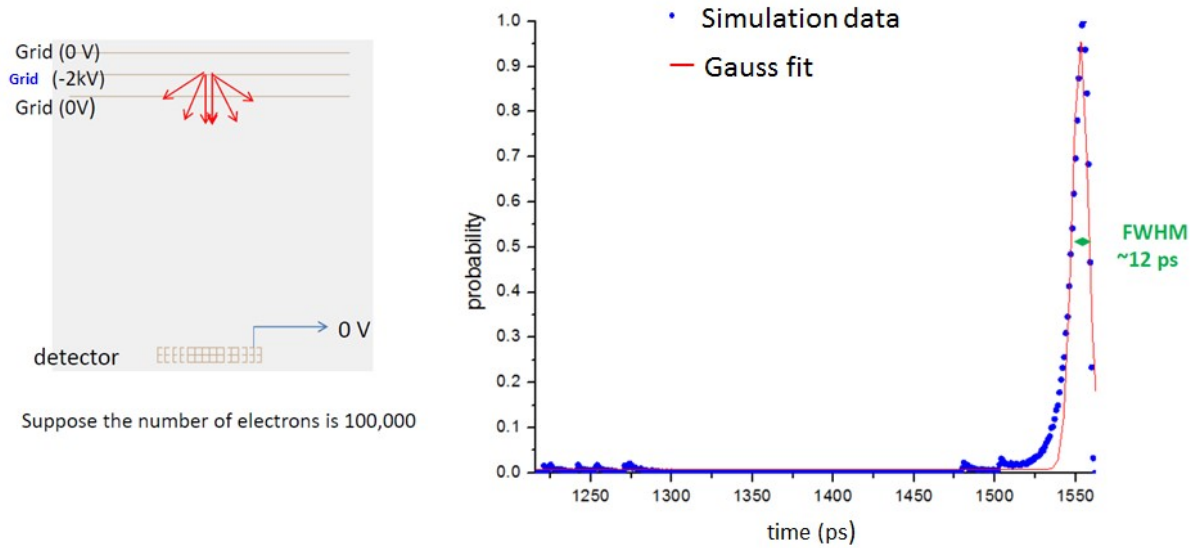


Figure 3.48 Left: The sketch for measuring the time of flight for electrons with a cosine distribution of ejected angles. Right: The corresponding simulated TOF spectrum of electrons by assuming that electrons are emitted from the mesh at the same time with a cosine ejected angular distribution and a specific initial energy distribution. The time resolution (FWHM) of the TOF spectrum due to the initial energy and angular distributions of secondary electrons is about 12 ps.

resolution (FWHM) caused by the initial angular and energy distributions of ejected secondary electrons is very small.

### 3.2.1.2 Consideration of the 45 degree incident angle of the bombarding ions

The inclination of the mesh relative to the direction of the incident ions is an essential factor which constrains the detector resolution. Assuming that the incident ions in the simulation are alpha particles with a filled circular beam profile of 5 mm diameter and that these bombarding particles arrive the entrance of the detector chamber at the same time, each particle hits the mesh at different time and position of the mesh because of the 45° incident angle. The simulated time-of-flight spectrum for 1.2 MeV alpha particles is shown in Figure 3.49. . The time interval between the start signal when particles go through the detector chamber entrance and the stop signal when particles hit the mesh is plotted. The decrease in the number of alpha particles with the shorter or longer time of flight is due to the fact that the outer edge of the beam containing fewer particles

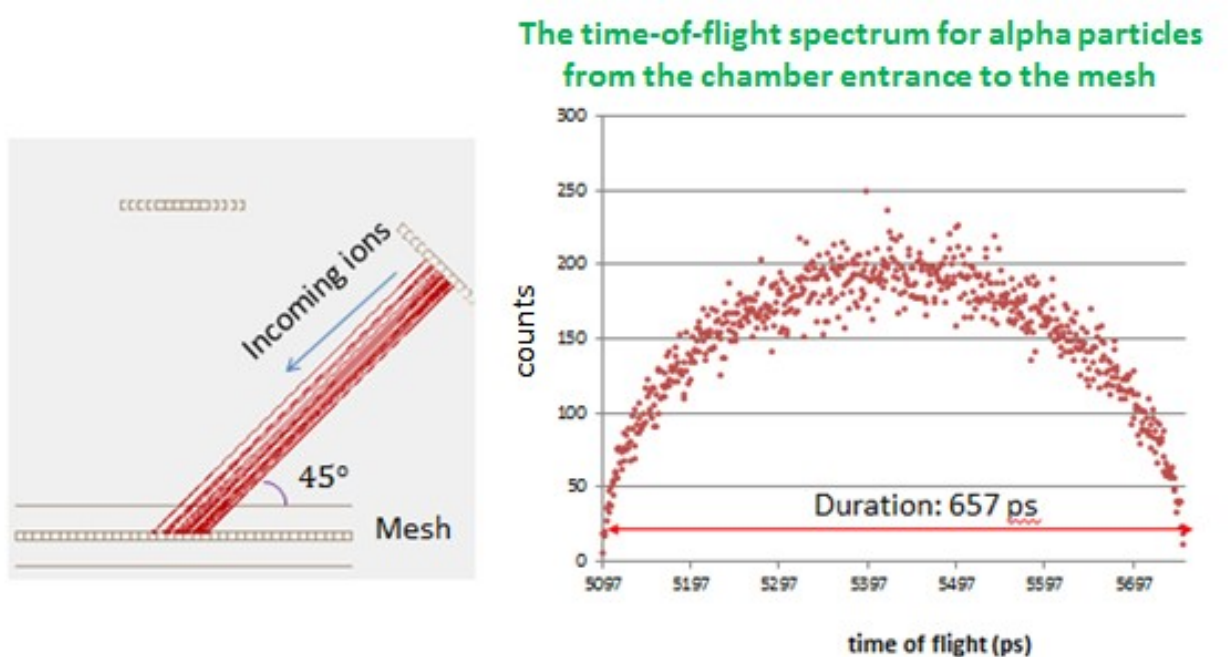


Figure 3.49 Left: The sketch for measuring the trajectory of incoming ions. Right: the simulated TOF spectrum of incoming alpha particles with the  $45^\circ$  incident angle.

hits the mesh. The duration between shortest and longest time of flight for alpha particles is about 657 ps, which is mainly determined by the velocities, incident angle and the beam diameter.

It is assumed that the time difference between the impinging of incoming ions and the emerging of secondary electrons ejected by bombarding ions is very small, compared with the time resolution of the detector. This time difference is neglected. Each bombarding ion with the energy 1.2 MeV generates approximately one secondary electron on average [ Sternglass (1957)]. Hence, the TOF probability distribution of incoming alpha particles shown in Figure 3.49 is translated to the time-of-birth (TOB) probability distribution of secondary electrons. The TOF spectrum of SEs from the mesh to the MCP plate in Figure 3.50 is obtained by combining the TOB probability distribution of SEs with the TOF spectrum of SEs assuming that the TOB is equal to 0 (shown in Figure 3.48). The full width at half maximum of SE TOF spectrum in Figure 3.50 is approximately 559 ps. The time resolution (FWHM) deteriorates with increasing beam diameter or incident angle of bombarding particles. Low velocities of bombarding ions also worsen the time resolution.

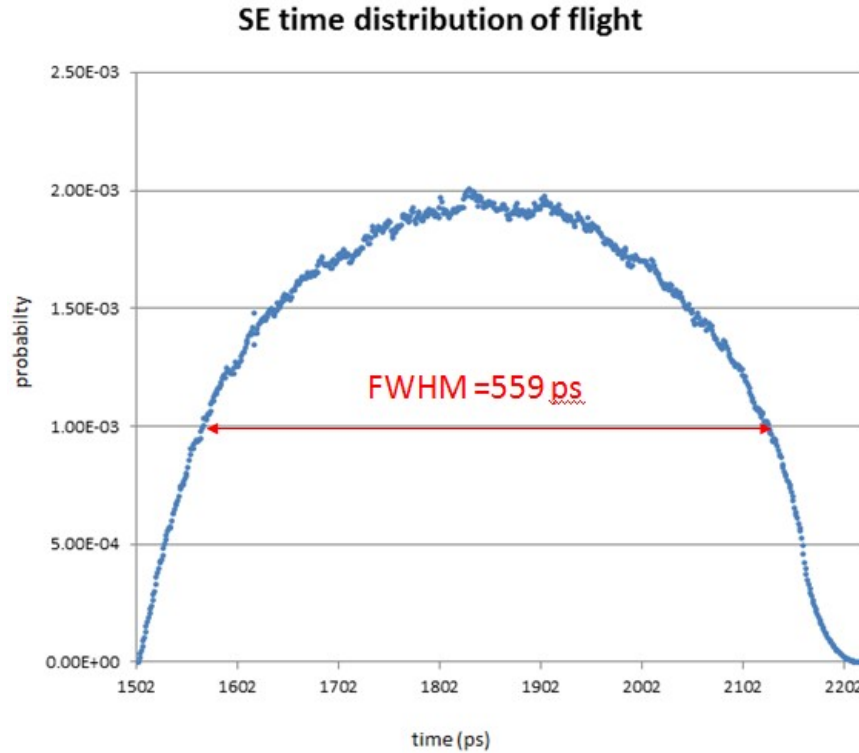


Figure 3.50 A simulated TOF spectrum of secondary electrons generated by the 1.2 MeV incoming alpha particles at the incident angle  $45^\circ$ .

### 3.2.1.3 Consideration of beam bunch length

I consider that the ion beam is well bunched and the incoming particle distribution at one bunch can be described by a Gaussian distribution. Therefore, the ion particles of one bunch pass through the entrance of the detector chamber at different time. When 1.2 MeV alpha particles impinge on the mesh and create ejected secondary electrons, the TOF spectra of SEs from the mesh to the MCP plate is simulated for the beam bunch length 200 ps (FWHM) in Figure 3.51 (a) and 500 ps in Figure 3.51 (b). By fitting the peaks in Figure 3.51 with a Gaussian, the FWHM of SE TOF spectra is about 495 ps for beam bunch length 200 ps and 660 ps for beam bunch length 500 ps. The time resolution (FWHM) of electron TOF spectra is constrained by the effect of the  $45^\circ$  inclination of the mesh, resulting in the time resolution of the detector much larger than the actual beam bunch length.

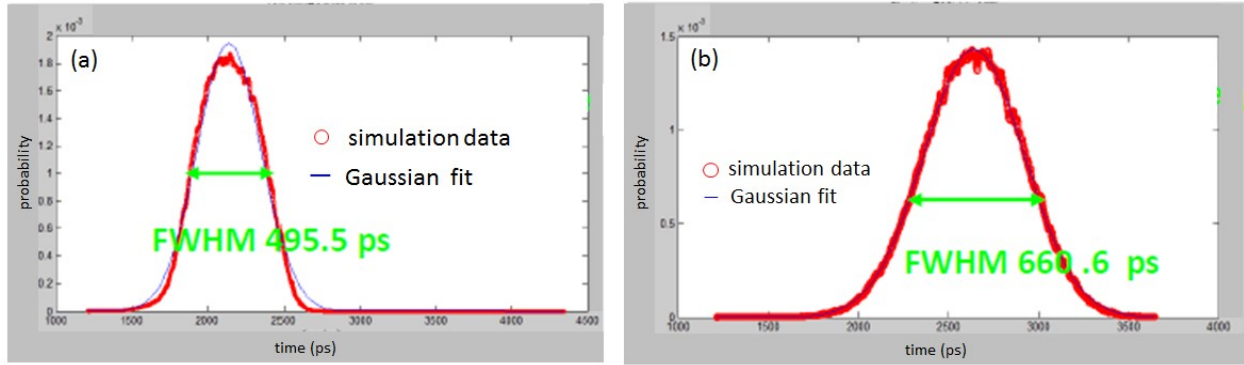


Figure 3.51 The TOF spectra of secondary electrons generated by the 1.2 MeV incoming alpha particles at the incident angle 45 degree with (a) the beam bunch length 200 ps (FWHM) and (b) the beam bunch length 500 ps (FWHM).

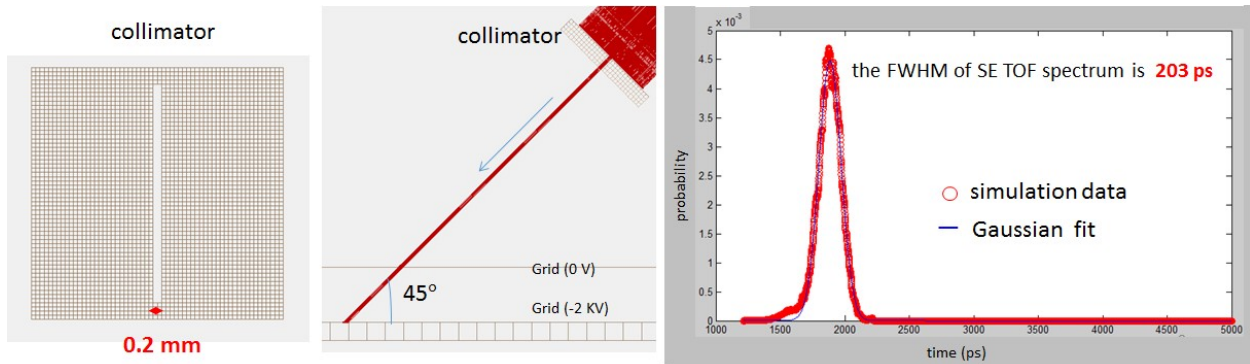


Figure 3.52 Left: The collimator in front of the mesh. Middle: The sketch for measuring the trajectory of incoming ions. Right: The corresponding simulated TOF spectrum of secondary electrons from the mesh to the MCP plate.

### 3.2.1.4 A Method for time-resolution improvement of a grid-MCP detector

Based on the previous discussion, the inclination of the mesh plays a role in deteriorating the time resolution of the detector. However, by installing a narrow collimator in front of the mesh, better detector time resolution can be achieved. If the incoming beam particles pass through a narrow collimator, the area of the ion impact on the mesh can be reduced, limiting the influence of 45° mesh inclination on the time resolution (FWHM) of secondary electron TOF spectra. In my simulation, I assume that the 1.2 MeV alpha particles with the beam bunch length 200 ps and a beam diameter of 5 mm pass through a collimator with the width of 0.2 mm, as shown in Figure 3.52. The time resolution (FWHM) of electron TOF spectrum is about 203 ps, which is very close

to the beam bunch length. As we can see, the use of the collimator can improve the detector time resolution. However, the loss of the SE yield due to the reduced bombarding particles onto the mesh needs to be compensated with the gain of the MCP.

### **3.2.2 Experimental setup**

#### **3.2.2.1 Detector hardware**

Figure 3.46 (right) shows the prototype of a grid-MCP timing detector which adds a collimator with the width of 1 mm in front of the three Nickel meshes. The collimator is used to improve the detector time resolution (more discussion in Section 3.2.1.4). The timing signal of the ejected secondary electrons from the second mesh is read by a fast micro-channel plate (MCP) Hamamatsu F4655-12. The MCP detector consists of a 2-dimensional array of many parallel microscopic capillaries or channels. When an electron enters one of the channels of the detector and strikes the inside wall of the channel, a large number of secondary electrons are emitted from the channel wall. These secondary electrons are accelerated along the channel due to a strong potential difference of the order of a kV applied across the front and rear sides of the channel. The incoming electron can create an avalanche of secondary electrons while traveling along its trajectories inside the channel. Eventually, a cloud of secondary electrons is released from the rear of the channel and collected on the single anode of the detector for the signal readout. Typically 1500 ~ 2000 V is applied to the rear of the MCP (the MCP exit) while the MCP input side is at ground potential, as shown in Figure 3.53. An additional 500 volts is applied between the MCP exit and the anode to direct the output secondary electron cloud to the collection anode.

The leading edge of a pulse signal from the MCP is detected by a VME-based V812 Constant Fraction Discriminator (CFD) by CAEN to determine if a hit has occurred. Two outputs from the CFD are generated. One output goes to a CAEN V1290A Time-to-Digital Converter (TDC). The V1290A module digitizes the timing information of a pulse signal with a resolution of 25 ps and passes it to the VM-USB module. The other output from the CFD is sent to a JTEC XLM universal

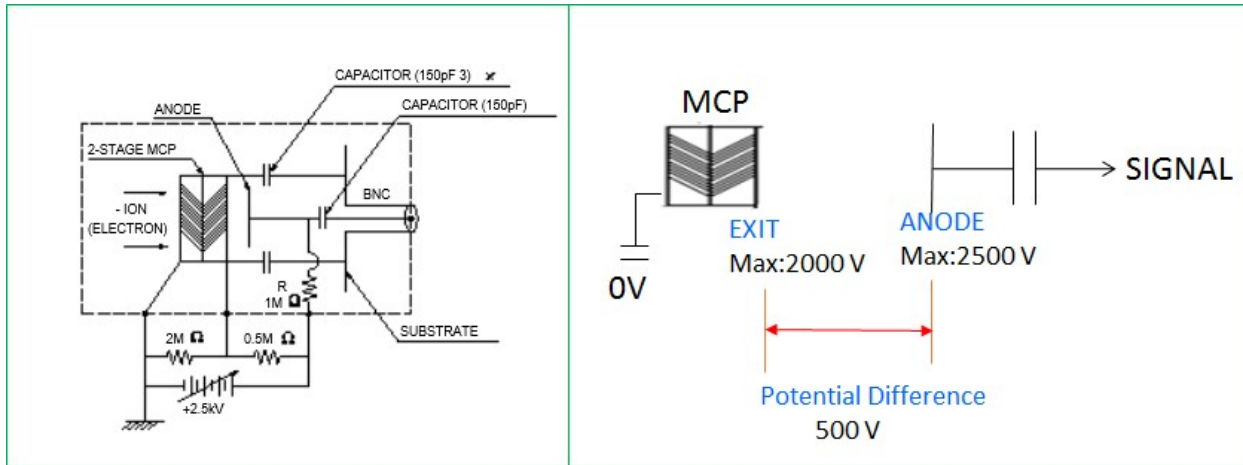


Figure 3.53 Schematic diagrams of a fast micro-channel plate (MCP) Hamamatsu F4655-12.

logic module (XLM72) and turned into a logic pulse. This logic pulse is used to trigger the VM-USB module. The VM-USB is an FPGA based intelligent readout system to collect the data from the V1290A module and then transfers the data to a host computer at full USB-2 data rates. The VM-USB can initialize, configure or query the other modules (i.e. the V1290A TDC, the XLM72 and the CFD) in the VME crate through the user's instructions. In principle, the VM-USB serves as a gateway to the other modules in the VME crate.

### 3.2.2.2 Detector software implementation

The VM-USB is connected to the host computer (name: spdaq32) via a USB cable. The detector readout is processed through the NSCL data acquisition system (NSCLDAQ). The NSCLDAQ provides predefined classes which are specific to the individual modules in the VME crate. All the user's instructions for initializing, configuring or querying the modules in the VME crate are stored in the Tcl/Tk configuration files that interact with the specific classes of these modules. The NSCL Readout software (ReadoutShell) in Figure 3.54 executes the Tcl/Tk configuration files of the VME-modules and provides the interface between the VME-modules and the user. The ReadoutShell program is responsible for data readout from the VM-USB and the control of the modules. The data readout in the ReadoutShell during an experiment run can be timed and

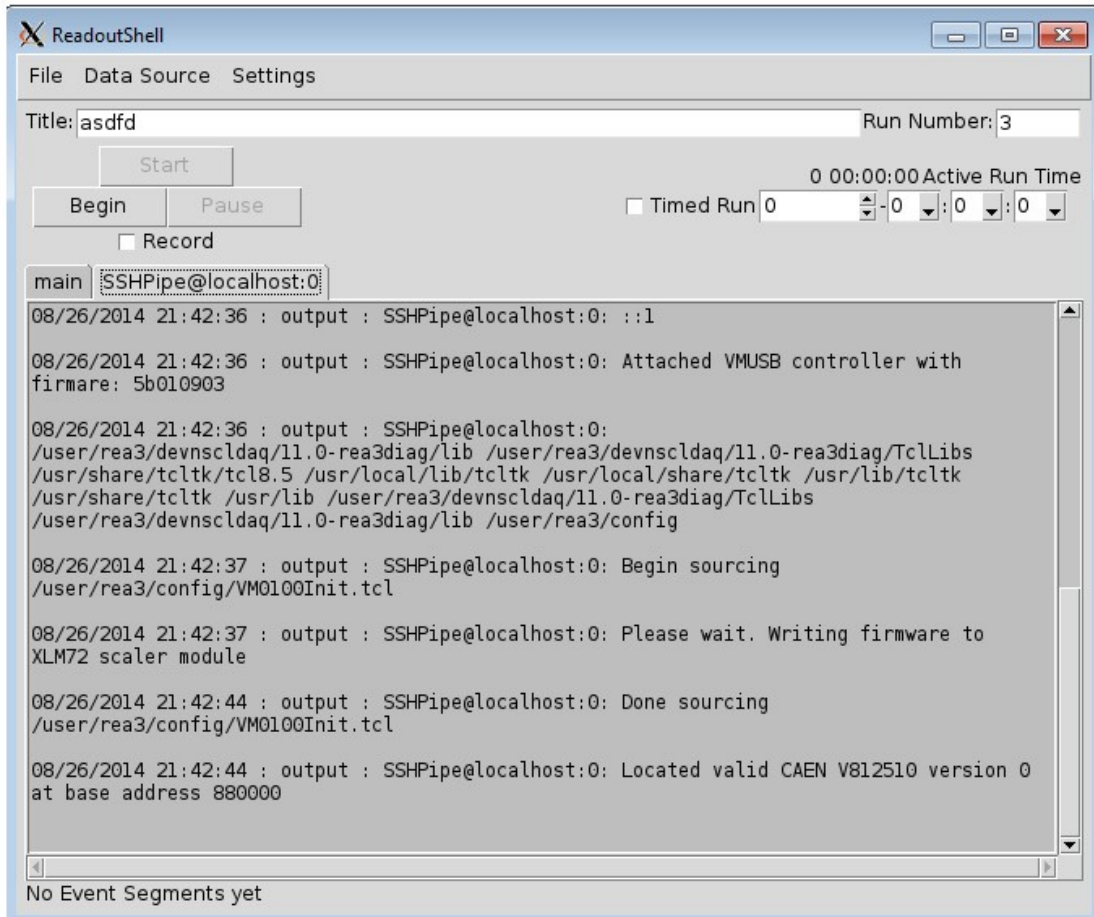


Figure 3.54 The ReadoutShell program is responsible for data readout of a grid-MCP detector.

terminated at any time. The ReadoutShell allows the user to save the recorded data or view it online.

Before starting an experimental run, the CFD threshold settings for the grid-MCP detectors are adjusted via the ACAENV812 CFD GUI (Figure 3.55 (left)). In addition, the trigger events for each detector are counted in the XLM72 running 32-channel scaler. The individual rates of the detectors are displayed in the AXLM72Scaler Control Panel (Figure 3.55 (right)) designed by Jeromy Tompkins for beam tuning purpose.

During an experimental run, the recorded data from the ReadoutShell is viewed online via the SpecTcl program. SpecTcl is a powerful NSCL histogramming program. The spectra of several timing detectors can be displayed in one panel. SpecTcl consists of four windows listed in Table

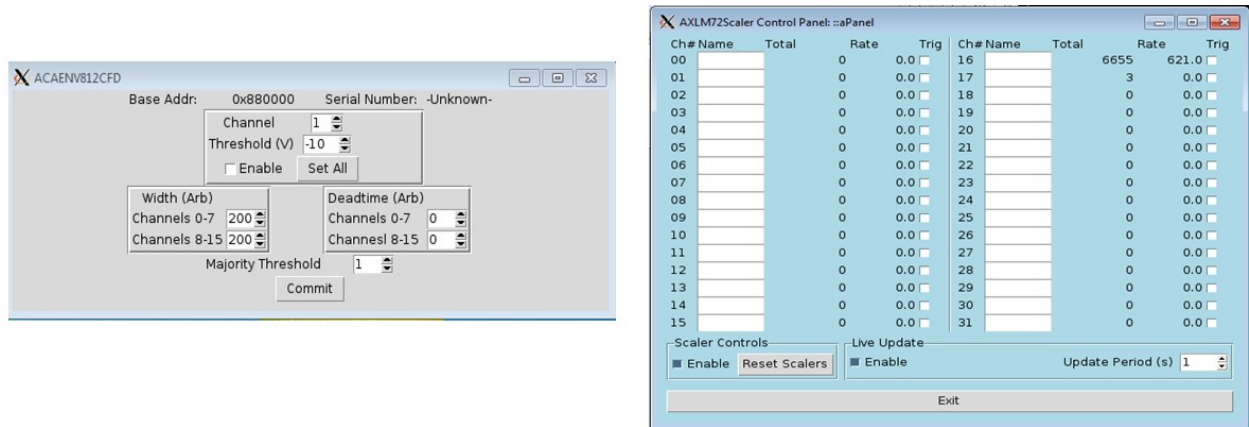


Figure 3.55 Left: The V812 CFD GUI for the timing detectors. Right: the XLM72 Scaler Control Panel.

Window	Description
treogui	Definition of spectra
Xamine	Display of spectra
SpecTcl	Control window for clearing spectra and SpecTcl exit
TKCon	Console to run a user-defined command to save recorded spectra

Table 3.10 Four SpecTcl windows.

3.10 and shown in Figure 3.56. Xamine is capable of displaying multiple spectra from different timing detectors at once, as shown in Figure 3.57. Xamine provides automatic data update function, zoom in/out and integrate function with user defined borders. The integrate function allows the user to estimate peak centers and widths. For each timing detector, the electron pulse arrival time is compared with the RF timing signal (80.5 MHz). The time difference between the signal arrival time of a detector and the RF clock is filled into a histogram. A resulting histogram (spectrum) can be saved in a NSCL ASCII formatted file for off-line analysis.

### 3.2.2.3 Beam transport

Two identical grid-MCP detectors were installed in the diagnostic station 10 and 13 with a separation distance of  $\sim 8$  m, as shown in Figure 1.3, for the time-of-flight measurements. The  $H_2^+$  stable pilot beam from the off-line injector ion source was accelerated by the RFQ and the QWR cavities of the second cryomodule. A parallel beam through the long drift in the CM3 was main-

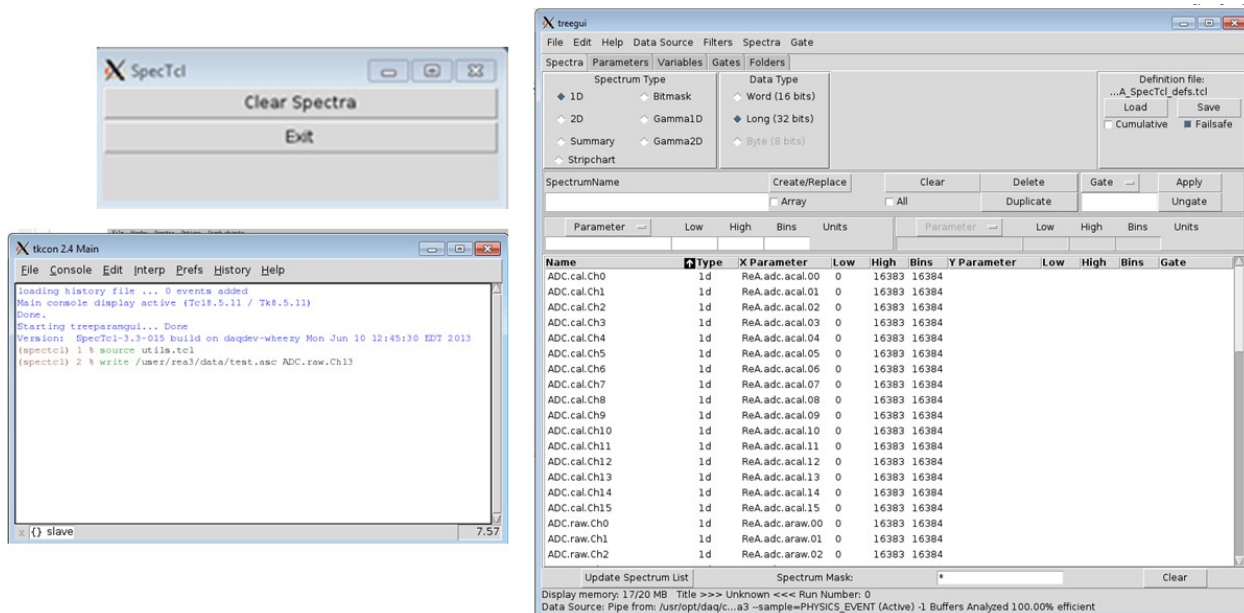


Figure 3.56 SpecTcl, TKCon, Tregui windows in the SpecTcl program

tained by centering the beam at the two apertures in the diagnostic stations 6 and 7 and delivered through the 45° magnetic analyzer in the S-bend beam line. After the beam passed through the magnetic analyzer, the vertical centroid position of the beam was verified on the beam axis by using the vertical slit in the diagnostic station 9. In the end, the ion beam was delivered to the detector stations. The four beam energies at 600 keV, 992 keV, 1400 keV and 2100 keV were performed for the TOF measurements. The TOF measurements at the beam energies of 992 keV/u and 600 keV/u were used for TOF calibration. The 600 keV/u energy is the RFQ output energy which has been verified previously and is independent of the RFQ tuning. The 992 keV/u energy can be precisely achieved by the 45° magnetic analyzer since the magnetic analyzer has been well calibrated around the energy region of 992 keV/u with the use of  $^{27}\text{Al}(p,\gamma)^{28}\text{Si}$  at  $E_p = 992$  keV resonance by the SuN detector. The TOF energy measurements at 1400 keV/u and 2100 keV/u were utilized to calibrate the 45° magnetic analyzer at these two energy regions. In order to minimize the damage on the MCP caused by secondary electron fluxes, the beam current of few nA was used for the experiments.

The structure of  $\text{H}_2^+$  ion beam was well bunched with desired bunch lengths in the detector locations by using the Multi-Harmonic Buncher (MHB), the RFQ and the rebuncher cavity in

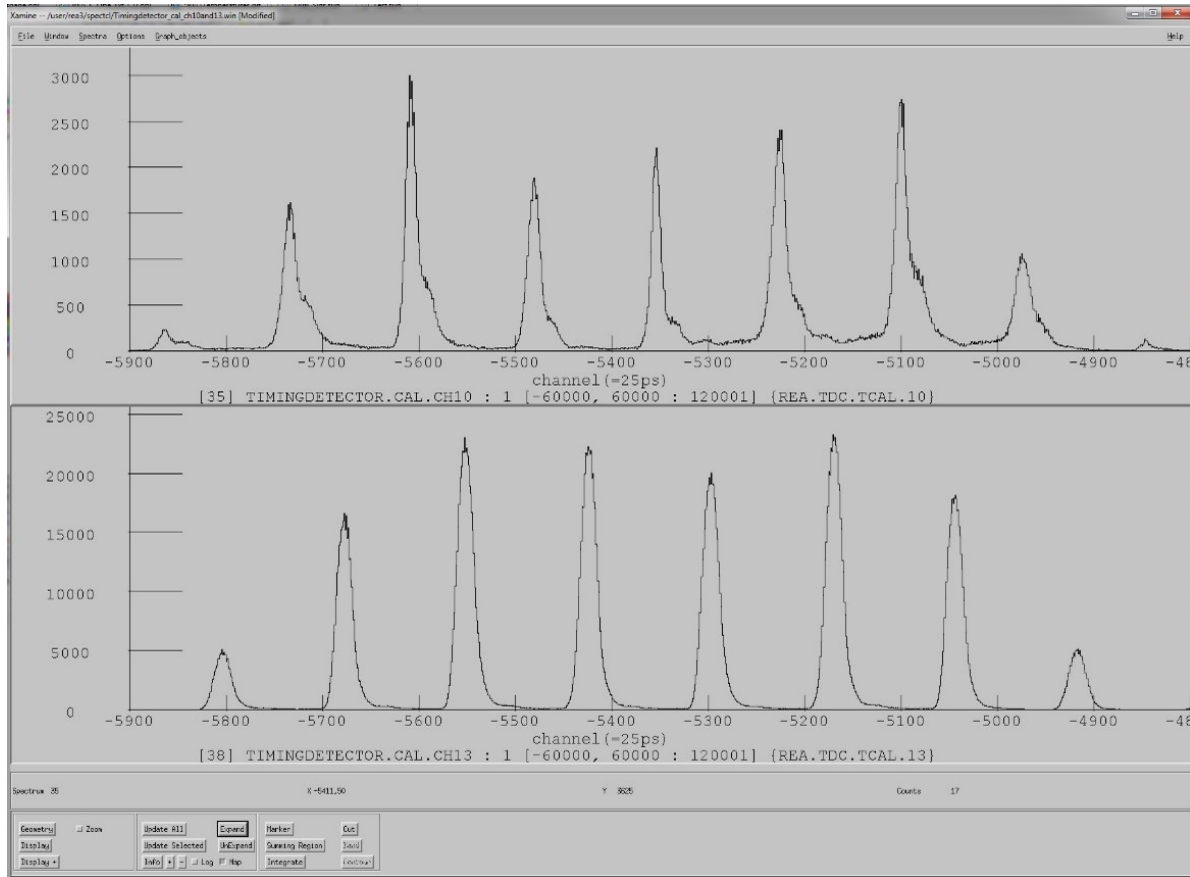


Figure 3.57 Xamine window in the SpecTcl program. The spectra of two grid-MCP detectors for TOF measurements is displayed as an example. The upper spectrum is the first timing detector in the diagnostic station 10 while the lower spectrum is the second detector in the diagnostic station 13.

the first cryomodule. Each bunch of the ion beam was separated by 12.42 nsec (RF period) and traveled through these two timing detectors. When one of beam bunches passed through the first timing detector, a small fraction of this bunch was intercepted by the second mesh of this detector, producing ejected secondary electrons which were rapidly accelerated toward the MCP. Another fraction of the same bunch passed through the first detector and was detected by the second timing detector. The arrival time of the bunched beam signal on the first and second timing detectors was simultaneously measured with the V1290A TDC by sending the RF timing signal to one of the TDC channels. Data was accumulated over several minutes (and integrated over many bunches) to achieve sufficient counts. A histogram of the bunched beam arrival time with respect to the RF clock was obtained in SpecTcl for each detector, representing the bunch shapes in real-time.

Figure 3.57 shows an example of the TOF measurements.

### 3.2.3 Data analysis and results

A timing spectrum was obtained by calculating the time difference between the instant when the bunched beam struck a detector and the nearest RF pulse. As mentioned in the previous section, for the calibration of our TOF system, the beam energies at 600 keV/u and 992 keV/u were chosen as known beam energies. The  $\text{H}_2^+$  ion beam timing spectra simultaneously measured by the two grid-MCP detectors in the diagnostic station 10 and 13 at the beam energies of 992 keV/u and 600 keV/u are presented in Figure 3.58. Each peak had a nearly Gaussian shape. Depending on the beam tuning, the peak shape can vary significantly and needs to be optimized for these measurements. Each timing spectral peak in these measurements was partially fitted with a Gaussian to determine its center position, as shown in Figure 3.59. The average uncertainty in determining the peak centroids for these timing spectra is 9~12 ps (Table 3.11). The number of bins spanning the FWHM of each timing spectral peak is large enough to reasonably neglect the peak-centroid error caused by the finite bin width in the timing histogram. Since the beam bunches were accurately synchronized with the acceleration RF, each detector can be calibrated by comparing the time interval between two neighboring peak centroids with the RF period of 12.42 nsec, giving 0.0979 nsec per channel in average. The value of  $\Delta t$  in Equation 3.25 was determined from the time difference between the centroids of the nearest peaks of the two timing detectors, as shown in Figure 3.58 (marked with red arrows). The average  $\Delta t$  values for the TOF measurements at beam energies 992 keV/u and 600 keV/u are listed in Table 3.12. The numbers of beam bunches between the two detectors were precisely determined by the  $45^\circ$  magnetic analyzer in the S-bend beam line. By applying the ion mass  $m = 2.01533$  a.m.u for  $\text{H}_2^+$ , the RF period  $T_{RF} = 12.42$  nsec, the known beam energies and the  $\Delta t$  values into Equation 3.25, the TOF system was calibrated. The distance  $L$  between the two detectors was given as  $8.0575 \pm 0.0054$  m while the time offset of the system  $t_0$  was  $7.530 \pm 0.016$  ns. The errors of  $L$  and  $t_0$  are contributed from the uncertainties in the estimation of timing spectral peak centroids and the precision of the 992 keV/u energy.

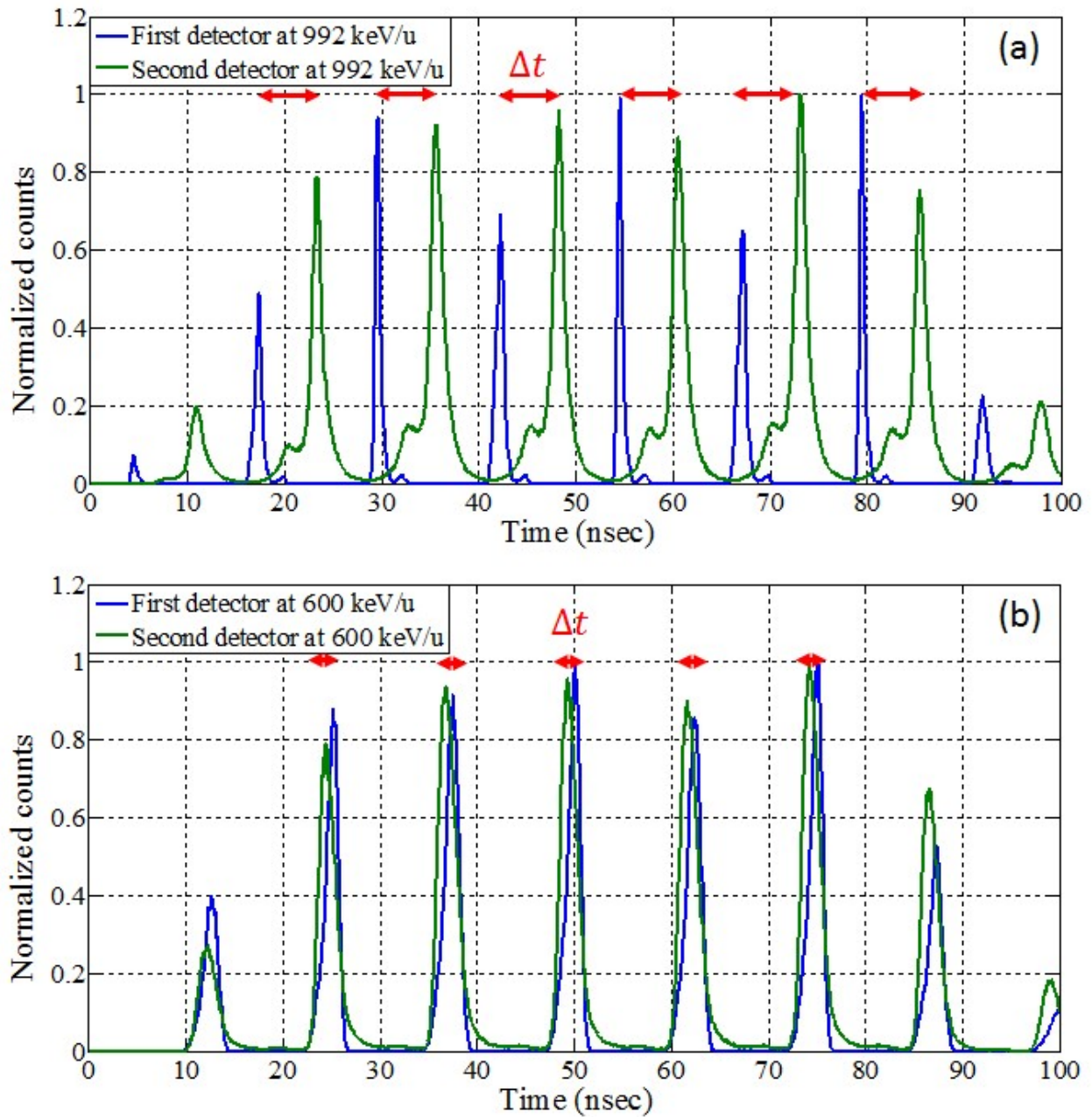


Figure 3.58 The  $\text{H}_2^+$  ion beam timing spectra simultaneously measured by the two grid-MCP detectors in the diagnostic station 10 and 13 at the beam energies (a) 992 keV/u and (b) 600 keV/u. The peaks in each time spectrum are normalized to the maximum of the spectrum.  $\Delta t$  represents the arrival time difference of beam bunches at the two detectors with respect to the RF signals.

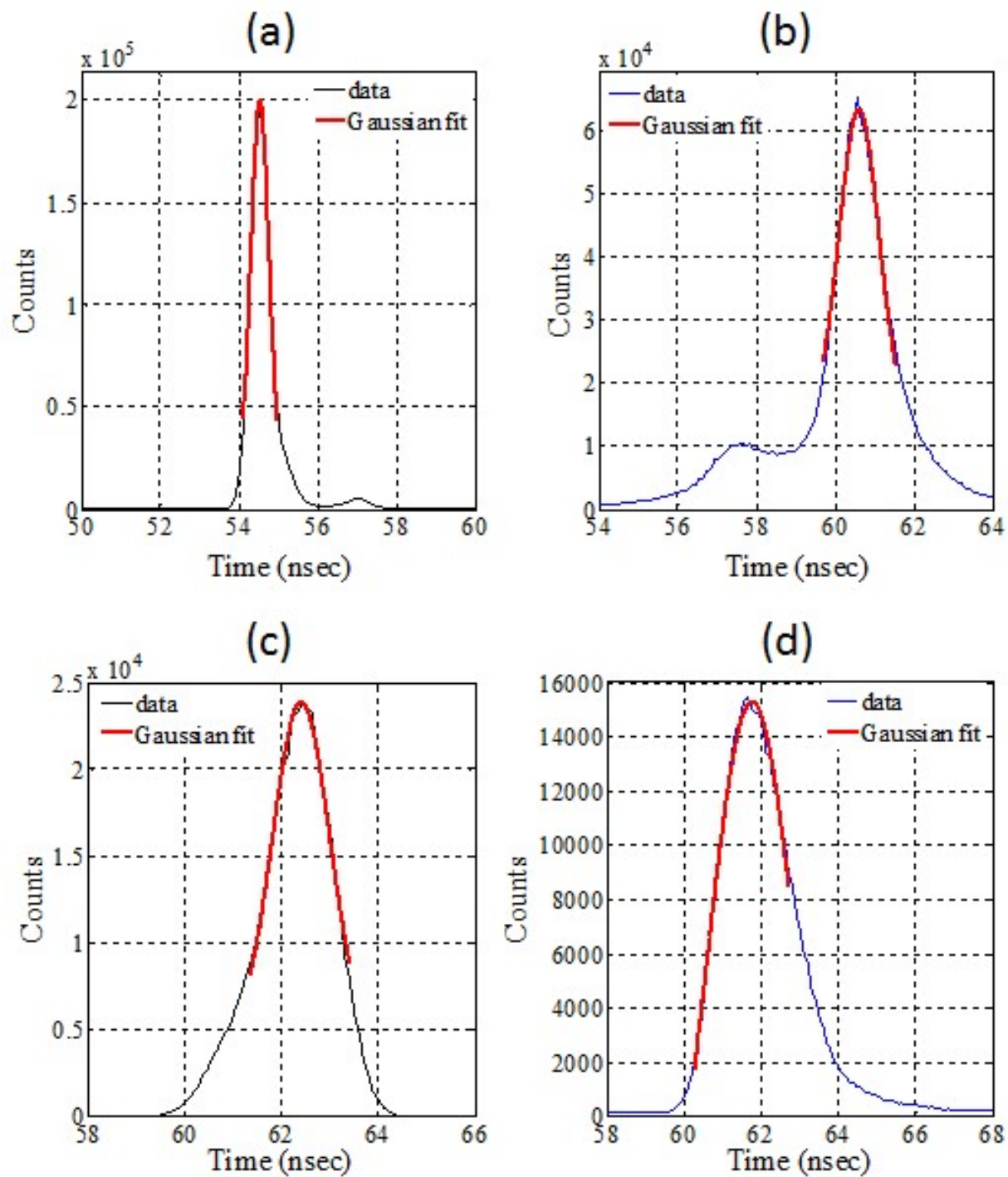


Figure 3.59 The timing spectral peaks measured by (a) the first grid-MCP detector and (b) the second grid-MCP detector at 992 keV/u beam energy; (c) the first grid-MCP detector and (d) the second grid-MCP detector at 600 keV/u beam energy. Each peak is partially fitted with a Gaussian in order to estimate the peak center.

Beam energy (keV/u)	The first timing detector	The second timing detector
992	9 ps	9 ps
600	10 ps	12 ps
1400	8 ps	8 ps
2100	6 ps	6 ps

Table 3.11 The average uncertainties in the estimation of the peak centroids by fitting peaks with a Gaussian for eight timing spectra measured by the two timing detectors at four different beam energies.

Known beam energy (keV/u)	Dipole field (T)	Bunch numbers $n$	$\Delta t$ (nsec)
992.098	0.294500	46	$6.013 \pm 0.012$
600	0.228978	60	$-0.666 \pm 0.015$

Table 3.12 Results of time-of-flight measurements at beam energies of 600 keV/u and 992 keV/u. The 600 keV/u is the RFQ output energy and the 992.098 keV/u beam energy was precisely determined by the 45° magnetic analyzer.

Rough energy (keV/u)	Dipole field (T)	Bunch numbers $n$	$\Delta t$ (nsec)	Measured energy by TOF
1400	0.350881	39	$-0.369 \pm 0.011$	$1404.814 \pm 1.339$ keV/u
2100	0.428266	32	$-2.850 \pm 0.009$	$2098.029 \pm 2.003$ keV/u

Table 3.13 Results of time-of-flight measurements at beam energies of 1400 keV/u and 2100 keV/u.

The timing spectra obtained by the TOF energy measurements at beam energies of 1400 keV/u and 2100 keV/u are shown in Figure 3.60. The centroids of the peaks were estimated by a computer fit with a Gaussian function. Figure 3.61 gives some typical examples of the timing spectral peaks partially fitted with a Gaussian. The average uncertainties in the estimation of the peak centroids for each timing spectrum are listed in Table 3.11. The beam bunch numbers between the two detectors and the average  $\Delta t$  values are listed in Table 3.13. The beam energies of these two TOF measurements were calculated to be 1404.814 keV/u and 2098.029 keV/u. The uncertainty in determining beam energy by the TOF ( $\Delta E/E$ ) is about  $\sim 0.095\%$ . The obtained beam energies from the TOF measurements were used to calibrate the 45° magnetic analyzer with the corresponding magnetic fields. Based on Equation 2.5, the dipole calibration factor  $k$  can be estimated, as listed

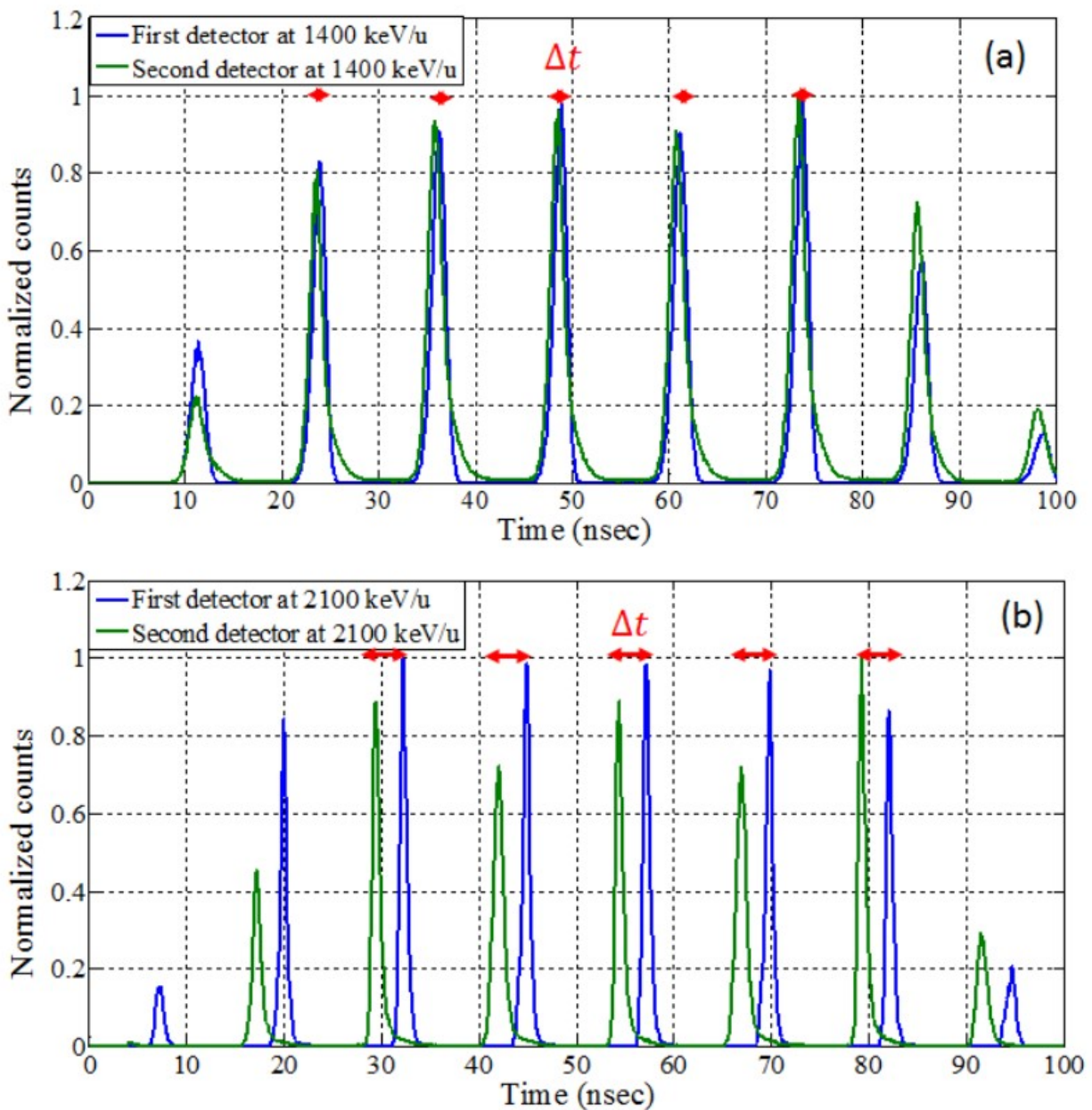


Figure 3.60 The  $H_2^+$  ion beam timing spectra simultaneously measured by the two grid-MCP detectors in the diagnostic station 10 and 13 at the beam energies (a) 1400 keV/u and (b) 2100 keV/u. The peaks in each time spectrum are normalized to the maximum of the spectrum.  $\Delta t$  represents the arrival time difference of beam bunches at the two detectors with respect to the RF signals.

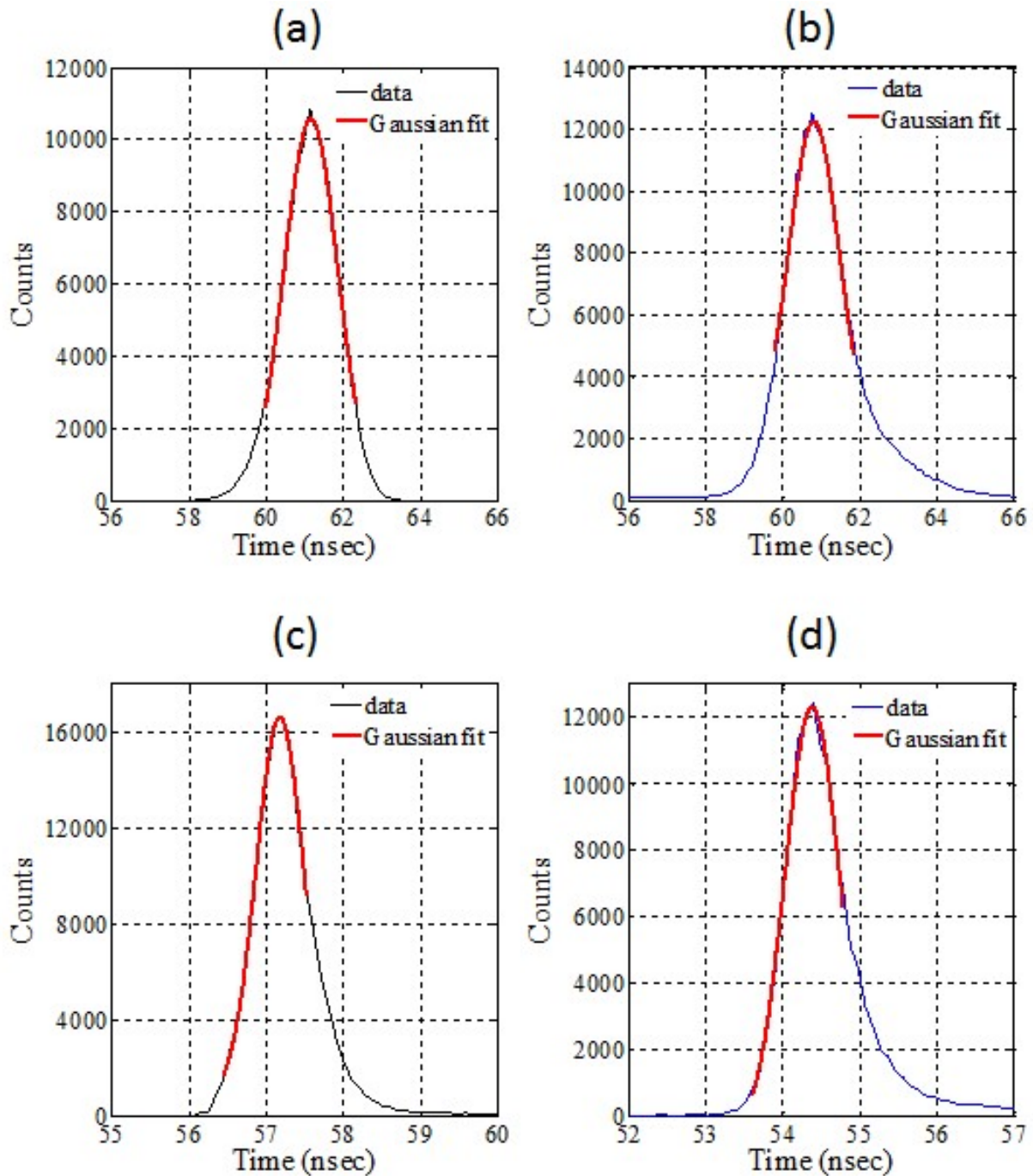


Figure 3.61 The timing spectral peaks measured by (a) the first grid-MCP detector and (b) the second grid-MCP detector at 1400 keV/u beam energy; (c) the first grid-MCP detector and (d) the second grid-MCP detector at 2100 keV/u beam energy. Each peak is partially fitted with a Gaussian in order to estimate the peak center.

Rough energy (keV/u)	Dipole field (T)	dipole calibration factor $k$ (T/ $\sqrt{\text{keV} \cdot \text{amu}}$ )
1400	0.350881	$(4663.383 \pm 2.222) \times 10^{-6}$
2100	0.428266	$(4656.401 \pm 2.220) \times 10^{-6}$

Table 3.14 Dipole calibration factor  $k$  obtained by the TOF energy measurements.

Beam energy keV/u	Energy uncertainty per cm distance uncertainty (keV/cm)	Energy uncertainty per ns timing uncertainty (keV/ns)
600	1.49	1.59
992	2.46	3.34
1400	3.48	5.69
2100	5.25	10.36

Table 3.15 Energy uncertainty estimation of TOF measurements.

in Table 3.14.

The energy uncertainties due to the variation of flight length between the two detectors and the errors of determining timing peak centroids or the time offset  $t_0$  are estimated in the four different energy domains in Table 3.15. On average, the flight distance uncertainty of 1 cm induces 0.25 % beam energy uncertainty. The timing uncertainty of 1 nsec leads to 0.26 ~ 0.50 % beam energy uncertainty over the beam energy range of 600 – 2100 keV/u.

## CHAPTER 4

### SCINTILLATION DEGRADATION MEASUREMENT UNDER ION BOMBARDMENT

The wide use of scintillator screens in beam profile measurements and pepper-pot emittance systems has motivated a number of studies [ Ripert et al. (2010)] [ Strohmeier et al. (2010)] regarding the stability of scintillators under ion irradiation. The scintillation degradation caused by radiation damages can deteriorate the accuracy of beam width and emittance measurements. The degradation of luminescence can be attributed to many factors, some of which are related to the nature of the scintillator materials, the accumulated fluence, and the energy of bombarding particles. In this chapter, two measurements to investigate the scintillation response and timing behavior of various scintillator materials under  $\text{He}^+$  irradiation at energies of 28-58 keV and  $\text{H}_2^+$  irradiation at energies of 600-2150 keV/u are described.

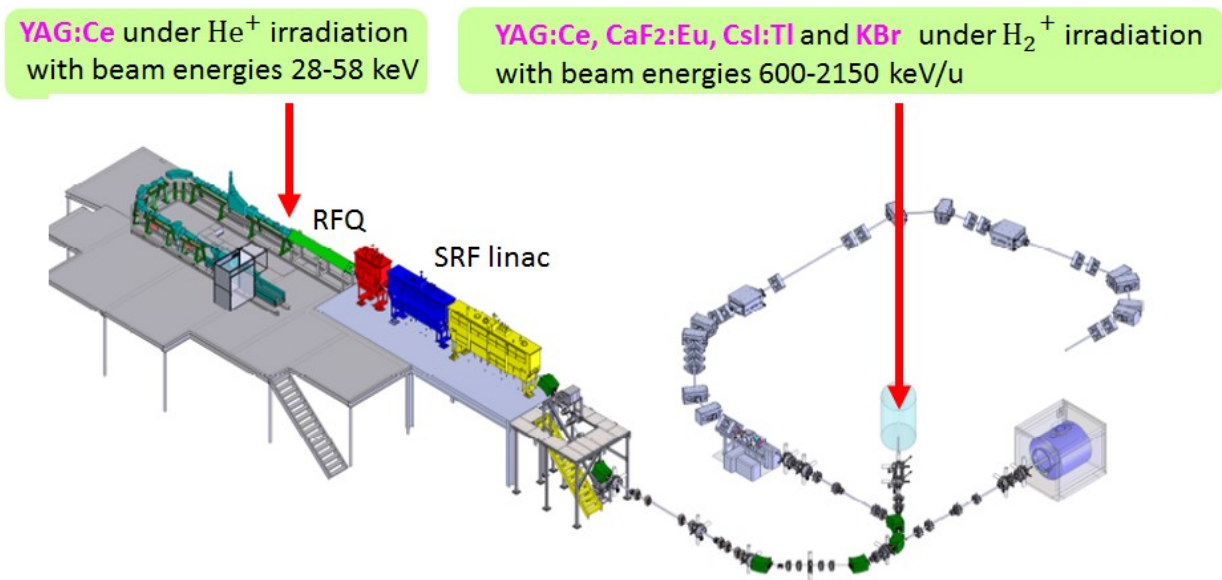


Figure 4.1 Locations of two irradiation measurements on various scintillator materials performed in the ReA3 facility of NSCL.

Beam energy (keV)	Beam current (pA)	Test
28	506	5
38	300	4
48	495,100,200	1,2,3
58	394,303	6,7

Table 4.1 Test Specifications.

## 4.1 Experimental setup

The scintillation measurements of various scintillation screens under low- and high-energy irradiation were performed in the low energy beam transport section and the experimental hall of the rare isotope ReAccelerator (ReA3) facility, as shown in Figure 4.1.

For the scintillation measurements under low energy bombardment, a YAG:Ce scintillator was irradiated with He<sup>+</sup> beams at energies between 28 and 58 keV (varied in 10 keV steps) in the LEBT line before the RFQ. The YAG: Ce single-crystal sample investigated in this work had a diameter of 19 mm. The sample was manufactured by SPI Supplies, USA. The density of YAG is about 4.57 g/cm<sup>3</sup>. The experimental parameters used in this analysis are listed in Table 4.1. In order to suppress thermal effects on the irradiated scintillator, the beam currents (measured by a Faraday cup) were limited to intensities of less than 500 pA. Figure 4.2 is an example of one set of irradiation images where the initial irradiation spots for all tests are overlaid. The beam spot for each test was steered to a different (virgin) location on the scintillator to make sure the beam impinged upon a fresh surface without breaking the vacuum. For these low energy beams it is particularly important to prevent local charge buildup on the insulating scintillator surface. Without a metal mesh to create free electrons upon ion impact to compensate the positive charges collecting on the scintillator surface, the incident ion beam will be distorted and finally reflected. Therefore, a fine Ni mesh was attached to the scintillator surface for these measurements. The angle of the scintillator surface normal with respect to the beam axis was chosen at 45°. The scintillation light as a function of the irradiation time was recorded outside of the vacuum chamber by a CCD camera. The camera (Prosilica GC750) has a resolution of 752×480 pixels with a 6×6 μm<sup>2</sup> size

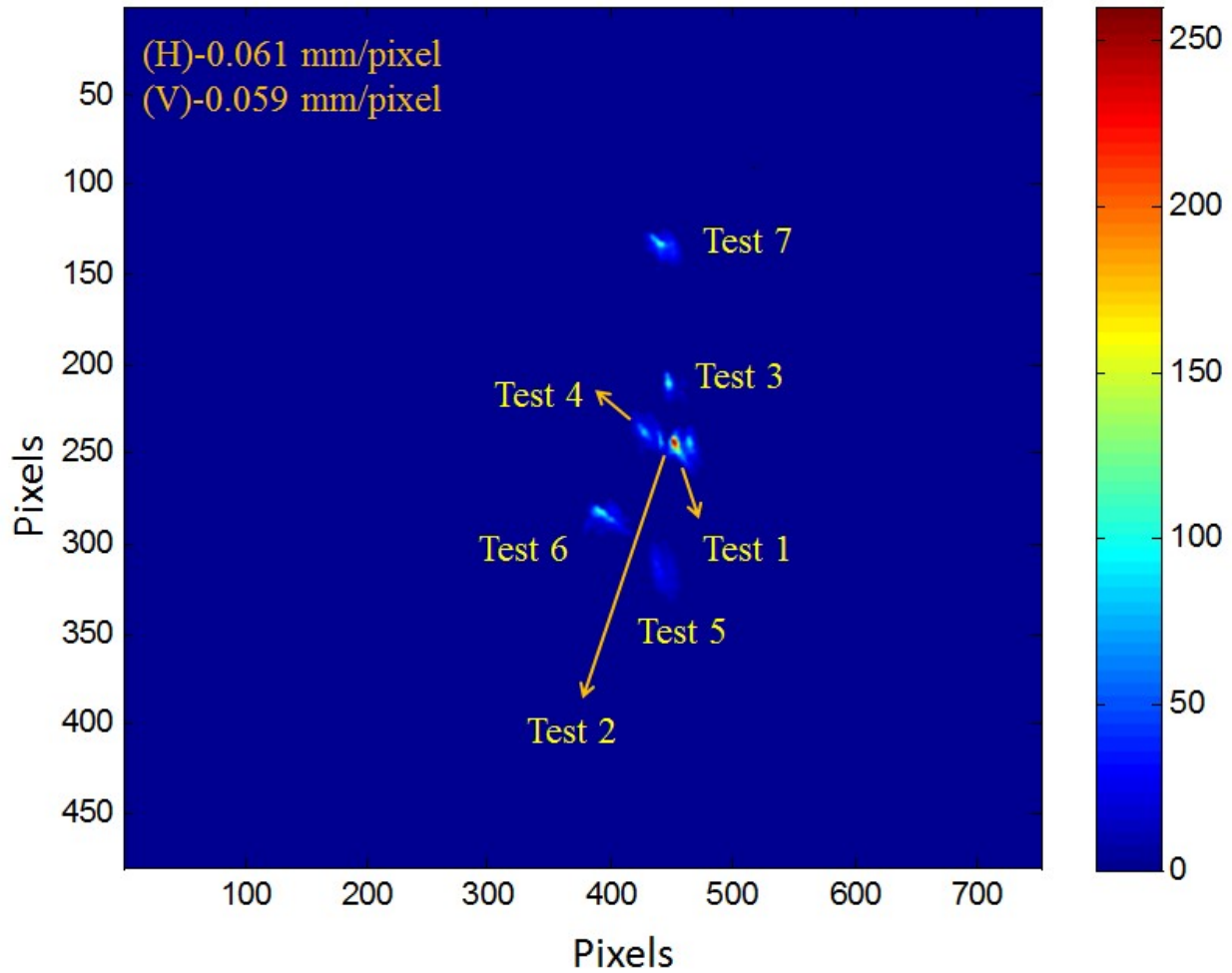


Figure 4.2 One set of irradiation images where the initial irradiation spots on the scintillator for 7 tests listed in Table 4.1 are overlaid. Each spot irradiated a different area of the scintillator surface for each measurement.

and was mounted perpendicular with respect to the beam axis as shown in Figure 4.3 and Figure 4.4. The camera was shielded from ambient light by covering the entire camera with a black cloth. The camera parameters (gain and exposure time) were manually adjusted during the duration of each test to obtain better quality of the images as the light yield of the scintillator decreased with the irradiation time.

For the scintillation measurements under high energy bombardment, the KBr, YAG:Ce, CaF<sub>2</sub>:Eu and CsI:Tl single crystals were irradiated with H<sub>2</sub><sup>+</sup> irradiation at the energies of 600-2150 keV/u. The scintillation materials and their optical properties are listed in Table 4.2 together with their dimensional sizes. The single-crystal CaF<sub>2</sub>:Eu and CsI:Tl samples were provided by Saint-Gobain

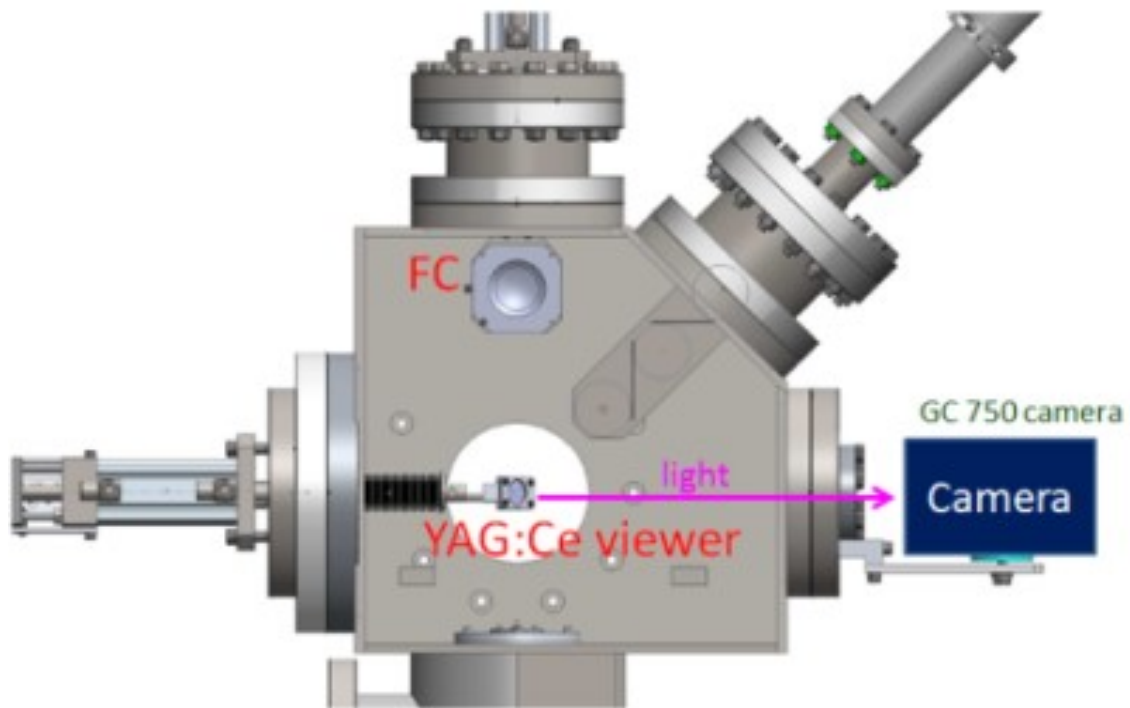


Figure 4.3 The setup of the YAG: Ce scintillator at the rare isotope ReAccelerator. After the beam was tuned into the Faraday cup and a beam current measurement was acquired, the Faraday cup was retracted and the scintillator plate was inserted into the beam. The emitted light was observed with a camera. The beam entered from the front plane.

Materials	CsI:Tl	CaF <sub>2</sub> :Eu	YAG:Ce	KBr
Density (g/cm <sup>3</sup> )	4.51	3.18	4.55	2.74
Light yield (photons/MeV)	55,000	24,000	16,700	—
Thickness (mm)	1	1	1	2
Diameter (mm)	19	19	18	19

Table 4.2 The scintillator materials under study.

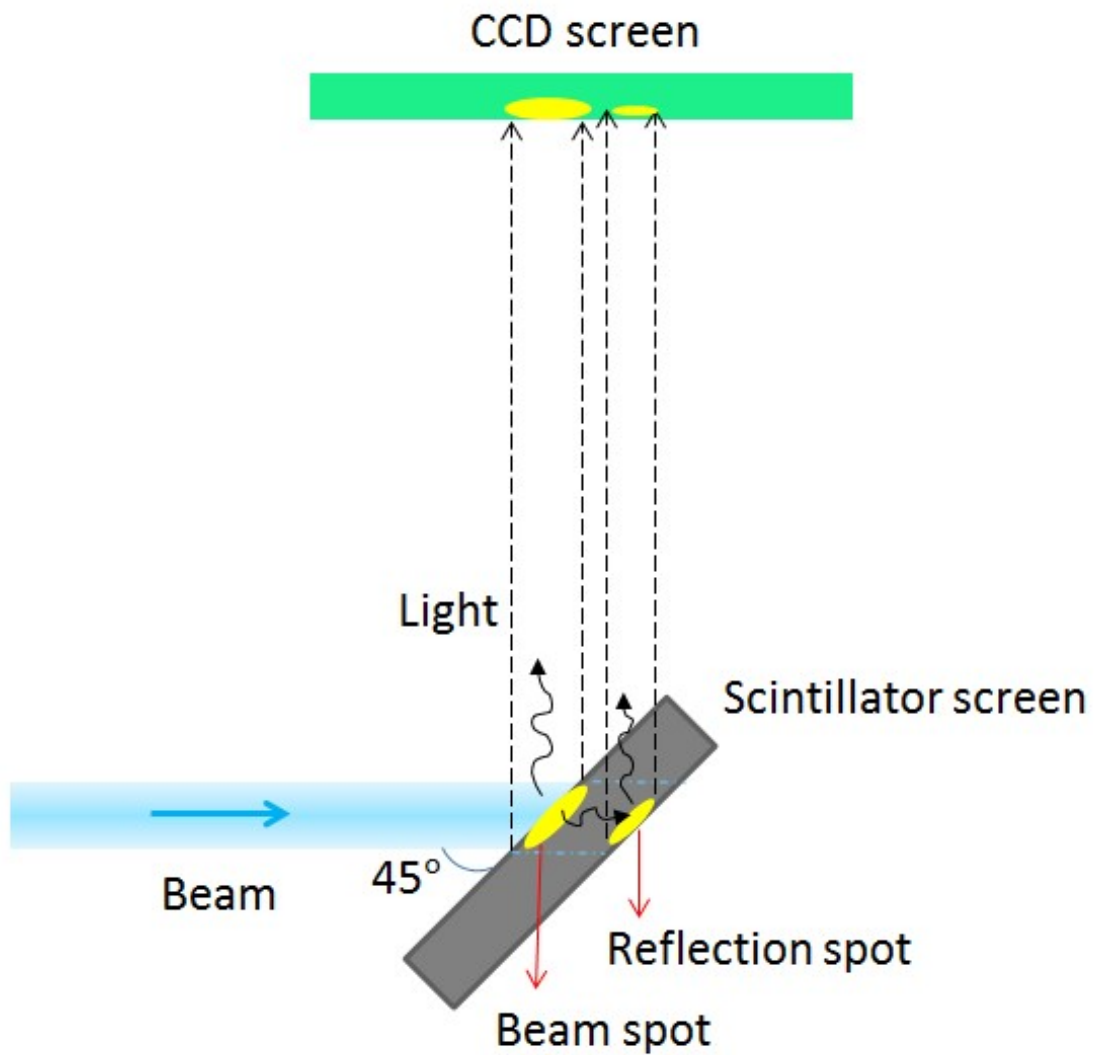


Figure 4.4 Illustration of the irradiation setup. The cause of image reflection in the scintillator is shown. The backward-emitted scintillation light is reflected at the substrate surface. The emitted light from the true beam spot and the reflected spot is both observed by the CCD camera.

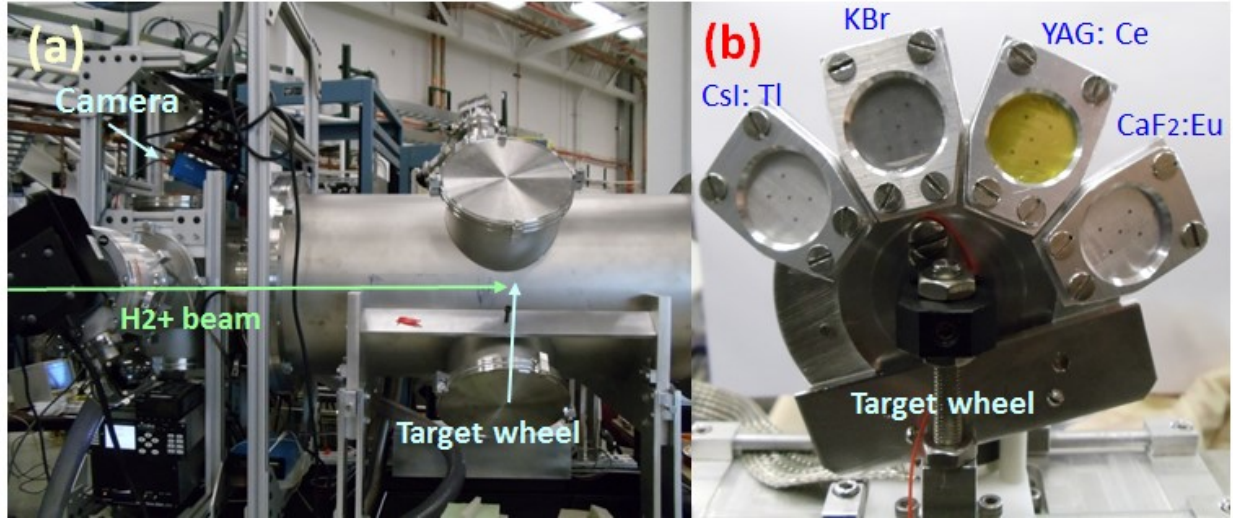


Figure 4.5 (a) Experimental setup for ion beam profile measurements; (b) a rotating target wheel with the four different scintillator materials. The target chamber is the ANASEN detector vacuum chamber [ Linhardt et al. (2012).

Crystal. The KBr and YAG:Ce crystals were from International Crystal Laboratory and Marketech International Inc., respectively. All the samples were optically polished on the front and back sides. A fine Ni mesh was attached to the scintillator surfaces to prevent local charge build-up and distortion of the beam image during ion beam bombardment. The four different scintillator materials were mounted on a rotating target wheel for subsequent irradiation inside a vacuum chamber located in the experimental hall, as shown in Figure 4.5. The specially designed target wheel allowed the ability to quickly switch between scintillators under investigation without breaking the vacuum, which ensured that the same beam conditions were applied for all scintillators. The luminescence of all the samples as a function of the irradiation time was recorded continuously outside of the target chamber by a cooled CCD camera (PCO 1600) [ Gütlich et al. (2010a)], equipped with a resolution of  $1600 \times 1200$  pixels with a  $7.4 \times 7.4 \mu\text{m}^2$  size and 14 bit dynamic range. The camera was shielded by an adjustable lens hood which extended far enough to block all stray light. For each individual measurement, a set of images were taken in time increments of 4 seconds. The scintillators were irradiated with  $\text{H}_2^+$  ion beams delivered by the ReA linac. A complete list of the beam energies used in this analysis as well as the simulated ion penetration ranges in the samples is listed in Table 4.3. The ion penetration ranges were much smaller than the sample thickness. In

Beam energy (keV/u)	Ion penetration depth ( $\mu\text{m}$ )			
	KBr	YAG:Ce	CaF <sub>2</sub> :Eu	CsI:Tl
600	9.52	4.64	5.79	8.11
1010	20.2	9.98	12.3	17.4
1500	36.4	18.0	22.3	31.4
2150	62.5	31.4	39.2	54.2

Table 4.3 The penetration depth of hydrogen ions in the four scintillators under different ion energies as estimated by the SRIM code [ Ziegler (2013)].

order to suppress thermal effects on the irradiated scintillators, the beam current was limited to be less than 400 pA ( $\approx 2 \times 10^{-7}$  Watt/mm<sup>2</sup>). The measurement of the beam current was carried out by a Faraday cup with suppression of the secondary electron emission. The beam spot had a width of about 5 mm. For each test, the beam impinged upon a virgin scintillator surface by either steering the beam to a new spot or changing to a new viewer.

## 4.2 Data analysis

The scintillation process was evaluated in terms of the particle fluence. The particle fluence  $N$  (mm<sup>-2</sup>) that corresponds to the light output recorded for each image is defined as the total number of beam particles per mm<sup>2</sup> striking the scintillator at a given time [ Hollerman et al. (2003)]

$$N = \frac{\Delta C}{q \cdot e \cdot A} \quad (4.1)$$

where  $\Delta C$  is the accumulated charge on an “analyzed area” within an irradiated beam spot on a scintillator at a given irradiation time,  $q$  is the charge state of incident particles, and  $A$  is the analyzed area (mm<sup>2</sup>).  $\Delta C$  can be derived from the total accumulated charge  $\Delta Q$  on the irradiated beam spot of the scintillator at a given irradiation time. Therefore,  $\Delta C$  is extracted by

$$\Delta C = \Delta Q \frac{I_0}{I_{total}} \quad (4.2)$$

where  $\frac{I_0}{I_{total}}$  is the relative initial scintillation yield on the “analyzed area” and the irradiated beam spot. The data analysis assumes that the initial scintillation yield increased linearly with beam

current, which was verified by changing the total beam current on the scintillator and summing the total light yield.

Matlab was used to process the images and evaluate the brightness level for each pixel in the irradiated areas. A few pixels in the central brightest region of the irradiated beam spot on the scintillator were selected as the “analyzed area” because of its high ratio of light signal to noise. The standard deviation of the brightness level on one pixel of a background-subtracted image can be estimated by [ Knoll (2010)]

$$\sigma_i = \sqrt{i + 2 \cdot B} \quad (4.3)$$

where  $i$  and  $B$  are the brightness levels on the same pixel of the background-subtracted image and background image, respectively. Hence, the pixels with higher light signal have lower uncertainty error.

The scintillation yield was evaluated from the background-subtracted images. These background signals recorded without beam originate mainly from the noise in the CCD sensor (e.g. CCD pixel defects or thermally generated electrons that build up in the pixels of a CCD) and remaining stray light. Several background images were recorded with varying setting of camera parameters without beam. A background image was subtracted from a raw image with the same setting of camera parameters to obtain a background-subtracted image.

The initial scintillation yield on a beam spot ( $I_{total}$ ) was estimated by eliminating scintillation reflection, stray radiation and the CCD electrical noise, and then summing the initial brightness levels of all the pixels on the beam spot. Stray radiation can directly enter the CCD camera, resulting in spike-like noise. A  $2 \times 2$  median filtering was used in image processing to eliminate spike-like noise with good image detail preservation. After that, a fixed threshold was subtracted from an image in order to remove electrical noise. The maximum value of electrical noise was selected as the threshold value. All data with brightness levels below the threshold value were considered as noise. The threshold value was less than 5 % of the full brightness range.

During the scintillation measurements in the LEBT, the beam spot images on the scintillator were reflected on the back plane of the crystal, as shown in Figure 4.4. Most of the images of our

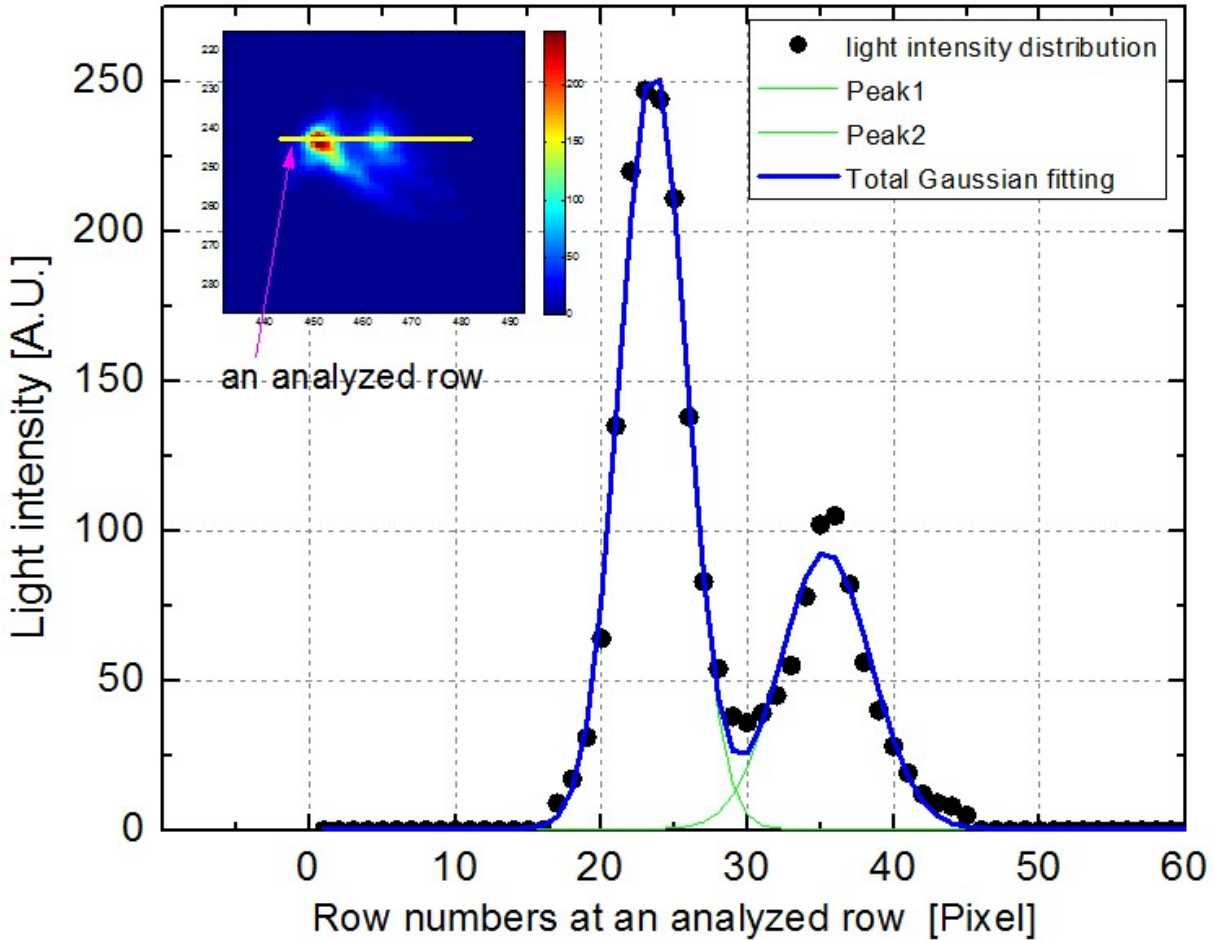


Figure 4.6 The initial image and an intensity profile of a specific row (represented by the yellow line) for the test 1.

tests show a double peak caused by such reflections. As an example Figure 4.6 shows an intensity profile of one row of pixels that were contaminated by a reflection peak. In order to remove this contamination, the intensity distribution of scintillation was fitted with two Gaussian functions using a least squares algorithm. The centers and standard deviations were allowed to vary during fitting. The smaller Gaussian corresponds to the reflected light because of its relatively lower light intensity. The reflected light was removed by subtracting the small Gaussian from the intensity profile for each row of the irradiation region to obtain the luminescence distribution attributable only to the ion bombardment.

In the scintillation measurements under high energy irradiation, for the comparison of the scin-

tillation performance under varying beam energies and scintillator materials, the light output of an analyzed area at a given particle fluence was normalized by the beam current and the camera's exposure time. The accuracy of the beam current measurement and beam jitter due to the finite regulation stability of the power supplies contributed to the experimental errors. In addition, beam spot image blurring due to light scattering inside a scintillator introduced an uncertainty of determining the beam spot area on the scintillator.

## **4.3 Results and discussion**

### **4.3.1 Scintillation investigation of YAG:Ce under low-energy ion bombardment**

#### **4.3.1.1 Scintillation efficiency**

The dependence of the initial total scintillation yield of an analyzed area ( $I_0$ ) on ion beam energy and current has been investigated. As expected, the initial scintillation yield increases linearly with the beam current at the same beam energy. And higher scintillation yields were observed at higher energy beams. Although a fraction of the kinetic energy lost by a beam particle through a scintillator is dissipated nonradiatively in the form of lattice vibration or heat [ Knoll (2010)], the remainder can be converted to produce excitons and emit visible light. Higher ion energy and current lead to more excitons and light yield.

#### **4.3.1.2 Scintillation degradation**

In order to study the degradation of the light output, the scintillation of an analyzed area at a given irradiation time ( $I$ ) was normalized by the initial scintillation of the same test. The normalized scintillation  $I_N$  is expressed by

$$I_N = \frac{I}{I_0} \quad (4.4)$$

where  $I_0$  is the scintillation of the analyzed area at an initial time with the camera gain  $g_0$  and exposure  $I_0$ . Since the light intensity was decreased during ion continuous irradiation, the camera

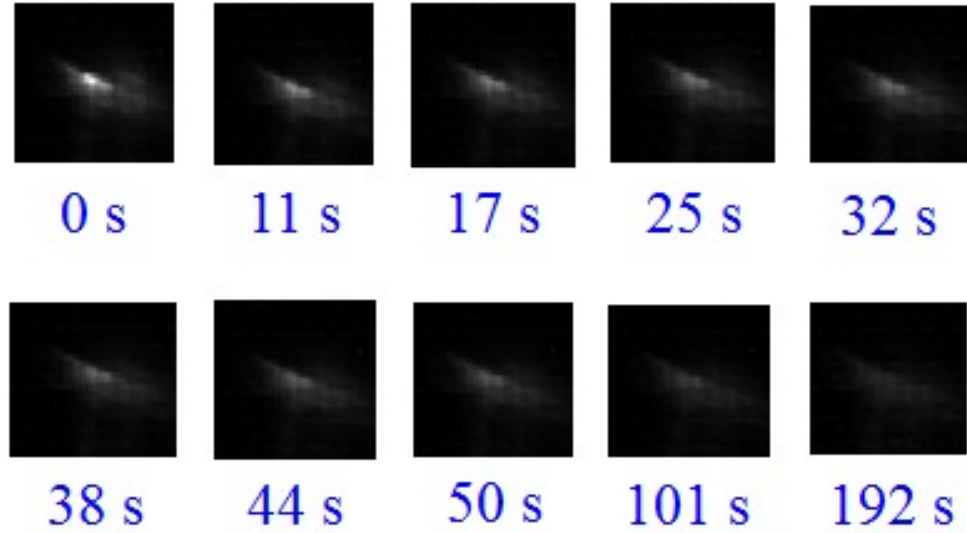


Figure 4.7 The degradation of YAG: Ce at incident ion energy  $E=58$  keV and beam current  $I=394$  pA.

settings for a set of images recorded at a different irradiation time were adjusted in order to maintain appropriate brightness levels on these images. It was assumed that the brightness levels on an image have a linear response to the camera gains and exposure time [ Wilkinson & Schut (1998)]. For the evaluation of  $I$  in Equation 4.4, the light output of the analyzed area on a background-subtracted image at a given irradiation time with the gain  $g$  and exposure time  $t$  was multiplied by a scale factor  $S$

$$S = \frac{g_0}{g} \cdot \frac{t_0}{t}. \quad (4.5)$$

An example for the time evolution of the 5d-4f luminescence images under continuous  $\text{He}^+$  bombardment is presented in Figure 4.7. After a total irradiation of 192 s, the light output becomes much weaker. Figure 4.8 plots the normalized scintillation intensity for an analyzed area versus the irradiation time at a constant  $\text{He}^+$  ion energy  $E=58$  keV and beam current  $I=394$  pA.

The degradation of the luminescence due to damage effects under ion beam bombardment can be clearly seen in the example shown in Figure 4.7. Several damage mechanisms are possible and described in more detail below. If a free mobile hole is captured by a  $\text{Ce}^{3+}$ , the luminescence center  $\text{Ce}^{3+}$  would be changed to a  $\text{Ce}^{4+}$  [ Hirouchi et al. (2009)] and reducing the number of  $\text{Ce}^{3+}$  activators as luminescence centre. In addition, the absorption band of  $\text{Ce}^{4+}$  overlaps the emission

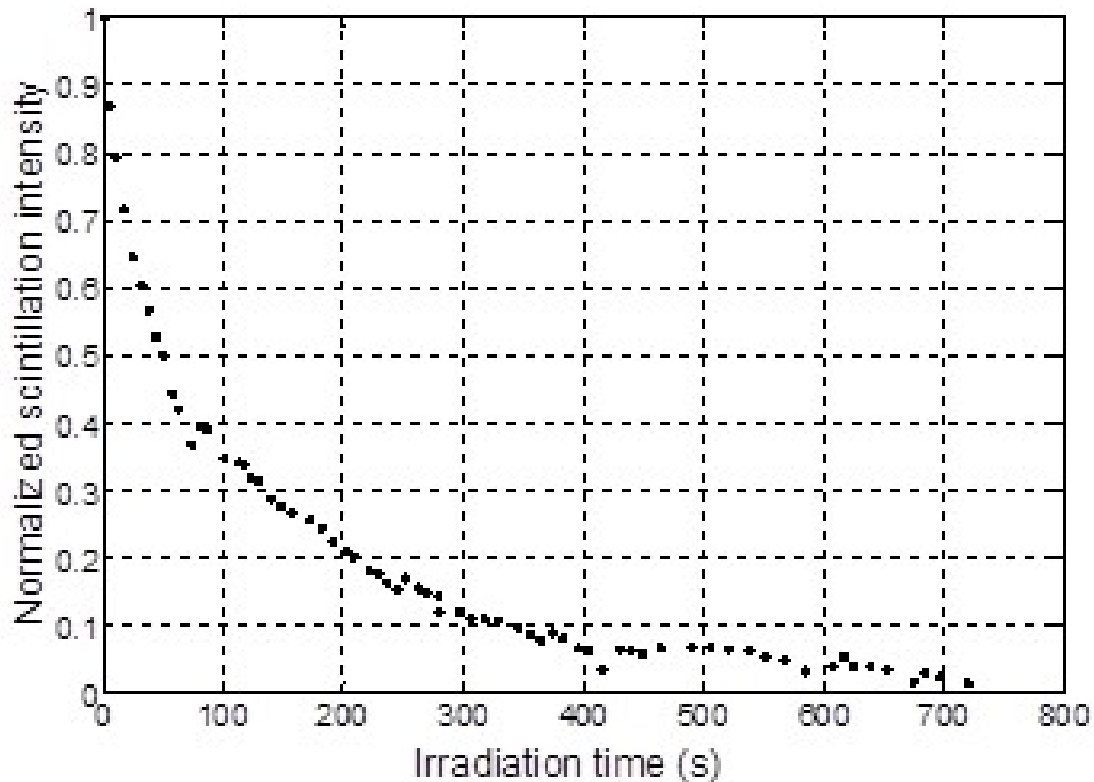


Figure 4.8 The luminescence response of YAG: Ce as a function of the irradiation time with a beam energy  $E=58$  keV and beam current  $I=394$  pA.

band of  $Ce^{3+}$ , thus quenching the light output. The formation of  $Y^{2+}$  by ion beam bombardment may also become color centers. The Yttrium atoms has  $[Kr]^{36}4d^15s^2$  electronic configuration. When the  $Y^{3+}$  ion with a configuration of  $[Kr]^{36}$  traps a free electron into its d-orbital state, it can be converted to the  $Y^{2+}$  ion [ Hirouchi et al. (2009)]. Electron paramagnetic resonance (EPR) studies indicate that the  $Y^{2+}$  centers have the potential to generate optical absorption, resulting in the reduction of the scintillation [ Yong-Feng et al. (2000)].

Probably the most common damage is caused by the knock-out of oxygen atoms. The ion bombardment can create the electron-hole pairs and the oxygen vacancies. The oxygen vacancies in  $Y_3Al_5O_{12}$  are able to capture one, two, or three free electrons giving rise to the one-electron  $F^+$  center, the two-electron  $F^0$  center and the three-electron  $F^-$  center, respectively. The existence of the  $F^-$  center has the absorption bands at 360, 480, and 830 nm. Therefore, the  $F^-$  center can absorb the photons mainly emitted from the  $Ce^{3+}$  sites. This absorption reduces the crystal's light

attenuation length and the light output [ Popov et al. (2010)].

#### 4.3.1.3 The Birks model

The degradation of the scintillation yield for YAG: Ce under He<sup>+</sup> irradiation can be analyzed by the Birks model [ Birks & Black (1951)]. In 1951, Birks and Black published an empirical formula to describe the luminescence efficiency of the scintillator bombarded by Helium ion beams. This empirical formula has been tested for many scintillator materials, such as anthracene, Y<sub>2</sub>O<sub>2</sub>S:Eu, Gd<sub>2</sub>O<sub>2</sub>S:Tb and YAG:Ce [ Hollerman et al. (1994)] [ Hollerman et al. (1992)] [ Broggio et al. (2005)]. The Birks model was derived from the idea that the luminescence of a scintillator is the result of a competition between the emission of photons from undamaged molecules and the absorption of photons by damaged molecules. The molecules damaged by ionizing radiation lead to a reduction in the scintillation intensity.

For an analyzed area of a scintillator within the irradiation region, the incident particle fluence as a function of the inversely normalized scintillation can be described in the Birks model by

$$N = \frac{1}{\sigma_d} \cdot \ln\left(1 + \frac{I_0 - I}{k}\right) \quad (4.6)$$

where  $I$  and  $I_0$  represent the scintillation intensity of the analyzed area for a given fluence and its initial scintillation yield, respectively.

There are two fitting parameters in the Birks model:  $k$  and  $\sigma_d$ . The relative exciton capture probability  $k$  is defined in the Birks model as the ratio of the number of excitons captured by a damaged molecule to the number of excitons captured by an undamaged molecule. Photons are emitted only from the excitons captured by undamaged molecules. If a damage molecule captures more excitons than an undamaged molecule, by definition the value of  $k$  would be more than 1. If  $q_0$  is the number of scintillator molecules in the irradiation volume per mm<sup>2</sup> and each beam particle damages  $p$  molecules, the damage cross section  $\sigma_d$  is expressed by

$$\sigma_d = \frac{p}{q_0}. \quad (4.7)$$

Source	Uncertainty
$I_{total}$	1 % ~ 10 %
irradiation time	$\pm 1$ sec
beam current	$\leq 5$ %

Table 4.4 Uncertainty budget for the particle fluence.

	28 keV	38 keV	48 keV	58 keV
k	$6.3 \pm 2.4$	$7.4 \pm 1.3$	$6.3 \pm 0.5$	$6.5 \pm 0.7$
$\sigma_d (\times 10^{-13} \text{mm}^2)$	$5.9 \pm 2.0$	$4.6 \pm 0.6$	$5.1 \pm 0.3$	$3.9 \pm 0.3$
$N_{1/2} (\times 10^{11} \text{mm}^{-2})$	$2.4 \pm 0.9$	$2.7 \pm 0.5$	$2.9 \pm 0.2$	$3.7 \pm 0.4$

Table 4.5 Results Summary of the relative exciton capture probability, the damage cross section and the half brightness fluence at low-energy He<sup>+</sup> bombardment in YAG: Ce.

Each set of experimental data at a specific beam energy and current has been fitted with the Birks model by determining the least chi-square  $\chi^2$  to evaluate  $k$  and  $\sigma_d$ . Once the values of  $k$  and  $\sigma_d$  were obtained from the fit, the half brightness fluence  $N_{1/2}$  was deduced through the expression

$$N_{1/2} = \frac{1}{\sigma_d} \cdot \ln\left(1 + \frac{1}{k}\right) \quad (4.8)$$

The examples of the experimental data and the fit of the particle fluence versus the inversely normalized scintillation intensity are shown in Figure 4.9. The errors in determining the fluence can be attributed to the calculation of the total initial brightness on the beam spot  $I_{total}$  and the measurement of the irradiation time and the beam current. The uncertainty budget for the particle fluence is listed in Table 4.4. The errors of  $I_{total}$  were derived from the threshold cut and the fit of two Gaussians in order to eliminate noise and the reflection, respectively.

The variations of  $k$ ,  $\sigma_d$ , and  $N_{1/2}$  with fitting uncertainty as a function of the beam energy are presented in Figure 4.10 and Figure 4.11. All of these values are summarized in Table 4.5. For example, the average values of  $k$ ,  $\sigma_d$ , and  $N_{1/2}$  for the two different currents at 58 keV are measured to be  $6.5 \pm 0.7$ ,  $(3.9 \pm 0.3) \times 10^{-13} \text{mm}^2$  and  $(3.7 \pm 0.4) \times 10^{11} \text{mm}^{-2}$ , respectively.

I do not find a significant energy dependence of  $k$  within the experimental uncertainty (Figure 4.10 a). The constant value of  $k$  may reveal that there is one dominant damage mechanism, such as oxygen vacancies, in competition with the scintillation production of the YAG: Ce crystal [ Broggio

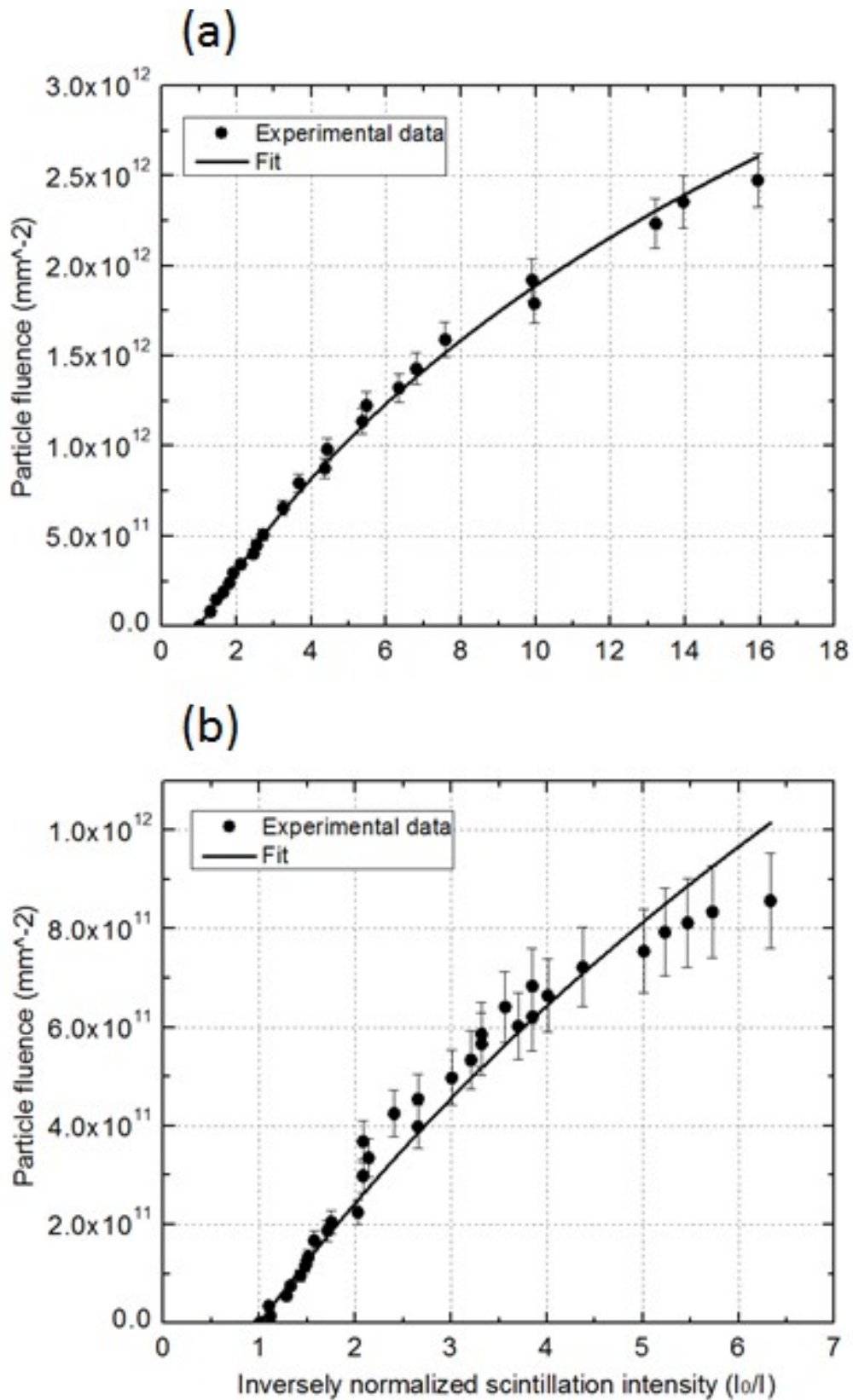


Figure 4.9 The particle fluence vs. the inversely normalized scintillation intensity for (a) test 1 and (b) test 5. The dots with error bars are the experimental points and the solid line shows the fit of the Birks model.

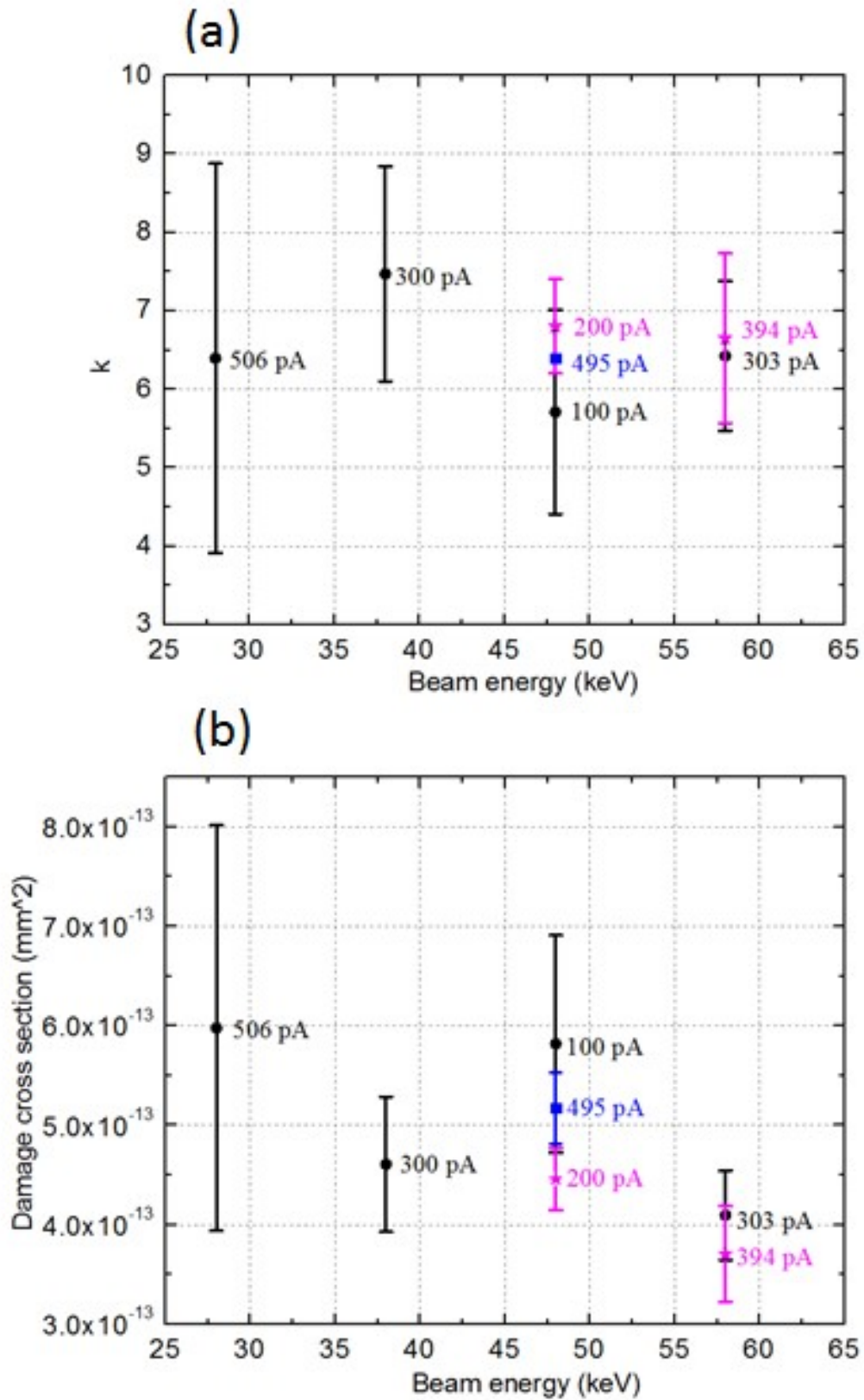


Figure 4.10 The relative exciton capture probability and the damage cross section as a function of the  $\text{He}^+$  energy. The error bars are the experimental uncertainty. Three symbols are used to represent different tests with different current at the same energy.

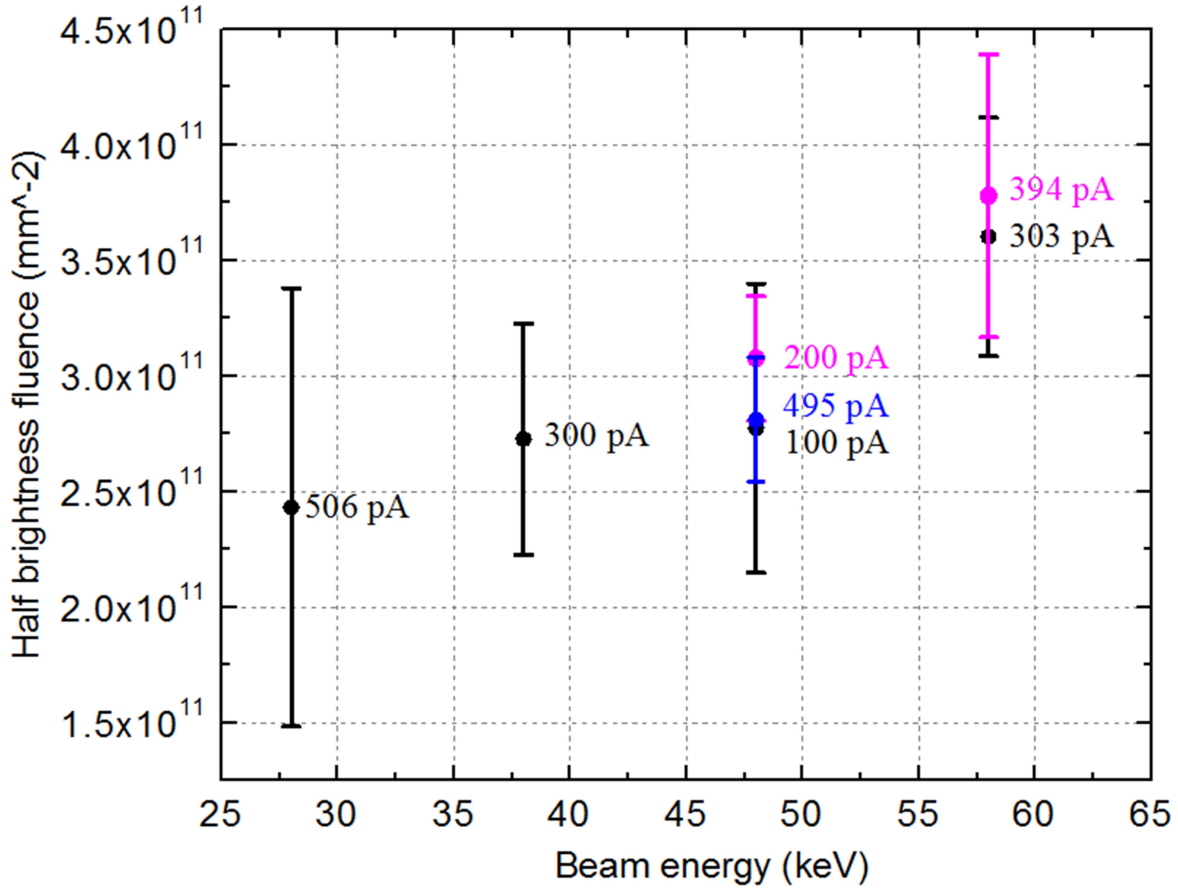


Figure 4.11 The half brightness fluence vs. the He<sup>+</sup> energy. Three symbols represent different tests with different current at the same energy.

et al. (2005)]. On the other hand, in comparison with the value of  $k$  ( $\sim 1000$ ) proposed by Birks [ Birks & Black (1951)] for anthracene under  $\alpha$ -particle excitation, the value of  $k$  for YAG: Ce crystals is considerably small. It shows the high resistance of YAG: Ce to radiation damage.

I assume that  $\sigma_d$  in Equation 4.7 is proportional to the ratio of the damaged molecules created per incident ion to the beam penetration depth in the scintillator. The beam particles could displace oxygen atoms of YAG from their normal lattice positions thus creating radiation damage. I used the SRIM code [ Ziegler (2013)] to study this ratio as a function of the ion energy. Figure 4.12 and Table 4.6 shows that this ratio decreases with the beam energy. The higher energy beam leads to less number of damaged centers created by one beam particle per unit of path length along its track. Therefore, the damage cross section can be expected to be reduced. From the experimental result, the damage cross section (Figure 4.10 b) seems to slightly decrease with the

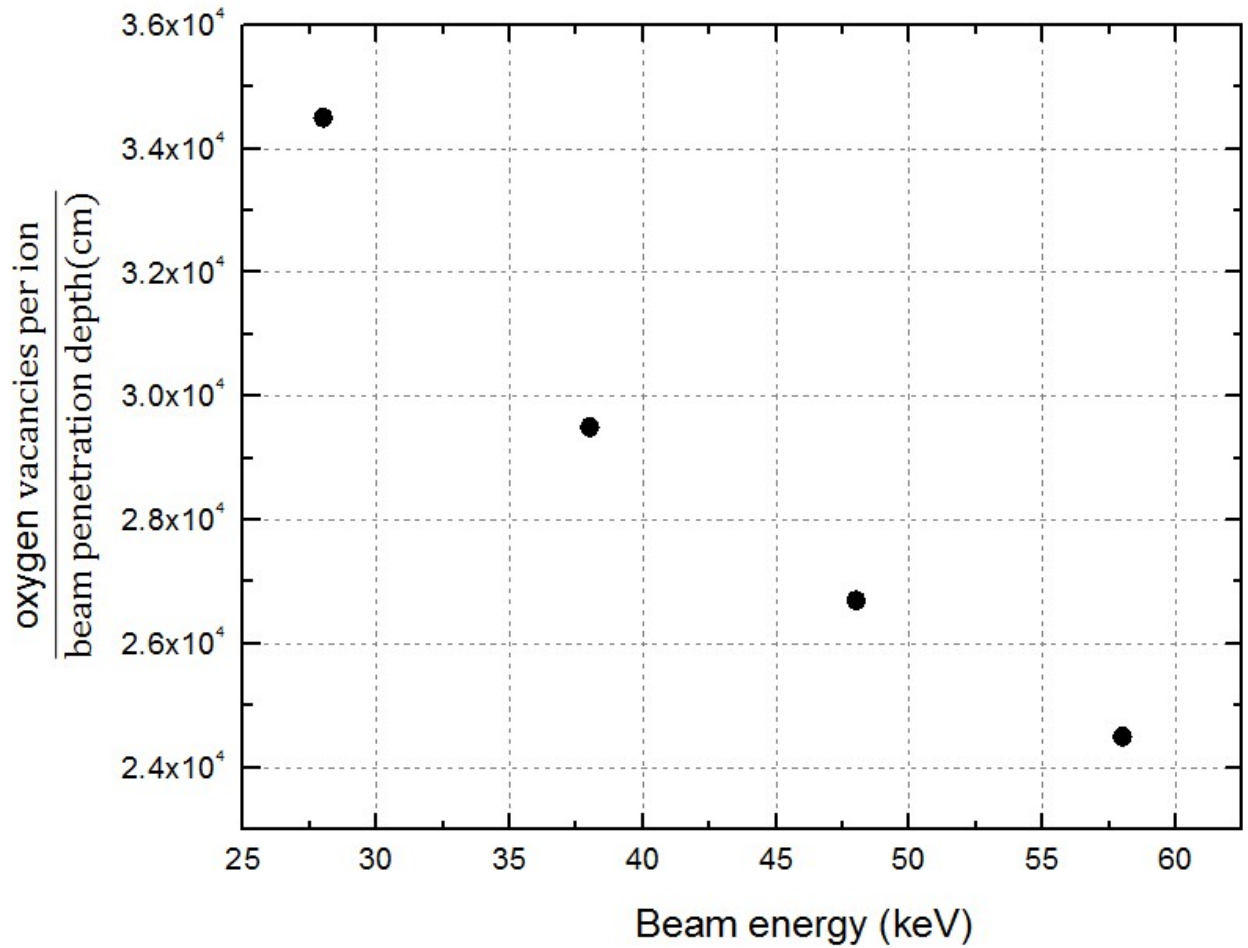


Figure 4.12 The SRIM calculation for the ratio of the oxygen vacancies created per incident ion to the beam penetration depth as a function of the beam energy.

Beam energy (keV)	Oxygen vacancies per ion	Beam penetration depth (cm)
28	0.40	$1.16 \times 10^{-5}$
38	0.44	$1.49 \times 10^{-5}$
48	0.47	$1.76 \times 10^{-5}$
58	0.50	$2.04 \times 10^{-5}$

Table 4.6 The SRIM calculation for evaluating the damage of the He<sup>+</sup> bombardment in YAG.

ion energy. As a result, the half brightness fluence (Figure 4.11) appears to increase as the ion energy. The  $\sigma_d$  at the ion energy  $E=58$  keV appears to be lower (and hence  $N_{1/2}$  is larger) than those at other energies. However, because of large experiment uncertainty and a narrow range of incident energies, the decrease of  $\sigma_d$  as well as the increase of  $N_{1/2}$  are still questionable. Therefore, I performed further experiments to investigate the energy dependence of scintillation degradation in a wide range of ion energy between 600 keV/u and 2150 keV/u, and the result is shown in Section 4.3.2.

It has been reported that the values of  $N_{1/2}$  for YAG:Ce beam viewers at proton energies of 3 and 45 MeV were  $1.3 \times 10^{14}$  and  $2.8 \times 10^{14}$  p/mm<sup>2</sup>, respectively [Hollerman et al. (1994)]. The  $N_{1/2}$  at 45 MeV was found to be 2.2 times higher than that at 3 MeV. These  $N_{1/2}$  obtained at high energies are much larger than all of the data deduced from our experiment at low energies between 28 and 48 keV shown in Figure 4.11, indicating that the half brightness fluence increases with higher energy. The higher the incident energy, the less the number of damaged centers created by one beam particle per unit of path length and the more the free excitons activated. Another contributing factor is the production of secondary electrons along the stopping path of the primary beam. The beam particle with a higher energy may produce more energetic secondary electrons to activate more luminescence centers for emission of photons outside of the quenching region [Michaelian & Menchaca-Rocha (1994)]. Thus the density of the deposited energy along the track of the beam particles will be smaller, resulting in less quenching. As the beam energy increases, the scintillation yield degrades less.

### **4.3.2 Scintillation investigation of KBr, YAG:Ce, CaF<sub>2</sub>:Eu and CsI:Tl under high-energy ion bombardment**

#### **4.3.2.1 Scintillation yield response**

The scintillation response of CsI:Tl and YAG:Ce for continuous  $H_2^+$  bombardment in the energy range between 600 and 2150 keV/u is depicted in Figure 4.13. The emission intensity of these two materials exhibits stable behavior in the energy range of this study. For CsI:Tl and YAG:Ce,

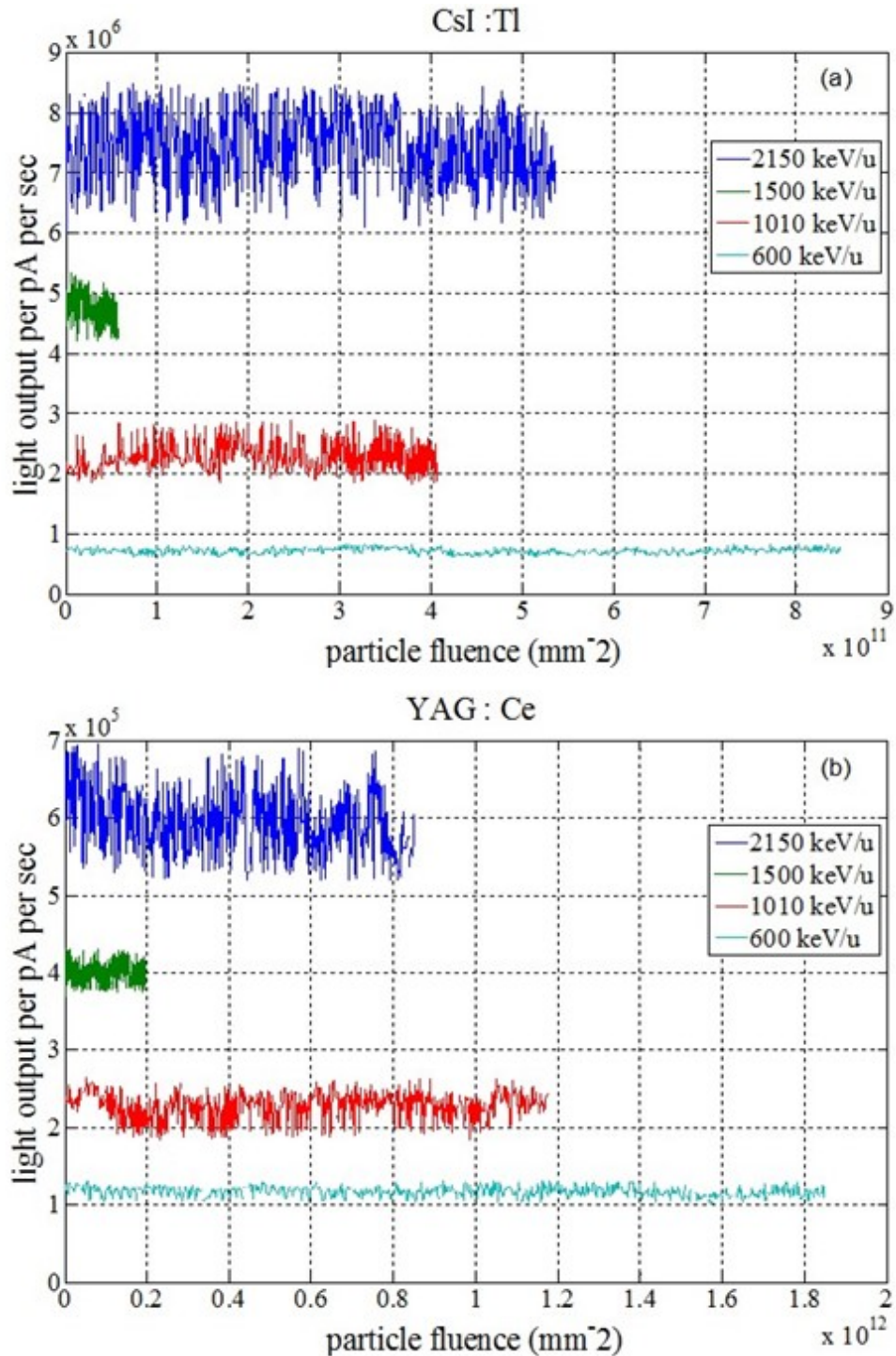


Figure 4.13 Scintillator luminescence response as a function of the accumulated particle fluence with  $H_2^+$  beam energies of 600, 1010, 1500 and 2150 keV/u for (a) CsI:Tl and (b) YAG:Ce. All the light yield curves were recorded during 1-hour irradiation, except for the yield curve of CsI:Tl at 1500 keV/u recorded during 1/3-hour irradiation. The light output for each curve was extracted from the analyzed area of a scintillator. Longer irradiation time or more beam current impinging onto the analyzed area of a scintillator can lead to larger accumulated fluence (longer curve length in the horizontal axis). The luminescence of CsI:Tl and YAG:Ce both exhibited very stable behavior under this irradiation energy range and low particle fluence.

the dopants can serve as luminescent centers. The scintillation efficiency is mainly determined by dopant materials and dopant concentration. Therefore, the scintillation efficiency of CsI:Tl and YAG:Ce is not fluence-rate dependent under low-fluence radiation. It is known [ Trefilova et al. (2007)] that the light yield of scintillators can be degraded by the transparency loss of the activator luminescence due to light absorption as it passes through color centers. The lack of scintillation degradation observed for CsI:Tl and YAG:Ce in Figure 4.13 suggests that there is negligible transparency deterioration of the scintillation photons in the irradiated crystals under the energy range and low radiation fluence of this study.

Figure 4.14 illustrates the light output of CaF<sub>2</sub>:Eu as a function of accumulated particle fluence measured for the four chosen beam energies. The scintillation of CaF<sub>2</sub>:Eu shows a significantly fast drop to about 65-75% of its initial value at the particle fluence of  $\sim 2 \times 10^{10}$  ions/mm<sup>2</sup>, and then approaches a stable state. The proton fluence required to reach the stable luminescence seems to be nearly independent of beam energy within the experimental uncertainty in the energy range of 600-2150 keV/u. The mechanism for the fast initial decrease in the light yield is still unclear. One possible explanation may be the charge transfer of Eu<sup>2+</sup>  $\rightarrow$  Eu<sup>3+</sup> ions during the bombardment with ionizing particles, as illustrated in Figure 4.15. CaF<sub>2</sub> has a face-centered cubic structure that exhibits simple cubic sub-lattices of F<sup>-</sup> ions with Ca<sup>2+</sup> ions at the centers of every other F<sup>-</sup> sub-lattices [ Sunta (1984)]. For CaF<sub>2</sub>:Eu crystals, the rare-earth Eu<sup>2+</sup> ions are added to substitute for Ca<sup>2+</sup> ions in the lattice. Under irradiation, Eu<sup>2+</sup> ions may be oxidized to Eu<sup>3+</sup> ions through charge compensation with interstitial fluorides ions at the center sites of the adjacent unoccupied F<sup>-</sup> sub-lattices [ Nakata et al. (1979)]. The Eu<sup>3+</sup> state has higher stability compared with the Eu<sup>2+</sup> state because of the smaller ionic radius. As a result, as the particle fluence increases, the optical luminescence spectra of the CaF<sub>2</sub>:Eu crystals may shift from the broad emission at  $\sim 425$  nm (from Eu<sup>2+</sup>) to the many sharp emission lines at 574, 612 and 626 nm (from Eu<sup>3+</sup>) [ Chen et al. (2007)]. Since the PCO 1600 camera has the lower quantum efficiency in the emission region of Eu<sup>3+</sup>, the overall light intensity recorded from the camera may decrease. After the transfer of Eu<sup>2+</sup>  $\rightarrow$  Eu<sup>3+</sup> along the ion track is complete [ Dhoble et al. (2011)], the collected luminescence can remain

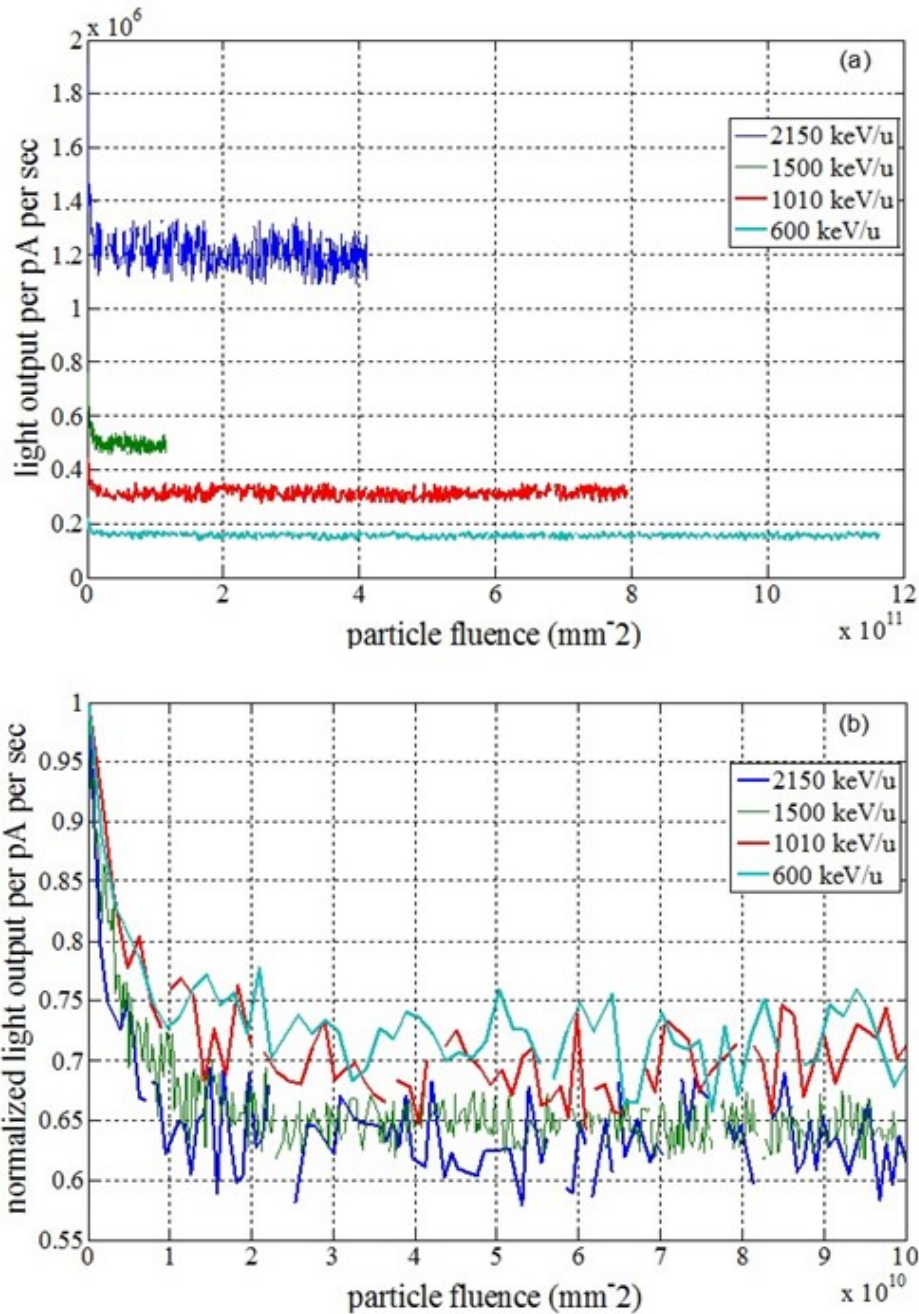


Figure 4.14 (a) Light yield of CaF<sub>2</sub>:Eu scintillators as a function of accumulated fluence for several beam energies. The light yield curves were recorded under the irradiation time of 1 hour for the H<sub>2</sub><sup>+</sup> beam energies of 600 and 1010 keV/u and 40 minutes for 1500 and 2150 keV/u. The particle fluence endpoint of the yield curve was determined by the irradiation time and the beam current impinging onto the analyzed area of a scintillator. (b) The luminescence intensity of CaF<sub>2</sub>:Eu was normalized by its initial luminescence. Plot (b) shows the detail of the scintillation degradation occurred when the particle fluence was below  $\sim 2 \times 10^{10}$  ions/mm<sup>2</sup>.

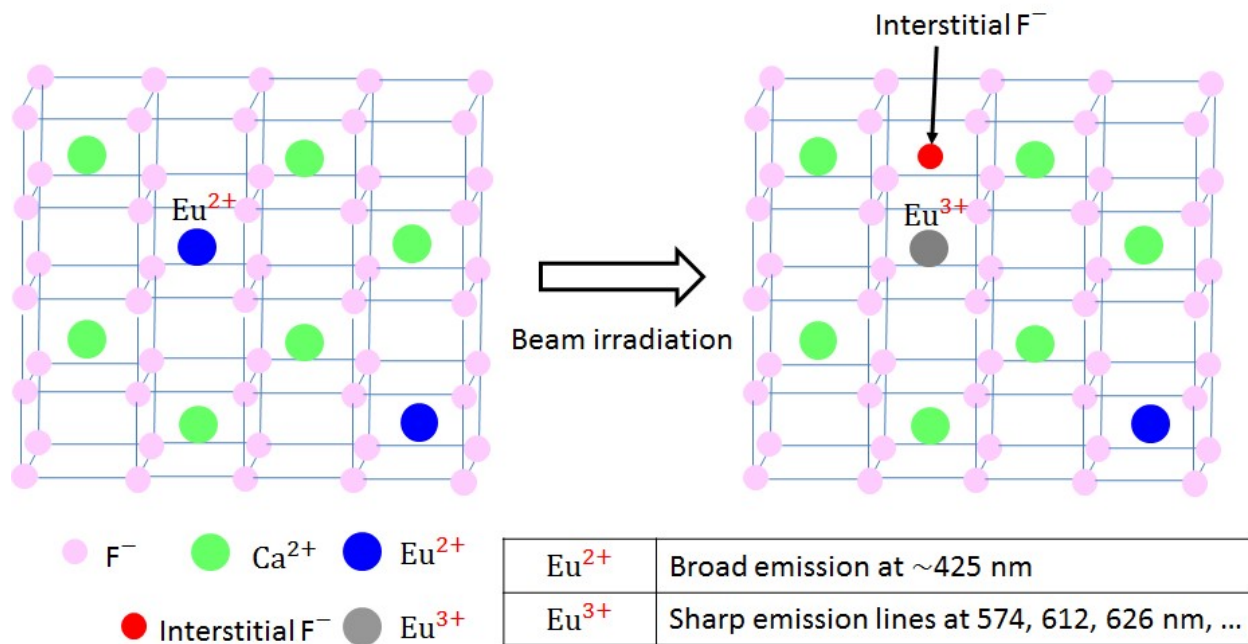


Figure 4.15 Illustration of possible radiation damages for CaF<sub>2</sub>: Eu at room temperature.

constant as the particle fluence is increased, assuming that the transparency loss of the activator luminescence is negligible. However, further experiments will be needed to verify this hypothesis.

I have analyzed the fluence dependence of the luminescence intensity for KBr irradiated with H<sub>2</sub><sup>+</sup> ions at the beam energies of 600, 1010 and 2150 keV/u as shown in Figure 4.16 (a). For all three investigated energies, the scintillation of KBr exhibits a fast increase up to the particle fluences of about (5~7) x10<sup>10</sup> ions/mm<sup>2</sup>, followed by a rapid decay and eventually a slow continuous decline. The irradiation time to reach a maximum luminescence was found to strongly depend on the beam current. A higher beam current results in less irradiation time required to reach a maximum scintillation. The fact that the emitted light of KBr is initially enhanced suggests that the luminescence centers must be some form of lattice defects (color centers) induced by ion bombardment. It is known that during irradiation at room temperature, KBr crystals can form stable F-centers and hole defects of V<sub>3-</sub> and V<sub>4-</sub> centers [ Bazhin et al. (1976)]. The combination of F-centers with V-centers would be responsible for KBr luminescence, as shown in Figure 4.17. The blue color shown on the damaged spots of the KBr crystals after ion bombardment in Figure 4.18 demonstrates the F-center formation during irradiation because the absorption band

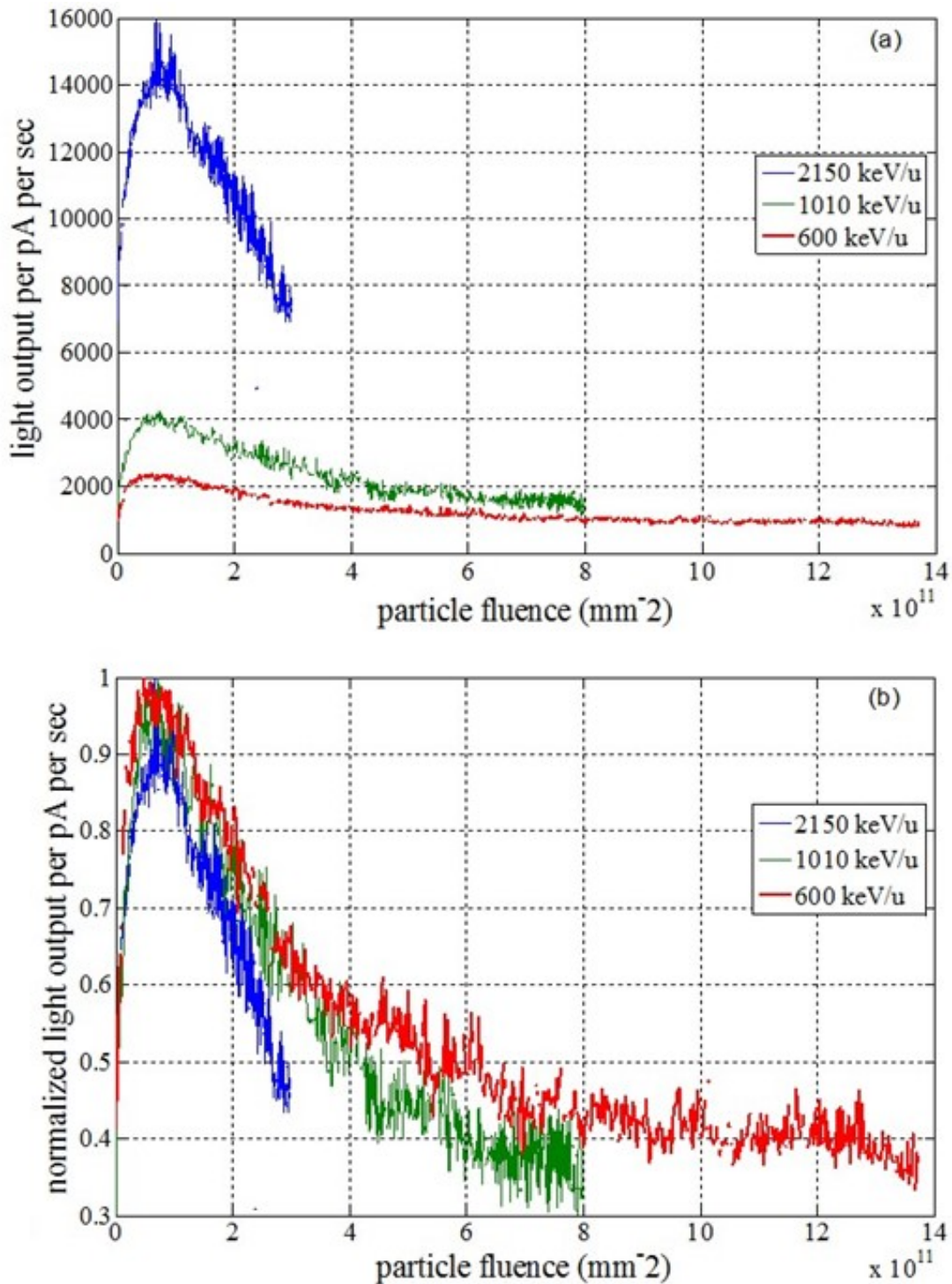


Figure 4.16 (a) Fluence dependence of the luminescence intensity of KBr under  $H_2^+$  ion bombardment for several beam energies. All the light yield curves were recorded during 1-hour irradiation. The comparison of the beam current bombarding the analyzed area of the KBr scintillator for the yield curves at the three beam energies is  $600 \text{ keV/u} > 1010 \text{ keV/u} > 2150 \text{ keV/u}$ . (b) The luminescence intensity of KBr was normalized by its maximum scintillation. The luminescence of KBr degraded faster at higher beam energy after reaching its maximum scintillation.

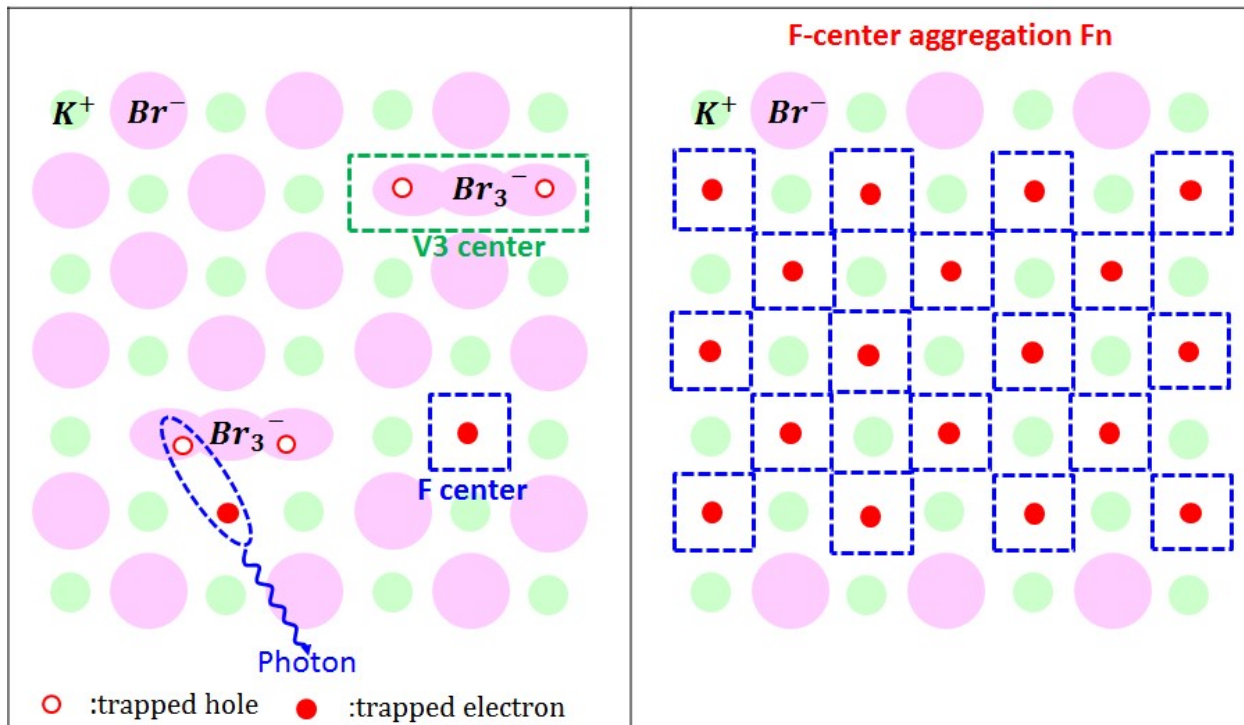


Figure 4.17 Schematic configuration of the F- and  $V_3$ - centers as well as the F-center aggregates in KBr. The F-center is an electron trapped by a  $Br^-$  vacancy and the  $V_3$ - center is formed by a  $Br_3^-$  molecule located at one cation and two anion vacancies.

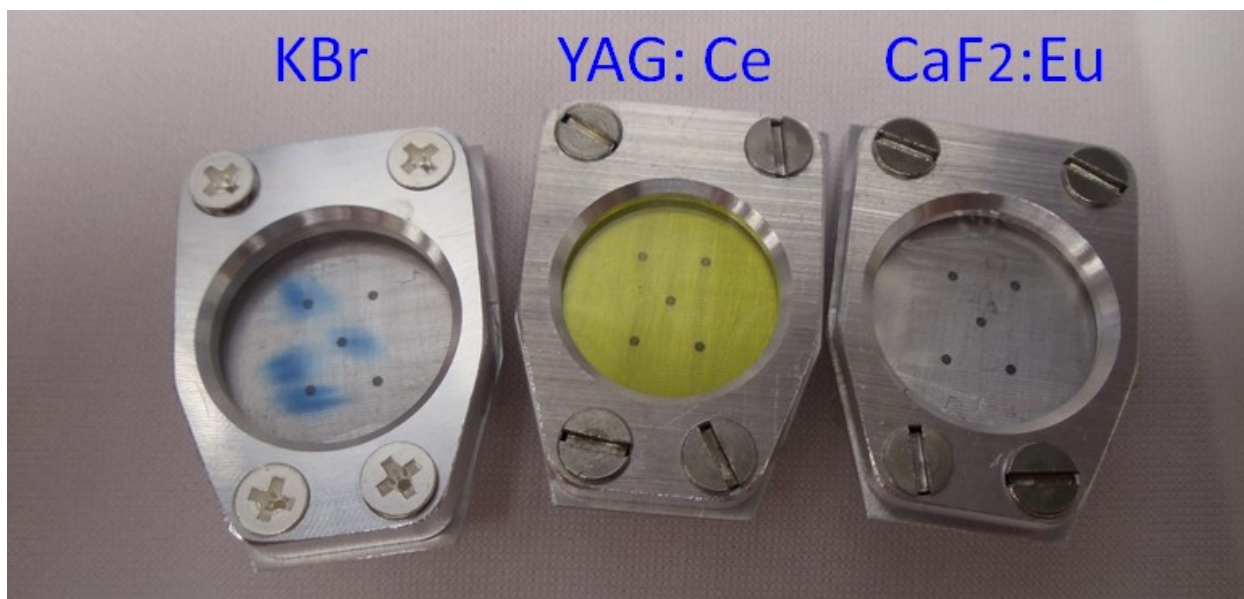


Figure 4.18 The KBr, YAG:Ce and  $CaF_2$ :Eu samples after ion irradiation. The KBr crystal shows damaged spots in blue color.

of F-centers is around 600 nm [ Mitsushima et al. (1976)]. The F-centers are complementary to the  $V_3^-$  and  $V_4^-$  centers. The F-center concentration (and hence  $V_3^-$  and  $V_4^-$  center concentration) is fluence-dependent [ Bazhin et al. (1976)]. The fact that the light yield of KBr first reaches a maximum and then decreases with further increase of the fluence might indicate that the concentration of F-centers reaches a critical concentration since the F-centers start to diffuse and combine with other F-centers to form F-center aggregates  $F_n(F+F \rightarrow F_2, \dots, F+F_{n-1} \rightarrow F_n)$  as illustrated in Figure 4.17. The  $F_n$  aggregates will suppress the production of photons and will lead to a reduction of the luminescence [ Bazhin et al. (1976)]. In addition, it was observed that after high-fluence irradiation, the luminescence of KBr decays faster under higher-energy bombardment as shown in Figure 4.16 (b). This property might be caused by a more efficient F-aggregate formation under high beam energy and a faster reduction of F-center concentration, leading to a lower light yield.

#### 4.3.2.2 Scintillation yield comparison

The luminescence intensity of the KBr, YAG:Ce,  $CaF_2:Eu$  and CsI:Tl scintillators as a function of the incident ion energy under  $H_2^+$  bombardment was plotted in Figure 4.19. In order to compare the scintillation response of all the materials at different ion energies under typical operational conditions in ReA3. A linear response for all the scintillators shows that no saturation effect is found within the investigated energy range. Even though the luminescence of KBr shows a very unstable behavior under continuous irradiation, the maximum luminescence of KBr still exhibits an approximately linear relationship with the beam energy. The light yield of  $CaF_2:Eu$  is approximately 1.3 to 1.4 times higher than that of YAG:Ce under the same conditions of ion bombardment. The KBr screen presents the lowest scintillation efficiency. However, the CsI:Tl screen is most sensitive and shows the highest scintillation efficiency, with more than two orders of magnitude higher light yield compared to the KBr screen.

#### 4.3.2.3 Stability of beam profile width

Figure 4.20 shows an example for the projection of the initial beam spot images in vertical axis

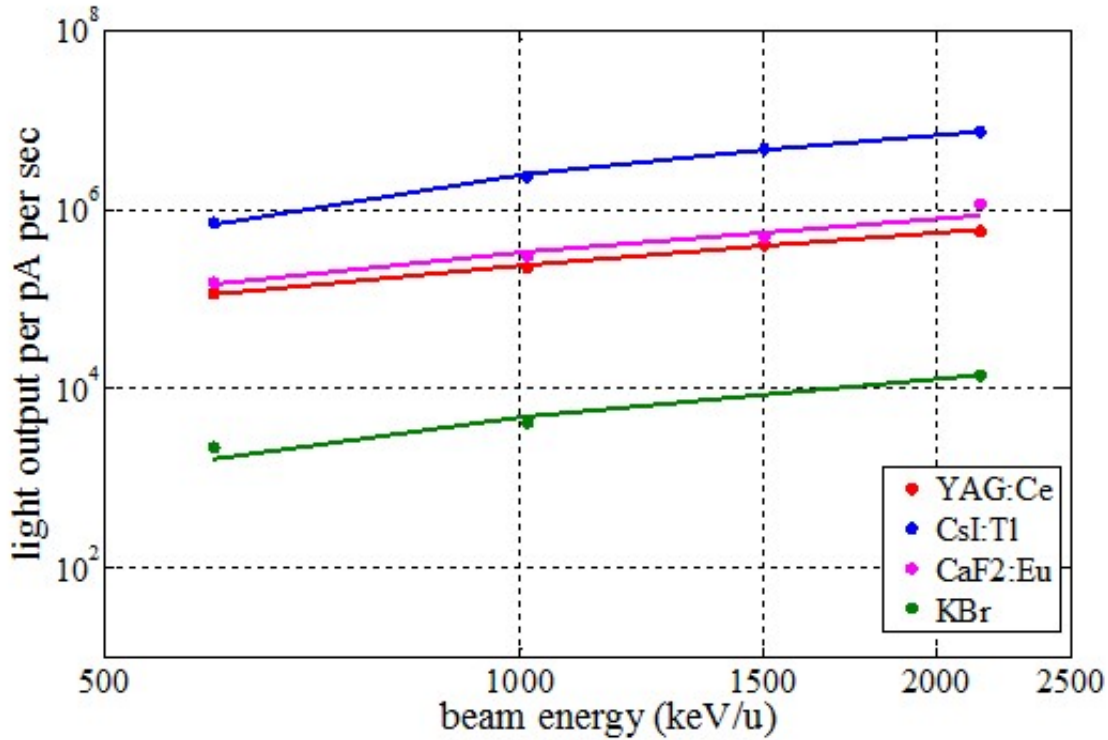


Figure 4.19 The relative light output of all the materials under study as a function of beam energy. For YAG:Ce and CsI:Tl, the average luminescence during irradiation is estimated. For CaF<sub>2</sub>:Eu, after the scintillation reaches its stable state, the average in the light yield was chosen for comparison. As comparison, the maximum luminescence of KBr is also plotted. The dots are the experimental points and the solid lines show a linear fit.

on YAG:Ce, CaF<sub>2</sub>:Eu and CsI:Tl under the same beam condition of H<sub>2</sub><sup>+</sup> irradiation. The shapes of the projected profiles for these scintillators are much alike. P. Forch et al. [ Forck et al. (2014)] measured the beam spot image projection on several scintillator materials with Uranium irradiation at 269 MeV/u and showed that the shape of the image projection on CsI:Tl and YAG:Ce has significant difference at the peak wings due to some unclear reason. One of the suspected causes may be attributed to backscattered radiation from their experiment environment. However, in this report, no significant difference on the edges of the projection between YAG:Ce, CaF<sub>2</sub>:Eu and CsI:Tl is observed.

When the vertical projected intensity in Figure 4.20 was fitted with a Gaussian curve to extract the beam width (standard deviation  $\sigma$ ), the result shows that the beam width of the three materials coincides within 4% despite their different absolute light yield. Furthermore, the beam width of all

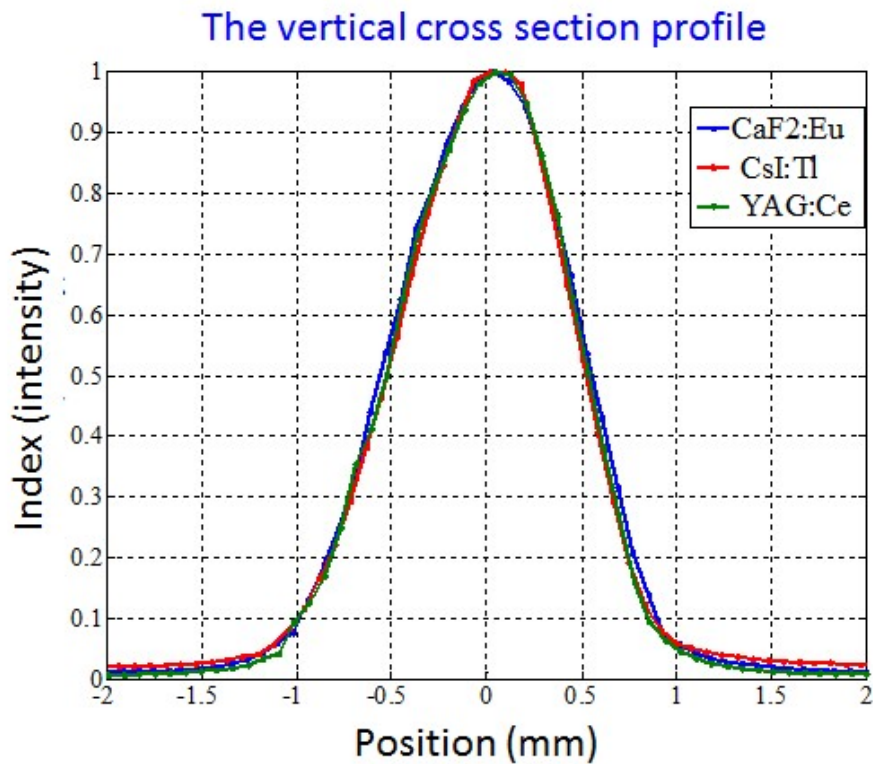
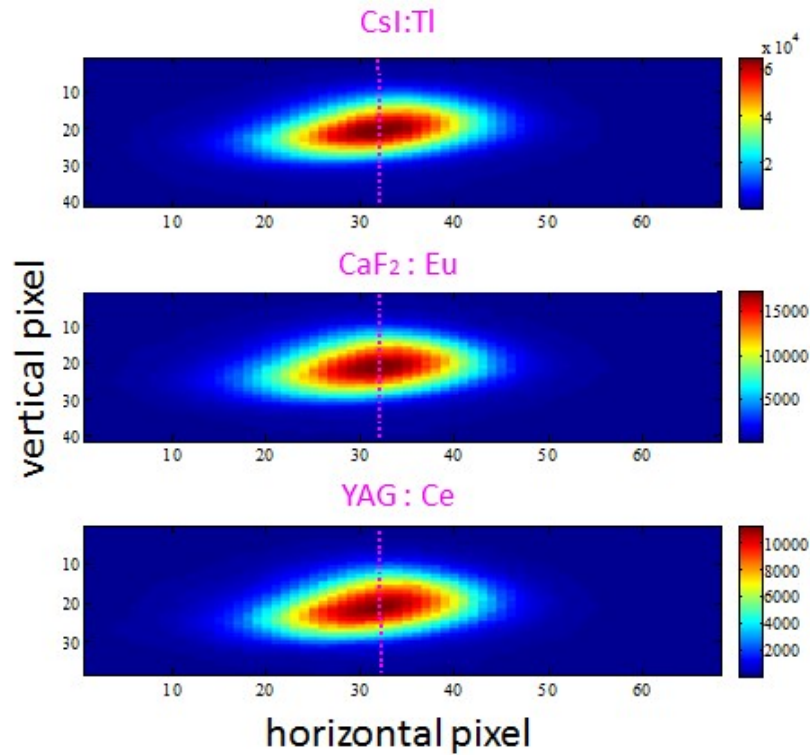


Figure 4.20 Normalized luminescence distributions of the initial beam spot images along a pixel column positioned at maximum luminescence for CsI:Tl, CaF<sub>2</sub>:Eu and YAG:Ce under the same camera setting and the same beam condition of H<sub>2</sub><sup>+</sup> irradiation at the beam energy of 2150 keV/u and the beam current of 12 pA.

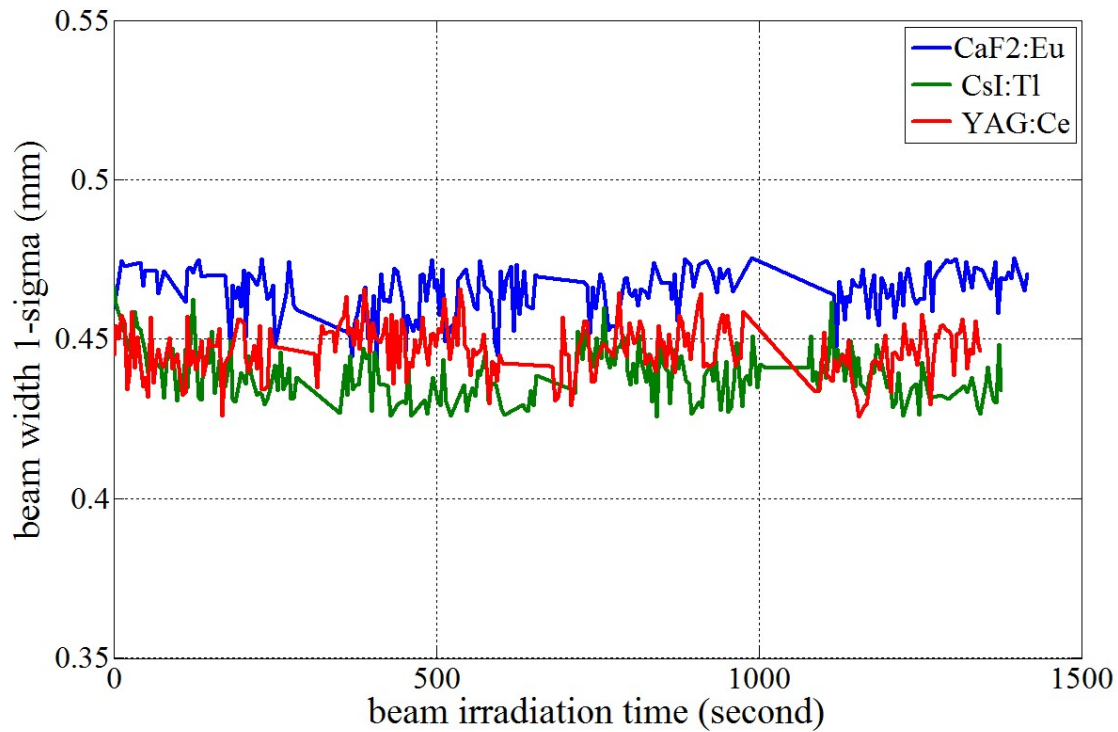


Figure 4.21 Beam width of YAG:Ce, CaF<sub>2</sub>:Eu and CsI:Tl materials determined from Gaussian fits to the vertical projection for H<sub>2</sub><sup>+</sup> irradiation under the unchanged beam condition of the beam energy 2150 keV/u with the beam current 12 pA.

the materials as a function of the irradiation time under the same beam conditions was compared. For similar beam parameters, YAG:Ce, CaF<sub>2</sub>:Eu and CsI:Tl show stable and consistent results for the beam width (Figure 4.21) within the experimental uncertainty of 10% which can be mainly attributed to the beam current variation. I notice that E. Gütlich et al. [Gütlich et al. (2010b)] have reported that the imaged beam width of YAG:Ce and CaF<sub>2</sub>:Eu showed a constant behavior during the irradiation of the 17 nA C<sup>2+</sup> ion beam at 11.4 MeV/u, but slight difference (<5%) in beam width between these two scintillators was observed. However, within our experiment uncertainty, no significant discrepancy was observed in beam width between YAG:Ce and CaF<sub>2</sub>:Eu in our test.

On the other hand, the beam width measured using KBr scintillators during continuous irradiation was not stable, as shown in Figure 4.22 (a). The beam width of KBr exhibits an initial fall, followed by a rapid increase and finally a very slow rise which appears to continue indefinitely. I have found that the beam width of KBr coherently changes with the light yield in opposite

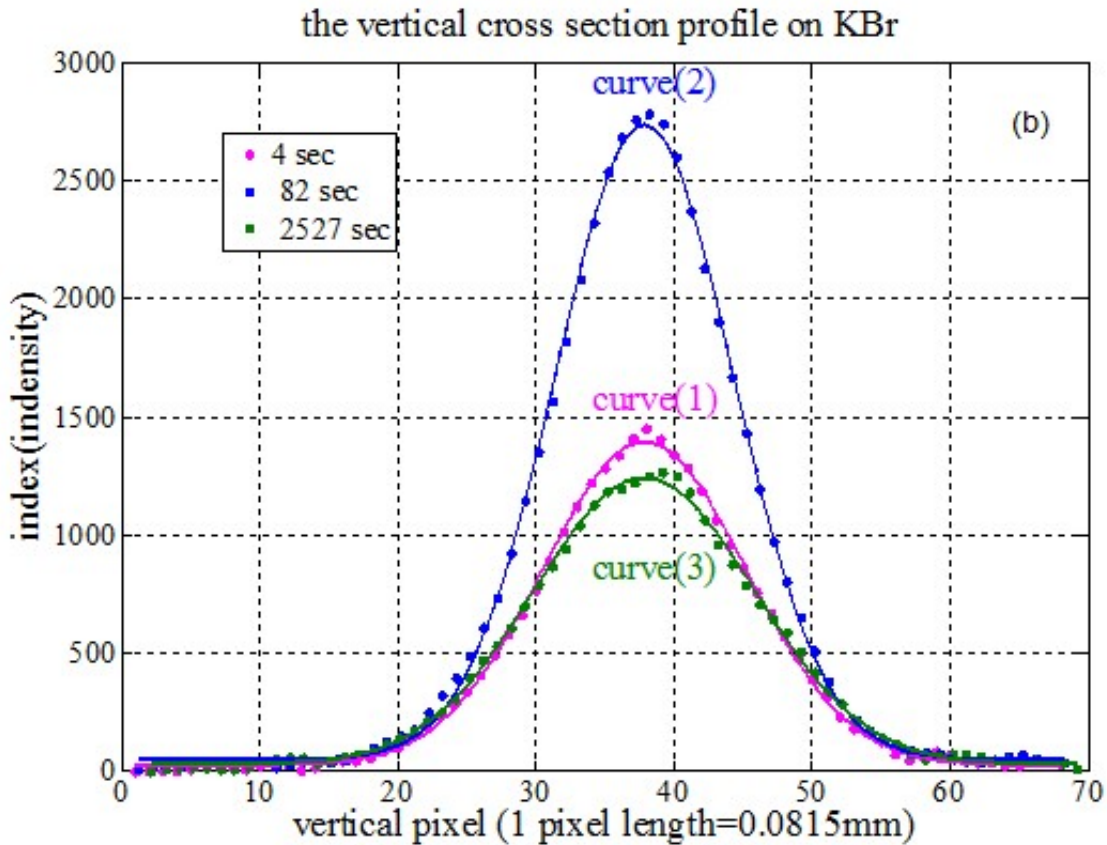
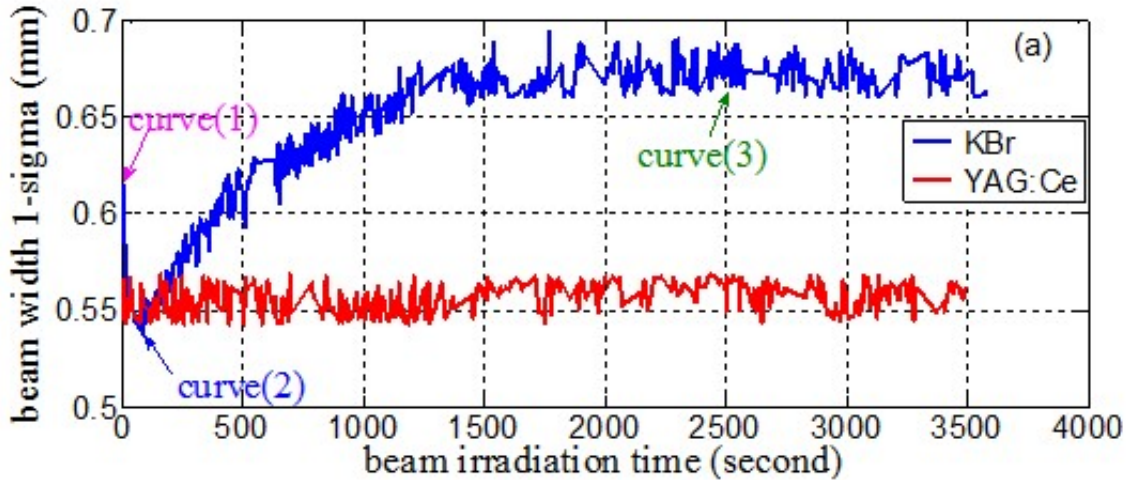


Figure 4.22 (a) Beam width of YAG:Ce and KBr materials determined from Gaussian fits to the vertical projection for  $H_2^+$  irradiation under the unchanged beam condition of the beam energy 600 keV/u with the beam current 380 pA. A constant beam width in YAG:Ce is plotted as a comparison. (b) The detail comparison of vertical projections at different irradiation time for the beam width evolution of KBr in plot (a). Curve (1), (2) and (3) represent the vertical projections at the irradiation time of 4, 82 and 2527 seconds, respectively. The dots are the experimental points and the solid lines show Gaussian fits. The beam widths in  $1-\sigma$  obtained from Gaussian fits are 0.616 mm for curve (1), 0.539 mm for curve (2) and 0.674 mm for curve (3).

directions. For some alkali halides such as KBr, the luminescence centers are formed by radiation-induced defects (color centers), resulting in the fluence dependence of scintillation efficiency. The luminescence of KBr is regulated by the fluence-dependent formation of F- and V- type color centers as well as the diffusion and recombination of these centers. Due to the fluence dependence of the luminescence in KBr and the non-uniform distribution of current density, the central region of the beam spot with a higher fluence shows a faster initial rise of luminescence than the outer region of the beam spot with a lower fluence, which leads to beam width reduction (as shown in Figure 4.22 (b), curve(1)→curve(2)). As the F-centers in KBr begin to form F-center aggregate, the central region of the beam spot with a higher fluence exhibits more rapid degradation of luminescence than the outer region of the beam spot, which increases the beam width (as shown in Figure 4.22 (b), curve(2)→curve (3)). As a result, the fluence-dependent scintillation efficiency of KBr leads to a significantly unstable behavior in the beam width.

### 4.3.3 Scintillation stability comparison in low- and high-energy irradiation

As expected, all the investigated materials exhibit more stable scintillation response in the ion energy range of 600-2150 keV/u, compared with that in low energies of a few keV/u. We have measured the scintillator yield of the YAG:Ce scintillator irradiated with  $H_2^+$  beam at 25 keV/u in the low energy beam transport section of ReA3. Figure 4.23 shows a comparison of the scintillation responses of YAG:Ce under  $H_2^+$  irradiation at bombarding energies of 25 keV/u and 600 keV/u. Strong scintillation degradation is observed at low energy bombardment where the ion penetration depth is less than 1  $\mu\text{m}$ . A similar degradation at low energies has also been observed for  $\text{CaF}_2:\text{Eu}$  and  $\text{CsI:Tl}$ . In order to clarify such different scintillation behaviors at the low- and high-energy bombardment, the displacement damage induced by ion irradiation was analyzed using the SRIM code [ Ziegler (2013)]. Under ion irradiation, the energy transferred by an energetic particle to a scintillator can be split between two channels: (1) nuclear collision and (2) ionization and electronic excitation [ Liu et al. (2014)]. The energy transfer through nuclear collision can induce a collision cascade of the lattice atoms to displace the atoms from their normal lattice positions.

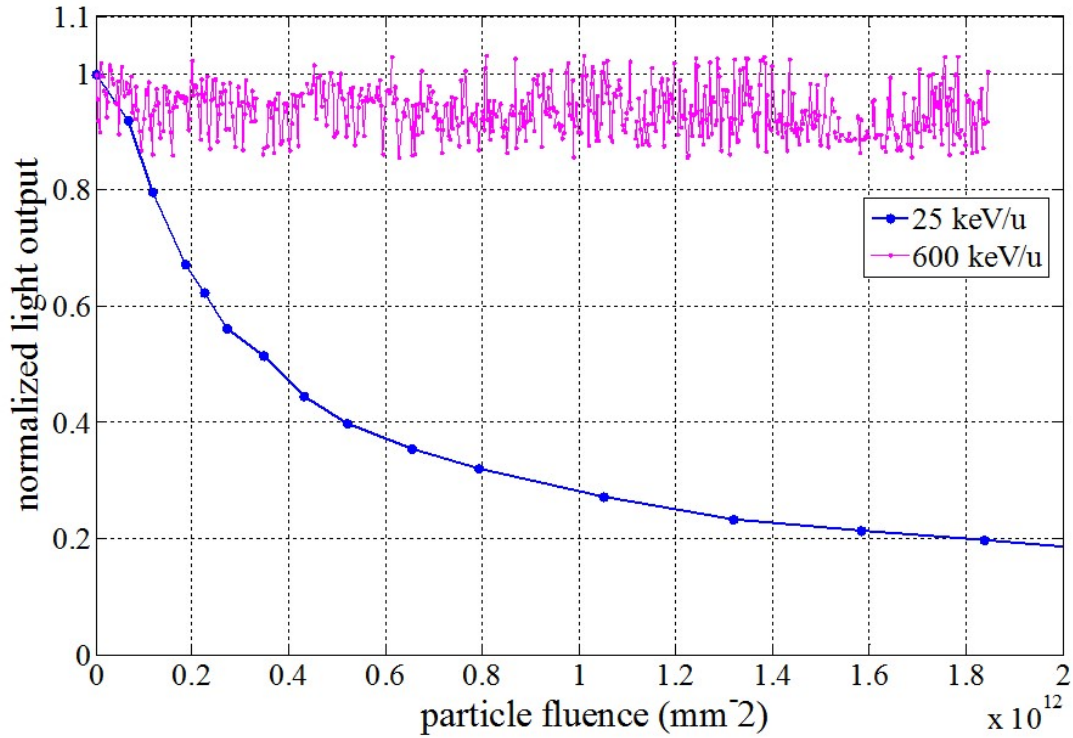


Figure 4.23 Scintillation response of YAG:Ce during  $\text{H}_2^+$  continuous irradiation at the bombarding energies of 25 keV/u and 600 keV/u. The data are normalized to the initial light yield. The irradiation experiment of the YAG: Ce scintillator at 25 keV/u was performed in the low energy beam transport section of the rare isotope ReAccelerator (ReA) facility.

As a result of the collisions, a large quantity of defects in the crystal, such as vacancies and interstitial atoms, can be created as color centers to absorb photons emitted from luminescence centers. The energy deposited into the target electrons through the ionization/excitation process, known as electronic-energy deposition density, can contribute to the production of the scintillation photons. I have used the SRIM code [ Ziegler (2013)] to simulate the electronic-energy deposition density  $(\frac{dE}{dx})_{elec}$  and the target-atomic displacement number  $(\frac{dN}{dx})_{dis}$  as a function of the ion penetration depth for YAG ( $\text{Y}_3\text{Al}_5\text{O}_{12}$ ) under proton irradiation at energies of 25 keV/u and 600 keV/u, as shown in Figure 4.24. The typical threshold displacement energies of 66 eV for Y, 56 eV for Al and 40 eV for O were taken from literature [ Ubizskii et al. (2014)] as the input parameters of the SRIM code. The target-atomic displacement number can characterize the defect distribution along the ion path. The results in Figure 4.24 reveal that the displacement damage is not uniformly

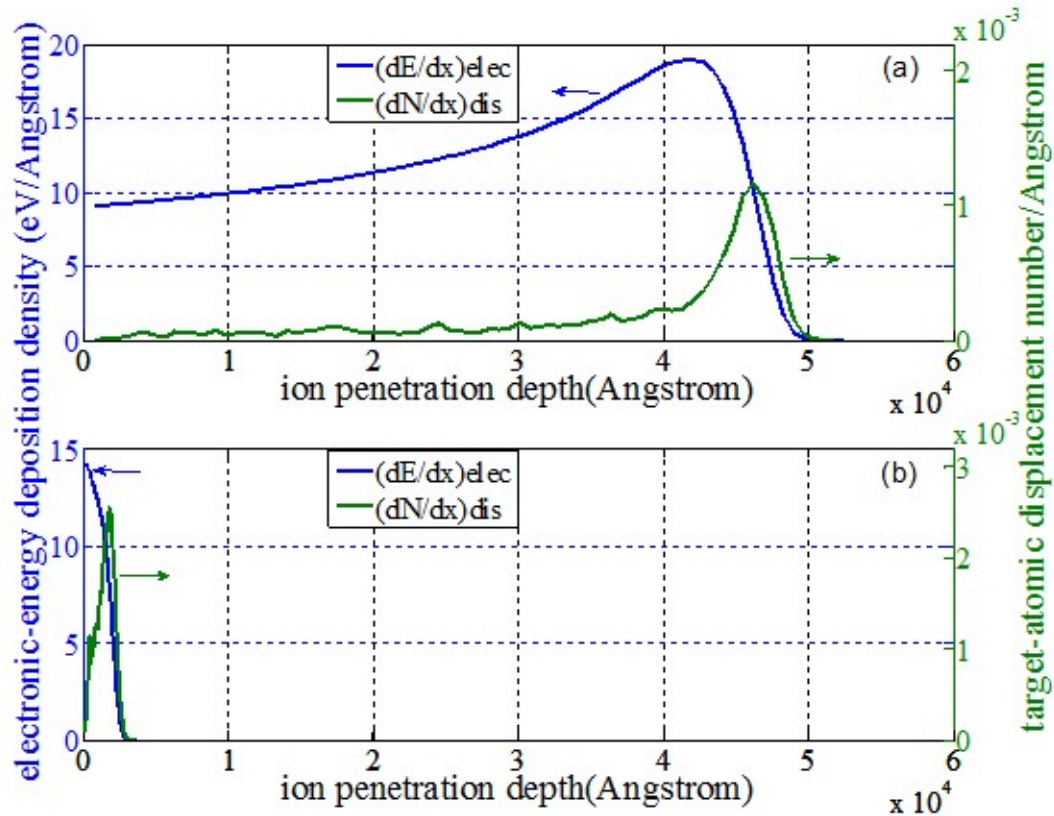


Figure 4.24 The simulated distributions of the electronic-energy deposition density and the target-atomic displacement number as a function of the ion penetration depth under proton bombardment at energies of (a) 600 keV/u and (b) 25 keV/u.

generated by the nuclear collision along the ion track, but is mainly concentrated in the end of the track. As a particle propagates through the scintillator, the energy loss per unit penetration depth along its trajectory can be characterized by the Bragg Curve. When the projectile slows down inside the scintillator, it deposits most of the energy towards the end of its trajectory, leading to the formation of the Bragg peak. At the high ion energy of 600 keV/u, the energy deposited to the target nuclei is much smaller than that to the target electrons. The displacement damage only contributes to the very end of the particle trajectory (quenching region). The vacancies and interstitials are few outside of the quenching region, leading to negligible absorption effects on the scintillation photons. The majority of photons are emitted from the luminescence centers outside of the quenching region and experience insignificant transparency loss of light propagation. The negligible transparency loss of the scintillation photons determines the stability of the scintillation

response under high-energy irradiation. On the contrary, at the low energy of 25 keV/u, the energy transfer through nuclear collision becomes significant. The damaged defects are highly efficient to absorb the luminescence emission along the entire ion track, resulting in significant degradation in the light output as the particle fluence increases.

## CHAPTER 5

### SUMMARY AND CONCLUSIONS

#### 5.1 Beam energy calibration and determination

The energy calibration of the  $45^\circ$  magnetic analyzer in ReA3 has been completed by measuring (p, $\gamma$ ) resonance reactions and developing a time-of-flight system. The resonances of the  $^{27}\text{Al}(p,\gamma)^{28}\text{Si}$  reaction at  $E_p=992$  keV and 632 keV and the  $^{58}\text{Ni}(p,\gamma)^{59}\text{Cu}$  at  $E_p=1843$  keV have been measured by the CAESAR and SuN detectors to determine the calibration factor of the magnetic analyzer. The methods for the dipole energy calibration as well as the analysis results are summarized in Table 5.1. In the first column, the beam energy of the calibration points are given. The methods for the measurements of the dipole calibration factor are described in the second column. All the results of the dipole calibration factor obtained from the (p, $\gamma$ ) resonance reactions and the TOF measurements are listed in the third column. The  $k$  values listed in Table 5.1 from (p, $\gamma$ ) resonance reactions were taken from the measurements without the use of the L091 rebuncher cavity or the slit in the horizontal  $90^\circ$  bending achromat to reduce beam energy spread.

Figure 5.1 shows the dipole calibration factor  $k$  as a function of beam energy for the three parts of the beam energy calibration measurements. The dipole calibration factor exhibits a field

Calibration energy (keV/u)	Methods	Dipole calibration factor $k$
632.2	$^{27}\text{Al}(p,\gamma)^{28}\text{Si}$ by the CAESAR detector	$4651.12 \times 10^{-6}$
991.88		$4648.66 \times 10^{-6}$
991.88	$^{27}\text{Al}(p,\gamma)^{28}\text{Si}$ & $^{58}\text{Ni}(p,\gamma)^{59}\text{Cu}$ by the SuN detector	$4657.146 \times 10^{-6}$
1843.5		$4662.968 \times 10^{-6}$
1404.814	Time-Of-Flight measurements	$4663.383 \times 10^{-6}$
2098.029		$4656.401 \times 10^{-6}$

Table 5.1 Summary of the measurements of dipole calibration factor  $k$  ( $\text{T}/\sqrt{\text{keV} \cdot \text{amu}}$ ).

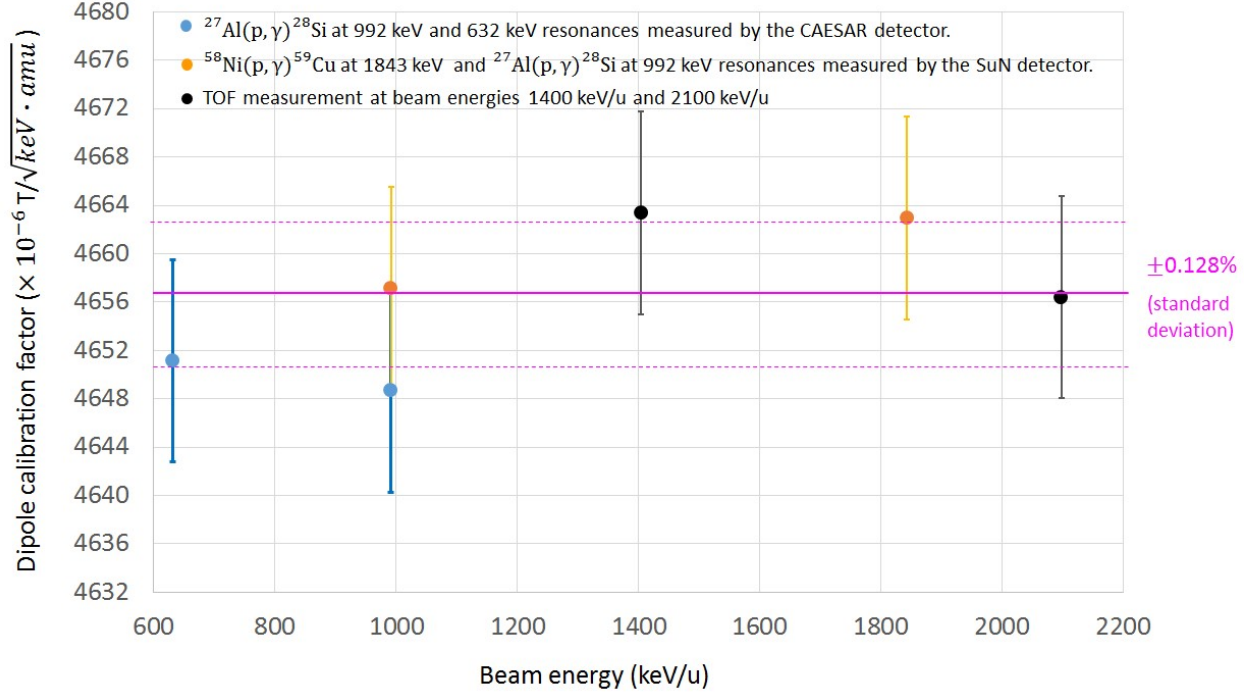


Figure 5.1 Results from the dipole calibration factor  $k$  are plotted as a function of beam energy for the three parts of the beam energy calibration measurements, as listed in Table 5.1. The error bar of each data point is mainly contributed from the systematic error of 0.18 % due to the inconsistent incident angle of the beam central ray into the magnetic analyzer (see the discussion in Section 3.1.4.3). The horizontal solid line with the pink color is the average  $k$  value with the standard deviation of 0.128 % as marked by the pink dashed lines.

independence in the beam energy range of 600 – 2100 keV/u (the magnetic field range of 0.22898 – 0.42827 T). The average value of the dipole calibration factor represented by the horizontal solid line in Figure 5.1 is  $(4656.61 \pm 6.00) \times 10^{-6} (T/\sqrt{keV \cdot amu})$  with the standard deviation of 0.128 %, leading to a beam energy determination uncertainty ( $\Delta E/E$ ) of  $\sim 0.25$  %. The main uncertainty in the dipole energy calibration is probably attributed to the inconsistent beam trajectory incident angle into the magnetic analyzer. For the example given in Figure 3.35, the inconsistent angle of the beam central ray into the magnet can induce the error of the magnetic field determination by  $\Delta B/B \sim 0.15$  %, resulting in  $\Delta k/k \sim 0.15$  %. The inconsistent beam trajectory through the magnetic analyzer may be caused by asymmetric beam profiles, a slight inclination of the ReA3 platform altitude, the misalignment of the slit scanners in diagnostic stations 6 and 7, or other beam tuning errors. Asymmetric beam profiles in the entrance and exit of the magnetic analyzer measured

by the slit scanners in diagnostic stations 6, 7 and 9 induced uncertainty of defining beam-peak centroids, leading to difficulty of maintaining the consistent beam trajectory through the magnet. The installation of the third cryomodule on the ReA3 platform may cause the slight inclination of the platform altitude and change the incident angle of the beam central ray into the magnet.

The uncertainty in the magnetic field of the magnetic analyzer (due to the dipole hysteresis effect, room-temperature variations and the Hall probe precision) shows a small contribution to the uncertainty of the dipole energy calibration measurements. The uncertainty of achieving reproducible magnetic field through the cycling of the magnet is  $\Delta B/B \sim 0.02 \%$ . The sensitivity of magnetic field to a daily room-temperature variation can result in a magnetic field variation of  $\sim 0.019 \%$  while the precision of the Hall probe is  $0.01 \%$ .

Compared with the use of the  $45^\circ$  magnetic analyzer, the TOF system can provide better beam energy precision of  $\sim 0.1 \%$ . The uncertainty of the flight length in 1 cm between two detectors gives a beam energy error of  $0.25 \%$ . The  $45^\circ$  magnetic analyzer and the TOF system both can become a useful tool to precisely determine the absolute beam energy in ReA3.

## 5.2 Scintillation degradation measurements

I have observed fast degradation of the scintillation yield for a single crystal YAG: Ce under alpha particle bombardment at low energies between 28 and 58 keV. In this low radiation energy range, I have explained the degradation of the luminescence efficiency quantitatively by the Birks model [ Birks & Black (1951)] and shown strong evidence of the competition mechanism between the creation of luminescence centers and damage defects. Using the Birks model, the relative exciton capture probability, the damage cross section and the half brightness fluence were estimated quantitatively for single charged helium ions in the energy range of 28keV to 48keV. The relative exciton capture probability  $k$  is weakly dependent on the ion energy. The average value of  $k$  over the measured energy is  $6.7 \pm 0.7$ . As the beam energy increases, the scintillation yield degrades less and the half brightness fluence increases.

Further investigation for the scintillation degradation of various scintillator materials irradiated

by ion beams in a wide energy range was pursued. I measured the scintillation response and imaging properties for KBr, YAG:Ce, CaF<sub>2</sub>:Eu and CsI:Tl scintillators under H<sub>2</sub><sup>+</sup> irradiation at energies of 600 - 2150 keV/u. Experimental results show that the luminescence intensity and beam width for YAG:Ce and CsI:Tl as a function of particle fluence are quite stable in the energy range of 600 - 2150 keV/u. The luminescence of CaF<sub>2</sub>:Eu screen shows an initial rapid decay, followed by a stable response, whereas the imaging beam width of this screen seems to be stable during the entire irradiation. The dependence of luminescence and beam width on particle fluence for KBr due to the recombination of F- and V- centers was observed and investigated. In general, the light yield for all the materials exhibits a nearly linear response with respect to the beam energy within the investigated energy range. The CsI:Tl scintillator provides the highest scintillation efficiency among all the materials. Under the same beam conditions, the shapes of the projected profiles for YAG:Ce, CaF<sub>2</sub>:Eu and CsI:Tl agree with each other very well. The extracted beam width from the images of these materials is very consistent. YAG:Ce and CsI:Tl are good candidates for our beam diagnostic application because of their high light yield and stable scintillation response. However, the KBr scintillator is not favorable due to very low scintillation efficiency and an unstable behavior in the light yield and beam width under irradiation.

The significant degradation in the emitted light output of scintillator screens under low-energy irradiation was found, which can limit the performance of the scintillator in ion source injector systems. Using the SRIM, it was demonstrated that under low-energy ion bombardment, ion-induced defects are highly efficient to degrade transparency of scintillation photons inside an irradiated scintillator.

## **BIBLIOGRAPHY**

## BIBLIOGRAPHY

- Bazhin, A. I., E. O. Rausch & E. W. Thomas. 1976. Luminescence induced by ion impact on alkali-halide crystals at high temperatures (-160 to 200 °C). *Phys. Rev. B* 14. 6.
- Birattari, C., M. Castiglioni & M. Silari. 1992. Absolute calibration of accelerator beam energies by the crossover technique. *Nuclear Instruments and Methods in Physics Research A* 320. 413–431.
- Birks, J. B. & F. A. Black. 1951. Deterioration of anthracene under  $\alpha$ -particle irradiation. *Proc. Phys. Soc. A* 64. 511.
- Bondelid, R. O. & C. A. Kennedy. 1959. Precise determination of nuclear reaction energies and measurements of resonance widths. *Phys. Rev.* 115. 6.
- Broggio, D., J. M. Jung, R. Barillon & T. Yamauchi. 2005. Degradation of the scintillation yield of anthracene under high-fluence carbon ion beams. *Radiat. Meas.* 39. 283.
- Chen, Wei, Sarah L. Westcott & Jun Zhang. 2007. Dose dependence of x-ray luminescence from  $\text{CaF}_2:\text{Eu}^{2+}$ ,  $\text{Mn}^{2+}$  phosphors. *Appl. Phys. Lett.* 91. 211103.
- Chronidou, C., K. Spyrou, S. Harissopulos, S. Kossionides & T. Paradellis. 1999. Resonance strength measurements of the  $^{27}\text{Al}(p,\gamma)^{28}\text{Si}$  reaction in the energy range  $E_p = 0.2\text{--}2.0\text{MeV}$ . *The European Physical Journal A* 6. 303–308.
- Chung, M. S. & T.E. Everhart. 1974. Simple calculation of energy distribution of low-energy secondary electrons emitted from metals under electron bombardment. *Journal of Applied Physics* 45. 707 – 709.
- Crisp, J., D. Constan-Wahl, B. Durickovic, G. Kiupel, S. Krause, D. Leitner, S. Nash, J. A. Rodriguez, T. Russo, R. Webber, W. Wittmer, N. Eddy, C. Briegel, B. Fellenz & D. Slimmer. 2013. Beam position and phase measurements of microampere beams at the michigan state university ReA3 facility. *Proceedings of PAC2013, Pasadena, CA, USA*. THPAC20.
- Dhoble, S. J., I. M. Nagpure, N. S. Dhoble & Pablo Molina. 2011. Effect of Bi ion on  $\text{Eu}^{2+} \leftrightarrow \text{Eu}^{3+}$  conversion in  $\text{CaF}_2:\text{Eu}$  phosphors for RPL dosimetry. *J. Mater. Sci.* 46. 7253.
- Din, G. U. & A. M. Al-Naser. 1975. A study of resonances in the  $^{58}\text{Ni}(p,\gamma)^{59}\text{Cu}$  reaction below 2.15 MeV. *Australian Journal of Physics* 28. 503–21.
- Dujardin, C., C. Pedrini, J. C. Gâcon, A. G. Petrosyan, A. N. Belsky & A. N. Vasilev. 1997. Luminescence properties and scintillation mechanisms of cerium- and praseodymium-doped lutetium orthoaluminate. *J. Phys.: Condens. Matter* 9. 5229–5243.
- Eijk, C.W.E. Van, J. Andriessen, P. Dorenbos & R. Visser. 1994.  $\text{Ce}^{3+}$  doped inorganic scintillators. *Nuclear Instruments and Methods in Physics Research Section A* 348. 546.

- Endt, P. M. & C. Van der leun. 1978. Energy levels of A=21-44 nuclei (VI). *Nuclear Instruments and Methods in Physics Research A* 310. 1–752.
- Evers, E. J., J. W. De Vries, G. A. P. Engelbertink & C. Van Der Leun. 1987. A simple method for energy calibration of heavy-ion beams. *Nuclear Instruments and Methods in Physics Research A* 257. 91–96.
- Facco, A., C. Compton, J. Crisp, K. Elliott, M. Hodek, M. Johnson, M. Leitner, I. Malloch, D. Miller, S. Miller, D. Morris, D. Norton, R. Oweiss, J. Ozelis, J. Popierlaski, L. Popierlaski, K. Saito, N. Usher, G. Velianoff, D. Victory, J. Wei, K. Witgen, Y. Xu & S. Zhao. 2013. Faced issues in ReA3 quarter-wave resonators and their successful resolution. *Proceedings of SRF2013, Paris, France*. THIOD02.
- Ferreroet, A. M. J., A. Garcia, S. Gil, A. Etchegoyen, M. Di Tasa, A. J. Pacheco, D. Abriola, D. E. Digregorio, M. Elgue, M. C. Etchegoyen, J. O. Fernández Niello, A. O. Macchiavelli & J. E. Testoni. 1989. Improved beam-energy calibration technique for heavy-ion accelerators. *Nuclear Instruments and Methods in Physics Research B* 42. 389–392.
- Forck, P., C. Andre, F. Becker, R. Haseitl, A. Reiter, B. Walasek-Höhne, R. Krishnakumar & W. Ensinger. 2014. Scintillation screen investigations for high energy heavy ion beams at GSI. *proceedings of DIPAC2011, Hamburg, Germany*. MOPD53.
- Freye, T., H. Lorentz-Wirzba, B. Cleff, H. P. Trautvetter & C. Rolfs. 1977. Voltage calibration of low-energy accelerators. *Zeitschrift für Physik A* 281. 211–218.
- Greskovich, C. & S. Duclos. 1997. Ceramic scintillators. *Annu. Rev. Mater. Sci.* 27. 69.
- Gütlich, E., W. Ensinger, P. Forck, R. Haseitl & B. Walasek-Höhne. 2010a. Light yield, imaging properties and spectral response of inorganic scintillators under intense ion irradiation. *Proceedings of BIW10, Santa Fe, New Mexico, US*. TUPSM019.
- Gütlich, Eiko, Peter Forck, Wolfgang Ensinger & Beata Walasek-Höhne. 2010b. Scintillation screen investigations for high-current ion beams. *IEEE Trans. Nucl. Sci.* 57. 1414–1419.
- Harissopoulos<sup>1</sup>, S., C. Chronidou<sup>1</sup>, K. Spyrou, T. Paradellis<sup>1</sup>, C. Rolfs, W. H. Schulte & H. W. Becker. 2000. The  $^{27}\text{Al}(p,\gamma)^{28}\text{Si}$  reaction: direct capture cross-section and resonance strengths at  $E_p=0.2\text{--}1.12\text{MeV}$ . *The European Physical Journal A* 9. 479–489.
- Hayes, W. & A. M. Stoneham. 1985. *Defects and defect processes in nonmetallic solids*. John Wiley & Sons, New York.
- Hirouchi, T., M. Nishiura, T. Nagasaka, T. Ido, D. Funaki, T. Kobuchi, A. Okamoto, S. Kitajima, M. Sasao, K. Fujioka, M. Isobe & T. Mutoh. 2009. Effect of ion beam and neutron irradiations on the luminescence of polycrystalline Ce-doped  $\text{Y}_3\text{Al}_5\text{O}_{12}$  ceramics. *J. Nucl. Mater.* 386-388. 1049–1051.
- Hollerman, W. A., J. H. Fisher, L. R. Holland, G. M. Jenkins, D. B. Nisen & E. K. Williams. 1994. Measurement of fluorescence phenomena from yttrium and gadolinium fluors using a 45 MeV proton beam. *Nuclear Instruments and Methods in Physics Research Section A* 353. 20.

- Hollerman, W. A., J. H. Fisher, G. A. Shelby, L. R. Holland & G. M. Jenkins. 1992. Spectroscopic analysis of proton-induced fluorescence from yttrium and gadolinium oxysulfide phosphors. *IEEE Trans. Nucl. Sci.* 39. 2295.
- Hollerman, William A., Stephen W. Allison, Shawn M. Goedeke, Philip Boudreaux, Robert Guidry & Earl Gates. 2003. Comparison of fluorescence properties for single crystal and polycrystalline YAG:Ce. *IEEE Trans. Nucl. Sci.* 50. 4.
- Johnson, Michael L. & Lindsay M. Faunt. 1992. Parameter estimation by least-squares methods. *Methods in Enzymology* 210. 1–37.
- Kester, O., D. Bazin, C. Benatti, J. Bierwagen, G. Bollen, S. Bricker, S. Chouhan, C. Compton, K. Davidson, J. DeLauter, M. Doleans, T. Glasmacher, W. Hartung, M. Johnson, F. Marti, J. Ottarson, L. Popielarski, J. Popielarski, M. Portillo, D. Sanderson, S. Schwarz, N. Verhanovitz, J. Vincent, J. Wlodarczak, X. Wu, J. Yurkon, A. Zeller & Q. Zhao. 2009. The MSU/NSCL Re-Accelerator ReA3. *Proceedings of SRF2009, Berlin, Germany*. MOOCAU05.
- Knoll, G. F. 2010. *Radiation detection and measurements*. John Wiley & Sons, Inc.
- Kotomin, E. A. & A. I. Popov. 1998. Radiation-induced point defects in simple oxides. *Nuclear Instruments and Methods in Physics Research B* 141. 1–15.
- Krebs, Karl Heinz. 1968. Electron ejection from solids by atomic particles with kinetic energy. *Fortschritte der Physik* 16. 419–490.
- Leitner, Daniela, Chris Compton, Alberto Facco, Matt Hodek, Alain Lapiere, Sam Nash, Dan Morris, Georgios Perdikakis, John Popielarski, Nathan Usher, Walter Wittmer, Q. Zhao & X. Wu. 2011. Status of the reaccelerator facility REA for rare isotopes beam research. *Proceedings of SRF2011, Chicago, IL, USA*. THIOB03.
- Linhardt, L. E., L. Baby, D. W. Bardayan, J. C. Blackmon, H. Gardiner, E. Johnson, E. Koschiy, K. T. Macon, M. Matos, B. C. Rasco, G. Rogachev, D. Santiago-Gonzalez & I. Wiedenhoever. 2012. Measurement of  $^{17}\text{F} + \text{p}$  reactions with ANASEN. *J. Phys.: Conference Series* 403. 012036.
- Liu, Peng, Yanwen Zhang, Haiyan Xiao, Xia Xiang, Xuelin Wang & William J. Weber. 2014. Nonlinear luminescence response of  $\text{CaF}_2:\text{Eu}$  and  $\text{YAlO}_2:\text{Ce}$  to single-ion excitation. *J. Appl. Phys.* 115. 033108.
- Maas, J. W., E. Somorjai, H. D. Graber, C. A. Van Den Wijngaart, C. Van Der Leun & P. M. Endt. 1978. Investigation of  $^{28}\text{Si}$  levels with the  $(\alpha, \gamma)$  and  $(\text{p}, \gamma)$  reactions. *Nuclear Physics A* 301. 213–236.
- Mak, H. B., H. B. Jensen & C. A. Barnes. 1973. Absolute measurement of accelerator beam energy by the time-of-flight techniques. *Nuclear Instruments and Methods* 109. 529–532.
- Manura, D. & D. A. Dahl. 2007. SIMION 8.0 user manual. Scientific Instrument Services .
- Marion, Jerry B. 1966. Accelerator calibration energies. *Reviews of Modern Physics* 38. 4.

- Martin, Bernd, Rainer Michaelsen, Ram C. Sethi & Klaus Ziegler. 1985. A method for the energy calibration of a heavy ion accelerator. *Nuclear Instruments and Methods in Physics Research A* 238. 1–4.
- McParland, Brian J. 2010. *Nuclear medicine radiation dosimetry: Advanced theoretical principles*. New York, NY: Springer.
- Meyer, M. A., I. Venter & D. Reitmann. 1975. Energy levels of  $^{28}\text{Si}$ . *Nuclear Physics A* 250. 235–256.
- Michaelian, K. & A. Menchaca-Rocha. 1994. Model of ion-induced luminescence based on energy deposition by secondary electrons. *Phys. Rev. B* 49. 15550.
- Minty, B. R. S. 1997. Fundamentals of airborne gamma-ray spectrometry. *AGSO Journal of Australian Geology and Geophysics* 17. 39–50.
- Mitsushima, Y., K. Morita, N. Matsunami & N. Itoh. 1976. Determination of the  $V_4$ -center structure in KBr crystal by means of double alignment channeling technique. *J. Phys. Colloques* 37. C7–95.
- Moszyński, M., T. Ludziejewski, D. Wolski, W. Klamra & L. O. Norlin. 1994. Properties of the YAG:Ce scintillator. *Nuclear Instruments and Methods in Physics Research Section A* 345. 461.
- Nakata, Ryohei, Katsuyasu Kawano, Minoru Sumita & Eiichi Higuchi. 1979. ESR study of europium ions in hydrolyzed  $\text{CaF}_2$ : Eu crystals. *J. Phys. Chem. Solids* 40. 955.
- Olsen, D. K., N. H. Merrill, S. F. Biagi, W. R. Phillips & A. R. Barnett. 1974. A simple beam-energy measurer for heavy ions. *Nuclear Instruments and Methods* 114. 615–617.
- Perdikakis, G., D. Bazin, J. Browne, L. Lin, D. Leitner & W. Wittmer. 2012. Instrumentation at the low intensity frontier: diagnostics for the stopped and reaccelerated beams of NSCL and FRIB. *Proceedings of BIW2012, Newport News, VA, USA*. MOPG038.
- Popov, A. I., E. A. Kotomin & J. Maier. 2010. Basic properties of the F-type centers in halides, oxides and perovskites. *Nuclear Instruments and Methods in Physics Research Section B* 268. 3084.
- Ripert, M., A. Buechel, A. Peters, J. Schreiner & T. Winkelmann. 2010. A low energy ion beam pepper pot emittance device. *proceedings of BIW10, Santa Fe, New Mexico, US*. TUPSM060.
- Rolfs, Claus E. & William S. Rodney. 1988. *Cauldrons in the cosmos*. The University of Chicago Press.
- Rotberg, V., D. Pereira, M. N. Rao, N. Ueta & O. Sala. 1976. Calibration of the tandem pelletron accelerator. *Revista Brasileira de Física* 6. 3.
- Santra, S., K. Mahata, P. Singh, C. V. Fernandes, M. Hemalatha & S. Kailas. 2003. Beam energy calibration for the folded tandem ion accelerator. *Nuclear Instruments and Methods in Physics Research A* 496. 44–50.

- SCHWARTZ, K. 1996. Excitons and radiation damage in alkali halides. *RAU Scientific Reports & Solid State Electronics and Technologies* 1. 14.
- Simon, A., S. J. Quinn, A. Spyrou, A. Battaglia, I. Beskin, A. Best, B. Bucher, M. Couder, P. A. DeYoung, X. Fang, J. Gorres, A. Kontos, Q. Li, S.N. Liddick, A. Long, S. Lyons, K. Padmanabhan, J. Peace, A. Roberts, D. Robertson, K. Smith, M. K. Smith, E. Stech, B. Stefanek, W. P. Tan, X. D. Tang & M. Wiescher. 2013. SuN: Summing NaI(Tl) gamma-ray detector for capture reaction measurements. *Nuclear Instruments and Methods in Physics Research A* 703. 16–21.
- Spyrou, A., H. W. Becker, A. Lagoyannis, S. Harissopulos & C. Rolfs. 2007. Cross-section measurements of capture reactions relevant to the p process using a  $4\pi$   $\gamma$ -summing method. *Physical Review C* 76. 015802.
- Sternglass, E. J. 1957. Theory of secondary electron emission by high-speed ions. *Physical Review* 108. 1.
- Strohmeier, M., J. Y. Benitez, D. Leitner, C. M. Lyneis, D. S. Todd & M. Bantel. 2010. Development of a pepper-pot device to determine the emittance of an ion beam generated by electron cyclotron resonance ion sources. *Rev. Sci. Instrum.* 81. 02B710.
- Sunta, C. M. 1984. A review of thermoluminescence of calcium fluoride, calcium sulphate and calcium carbonate. *Radiat. Prot. Dosim.* 8. 25.
- Sunta, C. M. 2014. *Unraveling thermoluminescence*. Springer Series in Materials Science.
- Tanke, E., W. Ding, J. A. Rodriguez, W. Wittmer, X. Wu & S. Valero. 2012. Status of the beam dynamics code DYNAC. *Proceedings of LINAC2012, Tel-Aviv, Israel*. THPB065.
- Tanke, E., S. Valéro, P. Lapostolle & Pierre M. 2002. Dynac: a multi-particle beam dynamics code for leptons and hadrons in complex accelerating elements. *Proceedings of LINAC2002, Gyeongju, Korea*. pp.e–proc. TH429.
- Trautvetter, H. P., K. Elix & C. Rolfs. 1979. Energy determination of heavy-ion beams. *Nuclear Instruments and Methods* 161. 173.
- Trefilova, L., B. Grinyov, V. Alekseev, I. Golub, V. Yakovlev & A. Meleshko. 2007. The reasons the scintillation efficiency decrease of CsI(Tl) crystals exposed by the high-dosed radiation. *Radiat. Meas.* 42. 839.
- Ubizskii, S. B., A. O. Matkovskii, N. A. Mironova-Ulmane, V. Skvortsova, A. Suchocki, Y. A. Zhydachevskii & P. Potera. 2014. Radiation displacement defect formation in some complex oxide crystals. *Nuclear Instruments and Methods in Physics Research Section B* 166-167. 40.
- Uhrmacher, M., K. Pampus, F. J. Bergmeister, D. Purschke & K. P. Lieb. 1985. Energy calibration of the 500 kV heavy ion implanter. *Nuclear Instruments and Methods in Physics Research Section B* 9. 234–242.

- Weisshaar, D., A. Gade, T. Glasmacher, G. F. Grinyer, D. Bazin, P. Adrich, T. Baugher, J. M. Cook, C. Aa. Diget, S. McDaniel, A. Ratkiewicz, K. P. Siwek & K. A. Walsh. 2010. Caesar-a high-efficiency CsI(Na) scintillator array for in-beam  $\gamma$ -ray spectroscopy with fast rare-isotope beams. *Nuclear Instruments and Methods in Physics Research A* 624. 615–623.
- Wilkerson, J. F., T. B. Clegg & E. J. Ludwig. 1983. An energy calibration of the tunl dual-90° magnet analyzing system. *Nuclear Instruments and Method* 207. 331.
- Wilkinson, M. H. F. & F. Schut. 1998. *Digital image analysis of microbes: Imaging, morphometry, fluorometry and motility techniques and applications*. John Willey and Sons, Inc.
- Yong-Feng, RUAN, Hiroshi NAKA & Takatomo SASAKI. 2000. BO<sub>2</sub>-F<sup>+</sup> centers in the radiation-damaged YCOB crystals. *Chin. Phys. Lett* 17. 896.
- You, Fangtian, Adrie J. J. Bos, Qiufeng Shi, Shihua Huang & Pieter Dorenbos. 2012. Thermoluminescence investigation of donor (Ce<sup>3+</sup>, Pr<sup>3+</sup>, Tb<sup>3+</sup>) acceptor (Eu<sup>3+</sup>, Yb<sup>3+</sup>) pairs in Y<sub>3</sub>Al<sub>5</sub>O<sub>12</sub>. *Physical Review B* 85. 115101.
- Zhu, R. Y. 1998. Radiation damage in scintillating crystals. *Nuclear Instruments and Methods in Physics Research Section A* 413. 297.
- Ziegler, J.M. 2013. Particle interactions with matter. <http://www.srim.org/>.